A comparative study of die attach strategies for use in harsh environments



Micaela Filipa Moreira de Sousa

Trinity College

A thesis submitted for the degree of

Doctor of Philosophy

Trinity Term 2012

Acknowledgments

First and foremost, I would like to express my sincere gratitude to my supervisor Professor Patrick Grant and co-supervisor Dr. Colin Johnston for their knowledge and guidance. Their supervision was of paramount importance in providing a model for my future career.

Appreciation must also be expressed with regard to EPSRC for funding this project, and to Trinity College and IMAPS for additional funding to attend conferences. The support for this research provided by GE Aviation Systems and industrial partners Gwent Electronic Materials, Vibro-meter, Sondex Wireline, Thermastrate must be acknowledged. Also, members of the GE Aviation Systems for training, practical advice, donation of samples and materials and use of facilities, particularly Steven Riches, Kevin Cannon, and Steven Jones. In addition, Larry Clarke and Glenn George founders of Alpha Contract Engineering Ltd., for technical assistance and use of facilities. Remarks of John Govier and Peter Ongley must also be acknowledged. I would like to thank to David Shaddock for receiving me at GE Global Research.

I would also like to thank all members of Patrick Grant's research group, especially Sophie Godard Desmarest, Hongtao Zhang, Enzo Liotti, Beatriz Mendoza, Aoife Kelly, Chaiyasit Banjongprasert, John Aveson, Vitor Marques and Jan Pearson for their support, friendship, and for furnishing the dark humor without which doing research in laboratory environment would be impracticable and probably overtly rigorous. Staff at the Begbroke Science Park are also acknowledged, especially Clive Downing, Radka Chakalova, Gamal Abbas, Kerstin Jurkschat, Dr. Robin Young and Dr. Alison Crossley for their help and kindness. I wish to thank John Critchell and Chris

Salter for providing numerous hours of advice and critiques, and Professor John Sykes for provision of laboratory facilities and helpful discussions.

I thank my parents, Maria and Antonio, and my brother Filipe, for their love, encouragement and endless support throughout my life. It was under their in-depth wisdom and foreknowledge that I gained the motivation and ability to tackle challenges head on. Finally I wish to thank to a great friend (and brilliant mathematician) Rui Morais for his huge support, and Mafalda Picarra, Nuno Nunes, Jonathan Moghal, Anuta Chindris, Rodrigo Molina, Natasha Todd-Burley, and Daniel Cornforth for their friendship during this Oxonian odyssey.

Micaela Filipa Moreira de Sousa
Trinity College
Trinity 2012

A comparative study of die attach strategies for use in harsh environments

Micaela Filipa Moreira de Sousa

Trinity College
Submitted for the Degree of Doctor of Philosophy, Trinity Term 2012
Oxford

ABSTRACT

Well-logging and aerospace applications require electronics capable of withstanding elevated temperature operation. A key element of high temperature packaging technology is the Si die attach material, and a comparative study of two die attach systems for use in harsh environment has been performed. Die bond sample packages, using commercial adhesives and an Au-Si eutectic solder, have been manufactured and were subsequently thermally exposed for various times at 250 and 300^{o}C respectively. The adhesive die bond packages comprised a high temperature co-fired ceramic (HTCC) substrate with W, Ni and Au metallisations whereas the Au-Si die bond packages used thick film Au metallised on a Al_2O_3 substrate. Optimisation of the eutectic die bonding parameters was successfully performed for the Au-Si system by an experimental design method, which improved mean and spread of maximum bonded areas and consequently, the shear load to failure. Bonded area was systematically assessed by scanning acoustic microscopy (SAM) followed by digital image analysis (DIA). Accelerated testing comprised thermal cycling and thermal shock and although showing some degradation, Au-2wt%Si die bonds were surprisingly robust, showing excellent subsequent stability during industrial device testing investigations.

Table of Contents

1 Introduction 1

1.1 Industrial context 1

1.2 Objectives 3

1.3 Scope 4

2 Literature review 5

2.1 High temperature electronics 5

2.1.1 Electronic packaging assembly 7

2.1.2 Substrate materials 13

2.1.3 Die attach materials 16

2.1.4 Interfacial intermetallic compound formation 40

2.1.5 Summary 46

2.2 Thermomechanical behavior and analysis 46

2.2.1 Reliability and accelerated testing 46

2.2.2 Scanning acoustic microscopy 48

2.2.3 Summary 53

2.3 Nanoindentation 54

2.3.1 Hardness and elastic modulus 56

2.3.2 Summary 58

2.4 Overall summary 58

3 Experimental procedure 61

3.1 Materials and manufacturing 61

3.1.1 Adhesive die attach 61

3.1.2 Au-Si eutectic die attach 64

3.2 Microstructural characterisation 69

3.3 Thermal Exposure 71

3.3.1 Isothermal ageing 71

3.3.2 Thermal cycling and thermal shock 71
3.4 Nano-indentation 72
3.5 Assessing bond quality 73
3.5.1 Scanning acoustic microscopy 73
3.5.2 Die shear testing 76
3.6 High temperature performance of SOI devices 78

4 Adhesive die attach: results and discussion 80
4.1 Staystik 415 and 482 81
4.2 GEM D4 85
4.3 Ablebond JM7000 88
4.4 Scanning acoustic microscopy 98
4.5 Adhesive strength 102
4.6 Conclusions 106

5 Au-Si die attach: results and discussion 109
5.1 Au-Si die bonding 109
5.1.1 First experimental design 110
5.1.2 Second experimental design 124
5.1.3 Experimental design 1 vs experimental design 2 128
5.2 Bond quality variability 135
5.2.1 Au-2wt%Si preforms 136
5.2.2 Au metallised substrate 143
5.3 Conclusions 161

6 Thermal exposure 163
6.1 As-manufactured 163
6.2 Ageing 172
6.2.1 Isothermal ageing at 300^{o}C 173
6.2.2 Accelerated ageing at 350^{o}C 185
6.3 Thermal cycling and thermal shock 191
6.3.1 Assessing bond quality 192
6.3.2 Microstructural characterisation 198
6.4 High temperature performance of SOI devices 202

6.4.1 SOI devices in HTCC packages 203
6.5 Conclusions 206

7 Conclusions and future work 209

Bibliography 213

A ANOVA 233

List of Figures

1.1 High temperature electronics design and implementation [7]. . 2

2.1 Caged full-bore flowmeter [12]. 7

2.2 Schematic illustration of the electronic package composed of die and die attach material [14]. 8

2.3 Schematic illustration of the screen printing process. 15

2.4 Percolation curve for ICAs and ACAs (ACFs refer to anisotropically conductive film) [34]. 18

2.5 Schematic illustration of (a) ACA, (b) ICA and (c) NCA in flip-chip bonding [34]. 19

2.6 Shape factors for adhesive fillets [52]. 24

2.7 Diagram of transient liquid phase sintering conductive adhesives [34]. 27

2.8 Moisture absorption and corresponding contact resistance shift of ECAs with 85^{o}C/85% RH aging (a) moisture absorption and (b) contact resistance shift [34]. 29

2.9 The relationship between the adhesion strength and the elastic modulus of ECA [34]. 31

2.10 Optical micrograph of a high temperature epoxy-based Ag-loaded ECA after 300 cycles of -55 to 125^{o}C [3]. 33

2.11 Au-Si phase diagram [85]. 35

2.12 Au-Sn equilibrium phase diagram [100]. 39

2.13 Au-Ge equilibrium phase diagram [85]. 40

2.14 The elastic modulus of Au-based eutectic die attach materials as a function of temperature [3]. 41

2.15 Typical metallisation arrangements comprising three distinct layers. 42

2.16 SEM images of the interfacial area between plated Ni and the Au-Si die attach material; (a) single mode failure between a Au-Si die attach and Ni plated layer; (b) doping Ni with Co frustrates IMC formation during Au-Si die attach [84]. 44

2.17 Failure at AuNiSn IMC when Au-Sn is soldered to Ni [84]. . . . 45

2.18 Schematic of the types of defects detectable in electronic packaging using SAM [116]. 48

2.19 By gating a specific A-scan echo in the time domain (A) and scanning the transducer over the entire X-Y sample area of interest (B), a C-scan image is obtained (C) [118]. 49

2.20 SAM images of a PLCC: (a) reflected mode image from the top side; (b) reflected mode C-scan image from the die attach interface [116]. 52

2.21 SAM images of a PLCC: (a) pulse-echo mode B-scan image of a cross-section of a PLCC package X-Z plane; (b) pulse-echo mode C-scan image of the molding compound of a PLCC [116]. 53

2.22 Scheme of load versus indenter displacement data for an indentation experiment [132]. 55

2.23 Schematic representation of a section through an indentation showing the various parameters used in the analysis [132]. . . . 56

3.1 Assembly process steps for adhesive die bonding. 63

3.2 Cammax EDB65 eutectic die bonder. 65

3.3 Test regime used for thermal cycling and thermal shock. 72

3.4 Representative waveform scan analysis. Orange arrow indicates an example of the front surface echo (water/Si die interface), red arrows point to examples of unbonded areas at the Si die/solder interface, yellow arrows represent examples of unbonded areas at the solder/substrate interface, green arrows indicate bonded areas, and corresponding waveforms. Black arrows define the gate. 75

3.5 Example of SAM images of Au-Si die bonds as inspected ((a), and (b)), and corresponding digital image analysis (DIA) ((c), and (d)). 76

3.6 Die shear testing schematic. 77

3.7 Dage 4000-series bond tester: (a) die shear test jig and push-off tool reading for testing; (b) during testing. 77

3.8 Assembly of demonstrator circuits. 78

3.9 (a) SOI test chip designed at GE AS; (b) SOI device assembled in HTCC package for assessment of electrical performance at 250^{o}C. 79

4.1 Cross-sectional optical micrographs of adhesive die bonds in the as-manufactured condition using: (a), (b) Staystik 415; and (c), (d) Staystik 482. 83

4.2 Cross-sectional optical micrographs of Staystik 415 and 482 die bonds under different conditions: stored at 250^{o}C for 168 hours [(a) Staystik 415; (b) Staystik 482]; thermal shock 250^{o}C to -65^{o}C, in 10 seconds [(c) Staystik 415; (d) Staystik 482]; and thermal cycling 200^{o}C to -55^{o}C, 10 cycles [(e) Staystik 415; (f) Staystik 482]. 85

4.3 Cross-section optical micrographs of GEM D4 die bonds in the as-manufactured condition: (a) typical fillet formed against the vertical wall of the Si die; (b) higher magnification view of the fillet exhibiting vertical cracking in the Si die and voiding within the adhesive; and (c) typical interfacial area showing voiding and cracking. 87

4.4 Cross-section optical micrographs of GEM D4 die bonds after thermal cycling from 200^{o}C to -55^{o}C, 10 cycles: (a) fillet region showing delamination and cracking; and (b) interfacial area exhibiting Si fragments with further delamination, and voiding within the adhesive. 88

4.5 Polymerization reaction on cyanate ester [140]. 89

4.6 Thermal stability of the JM7000 adhesive. 90

4.7 Cross-section SEM images of a typical JM7000 die bond in the as-manufactured condition: (a) typical fillet formed against the vertical wall of the Si die; (b) higher magnification view of the fillet showing cracking in the Si die arising from delamination on the vertical section of the fillet; (c) copious corner cracking in the Si die; and (d) typical interfacial area with the various parts of the package identified by EDX. 92

4.8 Cross-section SEM images of the Si die/JM7000/substrate region as-manufactured, exhibiting: (a) interfacial defects of cracking and voiding; and (b) large Si fragment. 93

4.9 Cross-section SEM images of JM7000 die bonds after isothermal ageing at 250^{o}C, for 168h: (a) fillet region exhibiting Si die fracture and voiding; (b) interfacial area showing delamination located at die/adhesive and adhesive/metallisation interfaces, (c) discontinuity of the JM7000 adhesive layer accompanied with delamination in both interfaces; and (d) higher magnification of the adhesive layer discontinuity. 94

4.10 Cross-section SEM images of JM7000 die bonds after isothermal ageing at 250^{o}C, for: (a), (b) 672h; (c), (d): 1008h; and (e), (f) 2016h. 95

4.11 Cross-section SEM images of JM7000 die bonds after thermal shock from 200^{o}C to -65^{o}C, in 10s, showing: (a) fillet reduction; and (b) die cracking and voiding within the adhesive matrix. . . 96

4.12 Cross-section SEM images of JM7000 die bonds after thermal cycling from 200^{o}C to -55^{o}C, 10 cycles, showing: (a) delamination and voiding in the interfacial area; (b) severe die cracking. 97

4.13 SAM images of the JM7000 die assemblies in (a) as-manufactured, and (b) after thermal exposure at 250^{o}C for 2016 hours showing voiding and unbonded areas. 99

4.14 SAM images of the JM7000 die bonds: (a) as-manufactured; and after isothermal ageing at 250^{o}C for (b) 168h, (c) 504h, (d) 672h, and (e) 1008h showing its effect on the bonded area. . . . 100

4.15 SAM images of GEM D4 die assemblies: (a) as-manufactured, (b) after isothermal ageing at 250^{o}C for 168h, (c) after thermal cycling [200^{o}C to -55^{o}C, 10 cycles], and (d) after thermal shock [250^{o}C to - 65^{o}C, 10 seconds]. 101

4.16 SAM images of Staystik die bonds: (a) Staystik 482 in the as-manufactured condition, and (b) Staystik 415 after isothermal ageing at 250^{o}C for 2016h. 102

4.17 Variation of mean die shear load to failure for JM7000, GEM D4 and Staystik 482 die bonds as a function of isothermal ageing at 250^{o}C, in air. 104

4.18 Comparison of mean die shear load to failure of JM7000 die bonds after ageing at 250^{o}C under air and N_2. 104

4.19 Comparison of mean die shear failure loads of Staystik 415 and 482 die assemblies after isothermal ageing at 250^{o}C in N_2, and in air, respectively. 105

4.20 Silver migration around JM7000 Si dies on HTCC substrates after ageing for 168, 504 and 1008 hours. 106

5.1 Top view of a Si die bonded to Au metallised Al_2O_3 substrate using a Au-Si preform. The darker irregular shape region around the Si die is the re-solidified Au-Si liquid. 111

5.2 Typical SAM images of Si dies attached to Al_2O_3 substrates using Au-Si preforms, manufactured under conditions specified in Table 3.3, and corresponding percentages of unbonded area and largest single defect, (lsd). 113

5.3 Examples of SAM images of Au-Si die bonds manufactured for a constant set of conditions, in accordance with Table 3.3 and, corresponding percentages of unbonded area and largest single defect (lsd). A, B, and C indicate repeats of the conditions so that specimens 6A, 6B, and 6C were nominally identical. The same applied for specimens 9 and 13. 114

5.4 Bonded area distribution of 48 Au-Si die bonds manufactured under different 16 conditions (3 repeats) as specified in Table 3.3.115

5.5 Typical load-displacement curve of eutectic Au-Si die bond. Test temperature was 25^{o}C. 115

5.6 Shear load distribution of 48 Au-Si die bonds manufactured under different 16 conditions (3 repeats) as specified in Table 3.3. 116

5.7 Example of a Au-Si die bond after die shear testing. The die bond failed at both Si die/Au-Si solder and Au-Si solder/metallisation interfaces; part of the Au-Si preform remained attached to the rest of the package while the rest broke off with the Si die. . . . 117

5.8 Plan view SEM images of fractured surfaces of Au-Si die bonds after die shear testing showing: (a) failure at the Si; (b) mixed failure mode. 117

5.9 Boxplot of the parameters (A, B, C and D) influence on bonded area of the Au-Si solder bonds. 123

5.10 Boxplot of interaction of parameters (B, C and D) on bonded area of the Au-Si solder bonds. 123

5.11 Typical SAM images of 27 Si dies attached to Al_2O_3 substrates using Au-Si preforms manufactured under conditions specified in Table 5.4, and corresponding percentages of unbonded area and largest single defect, lsd. 126

5.12 Examples of SAM images of Au-Si die bonds manufactured for a constant set of conditions, in accordance with Table 5.4 and, corresponding percentages of unbonded area and largest single defect, (lsd). A, B, and C indicate repeats of the conditions so that specimens 23A, 23B, and 23C were nominally identical. The same applied for specimens 26. 127

5.13 Bonded area distribution of the 27 Au-Si die bonds manufactured under 9 different conditions (3 repeats) as specified in Table 5.4. 128

5.14 Shear load distribution of 27 Au-Si die bonds manufactured under 9 different conditions (3 repeats) as specified in Table 5.4. . 129

5.15 Bonded area distributions comparing the Au-Si die bonds from batch 1 (48 specimens in the first experimental design) with batch 2 (27 specimens in the second experimental design). . . . 130

5.16 Boxplot of batch 1 (48 specimens in the first experimental design) and batch 2 (27 specimens in the second experimental design) for bonded area. 130

5.17 Shear load distributions comparing the Au-Si die bonds from batch 1 (48 specimens in the first experimental design) with batch 2 (27 specimens in the second experimental design). . . . 131

5.18 Boxplot of batch 1 (48 specimens in the first experimental design) and batch 2 (27 specimens in the second experimental design) for failure load. 132

5.19 Failure load versus bonded area for batch 1 (48 specimens in the first experimental design) and batch 2 (27 specimens in the second experimental design). 132

5.20 Effect of scrubbing frequency and scrubbing time on the assessed bonded area of Au-Si die bonds from batch 2 (27 specimens). The estimated error in the bonded area measurements is 2%. 134

5.21 Effect of scrubbing frequency and time on failure shear for bonds from batch 2. The estimated error in the shear test measurements is 0.5kg. 135

5.22 Schematic of a liquid drop in equilibrium with a surface. γ_{SV} is the surface energy of the solid-liquid interface, γ_{SL} is the surface energy of the solid-liquid interface, and γ_{LV} is the surface energy of the liquid-vapour interface. 137

5.23 Arrangement for bonding a Si die to a Au metallised Al_2O_3 substrate using Au-2wt.%Si. 138

5.24 XPS spectrum of the Au-2wt%Si preform in the as-received condition. Top image shows the Au XPS peak in detail; bottom image shows the aspect of the examined preform. 140

5.25 XPS spectrum of the Au-2wt%Si preform taken immediately after the sample was heated up to 450^{o}C. Image of the Au-Si preform, placed on top of the Au metallised substrate, after the bonding experiment exhibiting signs of oxidation and no evidence of bonding. 141

5.26 SEM images of the Au thick film on the Al_2O_3 substrate used for the Au-Si eutectic die bonding: (a) plan view of the Au thick film fired at 850^{o}C for 60min; (b) higher magnification image of the Au thick film; and (c) cross-section of the Al_2O_3 substrate as-received. 145

5.27 XPS spectra of the Au thick film on the substrate in the as-received condition: (a) at the surface, and (b) after Ar ion bombardment in vacuum to clean the surface. 147

5.28 WDX analysis of the Au metallised Al_2O_3 substrate: (a) typical cross-section SEM image of the substrate with three different regions where 1, 2 and 3 WDX was performed; (b), (c) and (d) corresponding WDX spectra taken from regions. 149

5.29 EPMA maps of the Au metallised ceramic substrate: (a) secondary electron image of the Au metallization/Al_2O_3 substrate interface; (b) Al map; (c) O map; (d) Si map; (e) Bi map; (f) Cd map; (g) Au map. 150

5.30 WDX analysis of the Au metallised Al_2O_3 substrate: (a) typical cross-section SEM backscattered electron image of the substrate with two different regions in which WDX was performed; (b) and (c) corresponding WDX spectra taken from regions 1 and 2. 151

5.31 EPMA maps of the Au thick film metallised ceramic substrate: (a) backscattered image of the Au metallisation/glass layer interface; (b) O map; (c) Al map; (d) Si map; (e) Au map; (f) Cd map; (g) Bi map; (h) Zn map. 152

5.32 Cross-section SEM backscattered image of the Au mettalised Al_2O_3 substrate and corresponding element depth profiling. . . 153

5.33 XPS spectra of the thick film Au metallised Al_2O_3 substrate with (a) 50nm Ti sputtered, and (b) 100nm Au evaporated each after Ar ion bombardment. 154

5.34 Aspect of the Au-Si die bonds after die bonding process in a tubular furnace (under N_2) using (a) sputtered Ti 50nm thick and (b) pure thin film Au on top of the Au metallised substrate. No evidence of bonding. 156

5.35 AFM image of the thick film Au metallised layer on the Al_2O_3 substrate. 157

5.36 Au-Si die bonds manufactured using Camax EDB65 semi-automatic die bonder under optimum conditions (heating stage temperature - 450^{o}C; scrubbing head force - 3.5g/mm^2; scrubbing frequency - 2Hz; and scrubbing time - 1s), comparing (a) pure thin Au film on sapphire substrate and (b) thick film Au on Al_2O_3 substrate. 160

5.37 SAM image of a model Au-Si solder bond. 161

6.1 Bonded area distribution of nominally identical Au-Si die bonds manufactured under optimum bonding conditions: heating stage temperature - 450^{o}C; scrubbing head force - 3.5g/mm^2; scrubbing frequency - 2Hz; and scrubbing time - 1s. 164

6.2 Cross-section SEM images of a typical Au-Si die bond in the as-manufactured condition: (a) general arrangement of Si die/Au-Si solder/Au metallised substrate interfacial region; (b) backscattered electron image of the fillet region exhibiting Si crystals randomly dispersed; (c) high magnification image of the fillet region exhibiting typical Au-Si eutectic structure; and (d) interfacial area exhibiting Au-Si eutectic structure located at the Si/Au-Si interface. 166

6.3 Cross-section SEM images of a Au-Si die bond in the as-manufactured condition showing: (a) etched regions formed along the Si/Au-Si interface and; (b) higher magnification image of a "crater" formed in the Si. 168

6.4 Schematic illustration of the potential voided region surrounded by craters. Even though a crater may pull in the Au-Si eutectic liquid uniformly, when some region is surrounded by craters, the region can have a lack of Au-Si and a void is then formed [167]. 169

6.5 Schematic illustration showing the void formation sequence in Si (100) die [167]. 169

6.6 EPMA mapping of a typical as-manufactured Au-Si die bond in the region Si die/Au-Si solder/Al_2O_3 substrate interface: (a) Au map; (b) Si map; (c) Al map; (d) Ag map; (e) Bi map, (f) Cd map, and (g) corresponding backscattered electron image. 170

6.7 EPMA line-scan from the Si die towards the substrate for a Au-Si die bond in the as-manufactured condition: (a) SEM backscattered electron image where the line-scan was performed, with a step size of $2\mu m$ and a total length of $60\mu m$; (b) diffusion profiles for Au, Si and O across the Si die/Au-Si solder/Al_2O_3 substrate region. 172

6.8 SAM images of Au-Si die bonds, from the optimised batch: (a), (c), and (e) in the as-manufactured condition; (b), (d), and (f) after isothermal ageing at 300^{o}C, for 168h. Percentages of unbonded area and largest single defect, (lsd) are given for each C-SAM image. 174

6.9 SAM images of Au-Si die bonds, from the optimised batch: (a), (c), and (e) in the as-manufactured condition; (b), (d), and (f) after isothermal ageing at 300^{o}C, for 672h. Percentages of unbonded area and largest single defect, (lsd) are given for each C-SAM image. 175

6.10 SAM images of Au-Si die bonds, from the optimised batch: (a), (c), and (e) in the as-manufactured condition; (b), (d), and (f) after isothermal ageing at 300^{o}C, for 2016h. Percentages of unbonded area and largest single defect, (lsd) are given for each C-SAM image. 176

6.11 Boxplot of bonded area of Au-Si die bonds as a function of isothermal ageing at 300^{o}C for 168, 672 and 2016 hours. 178

6.12 Boxplot of load to failure of Au-Si die bonds as a function of isothermal ageing at 300^{o}C for 168, 672 and 2016 hours. 179

6.13 Average die shear strength as a function of ageing at 300^{o}C with Si/Au-Si/Au metallised substrate bond. 180

6.14 EPMA mapping of a typical Au-Si die bond after isothermal ageing at 300^{o}C, for 2016 hours, in the region Si die/Au-Si solder/Al_2O_3 substrate: (a) backscattered electron image; (b) C map; (c) O map; (d) Al map; (e) Si map; (f) Au map; (g) Bi map; and (h) Cd map. 182

6.15 EPMA line-scan from the Si die towards the substrate for a Au-Si die bond after isothermal ageing at at 300^{o}C for 2016 hours: (a) SEM backscattered electron image where the line-scan was performed, with a step size of 1μm and a total length of 83μm; (b) diffusion profiles for Au, Si and O across the Si die/Au-Si solder/Al_2O_3 substrate region. 184

6.16 SAM images of two typical Au-Si die bonds before ((a) and (c)) and after accelerated ageing at 350^{o}C for 500h ((b) and (d)), and corresponding percentages of unbonded area and largest single defect, (lsd). Note the increase in white regions (unbonded areas) after ageing. 186

6.17 SAM images of various Au-Si die bonds after accelerated ageing at 350^{o}C for 850h. The percentage of unbonded area and largest single defect, (lsd) are given for each case. 187

6.18 Boxplot of bonded area of Au-Si die bonds before and after accelerated ageing at 350^{o}C for 500 hours. 188

6.19 Boxplot of bonded area of Au-Si die bonds before and after accelerated ageing at 350^{o}C for 850 hours. 189

6.20 Boxplot of shear load to failure of Au-Si die bonds after accelerated ageing at 350^{o}C for 500 and 850h. 190

6.21 Cross-section SEM images of Au-Si die bonds after accelerated ageing at 350^{o}C, for 850h, showing some interfacial defects: (a) fracture of Si die lower corner; (b) debonding at the Au-Si preform/substrate interface; (c) cracking in the die attach material and voiding at the Au-Si preform/substrate interface; and (d) fillet region exhibiting fractured surface in the Au-rich region. . 192

6.22 SAM images of Au-Si die bonds after thermal shock ((a), (b), and (c)) and thermal cycling ((d), (e), and (f)), from -40 to 250^{o}C, 3 hours dwell, for 10 cycles. Percentages of unbonded area and largest single defect, (lsd) are presented. 193

6.23 SAM images of the Au-Si die bonds after thermal shock, -40 to 250^{o}C, for 40 cycles. Percentages of unbonded area and largest single defect, (lsd) are given for each case. 195

6.24 Boxplot of bonded area for the Au-Si die bonds in the as-manufactured condition and after thermal shock (TS40), and as-manufactured and after thermal cycling (TC40), from -40 to 250^{o}C, for 40 cycles.197

6.25 Boxplot of shear load to failure of Au-Si die bonds after thermal shock (TS40) and thermal cycling (TC40) from -40 to 250^{o}C, for 40 cycles. 198

6.26 Correlation between bonded area and load to failure of the Au-Si die bonds after thermal shock (TS40) and thermal cycling (TC40) from -40 to 250^{o}C, for 40 cycles. 199

6.27 Cross-section SEM images of the Au-Si die bonds after thermal cycling, from -40 to 250^{o}C, for 10 cycles ((a), (b) and (c)) and 40 cycles ((d) and (e)), showing: (a) horizontal Si die cracking, voiding and microcracks within the solder region; (b) delamination at the Si die/solder interface; (c) and Si crystals located in the fillet region; (d) fillet unbonded from the Si die; (e) Si die fractured. 201

6.28 Cross-sections SEM images of the Au-Si die bonds after thermal shock, from -40 to 250^{o}C, for 10 cycles showing: (a) pronounced crack at the Au-Si solder region in a zig-zag path; (b) Au-Si solder cracking with a zig-zag propagation path. 201

6.29 Optical micrograph of surface of the adhesive bonded SOI devices after 11088h exposure to 250^{o}C showing whiskers centred around the bond pads, taken from [172]. 204

6.30 SEM images of (a) unbonded bond pad and (b) wirebonded bond pad of adhesive bonded SOI device, after 11088h exposure to 250^{o}C [172]. 205

6.31 SEM image of (a) unbonded bond pad and (b) wirebonded bond pad of Au-Si eutectic bonded SOI device, after 11088h exposure to 250^{o}C [172]. 205

List of Tables

2.1 Temperature guideline table for die attach materials [3]. 9

2.2 Classification of die attach materials [3]. 10

2.3 Sn/Pb solder compared with ECAs [34]. 12

2.4 Room temperature properties for common die attach materials [3]. 13

2.5 Physical properties of semiconductor and substrate materials [36]. 14

2.6 Relationship of shrinkage and electrical conductivity of ICAs [34]. 26

2.7 Examples of common IMC formed at electronic package metallisation interfaces [105]. 42

2.8 Room temperature properties of pure Cu, Sn, Ni, and their intermetallics [106]. 43

3.1 Properties of the various adhesives tested for adhesive die bonding. 62

3.2 Die bonder parameters. 67

3.3 Experimental design for Au-Si eutectic die bonding (sixteen experiments, two-level). Studied parameters: T - temperature of the heating stage; F - force of the scrubbing head; S_f - scrubbing frequency; S_t - scrubbing time. 70

3.4 Features contained within UPTEMP - SOI device for high temperature operation. 79

4.1 Bonded area (BA) percentages for the JM7000 die bonds as-manufactured (0h), and after isothermal ageing at 250^{o}C for different periods of time. The percentage of largest single defect (l.s.d) is also given or each case. 99

5.1 Mean bonded area, standard deviation and S/N$_L$ ratio for the Au-Si die bonds. 119

5.2 S/N$_L$ ratio analysis of bonded area for the Au-Si die bonds. A - temperature of the heating stage; B - force of the scrubbing head; C - scrubbing frequency; D - scrubbing time. 119

5.3 ANOVA method using the linear contrast technique to identify the parameters with the highest and lowest contribution in bond quality. *SST* - sum of squares total; *df* - degrees of freedom; *MSS* - mean sum of squares; *F* - Fisher test; *Alpha* - test probability; *Conf.* - confidence percentage. 121

5.4 First level optimised experimental design for Au-Si eutectic die bonding: nine experiments, three-level. Temperature of the heating stage and force of the scrubbing head were kept constant at 450^{o}C and 3.5g/mm^2, respectively. Parameters under study: scrubbing frequency (S_f) and scrubbing time (S_t). 124

5.5 Estimated atomic concentrations of various surface species obtained from the Au-2wt.%Si preforms, as determined by XPS in the as-received condition and after heating up to 450^{o}C. 142

5.6 Estimated atomic concentrations of various surface species obtained from the as-received Au thick film metallised on Al_2O_3 substrates, as determined by XPS in the as-received condition and after Ar ion bombardment to clean the surface. 148

6.1 Bonded area ranges of Au-Si die bonds before (BA_i) and after isothermal ageing (BA_f) at 300^{o}C, for various periods of time. . 177

6.2 Failure modes registered for the die sheared Au-Si die bonds aged at 300^{o}C for 168, 672 and 2016 hours. A total of 42 die bonds were subjected to die shear; 14 die bonds for each storage time. Mode 1 - shearing of Si die with residual Si remaining; mode 2 - separation of die from the die attach medium; mode 3 - failure within the die attach/substrate interface. 180

6.3 Bonded area range for Au-Si die bonds before and after accelerated ageing at 350^{o}C for 500 and 850 hours. 188

6.4 Variation in bonded area ranges for Au-Si die bonds in the as-manufactured condition (BA_i) and after thermal shock and thermal cycling (BA_f), from -40 to 250^{o}C, for 10 cycles. 194

6.5 Bonded area ranges for Au-Si die bonds before (BA_i) and after 40 cycles of thermal shock and thermal cycling (BA_f). 196

6.6 Electrical test results on SOI device assembled in HTCC packages [172]. 204

CHAPTER 1
Introduction

1.1 Industrial context

The growth of the microelectronics industry over the past 50 years had an enormous effect on human civilization that few other technologies could be said to be comparable, with an estimated 50 billion devices produced per annum. Impact is predicted to grow in the future, with the often quoted "Moore's Law" predicting that the available processing power of electronics is likely double every two years for the foreseeable future [1, 2].

In spite of the delicate nature of microelectronic circuits, several large and important industries rely critically on using microelectronic based sensing devices in significantly harsher environments than those experienced by domestic electronics [3, 4]. The desire to operate electronic and control systems in increasingly high temperature environments poses a challenge to the traditional industrial practical temperature limit of 125^{o}C for electronic systems [5]. An industrial desire to achieve an operating temperature above 200^{o}C in combination with high pressures, vibrations and potentially corrosive environments such as those found down oil or gas wells means that specialist semiconductors, passives, circuit boards and assembly processes are increasingly needed to meet target performance specifications [3, 6]. Similar environments can also be found in some space, geothermal power and high-end automotive applications [3].

Well-logging represents probably the most aggressive and most devel-

oped industry for high temperature electronics (HTE) technology. The penetration of HTE in this market exceeds that of other application sectors such as automotive or aerospace. Well-logging has been the primary driving force and leading financial sponsor for the development of high temperature electronics in the last decades. The use of high temperature components within the petroleum exploration and geothermal industry is characterised by [7]:

i) low volume;

ii) high level of specialisation / many different sensors used;

iii) high accuracy and frequency/performance requirement;

iv) high reliability for typically 5 years use at 150^{o}C.

Figure 1.1 shows the interaction of HTE design, implementation, production and testing aspects.

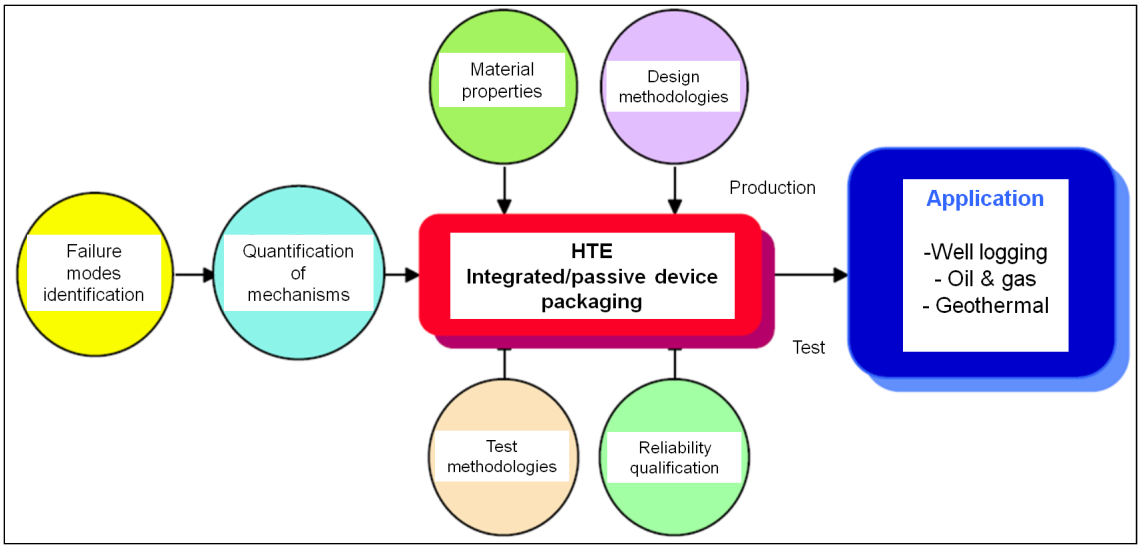


Figure 1.1: High temperature electronics design and implementation [7].

Reliability data concerning electronics systems tested under standard harsh environment of cycles between -55^{o}C to +125^{o}C established over many years and enshrined in the MIL-HDBK-217 standard [8] cannot be used for reliability assessment at higher temperature, as failures modes change, becoming more dominated by diffusion and creep rather than fatigue [5]. The

basis of the approach being pursued in this work is to measure the thermo-physical behaviour of generic high temperature Si (die) and package arrangements, and to perform supporting and microstructural analysis and other experiments, in order to identify harsh environment failure modes. Ultimately, the research aims to establish appropriate time-saving accelerated test conditions relevant for high temperature electronic packages for down-well and other severe environment applications.

1.2 Objectives

The project was part of a larger industry-university collaboration entitled UP-TEMP, that sought to address the specific needs of HTE market for down-well applications, operating at up to 250^{o}C. The project consortium comprised of a UK based supply chain with participation of specialist materials suppliers (Gwent Electronic Materials and Thermastrate), an electronic packaging company (GE Aviation Systems) and end-users (Sondex Wireline Ltd and Vibro-Meter) in the vanguard of well-logging tool supply for oil/gas extraction and recovery, and turbo-machinery.

The overall objective of the project was to identify and investigate packaging materials, namely die attach materials, for high temperature electronics that can be used in well-logging and turbo-machinery tools. The behaviour of die attach materials under harsh environments was studied and basic understanding of the factors controlling their lifetime was developed. The objectives are:

i) To investigate the microstructure of die attach materials as a function of thermal exposure.

ii) To measure the mechanical properties of die attach materials under harsh environments.

iii) To suggest optimum combinations of design, processing and materials for improved lifetime.

iv) To undertake highly accelerated testing studies on down-selected design-material combinations.

1.3 Scope

This thesis is composed of seven chapters. Chapter 1 is introduction and context. Chapter 2 reviews and summarises the current research for HTE focusing on (i) electronic packaging assembly, (ii) materials, (iii) interfacial intermetallic compound formation, (iv) reliability and accelerated testing, (v) scanning acoustic microscopy, and (vi) nanoindentation. Chapter 3 describes the experimental die bonding programme using adhesives and Au-Si eutectic, and the methods and techniques used to characterise the die bonds in terms of destructive cross-sectional microstructural analysis, mechanical properties, and non-destructive analysis to assess failure in the thermally stressed samples. Chapter 4 describes four commercial adhesives in terms of the adhesive shear strength after 250^{o}C storage and thermal cycling tests. Chapter 5 describes the behaviour of the Au-Si eutectic die bond in terms of manufacturing process optimisation for bonded area and bond area variability. In Chapter 6, microstructural analysis and nano-mechanical characterisation of the Au-Si eutectic are described and the effect of highly accelerated testing on bonded area discussed. The long term electrical performance of the packages/devices at elevated temperature is also described. Chapter 7 summarises the research findings and conclusions, and suggests some areas for further work.

CHAPTER 2
Literature review

2.1 High temperature electronics

The term high temperature electronics (HTE) is defined in various ways in the literature, depending on the areas of application. In general, HTE means electronics operating at temperatures greater than the upper limit for the standard MIL-SPEC 334 of 125^{o}C [9]. However, there are growing demands for electronics that must operate at a much higher temperature. High temperatures are often accompanied by other hostile factors such as vibration, shock or corrosion [3]. Interest in the area of high temperature electronics has increased dramatically in recent years. The primary applications for HTE include well-logging, aircraft, space exploration, automotive, nuclear reactors, and the power grid.

Air and ground vehicles are potential candidates for use of HTE as they have both regions of high temperature (due to combustion) where sense/control is required and engineering limitations on their ability to provide active cooling to electronic circuitry in these areas. Many of the potential applications are also safety critical, bringing stringent reliability requirements [3]. In spite of their delicate nature, critical industries rely on using sensing devices in significantly harsher environments than those experienced by domestic electronics [3]. The harshest of these environments exist within aero-engines and down oil or gas wells where devices may experience fluctuating temperatures of over 250^{o}C and pressures of over 1000 bar, as well as highly corrosive potentials and significant vibration [3]. Similar environments can also

be found within space, geothermal power and high-end automotive applications [3]. For example, measurement-while-drilling (MWD) tools for oil, natural gas, and geothermal wells have to withstand reservoir ambient temperatures up to 350^{o}C and, applications for Venus planetary exploration require electronics operating at 500^{o}C [10].

The US Department of Energy has indicated that HTE are necessary to develop deep gas resources. Down-hole tooling and electronics can currently endure up to 175^{o}C by careful screening of the electronic parts, designed for lower temperatures, although this process is complex, expensive and reliability is inevitably jeopardized when using components designed for lower temperatures [11]. Deep wells for the exploitation of petroleum and other minerals, and geothermal applications, represent a small volume but very high value niche market for HTE.

True HTE systems as opposed to conventional arrangements operated out of their specification require electronic circuits that preserve properties, function and reliability without costly and compromising active cooling [7]. Figure 2.1 shows a typical GE AS/Sondex-Wireline product that is inserted down a well and measures down-hole pressures, temperatures, casing surface roughness, oil/gas/water flow rate, fluid density, 3D position, etc, transmitting this data back to the surface in real time via a trailing cable. The electronics are contained within the central 2.5 cm diameter stainless steel pressure housing, with highly dense circuit boards often up to 10s of cm in length. These tools are generally sold or leased to well-logging companies, e.g. Schlumberger, who in turn operate the well-logging for the petrochemical giants. The efficient operation of a well is vitally dependent upon the information from the down-hole sensors and the operational time in these applications before failure is extremely limited. Errors or failures potentially result in the complete replacement of the probe, such as the GE AS/Sondex one displayed in Figure 2.1 [3, 12], and usually complete well shut-down that

can easily cost more than $1 million/day.

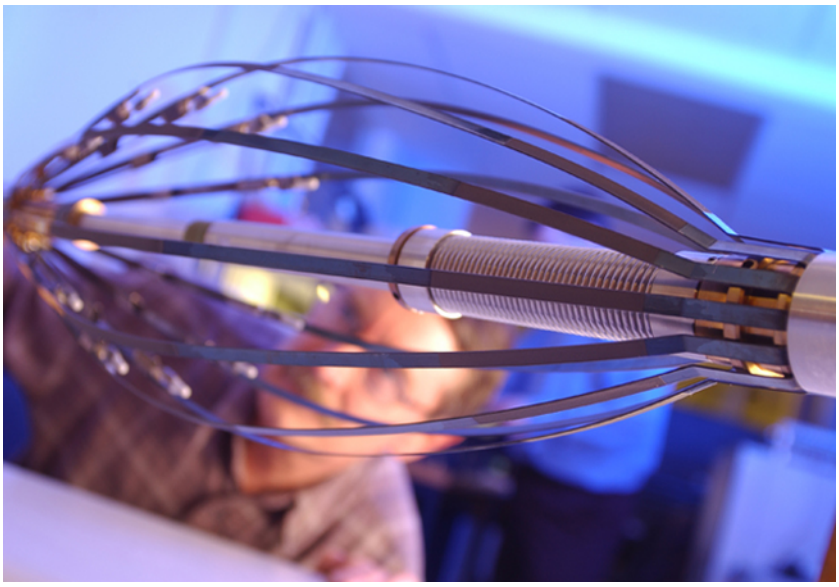


Figure 2.1: Caged full-bore flowmeter [12].

Even though the very expensive electronics placed down-well are protected by thermal barriers and other technologies, the time that the electronics can spend down hole is still limited. In order to overcome these difficulties, industry is seeking to develop new microelectronics packaging technology and, lifing methodologies so that devices are allowed to demonstrate long-term operation in harsh environments for up to 10 years. There is a growing body of evidence that HTE and sensors have greatly improved operating lifetimes at lower temperatures. Honeywell HT SOI electronics rated for 5 years at 225^{o}C have a potential for 10 years at 200^{o}C and 20 years at 150^{o}C [13].

2.1.1 Electronic packaging assembly

Package cost and performance is linked to its manufacturability, reliability, serviceability, size, weight, signal integrity, mechanical stability, power consumption and its accompanying heat dissipation. An electronic package includes interconnecting wire-bonds that carry the current to/from the package periphery to the Si die (the active Si chips), the die attach materials,

leadframe materials, plastic encapsulants, and others. In the present thesis, attention is focused on the critical die attach materials (adhesives or solders) that mechanically attach the die to a substrate, ensuring it does not detach/fracture over the operational lifetime. Figure 2.2 shows a schematic illustration of an electronic package comprising the die, the die attach material and the leadframe.

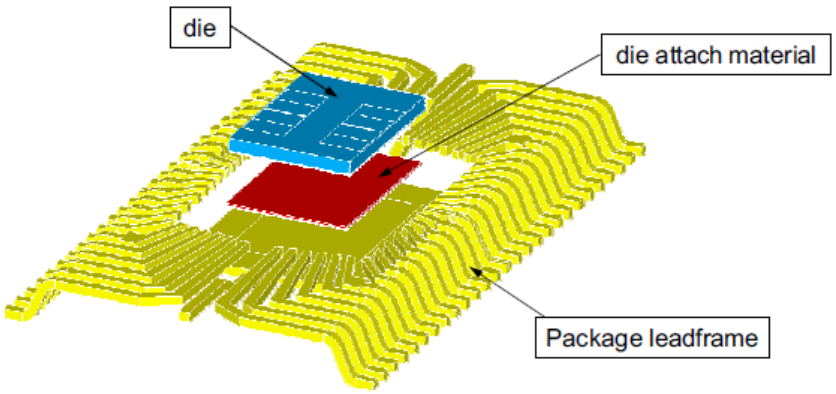


Figure 2.2: Schematic illustration of the electronic package composed of die and die attach material [14].

The die attach material also (i) creates a thermal path to conduct heat away from the base of the die; (ii) acts as an intermediate material to partially offset any differences in the coefficient of thermal expansion (CTE) between the die and substrate, reducing the stress at the interface and; (iii) provides for electrical grounding if the material used to secure the die is sufficiently conductive [3].

The theoretical maximum use temperatures for die attaches are those at which the die attach material melt/soften to a level that no longer keeps the die in place during operation. These temperatures are shown in Table 2.1 for few common die attach systems.

Solders and ECAs are the most widely used materials. Reliability of die attach materials may be compromised at temperatures below the solidus, melting, or decomposition temperature, as a result of failure mechanisms related to thermal stress induced by temperature cycling, power cycling, and die

Table 2.1: Temperature guideline table for die attach materials [3].

Die attach material	T_{max}	**Reason**
Au80-Sn20	280^{o}C	eutectic melting point
Au88-Ge12	356^{o}C	eutectic melting point
Au97-Si3	363^{o}C	eutectic melting point
Sn63-Pb37	183^{o}C	eutectic melting point
Epoxy novalac	200^{o}C	softening/depolymerization
Silver filled epoxy	200^{o}C	softening/depolymerization
Polyimide	300^{o}C	glass transition temperature
Silver filled glass	450^{o}C	softening point

bonding cool-down [3]. For ECAs failure usually occurs by cracking, debonding, excessive softening or oxidation to a carbonaceous char.

Common die attach materials may be divided in different categories according to their thermal/electrical conductivity and stiffness as shown in Table 2.2. The most used solder-based interconnect material for electronic packaging applications is near-eutectic Sn-Pb [3], although there are increasing concerns with Sn-Pb use because Pb is classed as a hazardous material. Each year, thousands of tons of Pb are manufactured into various products, especially consumer electronic products (e.g., cell phones, pagers, PDA, etc.) which tend to have a short life cycle (2-3 years) and millions of such Pb-containing products simply end up in landfills. In addition, recycling of Pb-containing consumer electronic products has proven to be very difficult.

The European Commission's (EC) draft directives, Waste Electrical and Electronic Equipment (WEEE) and Restriction of Hazardous Substance (RoHS) have approved banning the use of Pb in electronics in European Union countries effective July 2006 [15–20]. The pressure to eliminate the use of Pb in all electronic packaging is growing, and legislation and policies have been proposed in both the Senate House and the House Representatives in the US [21]. In response to the new legislations, most major electronic manufacturers have stepped up their search for alternatives to Pb-containing solders.

Table 2.2: Classification of die attach materials [3].

	High modulus (stiff)	**Low modulus (flexible)**
Electrical/ Thermal conductive	Gold eutectics Silver-filled glass	Silver-filled polyimides Silver-filled epoxies Tin-lead-based solders Tin-based solders
Thermal conductive	Tin oxide-filled glass Indium oxide-filled glass	AlN-filled epoxy Alumina-filled epoxy
Non-conductive	Unfilled glass	Unfilled epoxies Epoxy silicone Polyimides

A large number of Pb-free solders research studies [22–25] have been reported which were focused on microstructural analysis and mechanical properties (Young's modulus, Poisson's ratio, tensile strength), and creep properties for certain compositions of Pb-free solders.

Currently, aerospace avionics are exempt from such legislation on safety grounds. However, efforts are being made to find Pb-free alternatives for HTEs/harsh environments, as there is no agreement on how long the exemption will last, and the industrial supply base for Pb containing components or assemblies is shrinking [20]. Pb-free solders and ECAs are the most promising alternatives to Sn-Pb solder.

Pb-free solders, which are essentially low melting temperature alloys, suffer from relatively high cost or limited availability of some candidate metals, and the requirement for relatively high soldering temperature for some formulations that may damage other parts of the package. The most promising Pb-free solder alloys are Sn-based with a relatively low melting temperature close 232^{o}C, and have low cost and good wetting characteristics with other metals [3]. Most Pb-free solders are Sn-based alloys with additions of Ag, Cu, Bi, Sb, In, Zn, or Ge. The binary eutectic of Sn and noble metals

such as Cu, Ag, and Au, and the near-eutectic Sn-Ag-Cu (SAC) have received much attention [26–31]. Most currently commercial Pb-free solders, such as Sn-3.5Ag, Sn-4.7Ag-1.7Cu, have melting temperatures of 221^{o}C and 217^{o}C, respectively, higher than of the conventional Sn-37Pb eutectic solder (183^{o}C). Therefore, the reflow temperature during electronic assembly must be raised by 30 to 40^{o}C. This increased temperature reduces the integrity, reliability and functionality of printed wiring boards, components and other attachment. As such, the applicability of these metal alloys to organic/polymer packaged components and low-cost organic printed circuit boards are severely limited. Although some low melting point alloys are available (Sn-In, Sn-Bi, Sn-Zn-Ag-Al-Ga) their material properties and processability in assembly are still of concern. While inexpensive and proven for lower temperature applications, these will not withstand the temperatures experienced by HTE.

On the other hand, ECA die attach materials typically possess the following merits [15, 32, 33]: low processing temperature, environmental friendliness, fewer processing steps to reduce processing costs, lower thermal expansion mismatch stresses induced in the die and substrates, and finer pitch interconnect capability enabling miniaturisation of electronic devices. Additionally, no flux pre-treatment or post-cleaning procedures are required. Nevertheless, like all Pb-free materials, currently commercialised ECAs still have some limitations, such as metal migration, conductivity fatigue in reliability testing, relatively low electrical conductivity, and poor impact strength. For HTE, the main disadvantage is the very rapid deterioration in properties with increasing temperature. Table 2.3 gives a general comparison between Sn-Pb solder and generic ECAs.

Until recently, hermetic die attach was accomplished using inorganic adhesives such as Ag-filled glasses, Au-Sn or and Au-based eutectic. Eutectic die attach is a low throughput, manual method that cannot be easily adapted for high speed automation. Although Ag glass die attach has pro-

Table 2.3: Sn/Pb solder compared with ECAs [34].

Characteristic	**Sn/Pb solder**	**ECA**
Volume resistivity (Ωcm)	0.000015	0.00035
Typical junction R (mW)	10-15	25
Thermal conductivity (W/m K)	30	3.5
Shear strength (psi)	2200	2000
Finest pitch (mil)	12	<6-8
Minimum processing temperature (°C)	215	150-170
Environmental impact	Negative	Very minor

vided some processability improvements over the eutectic process, it still requires a lengthy and precise temperature profile in order to remove the organic vehicle at a controlled rate. As die sizes become larger, the Ag glass firing process becomes difficult to control.

High temperature eutectic and Ag-filled glass die attach materials raise concern because they tend to lead to increased stresses and strains in the die, due to both increased differences in the CTE within the die/attach/substrate combination and a higher elastic modulus. These strains lead to interfacial shear and other stresses, and premature failure. Peeling stresses at the edge of the die can cause horizontal crack and die lifting, while tensile stresses in the center of the die can cause vertical crack propagation, leading to die cracking. Room temperature properties for some common die attach materials are given in Table 2.4.

There are many die attach metallurgies that are currently being used for high temperature applications, mostly Au and Ag-based alloys and a few high temperature epoxies [35]. Many studies have suggested using a Ag-based material for die attachment, because of the cost advantages over Au. However, Ag atoms will migrate at higher temperatures, leading to Ag whiskers and a possible failure mechanism by electrical shorting. Au-based die attach materials, though more expensive, do not suffer from this potential failure

Table 2.4: Room temperature properties for common die attach materials [3].

Material	**Tensile strength (MPa)**	**Shear strength (MPa)**	**Elastic modulus (GPa)**	**CTE (ppm/K)**	**Electrical resistivity ($\mu\Omega$-cm)**
Au-Sn	198	185	69	16	36
Au-Si	255-304	220	69.5	11	775
Au-Ge	233	220	63	13	29
Epoxy novalac	55- 83	26.2	3	35	10^{13} - 10^{16}
Epoxy conductive	4-34	30	2.7-3.3	41	100

mechanism and may overall be a better choice for high temperature die attachment.

2.1.2 Substrate materials

Organic based substrates (e.g. FR4) have a glass transition temperature (T_g) between 125^{o}C and 200^{o}C. Above this temperature there is a significant increase in CTE and a decrease in mechanical properties. For high temperature applications, ceramic based technologies must be considered. The properties of Si and SiC materials along with Al_2O_3 and AlN ceramic substrates are shown in Table 2.6 [36]. Al_2O_3 is the most widely used ceramic substrate. The CTE of Al_2O_3 is relatively high compared with that of SiC, which will limit the number of thermal cycles to failure. However, for applications that do not require large numbers of thermal cycles, Al_2O_3 could be a better choice considering the mature metallisation technology on Al_2O_3 and the high cost of AlN.

Thick film technology

In the thick film process, a layer is deposited by screen printing onto a substrate. The thick film material to be printed is referred to as an ink

Table 2.5: Physical properties of semiconductor and substrate materials [36].

Properties	**Si**	**SiC**	**Al_2O_3**	**AlN**
Density (g/cm^3)	2.3	3.21	3.75	3.31
Hardness (GPa)	11.5	24.0	19.0	12.0
Strength (MPa)	250	450	350-400	350-400
Elastic modulus (GPa)	130	470	397	320
Thermal conductivity (W/mK)	150	300	25	200
Thermal expansion coefficient (ppm/^{o}C)	2.8	3.7	7.2	4.1
Dielectric constant (at 1MHz)	11.0	42	9.4	8.9
Dissipation factor (at 1MHz)	0.09	0.05	0.0004	0.0005

or paste, and is typically 5 to 50μm [37]. The screen printing process is illustrated in Figure 2.3. The substrate is usually held by vacuum and its position can be finely adjusted, ensuring good alignment between consecutive layers. The ink or paste is applied to the surface of the screen and the flexible squeegee travels across the screen, pushing the ink through the open areas of the screen mesh. At a point immediately behind the squeegee, the screen peels away from the substrate. A deposit of paste in the desired pattern on the substrate is obtained due to the surface tension between the ink/paste and the substrate. The metallised thick film for high temperature operation must resist surface oxidation and migration while maintaining good adhesion to the substrate.

The pastes are typically dried at 150^{o}C for 15min to allow the removal of any organic solvents. The film then proceeds to the firing stage, in which the firing temperature profile typically includes 10min at a peak temperature of 850^{o}C, and an overall firing cycle time of 30 to 60min. In the temperature range 600-850^{o}C, the glass flows, sintering of particles occurs, and chemical reactions take place to form the final film.

A typical thick film paste is composed of: a functional phase which defines the electrical properties of the fired film, a binder which provides adhesion between the fired film and the substrate, and the organic vehicle which

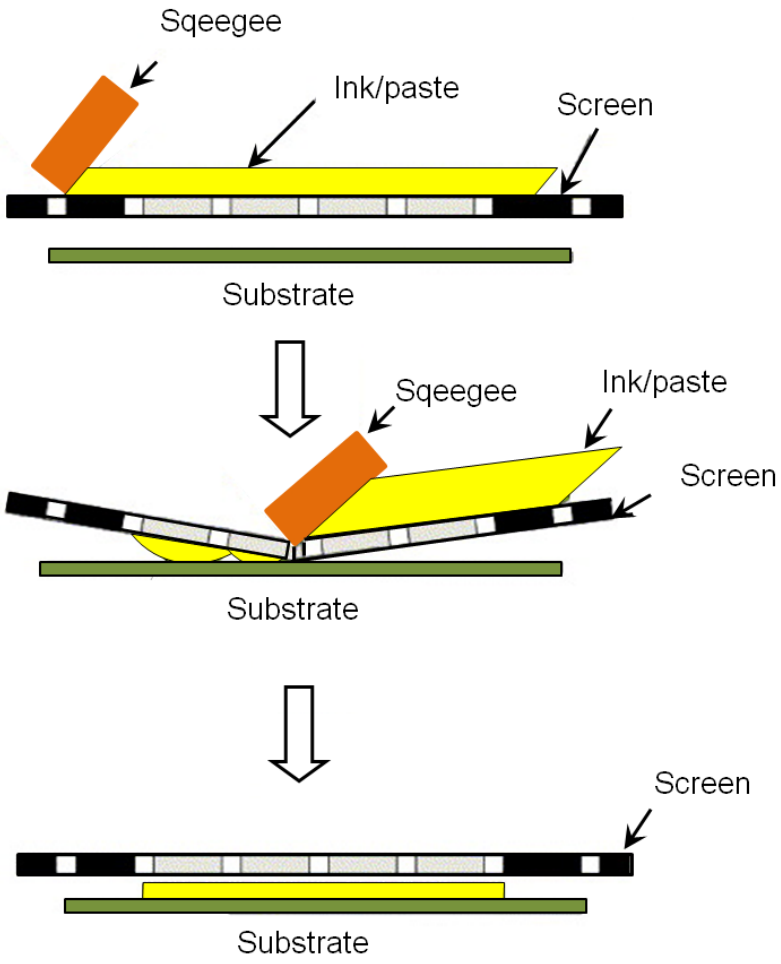


Figure 2.3: Schematic illustration of the screen printing process.

establishes the printing characteristics. The functional phase may be Au, Ag, Cu, Pd-Ag, Pd-Au, Pt-Au. Au-based thick film materials are preferred for electrical interconnections and conductive die attach for high temperature applications. The binder for the film conductor is generally formed of glass compositions and oxide additives, such as Cu oxide and Cd oxide. During the subsequent firing, Cu oxide and Cd oxide reacts with the substrate (usually Al_2O_3) to form a Cu spinel ($CuAlO_4$) and a Cd spinel ($CdAlO_4$), providing adhesion of the metal film.

2.1.3 Die attach materials

The die attach material must be compatible with the substrate and die backside metallisation, have a sufficiently high melting point after die attach, and not form intermetallics that may degrade the bond strength with time at temperature [38]. Although in some applications the device might require only a few temperature cycles (well-logging and space exploration), in other applications they may be subjected to many cycles (automobiles and aircraft). Therefore, thermal cycling behaviour needs to be considered depending on the application. Temperature cycling can be a more severe issue than continuous operation at an elevated temperature, due to the lack of time for strain from thermal expansion differences to relax [10].

Adhesives

ECAs consist of an insulating polymeric matrix and conductive fillers. The polymer matrix and its characteristics are mostly responsible for the adhesive ability to bond and withstand mechanical stresses. The electrical conductivity of the adhesive depends particularly on the fillers. As a result, the electrical and mechanical properties can, to a large degree, be adjusted independently [15].

The industrial application of ECAs for interconnecting and mounting electronic components is relatively new. The first use of ECAs in electronic technology was in 1956 through US patent "Electrically conducting cements containing epoxy resins and silver" described for fixing a semi-conducting crystal (Ge) to a metal base or holder. Thereafter, the number of publications regarding investigations on ECAs increased continuously.

Depending on the conductive filler loading level, ECAs are categorised as [34]:

a) Anisotropically conductive adhesives (ACAs): provide unidirectional con-

duction which is achieved by using a relatively low volume fraction of fillers (5-20% volume fraction) which is insufficient for inter-particle contact. Therefore, conduction in the X-Y plane of the adhesive is prevented. Nevertheless, enough particles are present to ensure reliable conduction between bonding electrodes in the Z direction. Conductive fillers measure typically between 3 to 5μm;

b) Isotropically conductive adhesives (ICAs): volume fraction of conductive fillers in the adhesive is between 20 and 35% volume fraction; this filler loading is so high that the adhesive can conduct equally well in all directions. Fillers are typically 1 to 10μm sized;

c) Non-conductive adhesives (NCAs): make no use of fillers.

The difference between an ACA and ICA is based on percolation theory. Percolation is the mechanism of conduction in ECAs where current flows through a three-dimensional matrix of contacting particles. Figure 2.4 shows typical results of how the electrical conductivity of a filled adhesive varies with the filler volume fraction where the fillers have a high aspect ratio. The non-linear behaviour is due to the non-idealised distribution of high aspect ratio filler that inevitably results and the onset of "percolation" of current through an interconnected network of clustered filler particles. The volume fraction at which percolation occurs is called the percolation threshold and depends on the filler shape and size, but is generally of the order of 15-25$\%$ volume fraction [34]. For ICAs, the loading fraction of conductive fillers generally greatly exceeds the percolation threshold, and thus there is electrical conductivity in all directions. In ACAs (in the form of films or a paste), the loading fraction is below the threshold, the filler has a high aspect ratio, and when combined with appropriate processing, the low volume loading is sufficient to establish a percolation network in the in-plane direction, but electrical conductivity in the through plane direction is avoided [39]. Lyons [40] studied

the effect of the composition and size distribution of conductive particles on the percolation threshold, and concluded that wide particle size distributions and particle types with higher density in adhesive formulations could reduce the percolation threshold.

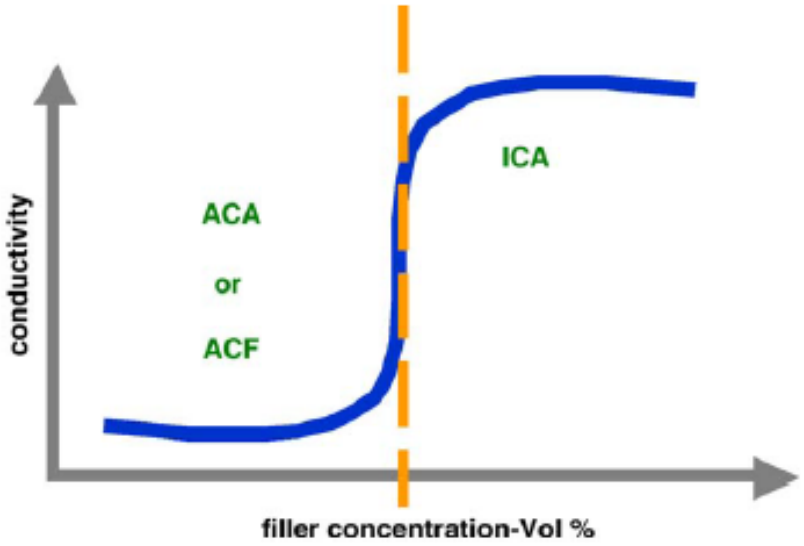


Figure 2.4: Percolation curve for ICAs and ACAs (ACFs refer to anisotropically conductive film) [34].

Figure 2.5 shows a schematic illustration of the bonding mechanism for all three types of adhesives. The first step in assembling components with ICAs (Figure 2.5(b)) is dispensing the adhesive in the correct location. Commonly used techniques include syringe dispensing, stencil and screen printing, and dipping. Automated equipment controls the dispensing time and pressure resulting in reproducible adhesive volumes. ICAs require no external application of pressure during curing (the process by which a polymer is hardened through cross-linking of polymer chains brought about by chemical additives, UV light or heat). ACAs (Figure 2.5(a)) are prepared by dispersing conductive fillers in an adhesive matrix, and are applied using the same methods. However, tolerances on the application area are significantly relaxed as the ACA can be applied to the entire interconnection area [41]. ACAs require the simultaneous application of pressure during the cure, but they may be applied over the entire surface to be bonded without creating un-

wanted short circuits. Temperature, pressure load, tacking time (time needed for the adhesive to soften and flow) and bonding time (final cure time) are the important parameters for ACA/ACF assembly. NCA bonding technology makes no use of fillers and relatively high bonding pressures can be used as shown in Figure 2.5(c). In this case, the electrical connection is achieved by sealing the two contact partners under pressure and heat. A small gap is created, approaching the two surfaces and thus enabling a small number of contact spots to form. These contact spots allows the electric current to flow [34].

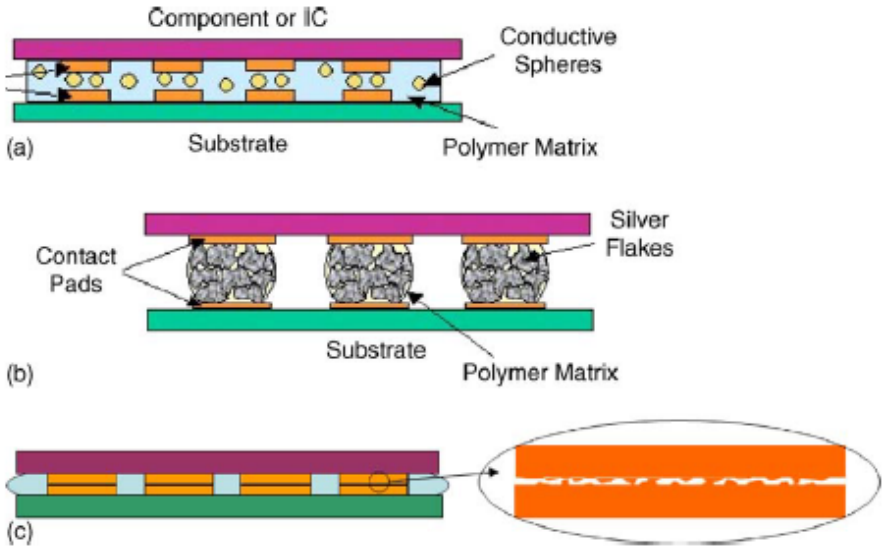


Figure 2.5: Schematic illustration of (a) ACA, (b) ICA and (c) NCA in flip-chip bonding [34].

An ideal matrix for ICAs should have relatively high glass transition temperature (T_g), fast cure, low moisture absorption, good adhesion and long shelf life. Both thermosetting and thermoplastic materials can be used as the polymer matrix.

Thermoplastics adhesives are high molecular weight molecules that are rigid at temperatures below their T_g. Above this temperature, polymer flow can occur, and reflow temperatures must exceed T_g to achieve good adhesion. Thus, T_g must be sufficiently high to avoid polymer flow in service but must be low enough to prevent thermal damage to the electronic cir-

cuits during reflow [41]. This flow is referred to as creep, which is thought to be a factor that may cause electrical resistance increases in thermal cycling tests [42]. Thermoplastics are reworkable and thus, can be easily repaired however they suffer more from degradation by high temperature. Phenolic epoxy, maleimide, acrylic preimidized polyimide, etc. are commonly used thermoplastics [34]. Voiding is a major concern in polyimides based adhesives as they contain up to 30wt% solvents and when heated during curing, voids are formed as the solvent evaporates. Any voids in the die attach material through poor processing could serve as crack initiation sites and reduce the effective heat transfer area of the package. Outgassing of polymers, trapped air in the attachment, or attachment shrinkage during solidification are the main causes of voiding [3, 43].

The thermosetting material is similar to thermoplastic excepting the short polymer chains are cross linked in three dimensions during the curing stage. The number of cross links determines the glass transition temperature (T_g) of the polymer; in general, the more cross links the higher is the T_g. Thermosetting materials include epoxy, cyanate-ester, silicone and polyurethane. Curing the mixture (by heat, UV light or catalysts) causes a chemical reaction between the curing agent and the resin to form a 3D cross-linked molecular network with a high T_g [41]. Shrinkage of the adhesive during curing provides additional compressive forces on the conducting particle contacts. Creep of the matrix might relax these loads but thermosets are less susceptible to creep owing to their high cross-link density [3].

Cyanate-ester based die attach adhesives have found increased popularity for many applications including hermetic as well as plastic moulded IC packages [3, 44, 45]. Cyanate thermosets offer high heat resistance, low outgassing of volatiles, and are easily modified to satisfy various application requirements. The unmodified cyanate/Ag system has gained rapid acceptance in the industry for solder seal hermetic applications because it offers

both ease of processing and high reliability [34]. New product developments include formulations with multi-modal Ag filler sizes and Ag loadings as high as 90wt% to enhance electrical and thermal performance.

Ag-filled epoxies are the most common adhesive binders due to their attractive balance of properties, such as low cost, good chemical and corrosion resistance, and excellent adhesive strength [34, 41, 46, 47]. They also have good resistance to moisture, solvents and chemical attack. The desirable properties may further be improved with suitable choice of solvents, fillers, colorants, flame-retardants, plasticizers and curing agents [48]. In [33], the development of novel conductive adhesives for surface mount applications was investigated. An epoxy-based ECA system was developed that had improved compatibility with Sn-Pb finished components, much lower moisture absorption, faster cure, compatible bulk resistivity, comparable adhesion strength, and higher glass transition temperature.

Potential conductive fillers come generally in the form of flakes, rods, plates or spheres and the particle size ranges between 5 and 20μm. ICA fillers include Ag, Au, Cu, and Ni, but use is dominated by Ag, because of its reasonable cost, high electrical conductivity, thermal inertness, high current carrying ability and low chemical reactivity [49]. In addition, unlike many other metals such as Cu that become non-conductive after being oxidised due to exposure to heat and humidity, Ag oxides have inherent conductivity. Although Au has better physical properties its cost is prohibitive for most applications. Au fillers are mainly used for highly demanding military and space applications [50]. C-based adhesives are only used for low conductivity applications due to their poor conductivity.

Ni has also found use in ACAs where spherical particles are commonly used, namely polymer spheres coated with metal (Ni-Au). Although the original intent of using plated particles was to reduce cost, various types of plated

particles have been specially designed for specific characteristics and end-uses. Ni particles can break the oxide layer on the electrodes and are suitable for interconnecting easily oxidised metallisations. Metal coated polymer spheres can provide high interconnection reliability due to the large elastic deformation during bonding. Even with added antioxidants, Cu-based conductive adhesives show an increase in bulk resistivity after ageing, especially under combined high-temperature and high-humidity conditions. The higher is the metal content the better is the electrical conduction, but the poorer is the strength of the adhesive.

Despite the advantages of ICA die attach, the wide use of this technology has not been adopted by the electronic industry. Long-term reliability is the main concern. In order for ECAs to be used in HTE applications they must have the same, or better, reliability than that of solders. ECAs must be able to survive, without serious degradation of physical or electrical properties, high temperatures for extended periods, mechanical shock, humidity, and thermal cycles (thermomechanical fatigue) [3, 51]. In most cases, reliability testing is often accelerated by increasing load/stress, humidity, temperature, etc. to simulate environmental influence factors and cyclic thermal loads, shock tests, etc.

Sufficient adhesion is required to ensure that the die remains in place when submitted to assembly or during actual device service. Thermally, it shall impart the least stress during expansion and effectively accommodate transfer of heat generated in the die to the package. Good dispensability is another concern, which is necessary to minimise non-uniform die attach especially in larger dies. Non-uniform die attach can enhance die stresses, promoting die cracking, thus becoming a reliability issue.

In order to get a good adhesive bond, it is important that the adhesive wets the bonding surface. It is then mandatory that the adhesive has lower

surface tension than the bonding surface. For instance, epoxies and polyimides have lower surface tension than Au, Sn, Pb, Cu and Pd. Therefore, a good adhesive bond is expected when bonding on Sn, Sn-Pb, Cu, Ag-Pd, and Au surfaces [15].

The "shape factor" of a given fillet (the region of excess adhesive outside the die, (Figure 2.6) is related to the type of adhesive combined with its wetting characteristics [52]. Besides viscosity, the surface-wetting ability of an adhesive is critical to capillary flow. For capillary flow to occur [52]: (i) the adhesive material must wet the surfaces so that the advancing contact angle is less than 90°; (ii) the intermolecular forces of attraction among adhesive molecules must be weaker than the intermolecular attraction of the adhesive for the die and substrate; this occurs when the surface tension of the underfill is lower than the surface energy of the surfaces being bonded.

Also, physical factors such as gap height, size of the die, and free volume beneath the die are accountable on the efficiency of capillary flow [52]. Small gaps are harder to fill and require low viscosity adhesives to keep the underfill times as short as possible. The size of the die is a further consideration in the time it takes for the underfill adhesive to traverse the distance and completely fill the gap. For a given die size, increased viscosity of the adhesive material also increases the time to fill the gap [52]. The volume of the adhesive must be controlled to assure complete filling beneath the die and some filleting around the die. The volume of the fillet is a function of the die length and width and the fillet height and width, as well as a shape factor (Figure 2.6).

Outgassing affects both die attach process and device functioning. Voids are considered stress raisers and can introduce inhomogeneity in the die attach, altering some operational properties. Moisture is the most commonly encountered service environment and thus it must be considered as a crit-

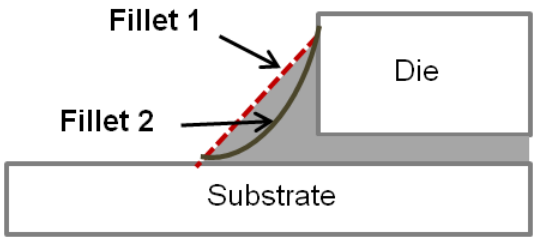


Figure 2.6: Shape factors for adhesive fillets [52].

ical factor when determining the long-term reliability of adhesive bonding. In some hermetic packages, outgassing of stored moisture increases moisture content in the package that could put the device function at risk. Moisture in epoxies has an adverse effect on both mechanical and electrical properties, including degrading bulk mechanical strength, decreasing interfacial adhesion strength [53] and causing delamination, promoting the growth of voids giving rise to swelling stresses in the joints. The water penetration inside the epoxy network causes weakness of the interchains interactions by forming hydrogen bonds with the water absorbed. Moisture can also modify the adhesives properties such as plasticization, which can cause depression of the T_g [54, 55], chemical degradation [56], or inducing cracking in the adhesive [57, 58]. Adhesive delamination by water is likely when high surface free energy substrates are used and the adhesion between adhesive and substrate is essentially due to van der Waals forces [59].

Proper curing is also very important to bond reliability as it is believed to be critical to develop the ultimate mechanical and electrical performance of ICAs. It is during cure that the electrical conduction of an ICA bond is primarily established [60]. The bond conduction is based on mechanical contact among conductive fillers. Lovinger [61] has shown that the conduction development during cure is accompanied by the decomposition of organic lubricants. This exposes the metallic surface of the fillers, and the cure shrinkage brings the fillers closer [62]. After curing, the adhesive fillers are randomly distributed, and thus forming a network within the polymer matrix. Elec-

trons are able flow from one adherent to the other across the filler contact points. As a consequence, numerous electron pathways are created, but with each path made up of a large number of mechanical contacts.

Reliability of ICAs is therefore dependent on every factor that influences the contact among fillers. The effects of degree of curing on the shear strength and electrical resistance of an epoxy conductive adhesive joint with Sn-37Pb bonding surface when exposed to environmental ageing was reported in [63]. It was concluded that a minimum degree of curing was needed to provide a certain level of mechanical and electrical performance in the adhesive bond. Below the critical degree of curing, the electrical resistance of the adhesive bond increased significantly upon exposure to environmental ageing. Because the adhesive was not fully cured it could absorb a significant amount of moisture which in turn caused oxidation/hydration at the adhesive/substrate interface. In addition, below the critical degree of curing, the shear strength of the adhesive joint was low compared with that of the adhesive bond which was optimally cured.

Several studies have been conducted to investigate the reliability of ECAs with an emphasis on electrical reliability [64–67]. Substrate metallisations and properties of the conductive adhesives influence the reliability of ECA joining, and the degradation mechanism of ECAs with different metallisations have been studied [64–66]. Jagt [66] explained the increasing electrical resistance of some ECA bondings after being exposed to environmental ageing, due to oxidation of non-noble metallisations, cracking, delamination, formation of Ag depleted surface layer in the adhesive, adhesive creep, intermetallic layer formation, etc.

Conductive adhesives typically have lower electrical conductivity than Sn-Pb solders (as shown in Table 2.3). Some methods to enhance electrical conductivity of ICAs have been reported [34]. Firstly, increasing the degree

of polymer matrix shrinkage on curing. Electrical conductivity is achieved during the polymer curing process caused by the shrinkage of polymer binder, and a more intimate contact results at the many metal-polymer interfaces within the adhesive. Table 2.6 shows the relationship between shrinkage and conductivity for three different cross-linking density ECAs. The cross-linking density of the ECAs increased as the shrinkage of the polymer matrix increased and resistivity decreased [34, 48].

Table 2.6: Relationship of shrinkage and electrical conductivity of ECAs [34].

Formulation	**Cross-linking density** ($\times 10^3$ **mol/cm**^{3})	**Shrinkage** (%)	**Bulk resistivity** ($\times 10^3 \Omega$ **cm**)
ECA1	4.50	2.98	3.0
ECA2	5.33	3.75	1.2
ECA3	5.85	4.33	0.58

Secondly, a further strategy is the optimisation of the lubricant / dispersant used to ensure low viscosity of the polymer/metal flake mixture. In an ICA, there is a thin layer of organic lubricant on the surface of metal filler, which plays an important role in the rheology of the adhesive. This organic layer (typically a fatty acid) forms a Ag salt complex between the metal surface and the lubricant. However, this lubricant layer is electrically insulating and reduces conductivity. Thus in order to improve conductivity, the organic lubricant layer should be partially or fully removed/replaced during curing, by a suitable lubricant remover such as dicarboxylic acid in the case of Ag. The incorporation of reducing agents such as aldehydes into the formulations can also improve conductivity because the aldehyde reduces low conductivity AgO that otherwise forms on the Ag/epoxy interfaces [34].

Low temperature transient liquid phase fillers is another approach to enhance electrical conductivity. The filler is a mixture of a high melting point metal powder (such as Cu) and a low melting point alloy powder (such as Sn-Pb or Sn-In). The latter alloy melts when its melting point is reached during

the polymer matrix cure. The high melting point particles are dissolved into the liquid, which exists only for a short period of time. An alloy is formed and solidifies. Figure 2.7 shows schematically how the electrical conduction is established through a plurality of metallurgical connections formed *in situ* by the two different powders. Because there are only certain combinations of metallic fillers that are mutually soluble, this technique is limited [34].

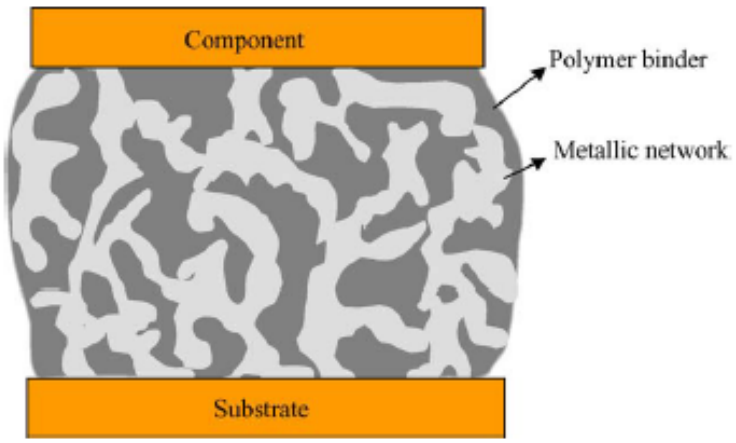


Figure 2.7: Diagram of transient liquid phase sintering conductive adhesives [34].

Metal-powder pastes, e.g. Ag, Ag-Pd or Cu copper pastes are widely used in the fabrication of hybrid and co-fired microelectronic packages. These metals offer high electrical and thermal conductivity. Furthermore, they do not present creep fatigue failure problems sometimes associated with solders. Because they have comparatively high melting points, the sintered joint operates at a much lower homologous temperature, translating to low inelastic deformation or accumulation of damage during temperature or power cycling, especially due to diffusion processes such as creep [68]. Recent studies have demonstrated the use of high quasi-static pressure (>40 MPa or 400kgf/cm^2 chip area) during sintering provides an additional sintering driving force that can lower the sintering temperature of existing thick-film pastes to less than 300^{o}C. However, the need for such a large pressure has hampered the quick adaption of the technology because it limits production throughput and places critical demand on substrate flatness and chip thickness [68].

The contact resistance between an ICA and non-noble metal finished components increases dramatically during elevated temperature and humidity ageing as shown in Figure 2.8. A stability criterion has been defined for solder replacement conductive adhesives as a contact resistance shift (increase) of less than 20% after ageing at 85^{o}C/85%relative humidity (RH) for 500h [34]. However, most commercial ECAs cannot pass this test on non-noble metal surfaces such as Sn/Pb, Sn, Cu, Ni, etc. Reliability and failure mechanisms of ICA joints on Sn37-Pb, Cu, and Au plated surfaces upon exposure to the 85°C, 85%RH environment were studied by Liu *et al.* [64]. They demonstrated that the mechanical strength and electrical performance were both reduced with increasing ageing time. They explained this related to the formation of Cu_2O on the Cu metallisation and the formation of PbO on the Sn-37Pb surface, as both Cu_2O and Sn-37Pb are both poor conductors and may form weak boundary layers at the interface. On the other hand, the Au metallisation system exhibited stable electrical performance after hot/wet humidity test because of it relatively noble nature. Nevertheless, the mechanical performance of the Au metallisation system after environmental ageing was not reported.

The formation of metal oxide layers resulting from corrosion is also possible [69] where water condensed from absorbed moisture at the interface between an ECA and metal surface gives rise to galvanic corrosion. ECAs with highest moisture absorption showed the fastest contact resistance increase and the ECA with the lowest moisture absorption showed the slowest contact resistance increase during ageing. Typically, ECAs formulated with high purity resins have lower moisture absorption and better contact resistance.

Besides low electrical conductivity and increased contact resistance, Ag migration is a significant reliability concern for Ag-filled ICAs [70]. This phenomenon is defined as an electrochemical process whereby Ag in a hu-

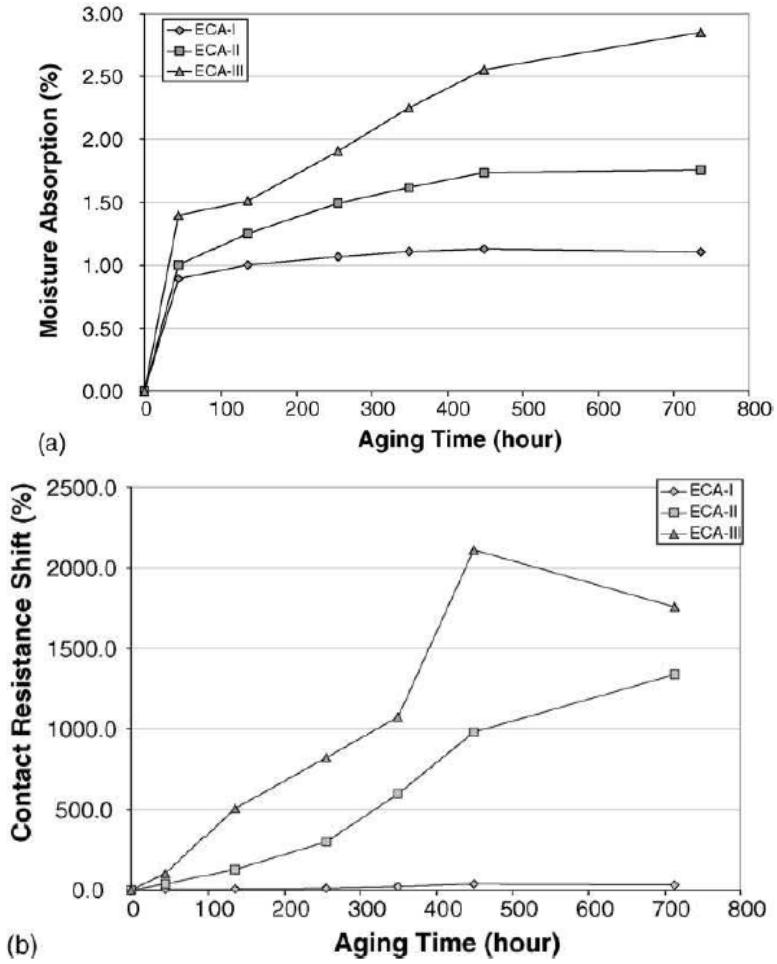


Figure 2.8: Moisture absorption and corresponding contact resistance shift of ECAs with 85^{o}C/85% RH aging (a) moisture absorption and (b) contact resistance shift [34].

mid environment and under an applied electric field leaves its initial location in ionic form and deposits at another location, forming metallic dendrites or "whiskers". As the dendrite or whisker grows, a reduction in electrical spacing and eventually a short circuit between interconnections may occur [3]. Although other metals may also migrate under specific conditions, Ag is more susceptible to migration, mainly due to the high solubility of Ag, low activation energy for Ag migration, high tendency to form a needle, whisker or dendrite shape, and lack of a stable passivating oxide layer [34, 49, 71].

The most common effect of Ag migration on device performance is to short the circuits promoting device failure. A semi-empirical model based on accelerated ageing tests for predicting the failure times and threshold voltage

for migration was proposed by Giacomo [72]. The failure time for the electrochemical migration process as a function of applied bias, relative humidity and temperature was given by:

$$t_f = \frac{BT[(1-RH)(1+(m-1)RH)]}{mRHD_0 \exp(-H_D/kT)E}, \tag{2.1}$$

where t_f is the time for failure, RH the fractional relative humidity, T is the temperature, E the electric field strength, B, M, H_D and D_0 are effectively best-fit parameters that depend on the material and surface conditions in the migration experiment.

Several methods to reduce Ag migration and to improve reliability have been reported. For instance, alloying the Ag with an anodically stable metal such as Pd, Pt or even Sn [34]. Ag and Pd exhibit complete mutual solubility, moreover, the addition of Pd to pure Ag improves solder leach resistance and reduces the migration of Ag because of solid solution formation. The required concentration of Pd to inhibit Ag migration was reported as 30%. Pd is of course, however, particularly expensive. A ternary alloy Ag-Pd-Au (60%-20%-20%) proved to be more effective in reducing Ag migration when compared to Ag-Pd alloy [73]. This is due to the presence of Au which forms an alloy with Ag, and thus reducing the Ag free available to promote migration [74]. Other steps to reduce migration include using a hydrophobic coating over the printing wiring board (PWB) to shield its surface from humidity and ionic contamination; plating the Ag with metals such as Sn, Ni or Au; coating the substrate with polymer; and employing siloxane epoxy polymers as diffusion barriers due to the excellent adhesion of siloxane epoxy polymers to conductive metals [34].

Another reliability issue is the lowering of adhesion strength due to the incorporation of the metallic fillers [3,34]. High adhesion strength is required for fine pitch interconnections and can be fragile to shocks encountered during

assembly, handling and lifetime. The relationship between the orientations of Ag flakes in an epoxy matrix and adhesive strength was investigated in [48]. The randomization of Ag flake orientation was effective in improving the adhesive strength. The adhesion strength can also be enhanced by lowering the elastic modulus of the adhesive as the thermal stress at the interface is reduced [34]. Figure 2.9 shows the relationship between the adhesive strength and the elastic modulus of an ECA. The adhesion increases with the elastic modulus decrease but a very low modulus can degrade the cohesive force, which will lower the adhesion. Also, surfaces with high roughness typically show higher adhesion strength. Increasing a surface roughness by chemical etching, plasma treatment or anodization has been used to improve adhesion strength, providing structural durability in humid environments [75].

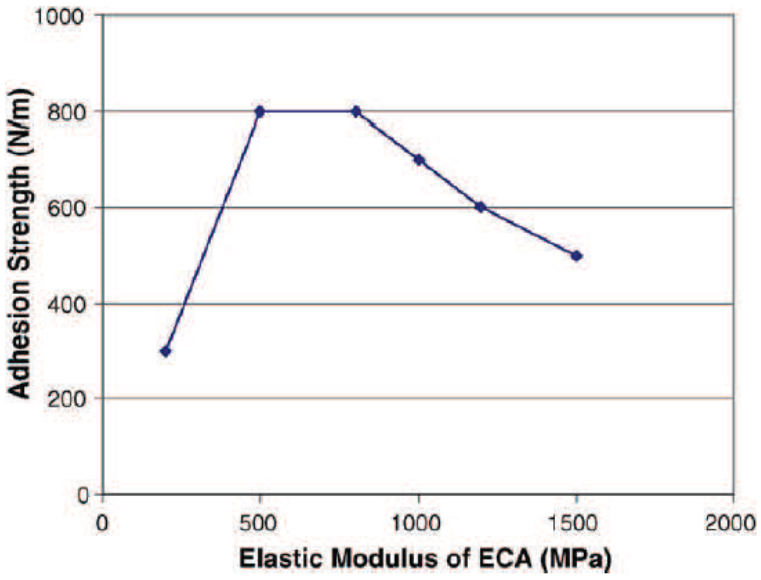


Figure 2.9: The relationship between the adhesion strength and the elastic modulus of ECA [34].

One of the most important properties of ECAs that favours them over solders is impact performance [3, 76–78]. A drop test for evaluating the impact strength is commonly used in which a mounted chip carrier and circuit board assembly are dropped onto a hard surface from a height of 1.5m - it is required for a die attach material to survive six drops [48, 79]. Besides this qualitative method, the falling wedge technique is capable of quantitatively

determining the impact performance of conductive adhesives for bonding purposes. Some approaches have been employed to improve the impact strength of ECAs [48]: (i) a decrease in filler loading but which can lead to decrease in electrical properties; (ii) using resins with low modulus so that ECAs are better able to absorb impact energy; and (iii) the incorporation of micron-sized carbon fibers to produce more efficient distribution of mechanical forces within the joint. A mechanical shear test investigation demonstrated that a significant internal strength improvement can be achieved with the addition of low weight percentages of carbon fibers into a commercially available conductive adhesive [34].

Under conditions of thermal shock, ECAs are susceptible to brittle failure in much the same way they are for isothermal mechanical shock. The problem of thermal shock is that the polymer cannot plastically respond to relieve expansion/contraction strains quickly, and the interconnect fractures. A high temperature epoxy-based Ag-loaded ECA was submitted to 300 cycles of -55 to 125 ^{o}C at 10% shear strain. Even after 500 cycles, the adhesive still had not failed electrically. Under the same conditions, Sn-37Pb failed after 220 cycles. Cracks appeared in the ECA interconnect but they ran perpendicular to the direction of deformation and electrical conduction paths were retained (Figure 2.10) [3].

Several issues dealing with reliability of ACA/ACF bonds have also been studied. The main degradation mechanism have been identified, namely oxide growth on less noble metallisation, causing increased contact resistance, stresses due to thermal load or influence of humidity inducing cracks within or delamination of the adhesive layer [34]. To obtain a more reliable assembly using ACFs, its CTE can be reduced. Hwang [80] incorporated non-conductive silica fillers into ACFs and studied their effect on cure kinetics and thermo-mechanical properties. The elastic modulus of the ACFs increased

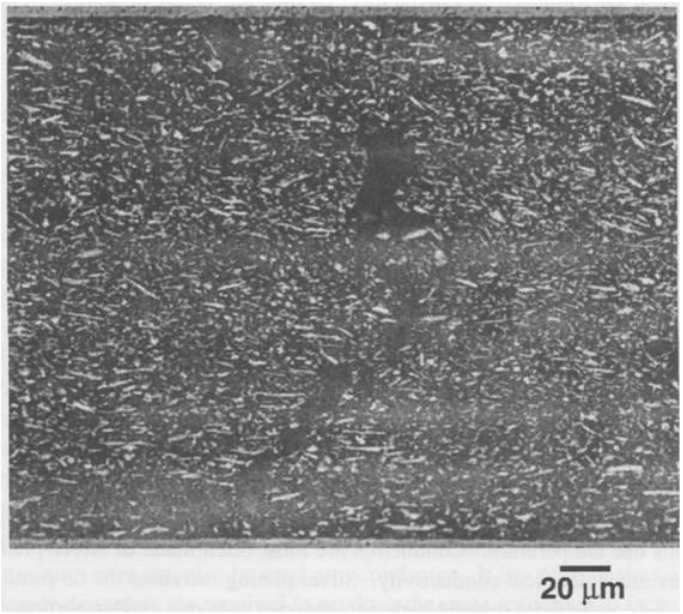


Figure 2.10: Optical micrograph of a high temperature epoxy-based Ag-loaded ECA after 300 cycles of -55 to 125^{o}C [3].

with filler content increasing and filler size decreasing. Also, the CTE of the ACFs and warpage of ACFs flip chip assemblies both decreased with the increase of filler content and decrease of filler size; this is in accordance with the increase of specific surface area of the silica fillers. Thermal cycling reliability was improved with higher content and smaller size of silica fillers in the ACFs [80].

Joints with NCAs avoid short-circuiting and so can be used for narrow connector pitches. Further advantages include cost-effectiveness, ease of processing, good compatibility with a wide range of contact materials, and low temperature cure.

High temperature solders

Eutectic die bonds also known as solders can be divided into hard solders and soft solders: the former have higher melting points and yield high stresses. Hard solders include Au-Si, Au-Sn and Au-Ge alloys. For high temperature applications, Au-based eutectic alloys have been proposed as promising die attach materials because of their good compatibility with the die and sub-

strate metallisations, excellent electrical conductivity, thermal conductivity and corrosion resistance [38, 81]. Eutectic solder alloys are typically supplied as a thin preform or ribbon, and are generally considered a "reliable" bonding material, even if they are comparatively expensive.

Solder alloys used for electronic applications must have a two-phase region (liquid+solid) for ease of processing but if the two-phase region is too large, the joints have the possibility to move with respect to one another during solidification, and solidification shrinkage can be problematical. As a result, irregular, coarse and sometimes cracked joint surfaces may occur. Therefore, most solder alloys for interconnects are near-eutectic alloys.

Au-Si is used as a high thermal performance die attach material for high power microwave and RF Si-based devices. To bond dies to metallisation layers using Au-Si, a Au-Si preform layer is used. This preform comprises Au-rich and Si-rich regions in the form of a foil, which is placed in between the upper Au metallisation of the substrate and the lower Au metallisation on the base of the Si die. The system is heated to above the eutectic temperature of 363^{o}C. Although this is the commonly accepted eutectic temperature, Kato [82] and Gerlach [83] have measured 360^{o}C and 370^{o}C respectively. Si and Au have melting temperatures of 1412^{o}C and 1063^{o}C, and the simple Au-Si equilibrium binary phase diagram is shown in Figure 2.11. The average composition of the preform is typically near the eutectic composition of Au-3.4wt%Si. Above the eutectic temperature, the Au and Si regions dissolve in one another, together with the Au from the metallisation. Once the liquid or solid/liquid composition reaches equilibrium for that temperature it will maintain these concentrations until there is no more gradients in the liquid. This mechanism is not ideal because Si is very easily oxidised at bonding temperatures, even though attempts are made to blanket the area with N_2 gas. The oxide interferes with interdiffusion, and the result is non-wetting and voiding. In practice, other layers are usually added to the basic system,

including Au on the back side of the die. Au is frequently used as the metallisation layer as cheaper Cu or Ni alternative tend to oxidise. In some cases, changes in composition as the Au is consumed makes it more dilute, so the melting temperature (liquidus) increases and eventually the joint becomes solid even without cooling (transient liquid phase). Reflow temperatures exceeding 400^{o}C for Au-Si raises concerns including the effects of such high processing temperature on the actives/passives/wirebonds elsewhere in package [84].

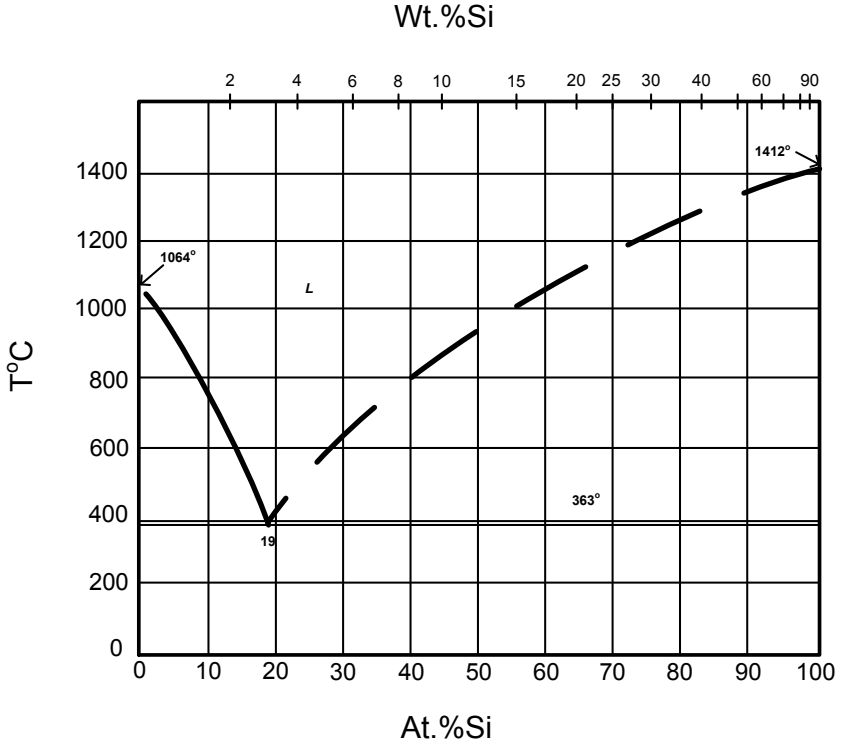


Figure 2.11: Au-Si phase diagram [85].

Bare Si is often used for dies of small surface area, particularly in low cost applications. However, most dies receive a back side coating of Au in order to protect the Si from oxygen or other impurities. Mencinger [86] reported a minimum Au thickness of 150nm in order to have a reliable die attachment. Shukla and Mencinger [87] reported some die back side metallurgies that can be used. They pointed out that that there is still the problem of rapid diffusion of Si through the Au layer, and subsequent Si oxidation on the Au surface. Metal barrier layers, such as Ti or Cr are sometimes deposited between

the Si and Au, thus preventing Si diffusion through Au at room temperature, but to allow it to occur at the bonding temperature [87]. Nevertheless, these barriers can also become a problem if they oxidise. Cr can also appear at the Au surface by grain boundary diffusion, forming its own surface oxide. A Cr-N-Au system has been proposed which reduces both Si and Cr diffusion. The deposition technique of the metallisation is also important. Hoge and Thomas [88] concluded that sputtering is preferred to evaporation.

Au-Si die bonding has been used for Si dies and SiC dies [89], and GaN wafer bonding [90]. The use of Au-Si eutectic preforms or pure Au preforms to initiate a reaction and to improve the bonding is common [91]. Au-Si preform composition may be varied in the range 2 to 6wt% of Si. In general, Au-2wt%Si has good wetting and flow characteristics during die bonding. On the other hand, die cracks can develop using Au-4wt%Si alloy preforms at a reflow temperature of 425^{o}C possibly due to void formation and uneven stresses [92]. Stresses can be minimised by using a thicker preform (1mm), a high die bonding temperature (500^{o}C or higher) and a slow cooling rate [92]. Pure Au preforms can only be used with Si dies because the Si for the reaction is taken from the back of the die. The use of a pure Au preform yields several advantages; not only does the preform not oxidise, it remains solid until the eutectic bond is formed with the die. This ensures a better scrubbing action to disrupt any oxides in the back of the die. However, a higher substrate temperature is recommended which enhances Ni diffusion to the surface of the Au metallised package, and strongly increases residual strain when the package cools back down to room temperature.

Au-Si die bonding has been used for die attaching Si substrates and sapphire substrates (with poly-silicon, Au or no coating on the back surface). Another method used for implementing die attach of ICs onto PCBs is by depositing Au directly onto the Si surface on the back of the IC chip, and then heating it above the eutectic temperature. The Si diffuses into the Au film,

and a "soft" Au-Si mixture is then created. Hydrofluoric acid (HF) is often used to remove the native oxide layer of the samples and wafers are forwarded directly to the evaporator/sputter vacuum chamber for Au deposition. The HF etch is necessary because Si oxidises almost instantaneously when in contact with oxygen. Although, oxide is practically unavoidable, scrubbing the die during the bonding process helps to break away any oxide layers as well as removing other contaminants in order to have a "clean" Si surface exposed to the bonding [87]. Scrubbing also helps to homogenise the liquefied interface, minimising segregation.

Subsequent solidification gives rise to epitaxial growth of both silicon and gold on top of the (Si) substrate. As a consequence, numerous small Si islands can be formed. The predominant presence of Au is not surprising considering the eutectic composition. Below the eutectic temperature, Au diffuses into the Si rather than the Si into the Au [93].

In order to achieve adequate wetting in a eutectic system it is important to minimise oxidation and use scrubbing. A die bond will fail in die shear testing, such as that in MIL. STD. 883C [94], if non-wetting occurs. This specification requires a value of 6MPa for dies less than or equal to 4.1mm^2 in area when there is evidence of greater than 50% adhesion of the die attach medium, and 12MPa when adhesion is less than 10%. In any case, there will always be some oxidation and voiding.

The main concern with voids in a eutectic die bond is that they have been identified as the main cause for die cracking [95, 96]. It has been reported that failure of eutectically bonded devices by vertical die cracking can be attributed to locally higher stresses due to voids [95]. Cracks often occur at the corner of the die and initiate at an edge void [96]. Furthermore, as the size of the die increases, the problems with voiding become more important. Larger stresses and greater difficulty in controlling void formation are

expected.

Eutectic Au-20wt%Sn solder is especially useful for applications where fluxing during soldering is not applicable [97,98]. Advances in manufacturing and bonding methods have extended the diversity of applications for Au-Sn solder, mainly in applications where Pb is no longer an option. Au-Sn is robust and will survive the high operating temperatures, including subsequent process temperature cycles as the package is soldered to a next-level assembly, such as a circuit board.

Au-Sn solder possesses excellent thermal and mechanical properties, and provides also excellent wetting characteristics (Table 2.4) making it well-suited to device packaging in which long-term device reliability is important [99]. It has a eutectic temperature of 280^{o}C, between that of conventional solders and Au-Si or Au-Ge. However, Au-Sn solders have comparatively high modulus and transfer thermo-mechanical stresses to the Si die, making it viable only for small die applications or else delamination or die cracking will occur. The complexity of the Au-Sn system and the many stable intermetallic compounds as well as two eutectic and at least three peritectic points, as seen in the phase diagram in Figure 2.12, cause complications in understanding Au-Sn performance. The two eutectic compositions (indicated by red arrows) consist of a relatively Sn-rich composition reported between 4.6 and 6.3at% at a temperature of 215-217^{o}C and another at 71at% Au and 279^{o}C [100].

Die bonding generally uses a preform of eutectic Au-Sn. Nevertheless, the use of preforms of Sn plated onto a thin layer of Au has been successfully reported. Sn plated Au is a transient liquid phase bonding method, in which the Sn layer will melt first and diffuse into the Au. Off-eutectic Au-Sn can also be achieved by using a smaller eutectic Au-Sn preform than the size of the die, and thus limiting the amount of Sn present. In order to achieve the off-eutectic composition, a source of Au is needed; a layer of Au (approx-

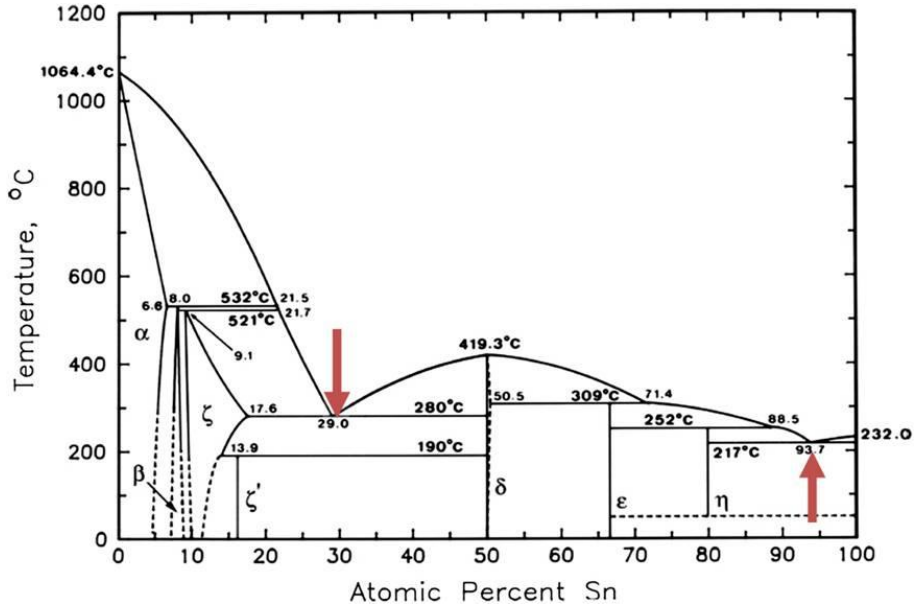


Figure 2.12: Au-Sn equilibrium phase diagram [100].

imately 20μm thick) on the (SiC) die was used [38, 89]. As a consequence, the melting point increases. The longer the Sn has to diffuse at processing temperatures, the higher the remelt temperature will be, because there will be a lower concentration of Sn. As a result, final composition will be moved to the left of the eutectic point. A major problem with Sn containing preforms is the formation of Sn oxide on the surface of the preform. This thin oxide layer inhibits bonding and results in a higher concentration of voids under the die [101].

Au-Ge has a eutectic melting temperature of 356^{o}C [102] and the Au-Ge equilibrium phase diagram is shown in Figure 2.13. As a die attach material it is generally supplied as a hypo-eutectic preform [103].

Die fracture and fatigue mechanisms depend on the modulus of the die attach (determines the fraction of stress imparted to the die), on the difference between thermal expansion of the die and substrate (determines the total thermal stress), and on the fracture toughness and pre-damage (due to load history) of the die. Figure 2.14 illustrates the temperature dependence of the elastic modulus of Au eutectic die attaches.

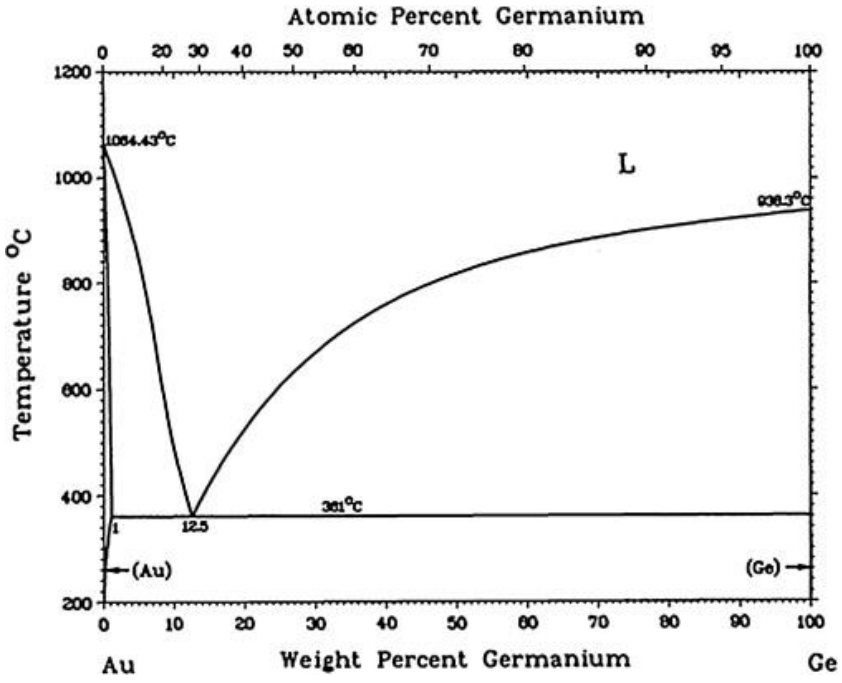


Figure 2.13: Au-Ge equilibrium phase diagram [85].

Die attachments with multiple metals always have the risk of forming harmful intermetallics depending on the metallurgy used on the die and substrate. From a metallurgical point of view, Au-Sn is very different to Au-Si. Whereas the Au-Si eutectic solidifies into a structure of practically pure Au and pure Si, eutectic Au-Sn solidifies into a mixture of two intermetallic compounds (discussed later).

2.1.4 Interfacial intermetallic compound formation

Electronic packages involve many bonds at interfaces between different materials. Many of the surfaces to be bonded have metallisation layers applied to resist oxidation, promote adhesion, etc. Consequently, there are many possibilities to form compounds at the interface by chemical reaction and interdiffusion either in the liquid or solid state. Intermetallic compound (IMC) formation is amongst the most important issue in electronic packaging applications since the CTE mismatch between the IMCs, die attach and package materials can give rise to significant strains, and then creep, coalescence,

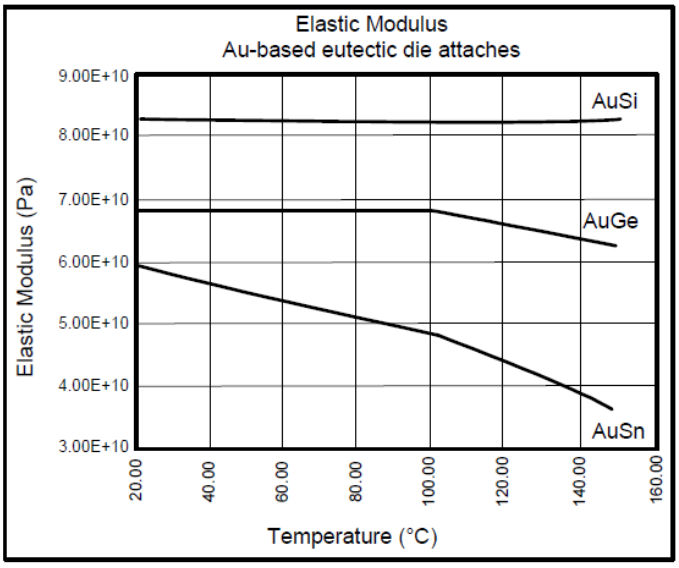


Figure 2.14: The elastic modulus of Au-based eutectic die attach materials as a function of temperature [3].

voiding, IMC cracking, IMC crack growth, etc.

IMC formation also often involves a volume change since the reaction product has a different crystal structure to either of the parent phases, possibly exhibiting distinct growth and mechanical anisotropy. Further, growth anisotropy that leads to faceted IMC particles, needles, plates, etc. leads to strain inhomogeneities at the interface. If IMCs have significantly different mechanical behaviour to the parent phases such as high stiffness (as is frequently the case), then the loads at the interfaces due to CTE mismatch may become concentrated in the less stiff material. Overall, stress/strain concentrating morphologies, high stiffness, different CTEs, low ductility (but high strength) and volume change effects are usually superimposed so that IMCs play a dominant role in the lifetime of dissimilar material interfacial regions. IMC growth can be reduced using high cooling rates during processing, although rapid cooling may induce thermal stress or strain in the substrate or package because it does not allow inelastic redistribution of strain, for instance by creep [104].

Typically, thin film metallisations of HTE low temperature or high tem-

perature co-fired ceramic (LTCC, HTCC) substrates are composed of three layers as shown in Figure 2.15. The bonding layer is designed to bond the LTCC/HTCC with the conducting adhesion layer, which is most commonly Ni for HTE applications. The adhesion layer is hard or soft solder, often with a Au "flash" for wire-bond or soldering applications [84].

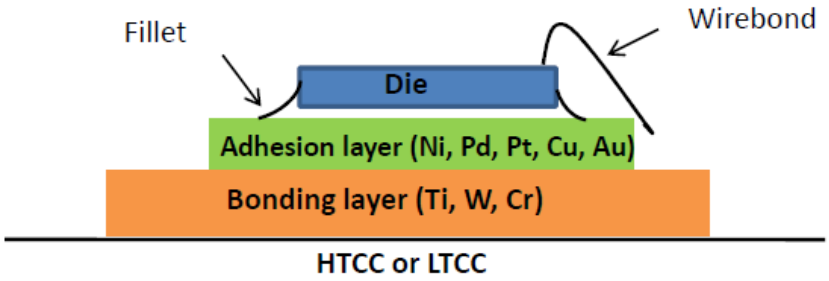


Figure 2.15: Typical metallisation arrangements comprising three distinct layers.

Table 2.7 lists typical elements/compounds in metallisation layers as well as the typical intermetallic compounds that may form. Only the binary IMCs are listed, and there are many additional ternary compounds.

Table 2.7: Examples of common IMC formed at electronic package metallisation interfaces [105].

Layer	**Possible IMC compositions forming between layers**
Diffusion barrier, wetting layer	Ti_2Ni, $TiNi_3$, Ti_2Pd, Ti_2Pd_3 $TiPd_5$ Ti_2Cu, Ti_3Cu_4, Ti_2Cu_3, $TiCu_4$
Solder, die, wirebond	Ni_3Sn, Ni_3Sn_2,Ni_3Sn_4, $NiSi$, $NiSi_2$, Pd_5Si, Pd_9Si_2, Pd_3Si, Pd_2Si, $PdSi$, Pd_3Sn, Pd_2Sn, $PdSn$, $PdSn_2$, $PdSn_3$, $PdSn_4$

The physical and mechanical properties of IMCs are important in governing die attach reliability, although they are quite difficult to characterise at the micro-scale of relevance. Typical properties for the common Cu, Sn, Ni and possible IMCs are shown in Table 2.8 [106]. IMCs formed between two

low strength, ductile elements can be very strong but brittle e.g. Cu_6Sn_5 and Cu_3Sn from Cu and Sn. IMCs also usually lead to the degradation of both thermal and electrical conductivity [84]. In designing reliable metallisation systems, it is essential to take IMC formation into account [107].

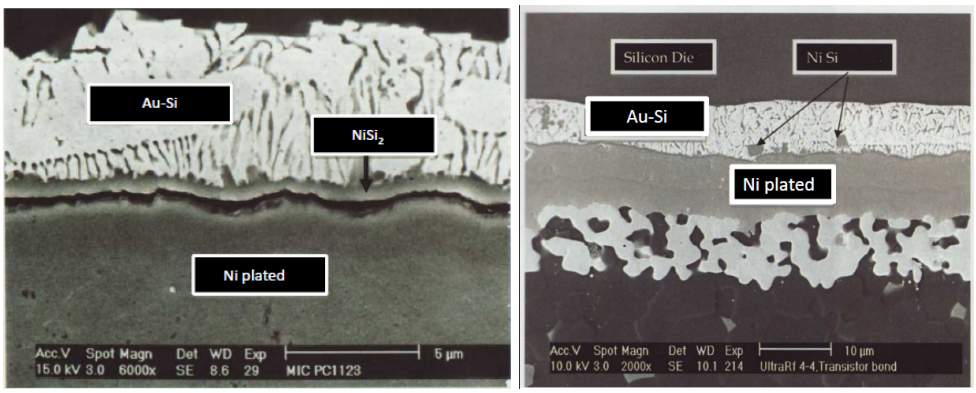
Table 2.8: Room temperature properties of pure Cu, Sn, Ni, and their intermetallics [106].

Property	**Cu**	**Sn**	**Ni**	**Cu_6Sn_5**	**Cu_3Sn**	**Ni_3Sn_4**
Density (g/cm^3)	8.9	7.3	8.9	8.3	8.9	8.7
Young's modulus (GPa)	117	41	213	85.56	108.3	133.3
Shear modulus (GPa)	—	—	—	50.21	42.41	45.0
Toughness ($MPa.m^{-1/2}$)	—	—	—	1.4	1.7	1.2
Vickers hardness (kg/mm^2)	30	100	15	378	343	365
Electrical resistivity (μOhm.cm)	1.7	11.5	7.8	17.5	8.93	28.5
Thermal conductivity (W/(m.K))	3.98	0.67	0.91	0.34	0.70	0.20
Specific heat (J/(g.K))	0.39	0.23	0.44	0.29	0.33	0.27
Thermal expansion (10^{-6}/K)	17.1	23	12.9	16.3	19.0	13.7

The presence of IMCs may indicate whether or not a good metallurgical bond has been formed. Nevertheless, as IMCs are almost always inherently brittle because of their frequently ordered crystal structure and often have stress concentrating morphologies, a thick IMC layer at the interface may cause reliability problems.

For HTE, the Au-Si system has been suggested since Pb- or Sn-based solders and many conducting adhesives have insufficient temperature capa-

bility [3]. An Au-Si die attach bond is formed using a Au coated Si device bonded to a Au/Ni plated electronic package using Au-Si solders. Figure 2.16(a) shows a scanning electron image of the interfacial area between plated Ni and the Au-Si die attach material. A continuous, brittle $NiSi_2$ intermetallic compound formed between the Au-Si die attach alloy and the plated Ni surface, which then readily fractured when exposed to a shear force. In order to slow the $NiSi_2$ formation in Figure 2.16(a), the Ni layer was doped with greater than 5at% Co [84]. The formation of a thick, continuous layer of $NiSi_2$ was frustrated because the kinetics of the $Ni(Co)Si_2$ formation were much slower than those of $NiSi_2$ formation, and the Ni(Co) layer acted as a barrier to the continued Ni diffusion to the interface. Figure 2.16(b) illustrates a cross-section of a Si die bonded with Au-Si die attach but with a Ni(Co) plated layer. $Ni(Co)Si_2$ was now isolated into discontinuous blocks; when die shear was performed, there was a mixed mode failure with areas of failure in the Si die and areas of failure in the Au-Si die attach. Reliability was improved with the Co alloying.



(a) (b)

Figure 2.16: SEM images of the interfacial area between plated Ni and the Au-Si die attach material; (a) single mode failure between a Au-Si die attach and Ni plated layer; (b) doping Ni with Co frustrates IMC formation during Au-Si die attach [84].

From a metallurgical point of view, Au-Sn is very different to Au-Si. If no Ni plating is used, the Au-Si eutectic solidifies into a structure of practically pure Au and pure Si, whereas eutectic Au-Sn solidifies into a mixture of

two intermetallic compounds: Au_5Sn and AuSn.

Figure 2.17 shows a scanning electron image of the interface between a Au-Sn solder and the plated Ni layer (with flash of Au) after thermal shock that produced a single mode interfacial failure in the region of $Au_{0.5}Ni_{0.5}Sn_4$ IMC growth.

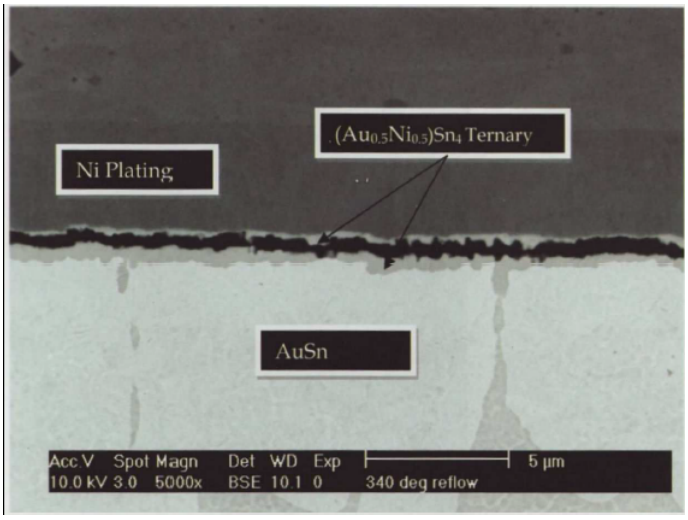


Figure 2.17: Failure at AuNiSn IMC when Au-Sn is soldered to Ni [84].

Ge forms also a brittle intermetallic with Ni which can cause problems. Nevertheless, for metal systems not containing Ni, Au-Ge has been investigated with successful results [108].

In general, IMC growth kinetics in the solid state obey a parabolic growth law, given by:

$$L = (Dt)^n, \tag{2.2}$$

where L is the thickness of the IMC layer, t is time, and D is the temperature dependent diffusion coefficient of the primary diffusion element [109]. In practice, n is estimated by curve fitting to experimental data, but has a theoretical value of n= 0.5 for bulk diffusion controlled growth [110]. The IMC growth rate is also often dependent on the composition [109].

2.1.5 Summary

An electronic package must physically support the active electronic device, protect it from the environment, provide a means of removing generated heat, and provide electrical connections to and from the device. HTE must function reliably in hostile conditions such as down deep wells and inside turbo-machinery. Neither solders nor ECAs offer an ideal solution for all HTE applications: each material has its own advantages and disadvantages, and selection of the appropriate material should be made on a case-by-case basis.

No commercially available ECAs offer sufficient performance and reliability for HTE, and the only commercially available solder of relevance is Au-Si. The disadvantage of Au-Si is very high processing temperature so that it is very difficult or impossible to eliminate IMC formation.

2.2 Thermomechanical behavior and analysis

2.2.1 Reliability and accelerated testing

Reliability is usually defined as the ability of a system to survive and to perform a required function, without failure or breakdown, for a specific period of time under stated operation and maintenance conditions [111]. Reliability is always important in electronic packaging. Electronic packages are expected to last many years, and it is usually unfeasible to perform reliability tests under service conditions due to the time and costs involved. The accelerated test conditions must be specifically designed for the required service conditions, considering the anticipated failure modes and mechanisms. Accelerated testing is accomplished by subjecting the components to exaggerated mechanical, environmental and/or electrical conditions.

In an accelerated thermal cycling test, a package is placed in an oven

and subjected to temperature excursions representing conditions considerably harsher than those expected in service. During this process, the packages are tested for their electrical resistance/continuity, where an increase in resistance suggests a crack has developed typically through the electrical interconnect. Post-test examination is also used by scanning acoustic microscopy (SAM) and various types of optical and electron microscopy. The average number of cycles needed to give a failure gives a measurement of reliability of the electronic package [112]. A commonly used thermal cycle is -55^{o}C to +125^{o}C with a 2-5^{o}C/min heating/cooling rate. Dwells at the upper temperature are at least 10-15 min, however many other variations are used, and a more aggressive thermal cycle is needed for HTE. A longer dwell period may be chosen in order to damage the interconnects more rapidly because there is less time for creep to relieve thermal mismatch strain at high temperature.

The degree of stress acceleration experienced in an accelerated test is usually described by an acceleration factor, defined as the ratio of the lifetime (cycles) under field conditions to the lifetime (cycles) under the accelerated conditions. The acceleration factor can be interpreted as the number of times the particular failure mechanism has been accelerated during the tests. Typically, there is a predominant region of stress accumulation or stress inducing mechanisms leading to a particular failure mechanism, and typical mechanisms include changes in material properties at high or low temperatures or time-dependent strains due to diffusion or creep at elevated temperatures.

In addition to accelerated testing, correlations, numerical analysis, statistics (Weibull) and modelling have been used in an attempt to predict failure of a package under field conditions of temperature, cycles, humidity, vibration, even at the package design stage [113]. Modelling of electronic packages behaviour with techniques such as finite element methods (FEM) has been used widely to try to understand the evolution of stresses and strains

in multi-material assemblies with complex geometries in particular under temperature cycling. FEM models are able to give a good prediction of local strains and stresses where suitable material property data is available but their challenge is converting macroscale, continuum stress and strain data into a criterion for microscopic failure in a meaningful way.

2.2.2 Scanning acoustic microscopy

The reliability of integrated circuit packages depends largely on their mechanical integrity. Typical failures in die attach packages (Figure 2.18), including delaminations, cracks, voids and die tilt, are generally located at the interface between the different layers constituting the package [114, 115]. These defects are usually non-obvious in the as-manufactured electrical performance characteristics and can cause premature failure [115].

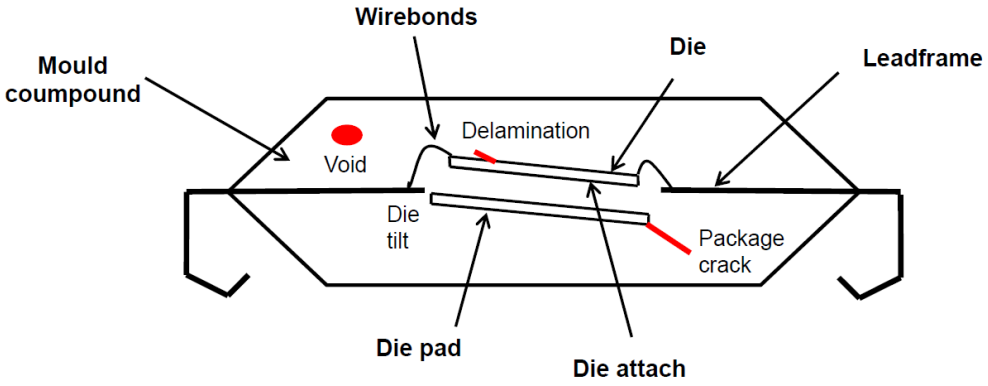


Figure 2.18: Schematic of the types of defects detectable in electronic packaging using SAM [116].

Scanning acoustic microscopy (SAM) is a technique for the non-destructive investigation of electronic package failure, with the potential to provide a qualitative image of package defects and their location within the package. SAM uses ultrasound to image by transmitting an acoustic wave through the device, and the detected transmission and reflection characteristics are used to generate an image of a region of the device by selecting various timing gates. Commercial acoustic microscopes are capable of scanning in three

imaging modes: A, B and C. Each one provides a different perspective of the sample and accomplishes specific functions. In the A-scan, the transducer stays still at a single point above the sample and is focussed to a specific depth within the sample. The B-scan mode is characterised by the scanning in X direction and increments in Z direction. Finally, C-scan is typically the type of analysis that is performed to produce SAM images that are often found in failure analysis reports. C-mode scanning generates an X-Y planar image at a specific depth within a sample (Figure 2.19). The latter is usually used to create interface scans to examine bonding, voiding, and interface integrity [117]. A X-Y resolution of up to 0.5μm can be achieved.

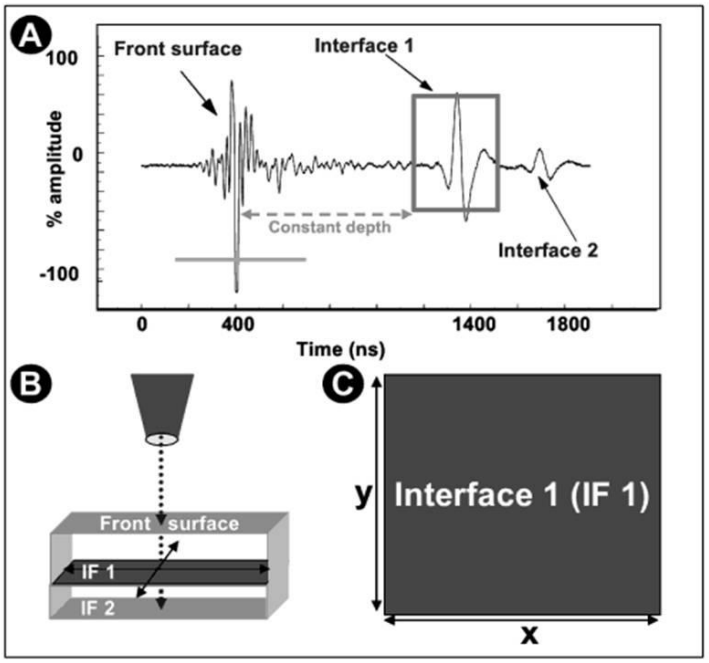


Figure 2.19: By gating a specific A-scan echo in the time domain (A) and scanning the transducer over the entire X-Y sample area of interest (B), a C-scan image is obtained (C) [118].

The generation and propagation of acoustic waves are strongly affected by various material parameters, such as elastic, thermal, electronic and magnetic properties [119]. The penetration and reflection of the acoustic waves are highly material dependent as each material has a different acoustic impedance. The penetration depth of SAM, using water as a coupling agent, into a solid is mainly determined by the penetration of the Rayleigh wave into the sam-

ple and the impedance of the sample [120]. For instance, with a frequency of 0.8GHz, the maximum penetration depths are in the range of 2-6μm for most oxides and metals. This range is reduced to 0.9-2μm at 2GHz. Every electronic package problem requires a matched optimum frequency, determined by the depth of the suspected defect or plane of interest and the acoustic properties of the overlaying materials, and the frequency used is also proportional to lateral resolution. Transducer properties play a key role in determining the "effective" resolution that can be achieved. Typically, best resolutions can be achieved at higher frequencies, larger lens diameters, and shorter focal lengths [118].

The initial application of SAM in the semiconductor industry was the high frequency inspection of device layers near the surface of the die. At these high frequencies (1GHz and above) the depth of penetration was severely limited by frequency-dependent absorption. Some SAMs were modified to take advantage of broad-band transducer in the intermediate frequency range of 30-100MHz for sub-surface studies such as die attach inspections [118]. Prior to acoustic inspection, die attach inspection was performed primarily with x-ray radiography. Experience soon showed that reflected sound indicates the true percentage of the total area of a die attach interface that is bonded whereas X-ray reveals only large voids in the die attach material.

SAM is sensitive to the presence of various inhomogeneities in a sample and to material discontinuities, because mismatch of acoustic impedances at the boundaries brings about intense reflections [121, 122]. For example, a small void in a plastic substrate will create an echo reflection due to the acoustic impedance of the plastic material that differs from that of the gas in the void [123]. By inspecting the reflected echoes, the ultrasonic pulse-echo method aims to characterise the propagation path and/or to determine the physical properties of the defects in terms of their location, size, orientation and microstructure [114]. Beside the ability to detect delaminations,

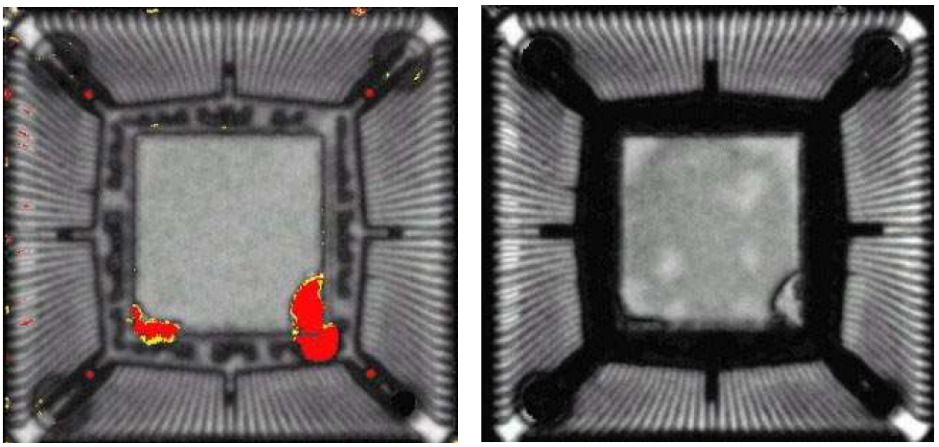
SAM can also provide quantitative information on the depth of this kind of defect [124]. Simple routines can be used to determine fractions of bonding/unbonding in die attach material in accordance with standard MIL-STD-883, Method 2030 [94].

Yalamanchili *et al.* [115] used SAM at 30 MHz to study electronic packages subjected to temperature excursions from room temperature up to 85^{o}C, and humidity cycling (50 to 85%), for one hour and for over 100 cycles. The primary defects were delamination at the plastic/die and leadframe/plastic interface. Corrosion in the area of delamination was also tracked and destructive analysis of the packages was then undertaken. SAM was able to detect voids as the predominant defect but it was not able to identify micro-cracks in this study. SAM detected the bond between the die and the substrate without the need to transmit ultrasound entirely through the substrate, allowing the analysis of the package from the top and the bottom sides. Therefore, any air-gap located on one side of the substrate could be analysed from the other side as air blocks the efficient transmission of ultrasound [115].

Hoppe and Hahn [120] listed the following defects in electronic packages, which they were able to detect acoustically: (i) resist/metal overhang; (ii) sub-surface blisters and inclusions; (iii) micro-cracks; (iv) delaminations; (v) "hillocks" shorting two-layer metallisations; (vi) defects in the Si die; and (vii) thickness variations.

Plastic encapsulated microelectronic devices are the most widely investigated by SAM. In [116], some examples of defects in a plastic leaded chip carrier (PLCC) using SAM are shown. For instance, Figure 2.20(a) illustrates a 15MHz pulse-echo (reflected) image from the top side of a PLCC package. The image contains information regarding the bond quality of the die top, die pad and top-side leadframe. Red areas represent debonding between the encapsulant and the die, and similar defects were also present on the lead

frame and die pad to encapsulant interfaces. A pulse-echo mode C-scan image of the die attach of the same PLCC package is shown in Figure 2.20(b). The same transducer was used but the timing gate that selects the particular reflections to be studied was selected to investigate regions deeper within the package, at the die attach interface. Debonding between the die and die attach, voiding within the attach or debonding between the die and die pad appeared as white indicating voiding within the epoxy die attach material.

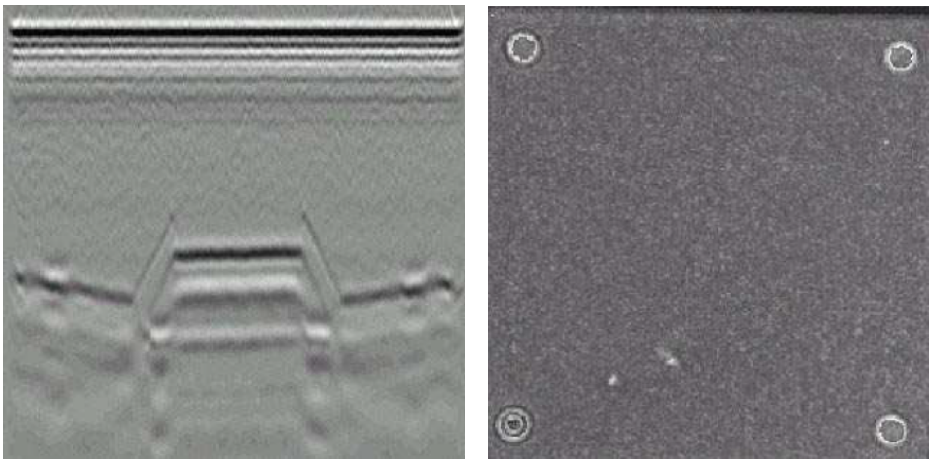


(a) (b)

Figure 2.20: SAM images of a PLCC: (a) reflected mode image from the top side; (b) reflected mode C-scan image from the die attach interface [116].

In Figure 2.21(a), a 15MHz pulse-echo B-scan image, shows a non-destructive cross-section of the X-Z plane of a PLCC package. The die was tilted within the package relative to the front surface of the package. Die tilt is caused either by misplacement/alignment or forces exerted upon it from thermal expansion. Several locations of air voids trapped within the encapsulant material are shown as white circular areas in Figure 2.21(b).

SAM has always been an important tool for crack detection. Studies were published which correlated electrical testing and destructive physical analysis with the result of acoustic inspection in order to understand the moisture sensitivity of surface mount packages during board mounting [125]. Large area die bonding and their corresponding mechanical and thermal properties were also studied for Au-Sn eutectic, Ag paste and solder



(a) (b)

Figure 2.21: SAM images of a PLCC: (a) pulse-echo mode B-scan image of a cross-section of a PLCC package X-Z plane; (b) pulse-echo mode C-scan image of the molding compound of a PLCC [116].

paste [126]. Samples were tested for ultrasound image, shear force and thermal resistance measurement.

Compared with other microscopy techniques SAM provides a unique combination of three features that make up its value for a wide range of applications: (i) sub-surface capability since ultrasound penetrates optically opaque materials even at visible light wavelengths; (ii) images can contain information about stiffness, viscosity, adhesion, density, and topography of the sample; and (iii) due to pulsed operation and high frequency, SAM is non-destructive for most samples. Despite its power, SAM studies are often insufficient on their own [127], and further types of investigations are often used to confirm failures, including visual inspection (optical microscopy), X-ray inspection, and scanning electron microscopy/energy-dispersive X-ray spectroscopy.

2.2.3 Summary

The ability of a system to survive and to perform a required function without failure/breakdown for a certain period of time under stated operation condi-

tions is critical. Accelerated testing is used to provoke failure quickly as it is unfeasible to perform reliability tests under service conditions due to the time and costs involved. During this process, the packages are tested regarding their electrical resistance/continuity. SAM is the most widely used analytical technique to study macro-scale electronic package failure behaviour since it is non-destructive, flexible and provides intuitive images of planes of specific interest.

2.3 Nanoindentation

Many efforts have been made in developing nanoindentation equipment and nanoindentation techniques for probing the mechanical properties of materials and thin films on the sub-micron and nano-scale. This technique allows the measurement of mechanical properties such as the modulus, hardness and creep behavior of different phases at the interface with micron spatial resolution [128–130]. It is then possible to introduce all this data into simulations to distinguish the mechanical behavior of discrete phases in an assembly representing the geometry of real interfaces [131].

Nanoindentation test involves indenting a specimen by a very small load using a high precision instrument, which records the load and displacement continuously. As load is applied to the indenter, the depth of penetration into the specimen is measured. A nanoindentation test instrument provides experimental results in the form of a load-displacement curve for the loading and the unloading parts of the indentation process. Both load and displacement are recorded as illustrated in Figure 2.22. P_{max} is the peak indentation load, h_{max} is the indenter displacement at the peak load P_{max}, h_f is the final depth of the contact impression after unloading, and S is the initial unloading stiffness [132–134].

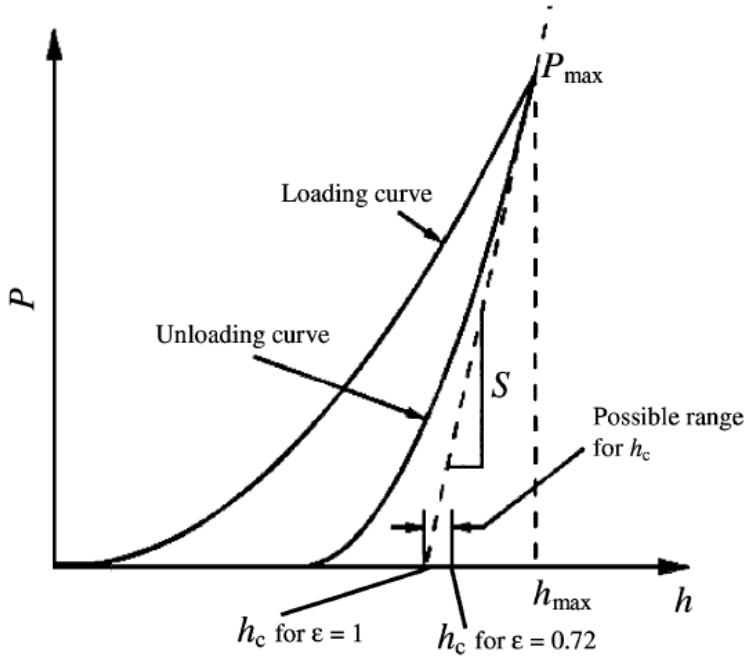


Figure 2.22: Scheme of load versus indenter displacement data for an indentation experiment [132].

Fused silica is often used for nanoindenters calibration since this material is hard and isotropic, and any indentation size effect is minimised [132]. This material has a large elastic recovery during unloading.

Spherical and conical indenters present two very distinct geometries, one being very sharp and one very blunt. If adjustments are made to geometrical parameters (tip angle of cone and effective radius of the sphere), loading and unloading of these surfaces is the same as that for a flat surface. It seems then logical that this behavior may hold for other axis-symmetric indenters. Figure 2.23 illustrates a cross section of an indentation with the parameters used in the analysis. h_c is the vertical distance along which contact is made and h_s is the displacement of the surface at the perimeter of the contact. At the peak load, the load and displacement are P_{max} and h_{max}, and a being the radius of the contact circle. h_f is the final depth of the residual hardness impression upon unloading.

The area of contact at peak load is determined by the geometry of the indenter and the contact depth, h_c. Following h_c, the projected contact area

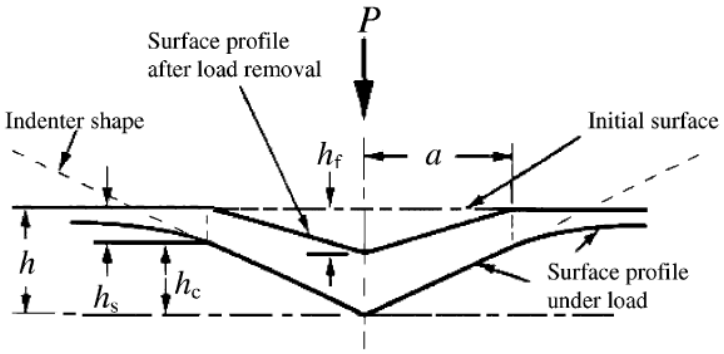


Figure 2.23: Schematic representation of a section through an indentation showing the various parameters used in the analysis [132].

of an indenter for a perfect Berkovich indentor is $A_c = 24.56h_c^2$. Nevertheless, an experimental area function for the indenter is often obtained from the calibration on fused silica due to the absence of an ideal indenter geometry. The contact A_c is usually fitted to the contact depth h_c, according to

$$A_c = C_1h_c^2 + C_2h_c + C_3h_c^{1/2} + C_4h_c^{1/4}, \tag{2.3}$$

where C_1, C_2, C_3 and C_4 are the empirical fitting constants.

2.3.1 Hardness and elastic modulus

Hardness (H) and elastic modulus (E) are two mechanical properties measured more often using load and depth indentation techniques [132]. Doerner and Nix [135] produced the most comprehensive method for determining both mechanical properties. With the contact area as a function of depth so determined, the hardness can be computed from Equation 2.4 [130, 133, 134]:

$$H = \frac{P_{max}}{A_c}. \tag{2.4}$$

Furthermore, the elastic modulus can be obtained through the contact stiffness (S). The authors suggested that the unloading stiffness could be computed from a linear fit of the upper one-third of the unloading part of

indentation curve, according to:

$$S = \frac{dP}{dh} = \frac{2}{\sqrt{\pi}E - r\sqrt{A}}, \tag{2.5}$$

where E_r is the reduced elastic modulus which is a result of the elastic modulus of the bodies in contact. The elastic modulus can be calculated by [130, 133, 134]:

$$E_r = \frac{\sqrt{\pi}S}{2\beta\sqrt{A_c}}. \tag{2.6}$$

The Oliver-Pharr method is often used in order to determine E_r and E_i by calculating the contact stiffness. It was suggested that the unloading part of the indentation curve can be fitted to a power-law relation [132]:

$$(h - h_f) = 2\frac{P}{S}. \tag{2.7}$$

The contact area of interest is that at peak load, therefore:

$$h_s = \epsilon\frac{P_{max}}{S}, \tag{2.8}$$

where ϵ is a constant that depends on the indenter geometry. ϵ is 1 for a flat indenter, 0.72 for a conical indenter and 0.75 for a three-sided pyramid indenter (Berkovich).

This methodology works well for hard materials as the indented material movement occurs in the indentation plane. In soft materials, pile-up effects are susceptible to occur misleading to the contact area value, and thus hardness and elastic modulus. The pile-up effect is the most problematic area in nanoindentation testing.

2.3.2 Summary

Nanoindentation is a new method to characterise material mechanical properties on a very small scale. Force displacement curves obtained during the indentation process indicate hardness and elastic modulus properties. The most extensively used method to determine the elastic modulus and hardness by nanoindentation was proposed by Oliver and Pharr, in which the slope of the unloading curve, which is usually nonlinear, is used to calculate the modulus and to provide a physically justifiable procedure for determining the depth which should be used in conjunction with the indenter shape function to establish the contact area at peak load. These tests are based on new technologies that allow precise measurement and control of the indenting forces and precise measurement of the indentation depths.

2.4 Overall summary

The operation of electronic packages under exceptionally harsh environments presents a significant challenge for the microelectronics industry, for example, in down-hole, well-logging and turbo-machinery applications. The traditional temperature limit of 125 ^{o}C for high temperature exposure of electronics system is now required to be extended to above 200 ^{o}C, together with resistance to high pressures, vibrations and potentially corrosive environments. The technical challenges range from IC design, use of passives, and the development of robust packaging structures to the use of the latest thermal management techniques.

The die attach materials in most use for HTE applications are high Pb content materials. European RoHS directives enacted in response to concerns regarding Pb toxicity currently exempt safely critical HTE. Nevertheless, there is a strong drive to find alternatives such as ECAs and Au-Si. ECAs

have gained recent interest due to their potential for low cost, easy processing and mechanical flexibility. However, poor resistance under some conditions, especially high humidity, and unstable long-term reliability concerns remain. Several approaches including incorporation of additives, process modification, improving formulation, changes of size and orientation, etc have been used to improve the properties of ECAs. No commercially ECAs have shown encouragement for operation at 200^{o}C or higher where metallic solders such as Au-Si are used.

When low melting point eutectic alloys are used for die attach, it is difficult to eliminate the formation of IMCs at interfaces with the various metallisations used. Adhesion layers, bonding layers and solders that are necessary to form effective interfaces in packaging applications also form numerous IMC when interacting with each other during bonding. Nevertheless, it is possible to slow IMC formation through alloying. Doping of plated Ni with Co to slow the formation of $NiSi_2$ is a good example. Sn-based solders suffer from oxidation problems and Au-Si and Au-Sn are the most promising non-Pb solders for die attach.

It is unfeasible to perform reliability tests under service conditions due to time and cost involved. Thus, accelerated testing is used to cause failure in a much shorter time than field conditions. Characterisation of the failure mechanisms and prediction of electronic packages under harsh environments is important to understanding long term reliability.

The reliability of electronic packages depends in many aspects on their mechanical integrity. Structural weaknesses caused by poor bonding, voids, cracks or delaminations which may not be evident in electrical performance may cause premature failure. SAM provides a rapid and comprehensive imaging of package defects and their location within the package. Moreover, it presents the big advantage to be a non-destructive inspection method.

Nanoindentation is a relatively new technique designed to probe material behaviour on a very small scale. The force acting on the tip is measured as a function of the indentation depth, and this relationship allows mechanical properties, especially hardness and Young's modulus, to be determined. The fine spatial accuracy available allows specific regions of solder joints to be probed, including specific phases and features.

CHAPTER 3
Experimental procedure

This chapter describes experimental methodologies and techniques used in this thesis. Firstly, details of the materials and manufacturing process used to assemble the in-house/GE AS die bonds are described in detail. Next, the techniques used to study the microstructure of both as-manufactured and thermally exposed die bonds is presented. This section is followed by the SAM procedures used in the characterisation of bonded area and complementary die shear testing. The mechanical properties of representative samples were extracted at room temperature through nano-indentation. Lastly, the reliability section gives details of the ALTs performed on die bonds in terms of electrical performance.

3.1 Materials and manufacturing

3.1.1 Adhesive die attach

At the out-set of the project, the industrial collaborator GE AS went through a selection process for various adhesives. The assessment of data sheet information was designed to assess the comparative suitability of die attach adhesives for up to 2016h operation at 250^{o}C, and was considered for comparative purposes only. The assessment of data sheet information was followed by screening tests based on accelerated testing. The commercial adhesives selected were:

i) two unfilled thermoplastic films known as Staystik 415 and 482;

ii) an Ag-filled epoxy termed GEM D4;

iii) an Ag-filled cyanate-ester known as Ablebond JM7000.

All the adhesives were model systems specifically formulated for this project, and their properties are presented in Table 3.1. The various adhesive die attaches were evaluated in detail in this thesis; although, the main focus was given to the JM7000 adhesive die attach which is described in more detail later in Chapter 4. A Perkin Elmer Pyris thermogravimetric analyser (TGA) was used to determine the weight loss of the JM7000 adhesive. TGA analysis was performed at a constant heating rate of 10^{o}C/min.

Table 3.1: Properties of the various adhesives tested for adhesive die bonding.

	JM7000	**GEM D4**	**Staystik 415**	**Staystik 482**
Supplier	Ablestik	GWENT	Cookson	Cookson
Filler	Ag	Ag	unfilled	unfilled
Attach temperature range (^{o}C)	150-300	150	300-375	160-275
Max excursion temperature (^{o}C)	340	—	<400	<300
Elastic modulus (MPa)	70	–	2480	2410
T_g (^{o}C)	240	–	180-185	98
CTE (ppm/^{o}C)	33	–	–	–

The arrangement investigated was a HTCC metallisation (12 $\times$ 12 $\times$ 1mm) with thick film Au above underlayers of Ni and porous W. These underlayers act as a barrier to diffusion through the equilibrium immiscibility of the Ni-Au system and the porosity of the W, which also counteracts any thermal expansion coefficient mismatch. The Ni layer also allows for the production of a relatively smooth Au bonding metallisation. Note the use of a W layer beneath the Ni metallisation on the upper part of the ceramic

substrate. Because this was a HTCC substrate based on Al_2O_3 and fired at 1600^{o}C, the diffusion barrier metallisation must have a melting point greater than 1600^{o}C, such as W which has a melting point (T_m) of 3370^{o}C.

The die assembly process using adhesives is very straight forward as shown in Figure 3.1. The substrate was secured to an unheated workstage. A small amount of the adhesive material was metered out onto the HTCC substrate. Using a small circular motion, the adhesive is "worked" to form the star pattern (Figure 3.1(a)), usually in a pattern conforming to the shape and size of the die (Figure 3.1(b)). This specific pattern is designed to minimise the entrapment of air when the die is placed onto the adhesive. The Si die was then placed on the adhesive (Figure 3.1(c)). A small load, with circular motion, was applied to the surface of the Si die moving the component over the adhesive surface (Figure 3.1(d)). This allowed the removal of any air pockets and spread the adhesive over the die surface creating the necessary fillets. The system was cured afterwards according to the respective technical data sheet.

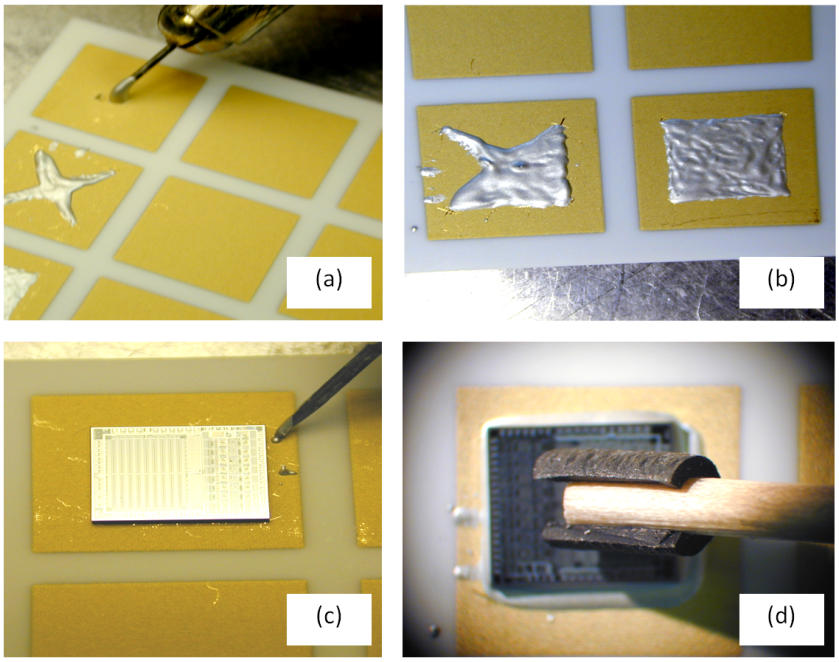


Figure 3.1: Assembly process steps for adhesive die bonding.

The die assemblies using the various adhesives were subsequently thermally exposed at GE AS.

3.1.2 Au-Si eutectic die attach

Ceramic substrates of 96% pure Al_2O_3 tiles 10mm $\times$ 10mm were used, which had been metallised with thick film Au (10μm) by screen printing and then fired for 1h at a peak temperature of 850^oC. The Si dies had dimensions of 4.62mm $\times$ 4.64mm. The Au-2wt%Si preforms were 5mm square and 25μm thick. Both components were cleaned in HF (7%), for 10 seconds, in order to remove any oxide layer. Preforms were stored in dry N_2 atmosphere to prolong their life by keeping them free from contaminants and oxidation. Note that contaminated preforms can only be spotted during the die bonding process. A poor quality preform will show sign of a blackish, dull tint and wrinkled, whereas a good quality preform will appear shiny and smooth, and will flow smoothly over the carrier surface. The preform was then placed in between the upper Au metallisation of the Al_2O_3 substrate and the base of the Si die.

The system was heated to above the eutectic temperature. After the preform and die were placed on the substrate, the bonder initiated a light scrubbing action with the bond head. This scrubbing action allows the rupture of the oxide films. A cover gas was employed which contained a passive component N_2 (90%) to prevent metal oxides from forming, and an active component H_2 (10%) to break away existing metal oxides.

A repeatable/controlled bond was ensured by the semi-automatic die bonder used - Cammax EDB65 (Figure 3.2). The die pickup head load is adjustable, providing very low loadings for small, fragile dice and the pick-up temperature may be accurately controlled up to 150^oC. The precision auto traverse table allows the viewing of both pick-up and placement during the bonding. A coarse movement of 51mm $\times$ 51mm is available until vacuum-

locked into position, whilst an 8:1 joystick manipulator provides fine control to achieve placement accuracy. The scrub system is driven about the pivoted arm in the X-axis by a pneumatic scrub cylinder. The complete arm is mounted on a precision Z-axis slide, lowered by a cam controlled Z-lever. Adjustments are provided by scrub time, frequency and amplitude which can then remain fixed throughout the process to ensure consistent yield. A digital temperature controller was used to control the working stage temperatures of up to 500^{o}C. A flow control provided heated cover gas to the working stage.

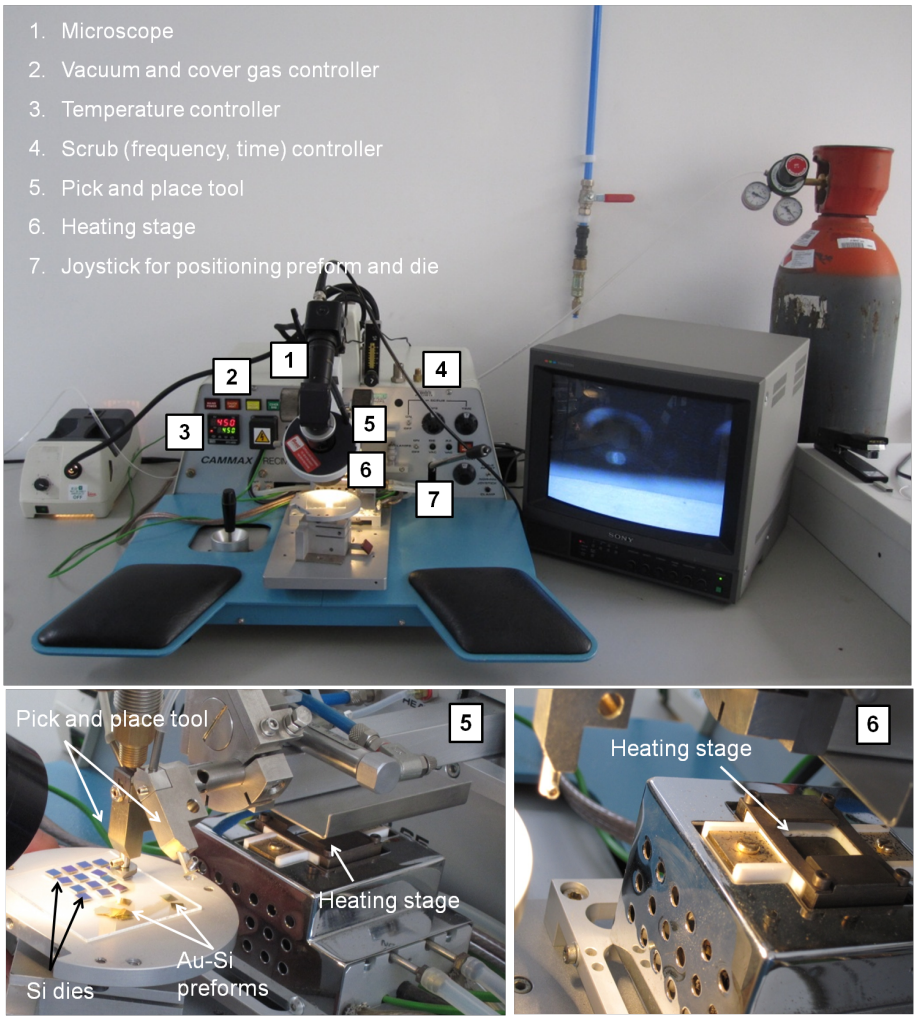


Figure 3.2: Cammax EDB65 eutectic die bonder.

Prior to die bonding, a Perkin Elmer Hyper differential scanning calorimeter (DSC) was used to determine the melting point of the Au-Si preform. A Au-Si preform in the form of a foil was heated and cooled at controlled rates in the DSC. Individual preforms were placed in an Al sample pan and heated

to 400^{o}C, at a 10^{o}C/min, in a N_2 atmosphere.

X-ray photoelectron spectroscopy (XPS) was used to confirm the elements present at the surface of the various components: Si dies, Au-Si preforms and ceramic substrates. The analysis was also conducted after Ar ion bombardment. XPS was performed in an ion pumped VG Microtech CLAM 4 MCD analyser system with 200Watts unmonochromated Mg X-ray excitation was used.

The surface roughness of the substrates was measured using a Dektak 6M profiler in which a sharp diamond tip travels over the surface measuring irregularities. The arithmetic average (Ra) is the most commonly used parameter as a measure of surface roughness.

Optimisation of the die bonder parameters

Au-Si die bonding is a technique in which quality control is problematic because of the critical scrubbing action that ruptures oxide films, which is difficult to regulate/automate leading to a wide variability in bond quality. This variability may become ambiguous when attempting to improve lifetimes and reliability.

In order to narrow down this variability, a major study for identifying the key parameters controlling the bond quality was carried out. This was followed by optimisation of the parameters to minimise the percentage of unbonded area of the Au-Si die bonds. An optimisation usually requires a large number of experiments because of the large number of processing parameters. In this study, an experimental design followed by statistical analysis of the experimental results were employed, to confirm the effectiveness of this approach. This reduced the number of experiments required to produce the optimised Au-Si die bonds. The optimised parameters were then used to manufacture 150 specimens of Au-Si assemblies for thermal exposure.

Although every application has its own specific set of requirements, with some machine parameters more critical than others, they all need to be in proper proportion to obtain the desired results. The choice of the parameters to be varied and those to be constant relies on the design of experiment methodology. Parameters that could influence the Au-Si eutectic die bond quality to some extent, were identified according to their level of importance, and are presented in Table 3.2.

Table 3.2: Die bonder parameters.

Parameter	**Function**	**Importance**	**Comments**
Heating stage temperature	Provides heat from substrate/package to reflow solder	High	No heat no flow
Bond head temperature	Provides heat from die to reflow solder	High	As long as above the eutectic temperature
Force of the scrubbing head	Provides force to hold the device in contact with substrate during reflow	High	Logically seems important
Scrubbing time	Time for scrubbing head during reflow	High	Determines how many scrubs
Scrubbing frequency	Number of scrub actions in a certain time	High	Determines how many scrubs
Scrubbing amplitude	Amplitude of the scrubbing motion	Medium	Needs to be above a certain amplitude
Gas cover mixture	Normally N_2-10% H_2, prevents oxidation during reflow	Medium	N_2 (10% H_2)
Gas flow rate	Amount of gas coverage during reflow	Medium	Affects the rate at which the solder reflows. Set using test piece
Vacuum	Applied to substrate and die to hold in place	Low	Kept constant
Pick up tool design	Designed specifically for die to be bonded	Low	Set up correctly (cannot be varied)

The final selection of parameters to be investigated was a natural result from evaluating the manufacturing process of the Au-Si eutectic. It was also defined by other issues such as the resources required to complete this

thesis work in a reasonable amount of time and expenditure. In addition, the accumulated experience of the sub-contractor for the Au-Si eutectic manufacturing, which totalled around 30 years in the electronics manufacturing process, was valuable in quickly eliminating many non-viable alternatives. Critical control parameters to be investigated were limited to the following:

i) Temperature of the heating stage: the substrate is heated to a background temperature which is boosted during bonding until reflowing occurs. It determines the amount of incremental thermal energy needed to initiate the solder to reflow. It also indirectly controls the bonding time.

ii) Force of the scrubbing head: the amount of force applied must be sufficient to break the oxide layer. Furthermore, it has to hold the die in place. Excessive force can damage the component by introducing microcracks that may affect, for instance, the electrical performance. Small stress sensitive die ranging up to 20mils can take a fair amount of head force, typically around 50g. A larger die generally requires head force of ≥ 100g.

iii) Scrubbing frequency: load force is translated into frictional heat by cyclically moving the die, while exerting head force. As the number of scrubbing cycles and displacement were programmable, this option offered great flexibility.

iv) Scrubbing time: time span of head force and incremental thermal energy determines the extent of the solder reflow. Bonding time varies from a few seconds to a dozen seconds, depending on the size of the die.

A complete matrix of all combinations of low and high values of each parameter was very time consuming. Based on the 4 selected parameters, it was decided then to allocate two levels for each parameter that could be manipulated to produce the desired parameter effect. Choosing a high and a

low value for each parameter would also increase the result variability. The two levels considered for each parameter were: i) temperature of the heating stage: 400 and 450^{o}C; force of the scrubbing head: 0.5 and 3.5g/mm^2; scrubbing frequency: 3 and 7 Hz; and scrubbing time: 1.5 and 3.5s. All possible combinations, in a full factorial of 2^4, were undertaken as presented in Table 3.3. Therefore, an improvement of the statistical confidence of the experiment was accomplished. Three replications for each combination were performed resulting in 48 data points.

This experimental design provided an initial set of optimised parameters and exposed the most influential ones on bond quality. Further optimisation was carried out afterwards. The quality of the Au-Si die bonds was investigated by SAM and die shear testing to failure (see later in this Chapter).

3.2 Microstructural characterisation

Die bonds were cross-sectioned and mounted in slow-cure epoxy resin using a vacuum impregnated process. Samples were then prepared for metallographic examination using standard metallographic procedures. For the adhesive die bonds, these involved grinding on 240 to 2500μm grit SiC abrasive paper (water cooled), followed by a two-stage polishing procedure (3μm paste and then colloidal silica). The Au-Si die bonds were ground on 1200μm SiC paper, using water cooling, until flat; standard polishing was carried out using 9, 3 and 1μm paste as final polishing.

Microstructural analysis was carried out using optical microscopy (Polyvar Met) and SEM (JEOL-840A) operating at an accelerating voltage of 15kV and beam current of 3×10^{-9}A, equipped with electron dispersive X-ray spectroscopy (EDX). SEM was used extensively to study the microstructure of

Table 3.3: Experimental design for Au-Si eutectic die bonding (sixteen experiments, two-level). Studied parameters: T - temperature of the heating stage; F - force of the scrubbing head; S_f - scrubbing frequency; S_t - scrubbing time.

Experiment no.	**T (°C)**	**F (g/mm^2)**	**S_f (Hz)**	**S_t (s)**
1	400	0.5	3	1.5
2	400	0.5	3	3.5
3	400	0.5	7	1.5
4	400	0.5	7	3.5
5	400	3.5	3	1.5
6	400	3.5	3	3.5
7	400	3.5	7	1.5
8	400	3.5	7	3.5
9	450	0.5	3	1.5
10	450	0.5	3	3.5
11	450	0.5	7	1.5
12	450	0.5	7	3.5
13	450	3.5	3	1.5
14	450	3.5	3	3.5
15	450	3.5	7	1.5
16	450	3.5	7	3.5

selected die bonds as-manufactured, and after thermal exposure. EDX was used occasionally to study the composition at the interfaces.

Electron microprobe analysis (EPMA) was performed in a JEOL microprobe operating, with 4 WDS detectors at an accelerating voltage of 15kV, beam current of 3×10^{-8}A. A typical mapping x-y step size of 500nm to map the distribution of several elements present in the as-supplied ceramic substrate. Selected Au-Si die bonds were also studied using EPMA analysis as regards to interdiffusion in as-manufactured condition, and after isothermal ageing. Quantitative EPMA diffusion profiles were obtained along a line perpendicular to the Si die/Au-Si solder/substrate region.

3.3 Thermal Exposure

3.3.1 Isothermal ageing

Isothermal ageing was undertaken to mimic the grain growth, interdiffusion, recrystallization and other changes in the adhesive and Au-Si during high temperature exposure after manufacture. Selected adhesive die bonds underwent thermal ageing at 250^{o}C for 168, 672, 1048 and 2016h. Sub-batches of optimised Au-Si die bonds were aged at 300^{o}C for 168, 672 and 2016 hours. Accelerated ageing was also undertaken in another sub-batch of solder bonds at 350^{o}C for 500 and 850h. Heating and cooling was always performed by direct insertion or removal from the oven with no additional thermal profile.

3.3.2 Thermal cycling and thermal shock

In an attempt to understand the effect of thermal cycling, thermal shock and microstructural change on die bond failure, highly accelerated testing was performed in collaboration with GE AS who provided access to their facilities.

The thermal cycling and thermal shock profiles were selected according to GE AS, and were typical of those used industrially based on MIL. STD. 883 [94]. The adhesive die bonds were examined in the following conditions:

i) Submitted to thermal shock (250^{o}C to - 65^{o}C, in 10 seconds);

ii) Submitted to thermal cycling (200^{o}C to -55^{o}C, 10 cycles).

Selected Au-Si die bonds were submitted to -40^{o}C to 250^{o}C, and Figure 3.3 illustrates the test regime used for both thermal cycling and thermal shock testing. The transfer time was <30 min and <5min for thermal cycling and thermal shock, respectively.

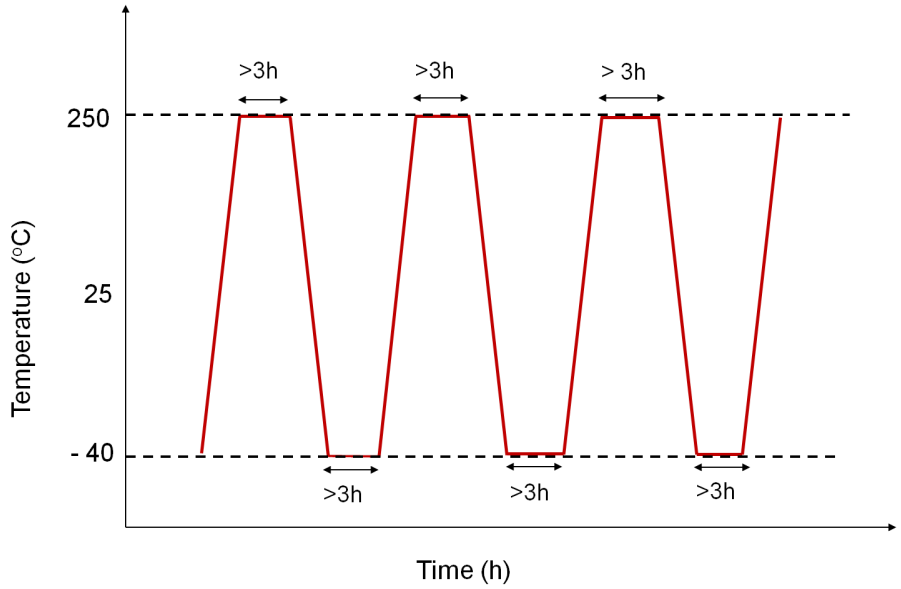


Figure 3.3: Test regime used for thermal cycling and thermal shock.

3.4 Nano-indentation

One of the main objectives of the nano-indentation testing was to evaluate the mechanical properties of the Au-Si eutectic die bonds evolution before and after high temperature storage. The elastic modulus was measured following the Oliver and Pharr method [132] as previously described in Chapter 2. The elastic modulus and hardness of the eutectic Au-Si solder region were measured in the as-manufactured condition, and after ageing at 300^{o}C for 2016h. The nano-indentation experiments were performed, at room temperature, using a Micromaterials Nanotest 600 machine equipped with a Berkovich indenter. A series of indentations were performed along the Au-Si solder region. The indentation tests were carried out at a maximum load of 20mN.

3.5 Assessing bond quality

3.5.1 Scanning acoustic microscopy

Scanning acoustic microscopy was extensively used to evaluate the quality of adhesive/solder die bonds. Specimens were inspected using the C-mode scan (C-SAM) at operating frequencies of 50/80 and 230/300MHz for adhesives and Au-Si die bonds, respectively. The field of view used for inspection of the adhesive die bonds was 0.564 x 0.564 with 512x512 pixel size. The Au-Si die bonds used a field view of 0.887x0.887 and 2048x2048 pixel size.

Low frequencies result in greater penetration whereas high frequencies result in higher resolution. The accuracy of measurements will be related to the resolution possible during scanning. As a result of the way the images is created from a raster scan, there are two inter-related factors - acoustic resolution and mechanical scanning resolution. The spot diameter varies according to several factors including material, depth, transducer type and focal length. This is the primary factor in determining the resolution of the scan. The other factor is the scanning resolution which can be set on the microscope to match the resolution to be achieved for each scan, and can be set to a finer resolution than the spot-size so that the errors due to scanning lines is negligible.

To generate the images, the ultrasound was directed through the top side of the die bond, i.e. through the Si die/die attach material/substrate. The acoustic micrographs were generated for each specimen using the Interface Scan technique. The ultrasound travels through the surface of the specimen, and continues until it encounters another material interface. The ultrasound is focused at this material interface, and some or all of the ultrasonic signal is reflected back to the transducer. The transducer collects these reflections and displays them in the images.

At a certain interface, unbonded areas (delaminations, voids) reflect all of the ultrasound and appear white in the image, while bonded areas reflect less ultrasound and appear grey. Areas with loss of ultrasound signal (where no ultrasound signal is returned back to the transducer) will appear black.

Data interpretation and image overview

Figure 3.4 displays a representative waveform analysis of some of the inspected Au-Si die bonds that will be shown in more detail in Chapter 5. The waveform analysis allows checking the waveforms to confirm that certain regions are in fact unbonded areas, rather than surface imperfections or other less serious anomalies. In this case, a waveform analysis was performed to confirm the presence of unbonded areas within the die attach material. The numbers on the image indicate the locations where the corresponding scans were taken for such confirmation.

The two black arrows on each scan (Figure 3.4) defined the "gate" which displays the portion of the scan used to generate the image. The echoes on the far left represent the top surface of the specimen (water/Si die interface); any echo following is reflected from inside the sample. In the colour map used, small echoes within the gate appear dark or gray (indicating bonded areas). Negative echoes with larger amplitude appear white (indicating unbonded areas).

Depth can also be determined using waveform analysis. The depth of a feature or defect is evident by how far the echo from the feature is to the right on the scan. The further to the right an echo is located, the deeper the feature or defect is located within the sample.

The scan at position 1 displays a defect free region indicated by a small echo amplitude in the gate. Position 2 displays a waveform from an unbonded area at the Si die to solder interface. Position 3 shows the waveform from a

somewhat unbonded area at the solder to substrate interface. Some of the C-SAM parameters used to generate this interface scan are also shown in the upper right corner. This information was useful for repeating procedures.

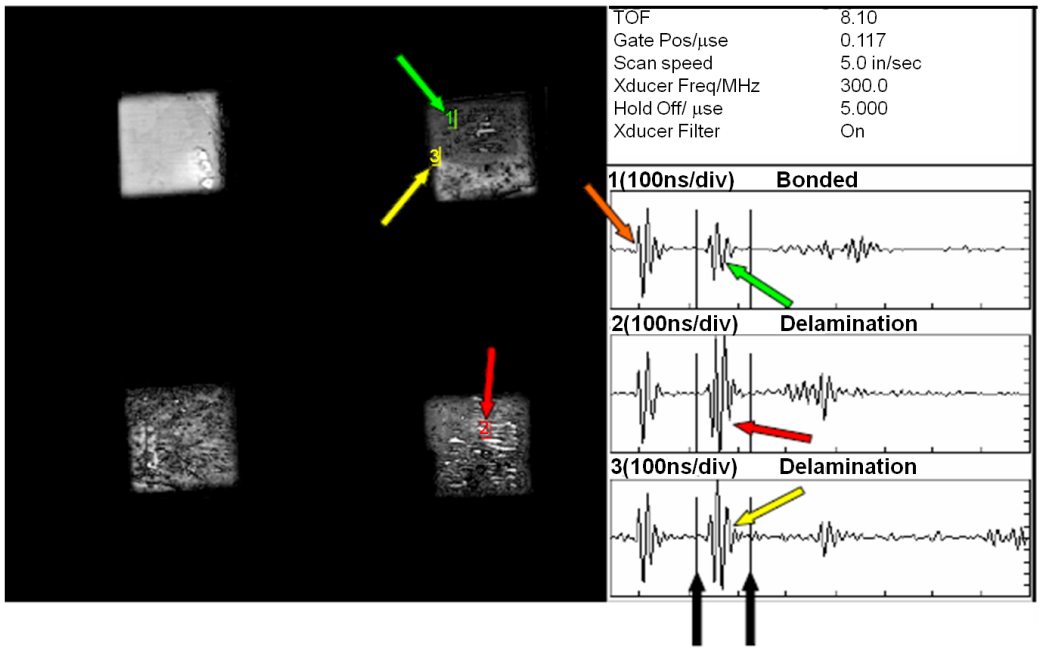


Figure 3.4: Representative waveform scan analysis. Orange arrow indicates an example of the front surface echo (water/Si die interface), red arrows point to examples of unbonded areas at the Si die/solder interface, yellow arrows represent examples of unbonded areas at the solder/substrate interface, green arrows indicate bonded areas, and corresponding waveforms. Black arrows define the gate.

In addition, Digital Image Analysis (DIA) was performed to quantify the percentage of unbonded area within each inspected die bond. This type of analysis uses advanced algorithms to quantify the interface data and establish automatic accept/reject criteria. Figure 3.5 was obtained using DIA on two Au-Si die bond interface scans. The evaluation was set to calculate the percentage of unbonded present at the interfaces, and to categorise unbonded areas by size. In a DIA image, a region of interest (ROI) is specified to be analysed (Figures 3.5(a) and (b)). With the ROI, pixel intensities are reduced two levels, with black (bonded areas) and white (unbonded areas) as shown in Figures 3.5(c) and (d). The data will then display the total percentage of unbonded areas throughout each ROI, and the size of the largest single defect. The results of this quantitative analysis can be found within the images. The

accuracy of the unbonded area measurements is 2%.

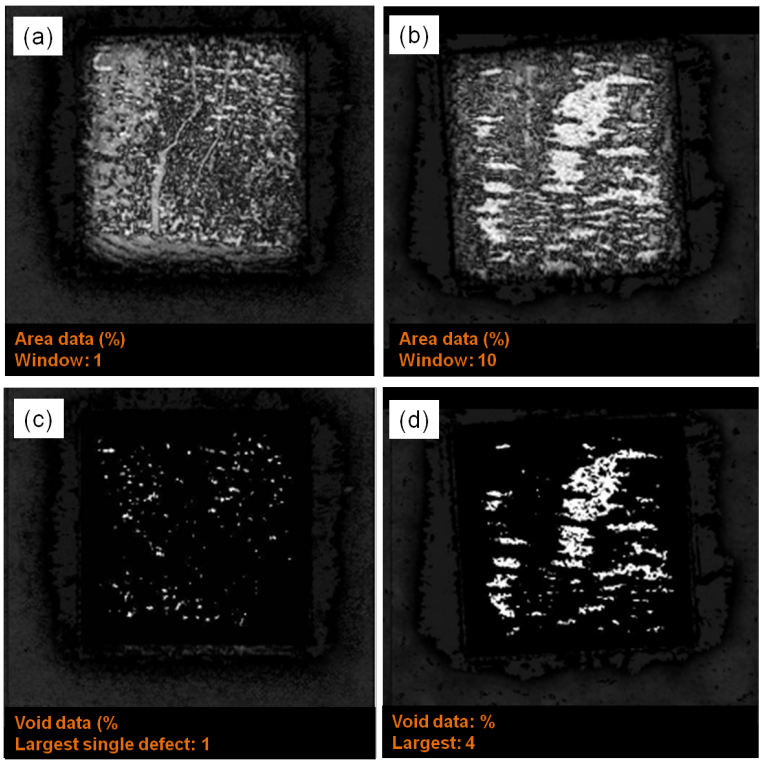


Figure 3.5: Example of SAM images of Au-Si die bonds as inspected ((a), and (b)), and corresponding digital image analysis (DIA) ((c), and (d)).

3.5.2 Die shear testing

Die shear testing is the process of determining the strength of adhesion of the die to the package, by subjecting the die to a stress parallel to the plane of the die attach material, resulting in a shear stress between the die/die attach material and the die attach material/substrate interfaces. Die shear testing is performed by pushing a flat edge attached to a load cell against one edge of a die. Force against the die is increased until the die fails. Figure 3.6 shows a schematic die shear testing.

The use of shear testing to evaluate accelerated life testing is a method that has recently been used for reliability assessment, and lifetime prediction. Die shear testing was performed using a Dage 4000-series bond tester equipped with a DS100kg shear tool. The height of the bottom of the testing

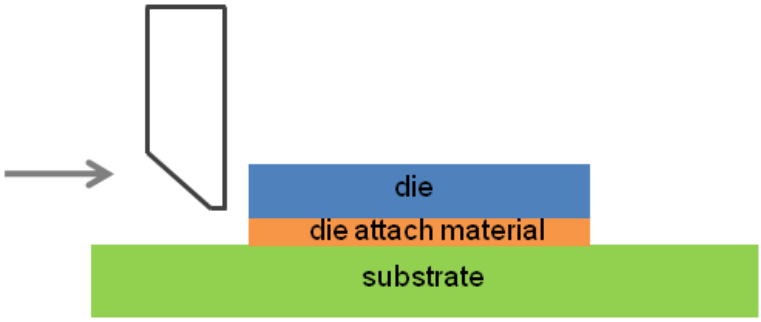


Figure 3.6: Die shear testing schematic.

wedge is adjustable and set at 20μm. The tool speed used was 186μm/s. Calibration was performed according to the machine specifications before the first run of tests.

Figure 3.7 shows the experimental arrangement of a Au-Si die bond within the jig ready for testing (Figure 3.7(a)) and during testing (Figure 3.7(b)). The results were considered in the context of the MIL. STD. 883, Method 2019.7 [136] and the failure modes recorded are discussed in greater detail in the results chapter.

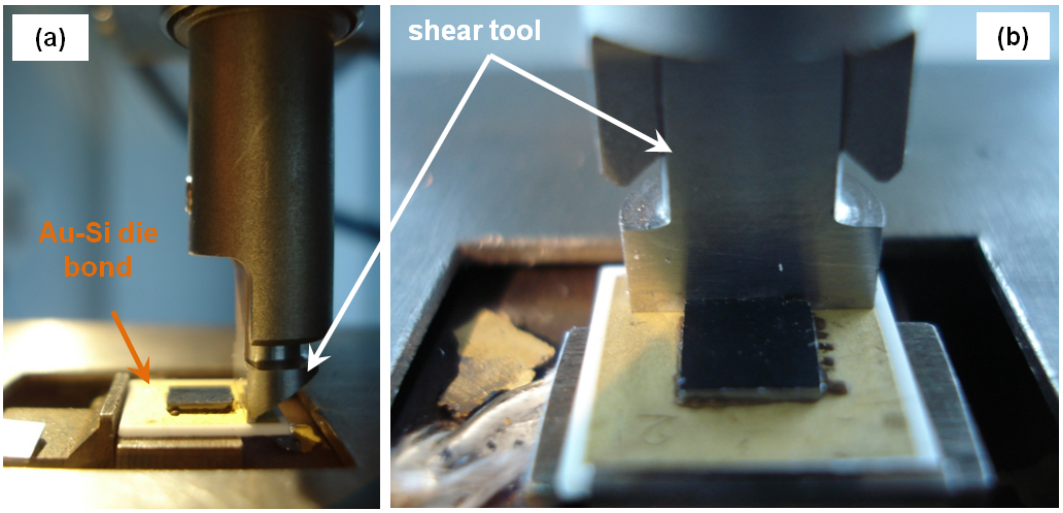


Figure 3.7: Dage 4000-series bond tester: (a) die shear test jig and push-off tool reading for testing; (b) during testing.

3.6 High temperature performance of SOI devices

Within this project, a SOI based integrated circuit based on the X-FAB $1\mu m$ SOI process was designed at GE AS and had dimensions of 4.5mm x 4.0mm. The test chip can be incorporated into a hybrid circuit with other active and passive devices. A schematic of the assembly of demonstrator circuits is presented in Figure 3.8.

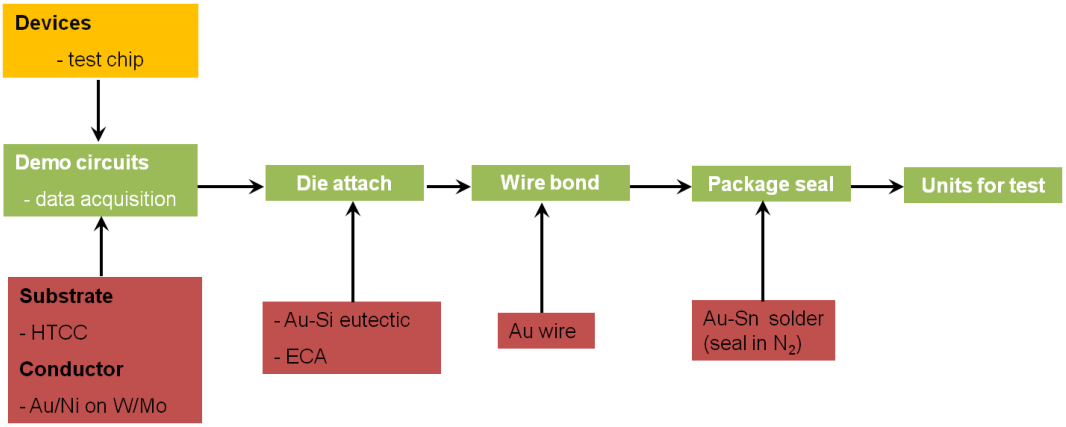
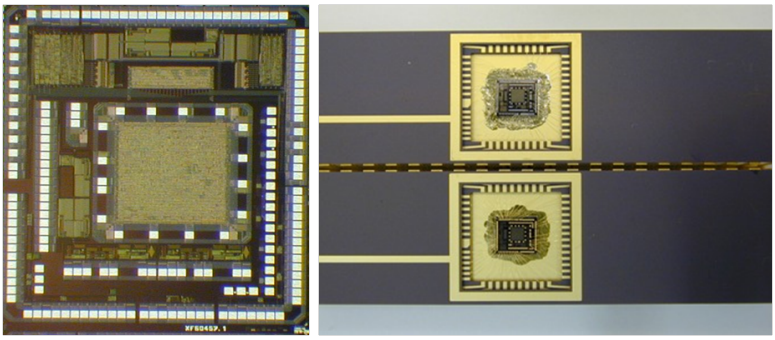


Figure 3.8: Assembly of demonstrator circuits.

Most of the work undertaken in the thesis was conducted on Au metallised Al_2O_3 substrates and HTCC packages which can withstand the 250^{o}C temperature exposure requirements. For the high temperature endurance study, samples using the SOI device (Figure 3.9(a)) were assembled in HTCC packages (Figure 3.9(b)). Different bonding options were tested and these included an adhesive and Au-Si eutectic die attach materials.

The SOI based integrated circuit was manufactured with analogue signal conditioning, ADC/DAC (analogue to digital conversion/digital to analogue conversion) and simple logic control. Table 3.4 summarises the functional blocks contained.

The assembled packages were submitted to temperature storage at 250^{o}C for up to 11088 hours, with measurements performed at 25^{o}C, 125^{o}C



(a) (b)

Figure 3.9: (a) SOI test chip designed at GE AS; (b) SOI device assembled in HTCC package for assessment of electrical performance at 250^{o}C.

Table 3.4: Features contained within UPTEMP - SOI device for high temperature operation.

Function	**Details**
Op-amps/comparators	Standard cells; larger transistors/higher voltage
ADC/DAC	Standard cells - 10 bit
Voltage regulator	Stabilised over temperature
Oscillator	RC Oscillator
Mux/comparators	4:1 Multiplexer
Logic	Voltage divider; data acquisition
Test cells	Op-amps; transistors; digital gates; and flip-flops

and 250^{o}C before high temperature storage (equivalent to 0 hours) and after storage for 3360, 4704 and 7056h. The following device functions were tested: (i) multiplexer; (ii) N-transistor; (iii) bandgap voltage; (iv) oscillator; and (v) voltage regulator.

CHAPTER 4

Adhesive die attach: results and discussion

In this thesis two die attach material systems - adhesives and high temperature solder - have been investigated for their performance in high temperature/harsh environment applications.

This chapter presents and discusses the experimental results to evaluate commercial adhesives (conductive and non-conductive) for their suitability as high temperature die attach materials for HTCC single chip packages. At the outset of the project, the industrial collaborator GE AS went through a selection process for various commercial adhesives. Assessment of data sheet information was followed by simple "yes-no" screening tests based on accelerated testing. The adhesives that were shown to be most promising were then evaluated in detail. As described in the experimental section in Chapter 3, four commercial adhesives were studied: (i) two unfilled thermoplastic films known as Staystik 415 and 482, (ii) an Ag-filled epoxy termed GEM D4, and (iii) an Ag-filled cyanate ester known as Ablebond JM7000 (which was the main focus of this part of the thesis). Full details were given in Chapter 3.

Die bonds comprising HTCC substrates, the different die attach materials and a Si die were assembled using the appropriate adhesive at GE AS, and were subsequently thermally aged for different periods of times at 250^{o}C. The effect of long term exposure of the adhesive bonds was investigated by microstructural analysis using optical microscopy and SEM. Non-destructive and destructive testing was undertaken on selected specimens in order to

understand the effects of thermal cycling, thermal shock and monitor any microstructural change that might help elucidate die attach failure mechanism. The thermal shock and thermal cycling method was typical of that used by high reliability electronics industry, and was based on the military standard MIL. STD. 883, methods 1011.9 and 1010.8 [94], respectively. SAM was performed on selected specimens in order to track interfacial defects within the adhesive die bonds. Die bonds were also mechanically tested according to the military standard die shear method MIL. STD. 883, method 2019.8 [94].

4.1 Staystik 415 and 482

Staystik 415 and 482 are unfilled thermoplastic film adhesives and are fully chemically polymerised as supplied and therefore curing in the conventional sense is not applicable. Their precise formulation was not available from the suppliers for reasons of confidentiality. Staystik 415 is promoted as being well-suited to applications where resistance to high temperature excursion is desired. Staystik 482 is promoted as having excellent bonding characteristics.

Die bonds using Staystik 415 and 482 were cross-sectioned for optical microscopy. Optical micrographs of hundreds of cross-sections in the as-manufactured condition and after thermal exposure were obtained. Representative microstructures of the various cross-sections of selective die bonds follow.

Figure 4.1 shows a set of cross-sectional optical micrographs of the Staystik 415 and 482 die bonds in the as-manufactured condition. As a result of the combined applied heating during the manufacturing and slight pressure during the tack process (holding the die down manually whist the substrate is heated to obtain the initial sticking of the adhesive) required to melt the polymer and to overcome surface tension, a small fillet is generated

at the edges of the die. An optical micrograph of the typical fillet region that lies around the edge of the Si die is shown in Figure 4.1(a). There was a Si fragment ($\approx 75\mu m$ in size) due to fracture of the Si in the die lower corner. Figure 4.1(b) shows the typical interfacial region of the Staystik 415 die bond. Voiding is common in thermoplastic materials due to outgassing, trapped air during attachment or attachment shrinkage during solidification [3,43]. Furthermore, voiding due to poor processing can serve as a crack initiation site, which can explain the horizontal cracking in the brittle Si. Also, the adhesive bondline thickness was approximately $35\mu m$, when generally a minimum thickness of $50\mu m$ is recommended [52]. Dispensing insufficient or non-uniform adhesive to cover the entire bondline can enhance die stresses and consequently die cracking. Resulting fragments of Si (varying from 35 to $85\mu m$ in size) were dispersed along the Si die/Staystik 415 interface. A similar scenario was observed for the Staystik 482 die bonds in terms of voiding as shown in Figure 4.1(c). In this case, the adhesive bondline was generally more uniform and was $\approx 50\mu m$ thick. Figure 4.1(d) shows vertical cracking in the Si die. It should be noted that Si cracking could also result from the cross-sectioning procedure for microscopy.

Comparing Staystik 415 and 482 die bonds in terms of interfacial defects, there was generally a higher occurrence of die cracking with Staystik 415. The reason may be the requirement for a higher bonding temperature of 300-375^{o}C compared with 160-275^{o}C for Staystik 482. This could promote higher residual stresses on cooling, and therefore lead to a greater tendency for cracking. Another reason for the higher cracking extent may also be T_g related, since a higher T_g means that the adhesive will tend to be more brittle and therefore prone to cracks. Staystik 415 adhesive has a T_g of $\approx$ 180/185^{o}C [137] approximately the double of Staystik 482. Note that the glass transition temperature T_g is not a precise "temperature" in thermoplastics.

Manufactured die bonds using Staystik 415 and 482 underwent isother-

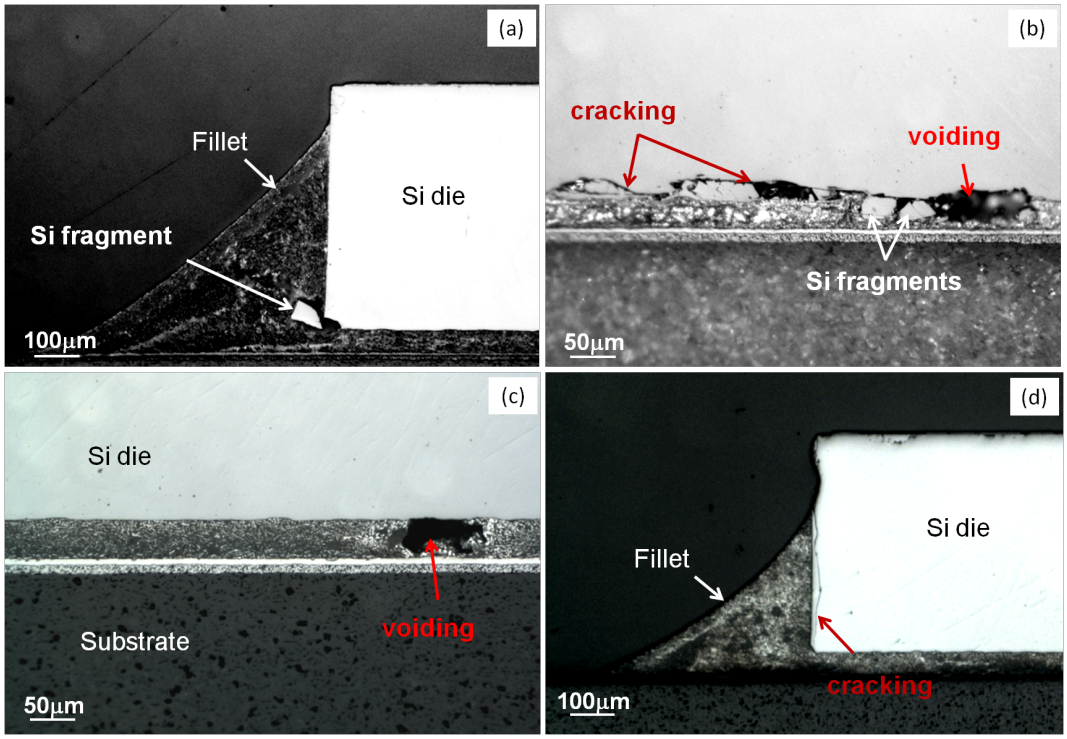


Figure 4.1: Cross-sectional optical micrographs of adhesive die bonds in the as-manufactured condition using: (a), (b) Staystik 415; and (c), (d) Staystik 482.

mal ageing, thermal shock and thermal cycling, and the resulting optical micrographs are shown in Figure 4.2. When artificially aged at 250^{o}C for 168h, both Staystik 415 (Figure 4.2(a)) and Staystik 482 (Figures 4.2(b)) die bonds showed fillet reduction or no fillets around the die edges. In thermoplastic materials, polymer flow may occur at elevated temperature under a force. Also, and in both cases, the absence/reduction of fillets was accompanied by delamination (loss of adhesion) with separation of the Si die/adhesive and adhesive/substrate interfaces. Oblique corner cracking (Figure 4.2(b)) was the main type of Si fracture observed in the Staystik 482 adhesive die bonds. Horizontal cracking also occurred. After thermal shock from 250^{o}C to - 65^{o}C in 10 seconds, the fillets around the Si edges were significantly reduced and delamination was visible for Staystik 415, as shown in Figure 4.2(c). Similarly, Figure 4.2(d) shows delamination and fillet reduction in Staystik 482. Small pieces ($\approx 25\mu m$) and larger fragments of Si die ($100\mu m$) were dispersed along the die/Staystik 482 interface. Note that the coefficient of thermal ex-

pansion (*CTE*) below T_g for Staystik 415 and 482 is 67.1ppm/^{o}C [137] and 26ppm/^{o}C [138] respectively, and in both cases is much greater than the *CTE* of Si at 3-5ppm/^{o}C. Consequently, in the absence of any stress-relief, large shear stresses could be expected to develop at the die/adhesive interface, exceeding the adhesive strength, and leading to delamination. In practice, some stress relief should be expected - by viscous flow of the polymer (as evidenced by the movement of material in and around the fillet), but the rapid decrease in temperature on thermal shock, inhibited stress relieve mechanisms, and residual stresses remained above the interfacial shear strength. After thermal cycling from 200^{o}C to -55^{o}C for 10 cycles, both Staystik die bonds suffered a smaller fillet reduction. The Staystik 415 die bond in Figure 4.2(e) shows that there was still some delamination; partial separation of the Si die from the adhesive was mainly located in the die upper corner (where the fillet forms against the vertical wall of the die) and the lower corner in the fillet region. This delamination propagated along the die/adhesive interface and at some point there was also separation of the adhesive from the HTCC substrate. Si fragments along the die/adhesive interface varied between 30 and 50μm in size. Figure 4.2(f) shows that thermal cycling again led to an increase in Si die cracking of the Staystik 482 die bonds, which may be an extension of die cracking in the as-manufactured condition. At room temperature, Staystik 415 has a shear strength of 24.1MPa [137] against 17.2MPa [138] for the Staystik 482, and the lower shear strength might suggest that the Staystik 482 interface may fail and so avoid transfer of high stresses to the fragile Si die [139]. However, the die bonds using Staystik 482 had a higher fraction of cracking, as shown in the same optical micrograph. The voiding in Figure 4.2(f) in the fillet area was likely to be generated during the manufacturing stage rather than the short thermal exposure of thermal cycling, since small voids can often be seen in the fillet region after processing.

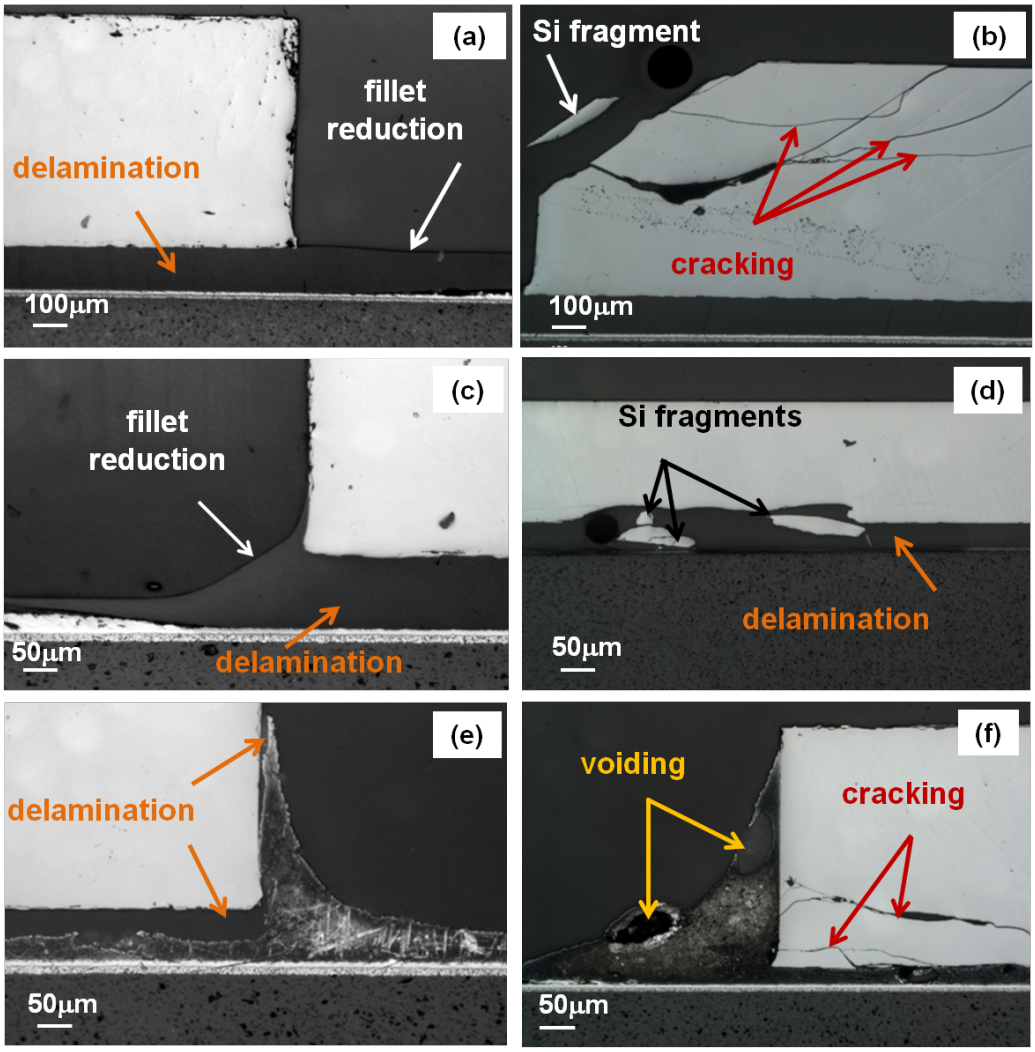


Figure 4.2: Cross-sectional optical micrographs of Staystik 415 and 482 die bonds under different conditions: stored at 250^{o}C for 168 hours [(a) Staystik 415; (b) Staystik 482]; thermal shock 250^{o}C to - 65^{o}C, in 10 seconds [(c) Staystik 415; (d) Staystik 482]; and thermal cycling 200^{o}C to -55^{o}C, 10 cycles [(e) Staystik 415; (f) Staystik 482].

4.2 GEM D4

An Ag-filled epoxy - GEM D4 - was supplied by the GWENT Group. GEM D4 is a thermoset polymer mix comprising 1-10%urea, 10-15% epoxy, 78.5% Ag and a ketone solvent. GEM D4 die bonds, manufactured at GE AS, were also cross-sectioned and prepared for metallography. Optical micrographs of cross-sections were obtained for the as-manufactured condition, and after thermal exposure. The conditions for thermal exposure were exactly the same used for Staystik 415 and 482 die bonds. Representative microstructures of the

various cross-sections are presented and discussed.

Figure 4.3 shows a set of cross-section optical micrographs of GEM D4 die bonds in the as-manufactured condition. Figure 4.3(a) shows a die bond using GEM D4 adhesive with the typical fillet formed and the Ag flakes within. The shape of the fillets in GEM D4 die bonds was different from those of both Staystik die bonds. The latter presented "sharper" fillets than those observed in the GEM D4 die bonds. The "shape factor" of a given fillet is related to the type of adhesive combined with its wetting characteristics [52], and both Staystik thermoplastic films suggested larger contact angles (lower wettability) than the GEM D4 adhesive. Note that dispensing the right volume of adhesives has to consider the tolerances of the die size and the adhesive gap. A small gap can leave a larger reservoir and produce a higher fillet comprised of the remainder, as suggested for the Staystik adhesives. On the other hand, a large gap allowed more material to flow under the die and less material remains for the fillet, as in the case of the GEM D4 adhesive. Figure 4.3(b) shows a higher magnification view of the fillet area where cracking occurred across the Si die. This cracking could result from the manufacturing process of the die bonds (when exerting a slight pressure on the die while attaching the component to the HTCC substrate), or as previously mentioned, during sample preparation. The Ag flakes within the adhesive matrix are shown in Figure 4.3(b). The Ag flakes were irregular in size (varying from 4 to 10μm) and in shape with many contacts between them. Because of shrinkage of the adhesive during curing additional compressive forces on the conducting particle contacts are provided. The fillers were distributed relatively homogeneously in the plane of the adhesive. There were only a few isolated voids in the fillet region, which varied from 7 to 20μm as shown in Figure 4.3(b). Figure 4.3(c) shows the interfacial area of the GEM D4 die bond as-manufactured with a bondline thickness of 20μm. There was horizontal die cracking with 5-20μm Si fragments distributed in the adhesive layer

and voiding also occurred here. The GEM D4 formulation was produced by GWENT by mixing the different components (urea, epoxy, Ag flakes and ketone solvent) by hand, and then passing over a three-roll mill to disperse the metallic filler. Three-roll milling is intended to minimise the incorporation of air during the mixing stage. Furthermore, an Ag-filled epoxy is known for its good resistance to moisture and solvents. However, the ketone solvent and/or any absorbed moisture could have outgassed during thermal curing, resulting in voids.

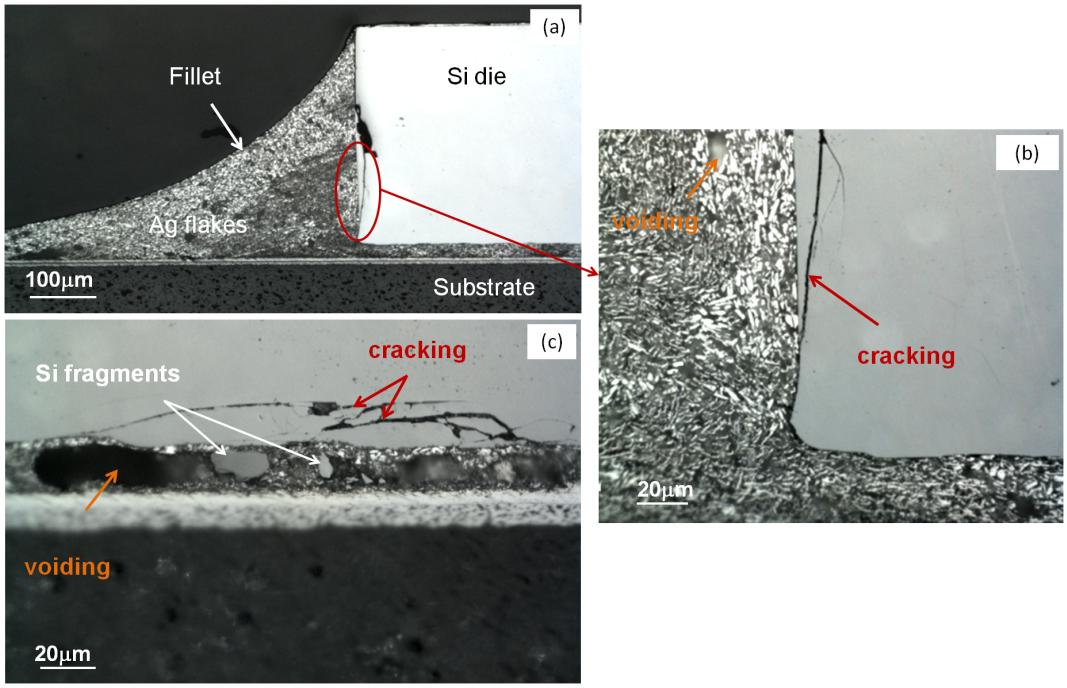


Figure 4.3: Cross-section optical micrographs of GEM D4 die bonds in the as-manufactured condition: (a) typical fillet formed against the vertical wall of the Si die; (b) higher magnification view of the fillet exhibiting vertical cracking in the Si die and voiding within the adhesive; and (c) typical interfacial area showing voiding and cracking.

The GEM D4 die bonds after different thermal exposures were also studied metallographically. Identical interfacial defects were observed and therefore only representative micrographs are shown here. Similarly to the thermoplastic Staystik 415 and 482 die bonds, the GEM D4 die bonds showed significant reduction of the fillets around the Si die edges after isothermal ageing at 250°C for 168h (again, the flow of material was a result of the el-

evated temperature). Ageing led once more to an increase in Si die cracking (horizontally and vertically). A similar scenario occurred for the die bonds after thermal shock treatment. Delamination with partial separation of the adhesive from the die, and horizontal cracking also occurred here. This type of catastrophic delamination and cracking was also shown to have occurred in Staystik 415 and 482 bonded assemblies under the same conditions. Figure 4.4 show optical micrographs of the GEM D4 die bonds after thermal cycling from 200^{o}C to -55^{o}C, for 10 cycles. There was again less fillet migration as can be seen in Figure 4.4(a). Figure 4.4(a) shows also die corner cracking in the Si and delamination (note the fillet partially detached from the die side). Large Si fragments of $\approx 150\mu m$ were also unbonded from the adhesive layer, as shown in Figure 4.4(b). A few small isolated voids ($\approx 7\mu m$) were typically also found, again most likely due to further outgassing.

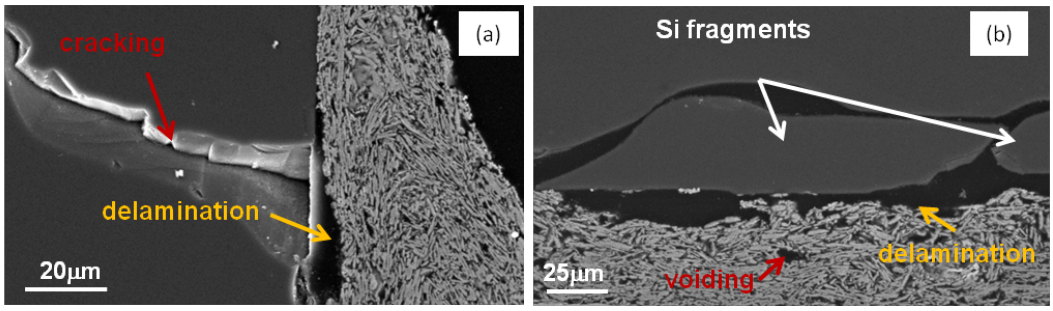


Figure 4.4: Cross-section optical micrographs of GEM D4 die bonds after thermal cycling from 200^{o}C to -55^{o}C, 10 cycles: (a) fillet region showing delamination and cracking; and (b) interfacial area exhibiting Si fragments with further delamination, and voiding within the adhesive.

4.3 Ablebond JM7000

A second Ag-filled adhesive, termed Ablebond JM7000, was investigated. This adhesive was studied in more detail as the screening trials indicated this adhesive to be one of the most promising for die attachment for high temperature application.

JM7000 is a cyanate-ester that is formed from resins that contain cyanate

groups (O-CN), which on heating, and in the presence of a catalyst, polymerize to form highly aromatic triazine ring structures, a process called cyclotrimerization. The polymerization reaction occurs as presented in Figure 4.5, and is used in JM7000 to form the polycyanate/Ag composite.

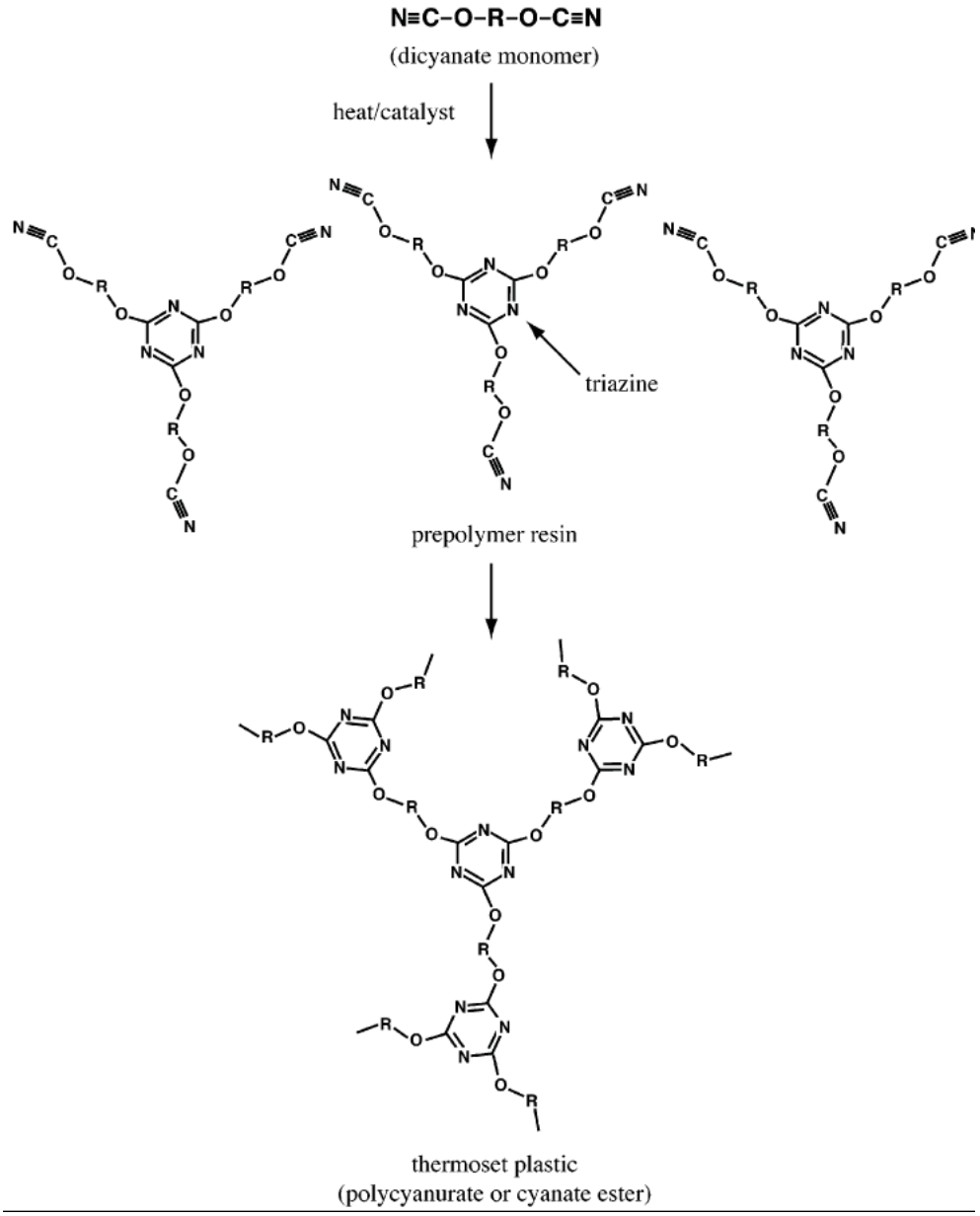


Figure 4.5: Polymerization reaction on cyanate ester [140].

Thermal stability of JM7000 was investigated, using thermo-gravimetric analysis (TGA), in order to determine the weight loss as a function of increasing temperature. Thermal stabilities for these types of materials are often reported as percentage weight loss at 300^{o}C. TGA analysis was performed at

a constant heating rate of 10°C/min. Figure 4.6 shows that the JM7000 had a very small weight loss of ≈ 0.15wt% at 300°C. Since 80% of this adhesive is comprised of the non-volatile Ag filler, the weight loss as a percentage of the adhesive weight was ≈ 0.12wt%, in agreement with [141]. Above approximately 300°C, the weight loss accelerated and indicated the onset of rapid thermal decomposition. Figure 4.6 also confirmed that the weight loss was relatively low around the curing temperature of 150°C. In a cyanate-ester, the molecular weights of the repeated units of polycyanate are the same as that of the monomers, i.e., there are no outgassed byproducts formed by this reaction. As a result, there is no significant weight loss during cure, a desirable feature for hermetic and plastic die attach [45].

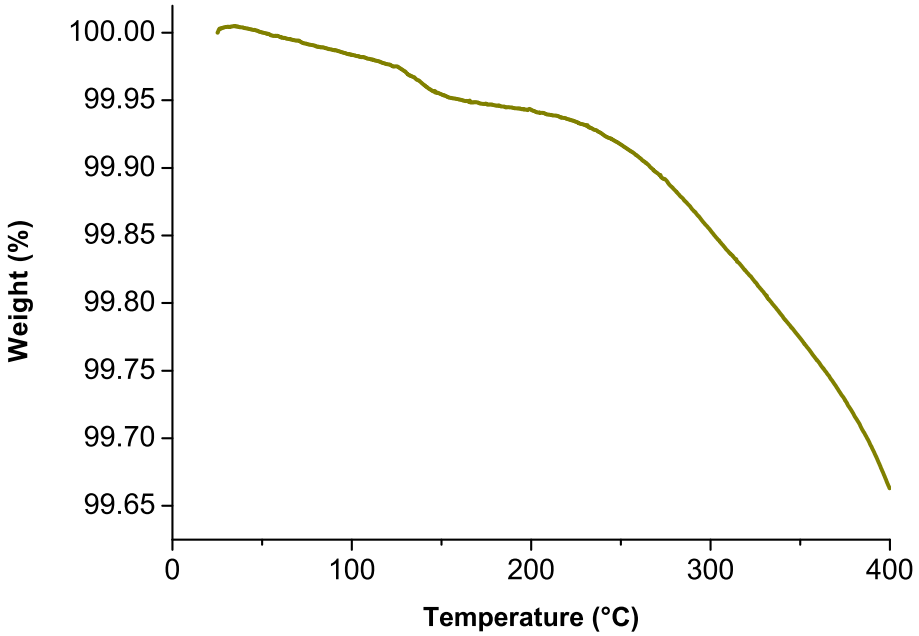


Figure 4.6: Thermal stability of the JM7000 adhesive.

Die bonds using JM7000, manufactured at GE AS, were cross-sectioned and examined using scanning electron microscopy (SEM). SEM micrographs of cross-sections in the as-manufactured condition, and after thermal exposure were evaluated in detail. Again, only representative micrographs are shown from hundreds of images obtained.

Figure 4.7 shows a set of SEM micrographs of JM7000 die bonds in

the as-manufactured condition. Figure 4.7(a) shows that a well built-up fillet was formed around the die edges. Again, the shape of the fillets developed here was rather different from the ones developed in GEM D4 die bonds (the other thermoset adhesive investigated). The JM7000 die bonds comprised the "sharpest" fillets among all the adhesives studied, which is likely related to viscosity. A higher Ag content (80%) in JM7000 imparts a greater viscosity (and higher contact angle) and, therefore less flow. Figure 4.7(b) shows vertical Si die cracking, delamination and voiding concentrated in the fillet area. Delamination occurred with partial separation of the fillet from the Si die at the top corner, presumably generated during the die assembly. This could be due to the pressure applied on the Si die during bonding. This delamination could have possibly caused the Si to crack vertically, as shown at the top corner of the die in Figure 4.7(b). There were comparatively few voids in the fillet region with a maximum void size of $\approx 40\mu m$. Copious corner cracking in the brittle Si die is shown in Figure 4.7(c). The local concentration of elements was investigated by EDX in order to identify unambiguously the various parts of the package such as the Al_2O_3 substrate, the HTCC substrate metallisations consisting of W ($\approx 12\mu m$), then Ni ($\approx 6\mu m$) followed by a top layer of Au ($\approx 3\mu m$), the JM7000 adhesive layer, and the Si die itself. These are labelled in Figure 4.7(d). Figure 4.7(d) shows that the JM7000 layer between substrate and die was approximately four times thicker ($\approx 82\mu m$) than GEM D4 layer manufactured under nominally the same conditions, which is due to higher viscosity associated with the high fraction of Ag flakes. After curing, the matrix shrinks and presses the Ag flakes against each other. The Ag-flakes were irregular in size, varying between 2.5 to $10\mu m$; bigger Ag flakes were also visible. Higher aspect ratio flakes tended to lie in the plane of the adhesive.

The key performance requirements for die bonding are adhesion (MIL. STD. 883) [94], no voids and crack-free bonding. In Figure 4.8, interfacial de-

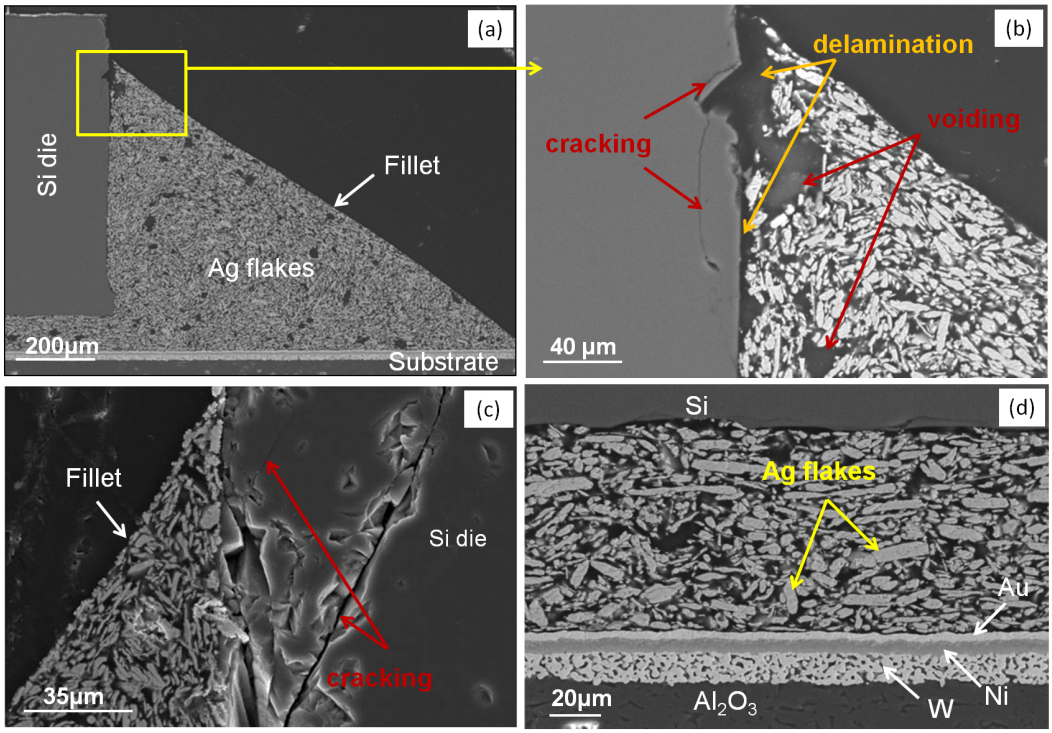


Figure 4.7: Cross-section SEM images of a typical JM7000 die bond in the as-manufactured condition: (a) typical fillet formed against the vertical wall of the Si die; (b) higher magnification view of the fillet showing cracking in the Si die arising from delamination on the vertical section of the fillet; (c) copious corner cracking in the Si die; and (d) typical interfacial area with the various parts of the package identified by EDX.

fects of cracking and voiding in the JM7000 die bonds are shown. Although this adhesive has been designed to have low voiding content (it comprises a low fraction of volatiles), voiding could be due to the fact that the adhesive is not flowing under the die because it is already full of Ag. A few big voids were visible, measuring $\approx 100\mu m$ as shown in Figure 4.8(a). Figure 4.8(a) shows also that cracks were prevented from propagating through the adhesive. This is because voiding can sometimes provide strain relief by reducing the modulus of the adhesive and by an expansion effect which increases bond thickness and helps reduce thermal mismatch stresses and strains [142]. However, in general, voids are considered stress raisers and are responsible for introducing some degree of inhomogeneity in the die attach. For die attachment using adhesives, the viscoelastic properties of the adhesive may allow thermally induced stresses (and stored strain energy) so that delaminating crack nu-

cleation and growth does not occur. JM7000 has a comparatively high T_g (240^{o}C) [141] and therefore, is more susceptible to the formation of cracks than those with a low T_g. The thermoplastic die attach materials (Staystik 415 and 482) had T_g's of 180-185^{o}C [137] and $\approx$ 98^{o}C [138] respectively, and did not developed such large accumulation of cracking in the as-manufactured condition (see Figure 4.1). Occasionally, small and large fragments of Si were visible in the interfacial area. One of these large fragments is shown in Figure 4.8(b). Also, the Au metallisation started to fill the upper layer. This was probably caused by the polishing technique; dissimilar materials assembled increase the difficulty in achieving a successful polishing.

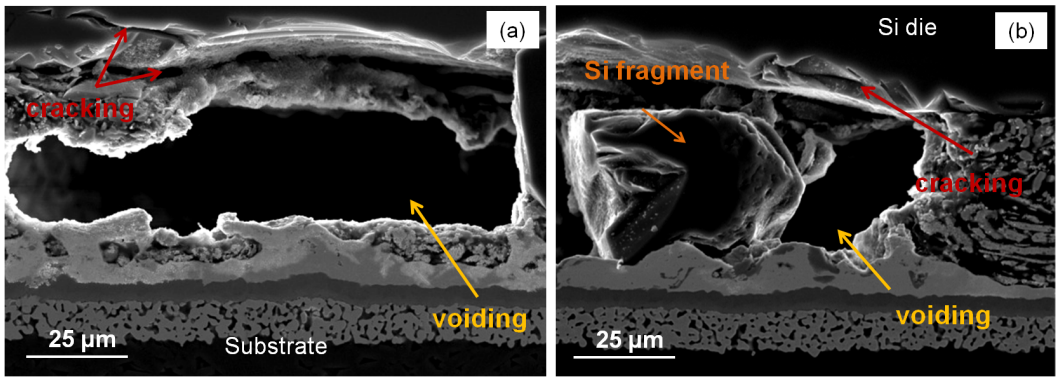


Figure 4.8: Cross-section SEM images of the Si die/JM7000/substrate region as-manufactured, exhibiting: (a) interfacial defects of cracking and voiding; and (b) large Si fragment.

As-manufactured JM7000 die bonds underwent isothermal ageing at 250^{o}C over different periods of time, and the microstructural evolution of the die bonds is shown in the next two sets of SEM micrographs (Figures 4.9 and 4.10). Figure 4.9 shows cross-sections of the JM7000 die bonds stored at 250^{o}C for a period of 168h. Similarly to the other adhesives previously studied, the fillets of the JM7000 die bond were reduced (however, only slightly), again driven by the softening and flow of the material at those high temperatures. This thermosetting adhesive softens as the temperature approaches the T_g (240^{o}C). It does not undergo melting and re-solidification behaviour once cured, because of the highly cross-linked molecular structure, it decom-

poses and chars on increasing temperatures. Figure 4.9(a) shows that the Si die was fractured in the lower corner and, voiding was visible in the fillet area. Again, similarly to GEM D4 there was some delamination which propagated along the die/adhesive and adhesive/metallisation interfaces as shown in Figure 4.9(b). The SEM micrograph in Figure 4.9(c) shows that the JM7000 adhesive layer was also not continuous. A higher magnification of the adhesive layer discontinuity is shown in Figure 4.9(d).

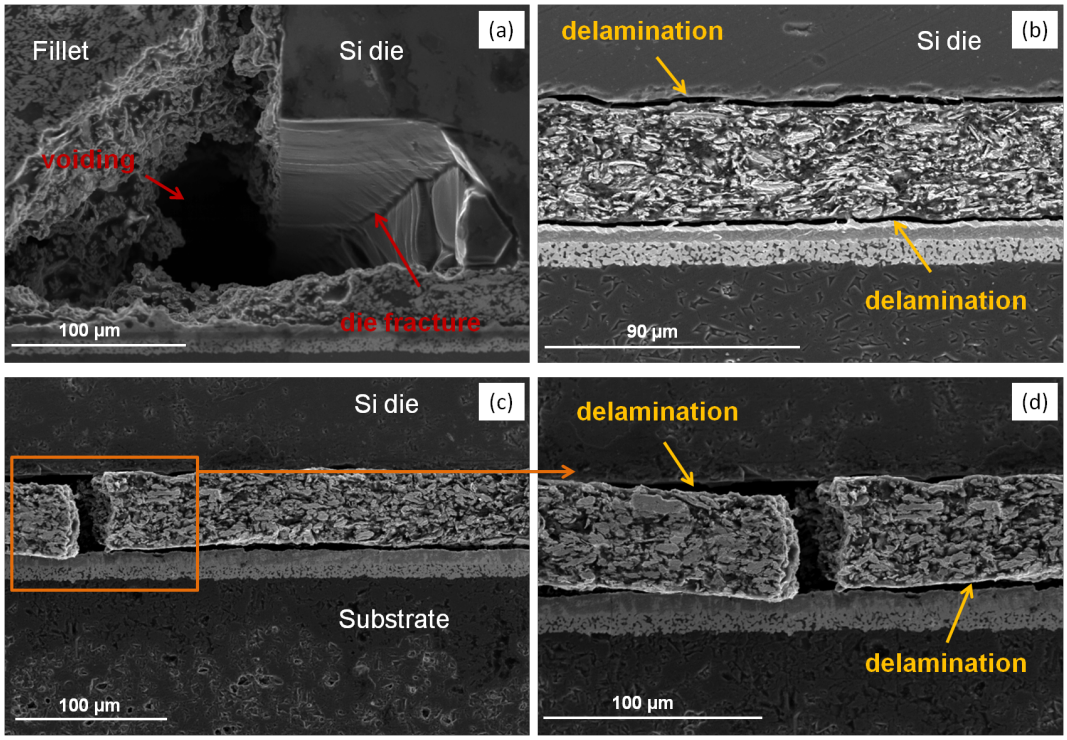


Figure 4.9: Cross-section SEM images of JM7000 die bonds after isothermal ageing at 250^{o}C, for 168h: (a) fillet region exhibiting Si die fracture and voiding; (b) interfacial area showing delamination located at die/adhesive and adhesive/metallisation interfaces, (c) discontinuity of the JM7000 adhesive layer accompanied with delamination in both interfaces; and (d) higher magnification of the adhesive layer discontinuity.

The JM7000 die bonds were also aged at 250^{o}C for extended periods of time: 672, 1008 and 2016h. The adhesive die bonds after 672h presented significant voiding in the fillet region accompanied with some delamination mainly located in the die lower corner (Figure 4.10(a)). The interfacial area also presented voiding with the largest void measuring $\approx 60\mu m$ as shown in Figure 4.10(b). These voids could be induced during manufacturing, and

tended to grow with ageing. After a period of 1008h of ageing, there was again partial separation of the Si die from the adhesive layer (Figure 4.10(c)). Figure 4.10(d) shows some horizontal cracking in the die with few Si fragments dispersed in the adhesive layer; one of these Si fragments measured $\approx 50\mu m$. There was also voiding in the interfacial area as shown in Figure 4.10(d). On increasing the ageing up to a total of 2016h, the die bonds showed in general that fillet reduction did not lead to excessive cracking in the Si with any cracks mainly limited to the die edge as shown in Figure 4.10(e). A higher extent of delamination occurred along the adhesive layer with separation of the Si die from the JM7000 layer.

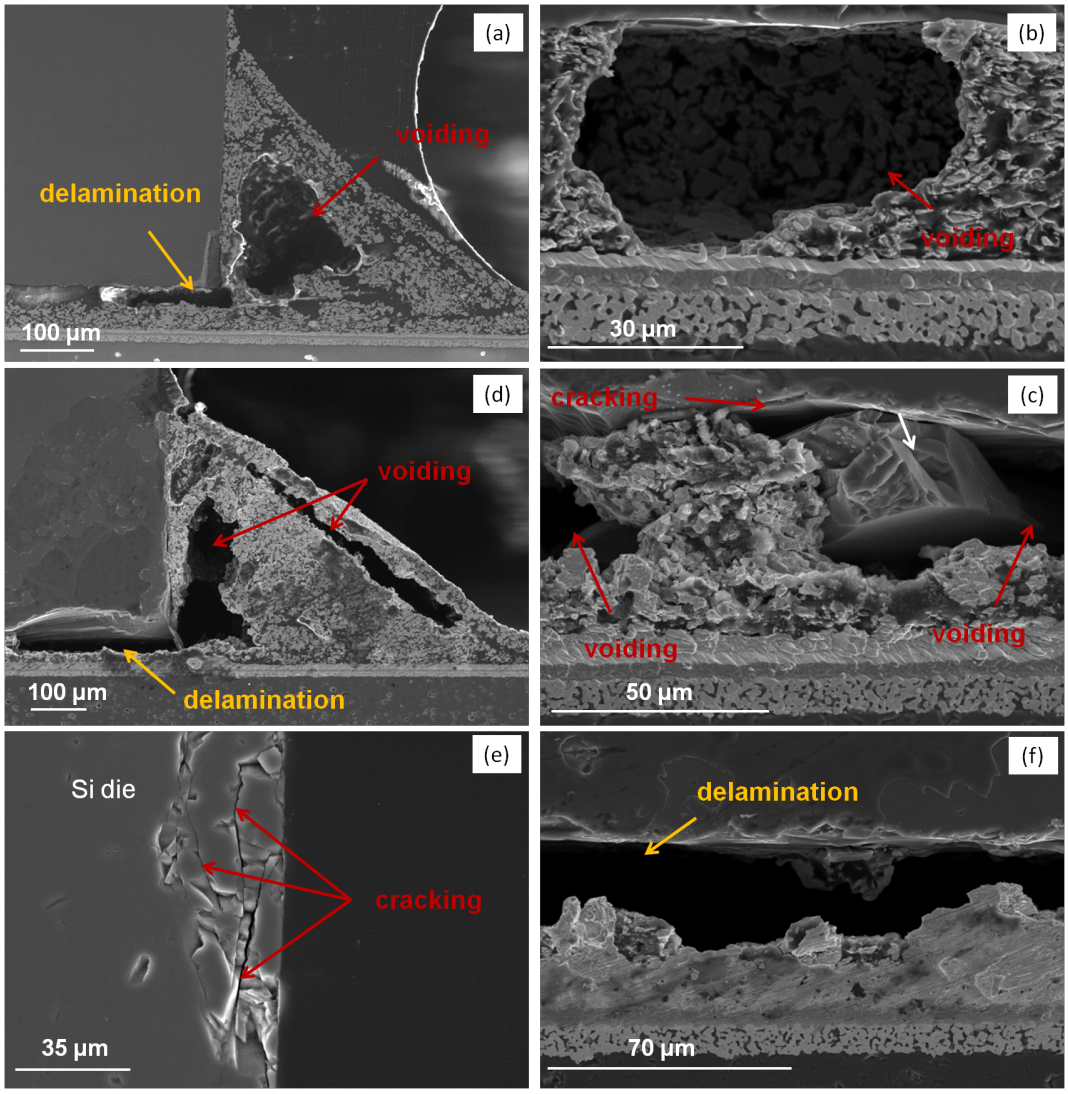


Figure 4.10: Cross-section SEM images of JM7000 die bonds after isothermal ageing at 250^{o}C, for: (a), (b) 672h; (c), (d): 1008h; and (e), (f) 2016h.

JM7000 die assemblies were also submitted to thermal shock from 200^{o}C to -65^{o}C in 10s, and the microstructural change of the adhesive die bonds is presented in Figure 4.11. Figure 4.11(a) shows that after thermal shock there was a considerable fillet reduction. Also, thermal shock treatments lead to an increase in Si die cracking. Under thermal shock, adhesives are susceptible to brittle failure because the polymer is not able to plastically respond to relieve expansion/contraction strains quickly. The fillets comprised some voids measuring between 10 and 20μm. The interfacial area, in Figure 4.11(b), contained bigger voids measuring $\approx$ 140μm. Voiding was more evident in the die bonds after thermal shock. It is unlikely that thermal shock alone led to voiding, so the voids in Figure 4.11(b) were likely induced during manufacturing. However, the voiding was also associated with significant cracking after thermal shock, and voids probably provided regions for easy crack nucleation. There was also delamination along the die/adhesive and adhesive/metallisation region with typically a few Si fragments (15 to 35μm) dispersed in adhesive matrix area.

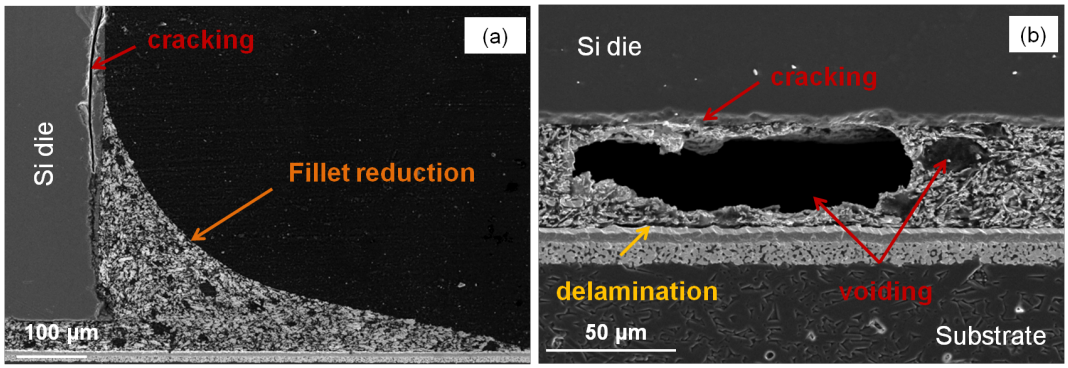


Figure 4.11: Cross-section SEM images of JM7000 die bonds after thermal shock from 200^{o}C to -65^{o}C, in 10s, showing: (a) fillet reduction; and (b) die cracking and voiding within the adhesive matrix.

The microstructural change of the JM7000 die bonds after thermal cycling from 200^{o}C to -55^{o}C, for 10 cycles was also investigated. One of the fillets remained around the die edges (yet reduced) while the other disappeared. Again, severe vertical die cracking was located in the die edges. Cracking in

the Si die was accompanied by delamination with partial separation of the die from the JM7000 adhesive interface. When an adhesive is used to bond dies to a substrate, most of the stress occurs in the bonding layer because it is much softer than the die and substrate due to thermal degradation of the polymer matrix itself [143]. As a result, during thermal cycling the bonding layer deteriorates because of thermo-mechanical fatigue caused by the dissipative deformation produced by the dynamic stress [96]. Thermal cycling again induced voiding in the die bonds; voids varied from 6 to 15μm in size and were located in the adhesive matrix (Figure 4.12(a). Horizontal die cracking also occurred after thermal cycling and propagated along the die into the adhesive as shown in Figure 4.12(b).

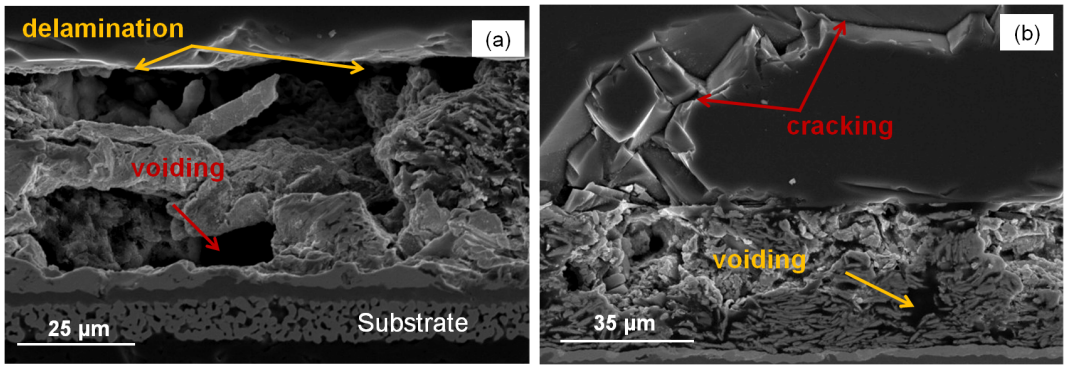


Figure 4.12: Cross-section SEM images of JM7000 die bonds after thermal cycling from 200^{o}C to -55^{o}C, 10 cycles, showing: (a) delamination and voiding in the interfacial area; (b) severe die cracking.

The cross-section studies of the adhesive die bonds microstructure showed the difficulty of: (a) getting representative insights into the interfacial region using a sectioning approach, and (b) the difficulties caused by inducing damage in the brittle Si using a destructive cross-section technique. Therefore, the need for SAM was reinforced as a non-destructive probe for study of the interfaces. It was not expected that SAM would lead to significant reassessment of the suitability of the adhesives, but that it might allow a more direct comparison of destructive and non-destructive approaches, as well as the development of a possible correlation of interface "quality" with destructive die bond strength measurements, which could be used more generally in the ex-

amination of other die attach materials.

4.4 Scanning acoustic microscopy

SAM was used to image interfacial defects in adhesives die bonds in the as-manufactured condition, and after different thermal exposure. *"Ultrasonic inspection of die attach"*, MIL. STD. 883, Method 2030 [94] was used to investigate if differences between unbonded and bonded areas within the die bonds could be detected as a function of manufacturing conditions and after different thermal exposure. The fraction of bonded area was, whenever possible, determined.

The first set of SAM images were obtained at an operating frequency of 80MHz. Figure 4.13(a) shows unbonded areas in a JM7000 die bond in the as-manufactured condition. The SAM image was obtained by scanning the specimen "downwards" from the Si die/adhesive/HTCC substrate. The JM7000 die bond exhibited small and random unbonded areas depicted by the brighter spots. Nevertheless, there was no major voiding. The bonded area of JM7000 die bond was reduced after thermal exposure at 250^{o}C, for 2016h, as shown in Figure 4.13(b). In this case, the image was generated by scanning the inspected specimen through the HTCC substrate/adhesive/die interface. Unbonded regions, shown by the brighter areas, increased although some residual bonded areas (dark grey) were still evident, which was consistent with the SEM analysis for the aged die bonds.

Figure 4.14 shows the effect of isothermal ageing on bonded area of the JM7000 die bonds. Inspection used an operating frequency of 50MHz, and was performed through the top of the Si die. In this arrangement, unbonded areas were more easily observed because of the enhanced contrast. Figure 4.14(a) shows small unbonded areas randomly dispersed in the adhe-

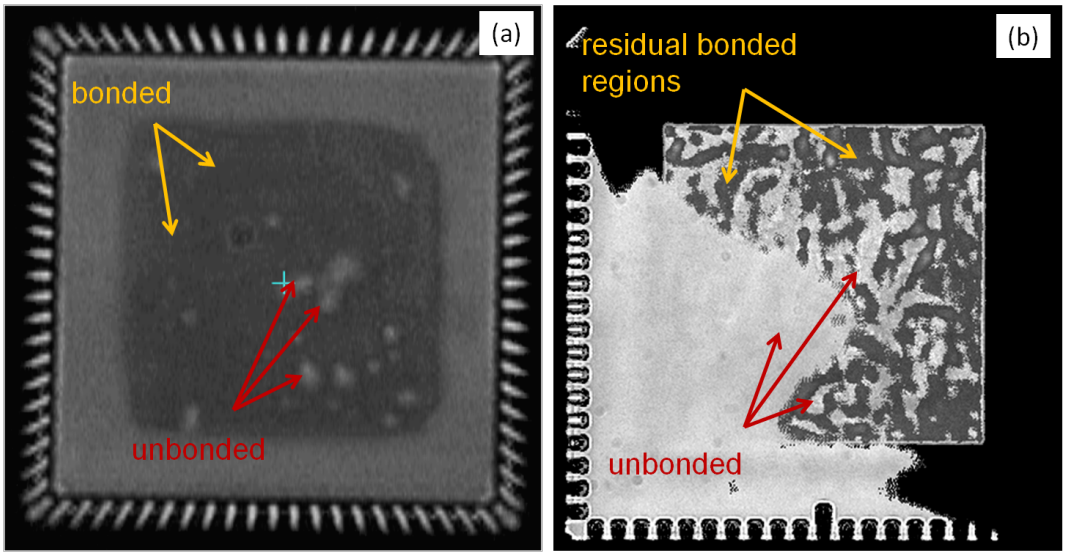


Figure 4.13: SAM images of the JM7000 die assemblies in (a) as-manufactured, and (b) after thermal exposure at 250^{o}C for 2016 hours showing voiding and unbonded areas.

Table 4.1: Bonded area (BA) percentages for the JM7000 die bonds as-manufactured (0h), and after isothermal ageing at 250^{o}C for different periods of time. The percentage of largest single defect (l.s.d) is also given or each case.

Storage time (h)	**BA (%)**	**l.s.d (%)**
0	98	1
168	42	29
504	47	48
672	75	4
1008	32	54

sive die bond in the as-manufactured condition. The initial bonded area was 98% and the largest single defect comprised 1% of the overall bonded region. Overall, the die bonds suffered degradation in bond quality (expressed as the percentage bonded area) after thermal exposure, as shown in Figures 4.14(b)-(e), and bonded areas decreased with increasing ageing time. Note that all images from these die bonds were from bonds manufactured under identical conditions but were separate specimens. Table 4.1 summarises the percentage bonded area as-manufactured and after isothermal ageing over different periods of time.

Unbonded areas in GEM D4 die bonds (as-manufactured and after

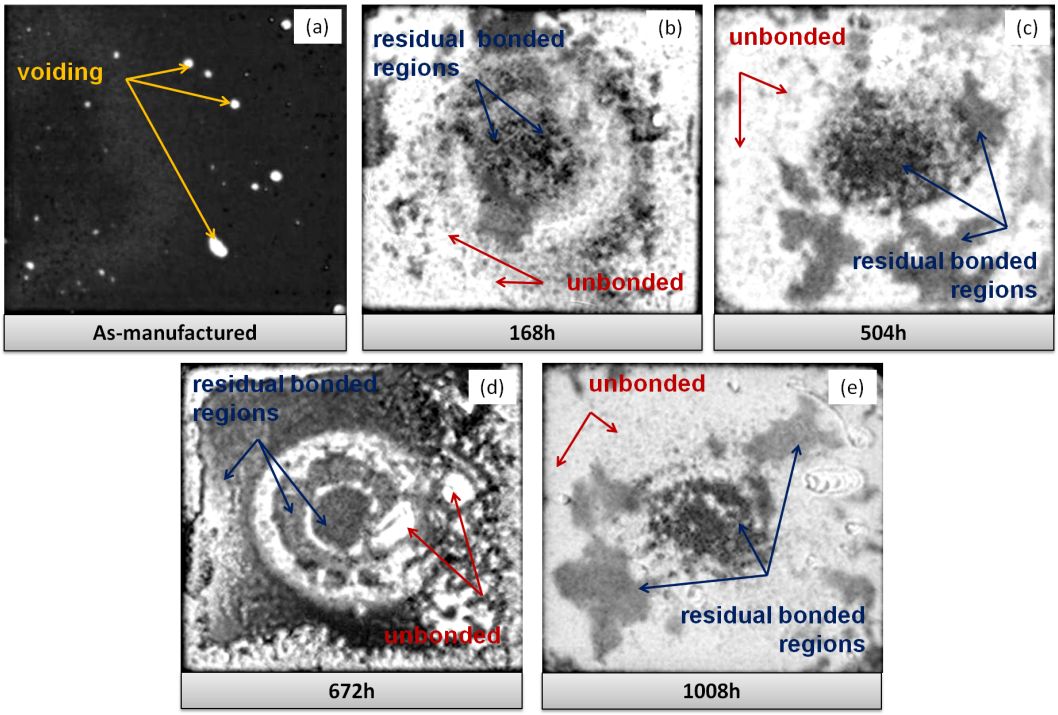


Figure 4.14: SAM images of the JM7000 die bonds: (a) as-manufactured; and after isothermal ageing at 250^{o}C for (b) 168h, (c) 504h, (d) 672h, and (e) 1008h showing its effect on the bonded area.

thermal exposure) are shown in Figure 4.15, at 50MHz, through the top side of the Si die while immersed in water. Figure 4.15(a) shows a bonded area of 20% as-manufactured and a large single contiguous defect measuring 79% of the die area. Some residual bonded regions were still visible, but after thermal exposure at 250^{o}C for 168h, the extent of bonded regions decreased significantly (<10%). Figure 4.15(b1) was produced under the same parameters that generated the image in Figure 4.15(b); the image on the right shows the die bond after water ingression into the specimen identified by the purple arrows. The water ingression, detected within the die bonds after a few minutes, can mask or perhaps even exacerbate, signs of unbonded areas in the adhesive die bonds.

Degradation in bonded area was also evident after thermal cycling [200^{o}C to -55^{o}C, 10 cycles], with only 29% bonded area with the largest single defect of 70% of the unbonded area, as shown in Figure 4.15(c). Figure 4.15(d) shows a greater degradation in bonded area for GEM D4 die bonds after ther-

mal shock [250^{o}C to - 65^{o}C, 10 seconds] with a final bonded area of 13% and the largest single defect occupying 87% of the unbonded region. In this case, water ingression was also detected as shown in Figure 4.15(d1). The water ingression into thermally shocked interfaces occurred much faster than in the bonds that were artificially aged, indicating that the voids/unbonded regions are open to the testing environment, i.e. were contiguous to the edge of the die.

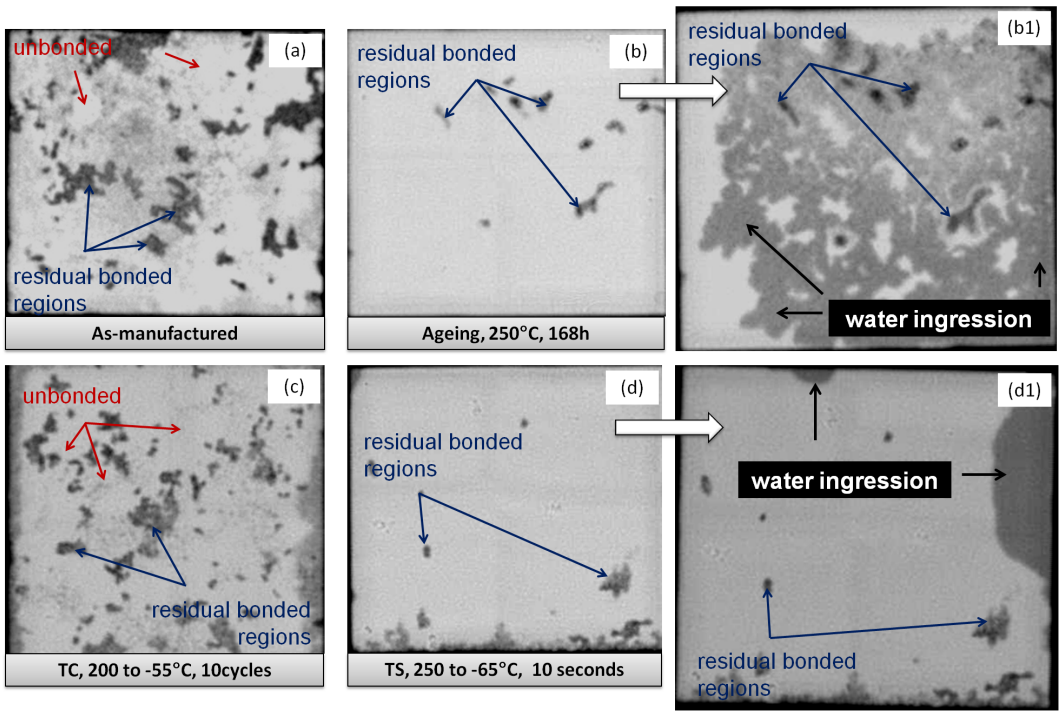


Figure 4.15: SAM images of GEM D4 die assemblies: (a) as-manufactured, (b) after isothermal ageing at 250^{o}C for 168h, (c) after thermal cycling [200^{o}C to -55^{o}C, 10 cycles], and (d) after thermal shock [250^{o}C to - 65^{o}C, 10 seconds].

The unfilled thermoplastic films Staystik 415 and 482 used in die bonds were also inspected with SAM (Figure 4.16). Figure 4.16(a) and (b) show the acoustic images generated for the die bonds using Staystik 482 in the as-manufactured condition, and Staystik 415 after isothermal ageing at 250^{o}C for 2016 hours, respectively. The bonded area was low in both cases, and absolute values were not taken because water infiltrated in the interface region very rapidly. In most of the cases, as a result of the water ingression, the Si dies were separated from the rest of the package after SAM imaging.

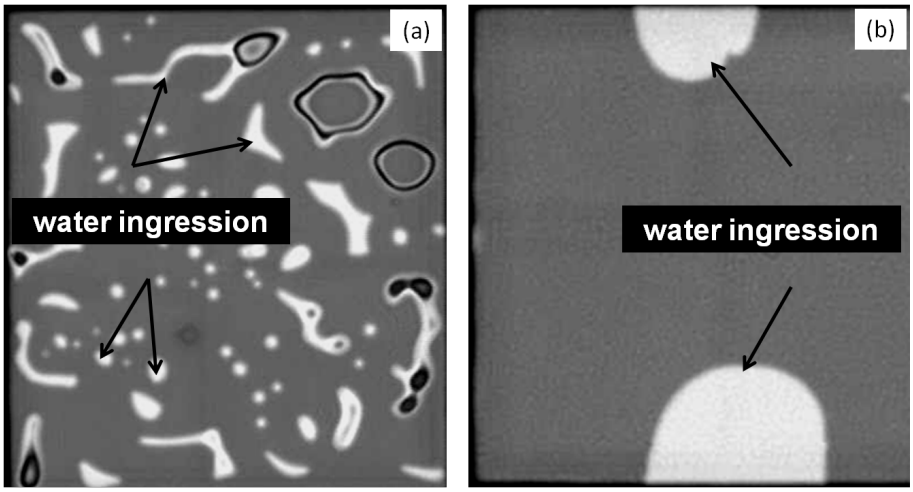


Figure 4.16: SAM images of Staystik die bonds: (a) Staystik 482 in the as-manufactured condition, and (b) Staystik 415 after isothermal ageing at 250^{o}C for 2016h.

4.5 Adhesive strength

Another critical reliability issue of the adhesives is their adhesive strength which ultimately controls the ability of the material to resist the thermally induced and/or shrinkage stresses developed in manufacture and in service. Typically, the strength of an adhesive bond is measured using a destructive test such as die shear testing. However, there are many difficulties in determining the bond strength or adhesive strength, including the brittleness of the Si die, that cracks (in preference to the interface) in unpredictable ways, and leading to a wide spread of measured strengths.

Shear testing was carried out in order to assess the die shear load to failure for 1.3mm x 1.3mm Si dies bonded to HTCC packages with the different adhesives investigated, stored in air, for up to 2000h at 250^{o}C.

Figure 4.17 shows the degradation of the mean die shear load to failure of the adhesive die bonds as a function of thermal exposure at 250^{o}C for different periods of time. All three different adhesive die bonds showed degradation in the shear load with increasing thermal exposure time. In the as-manufactured condition, the JM7000 die bond presented the highest mean

die shear load to failure (4.7kg).

After thermal exposure at 250^{o}C, the die bonds using JM7000 suffered a significant decrease in mean shear load to failure. Total separation of the Si die from the rest of the package occurred for 672 and 2016h of ageing. On the other hand, GEM D4 had an initial mean load to failure of 3.7kg, which increased after thermal exposure for 168h, and then decreased sharply with increasing storage time. The minimum acceptable load to failure defined in the MIL. STD. 883 is 2kg [94], and was not achieved for any die bond beyond 672h of ageing. Staystik 482 die bond had the lowest as-manufactured mean die shear load to failure (2.7kg), and after 2016 hours, the Si die was completely detached. Unlike thermosetting adhesives (GEM D4 and JM7000) that soften only gradually after reaching their T_g and retain much of their strength at elevated temperature, most thermoplastic adhesives (Staystik 482) melt at a specific temperature, or over a narrow temperature range, and lose all their strength above their T_g. So, adhesive degradation could explain the poor shear load.

In order to determine whether the ageing atmosphere could affect the adhesive strength of the adhesive die bonds, the JM7000 die bonds were also artificially aged in N_2. Figure 4.18 shows the comparison between the mean shear load to failure for aged die bonds in air and in N_2. The as-manufactured mean load to failure for the two sets of bonds in the as-manufactured condition were, within the experimental error, at $\approx$ 0.5kg. Under N_2, the mean shear load to failure remained $\geq$ 5kg even throughout the ageing treatment, and well above the minimum acceptable by the MIL. STD. 883 [94]. This means that providing an inert atmosphere for adhesive die bonds, there is some encouragement for high temperature use.

Die shear testing was also carried on Staystik 415 die bonds after artificially ageing at 250^{o}C, in N_2, and for Staystik 482 die bonds aged in air.

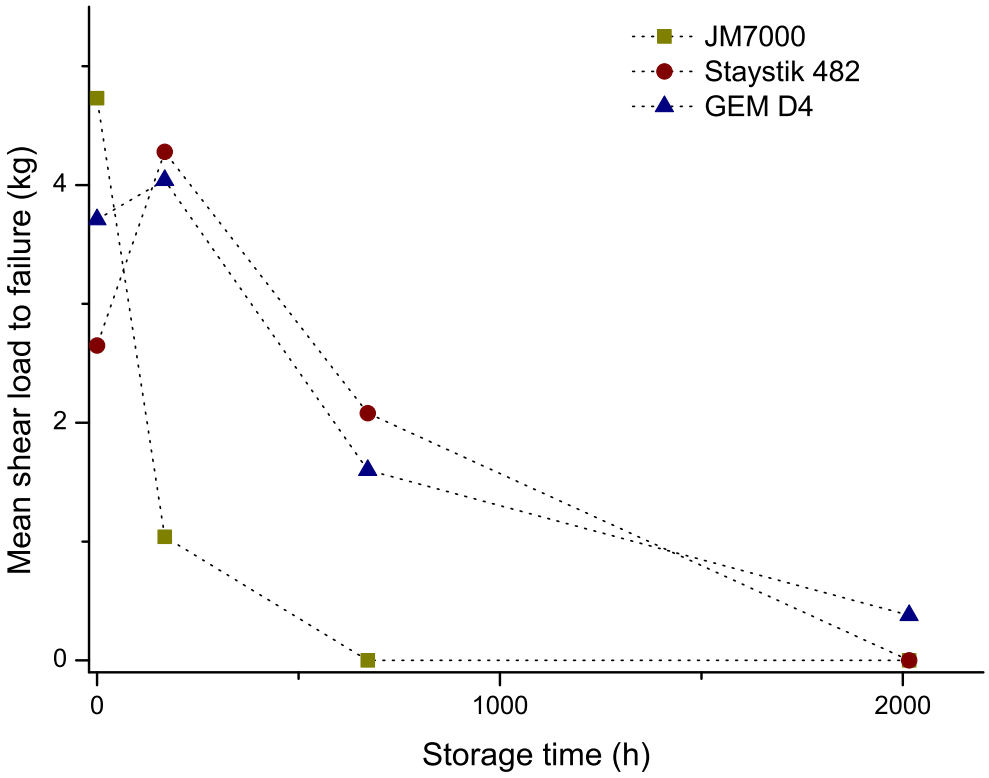


Figure 4.17: Variation of mean die shear load to failure for JM7000, GEM D4 and Staystik 482 die bonds as a function of isothermal ageing at 250^{o}C, in air.

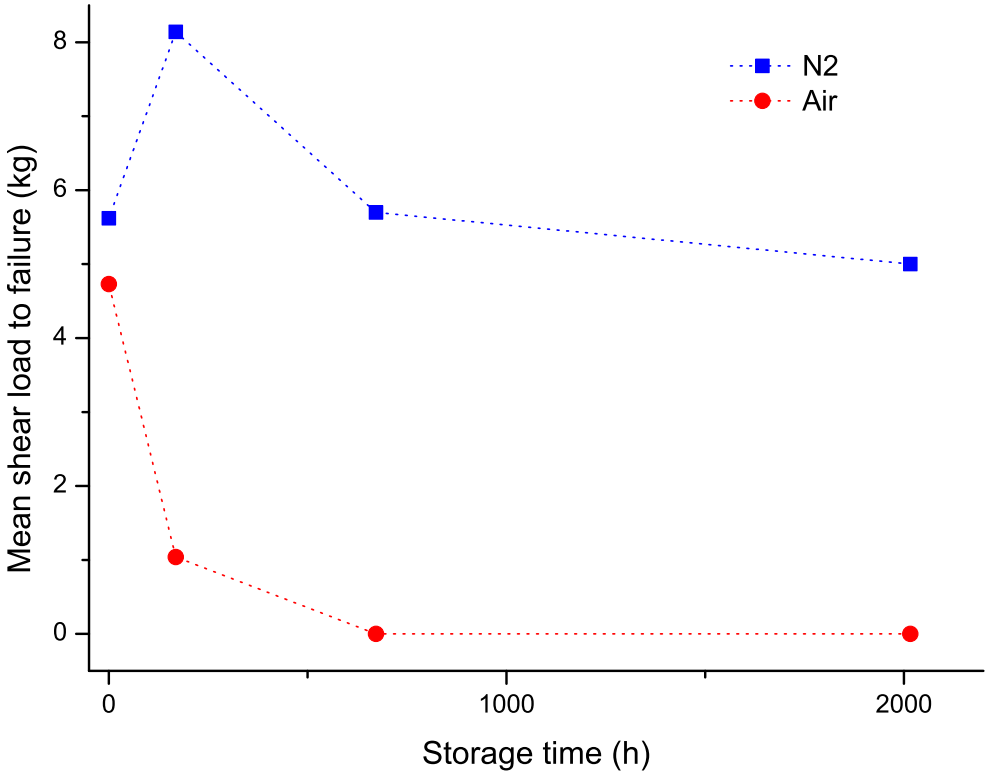


Figure 4.18: Comparison of mean die shear load to failure of JM7000 die bonds after ageing at 250^{o}C under air and N_2.

Figure 4.19 shows that the mean load to failure was higher for Staystik 482 with a higher T_g (180-185^{o}C) than Staystik 482 ($T_g \approx 98^o$C). Again, the adhesive strength was more stable when the bonds were sealed under N_2.

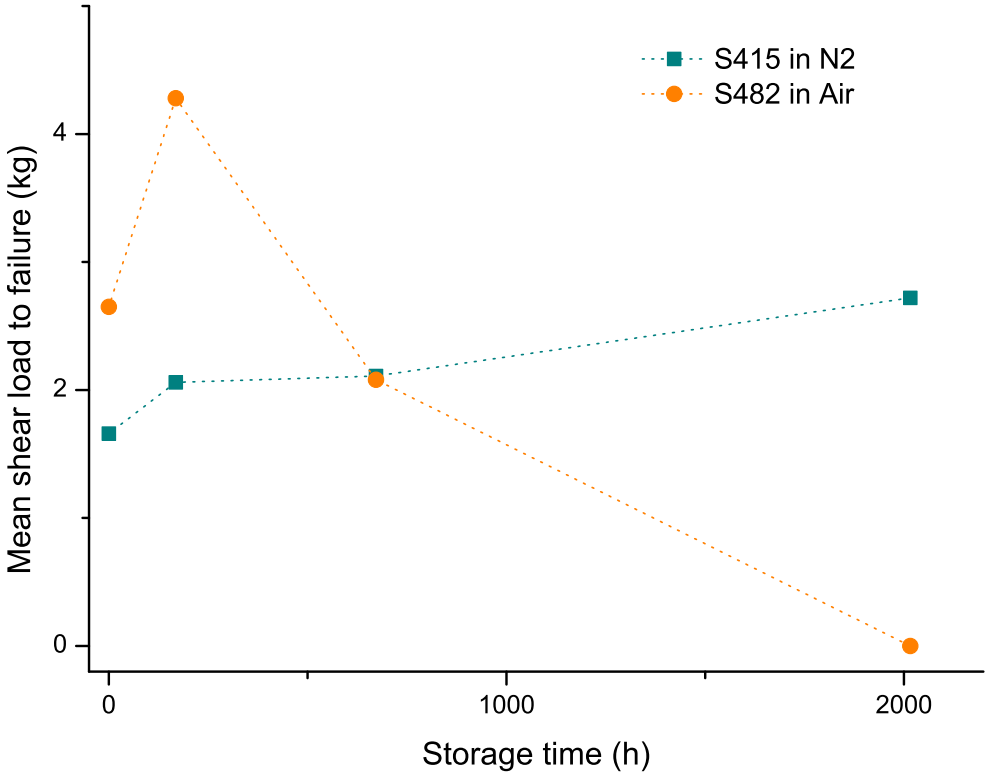


Figure 4.19: Comparison of mean die shear failure loads of Staystik 415 and 482 die assemblies after isothermal ageing at 250^{o}C in N_2, and in air, respectively.

Ag migration is another concern in package reliability when using Ag-filled adhesives because Ag can be a mobile species, and can be susceptible to electromigration that may lead to short-circuit failures. An Au coated HTCC substrate with a 3×3 array of Si dies attached using JM7000 is shown in Figure 4.20. One of the dies showed a distinctive Ag migration pattern through three concentric rings around the die, which were identified by a slight variation in colour after ageing for 168, 504 and 1008h.

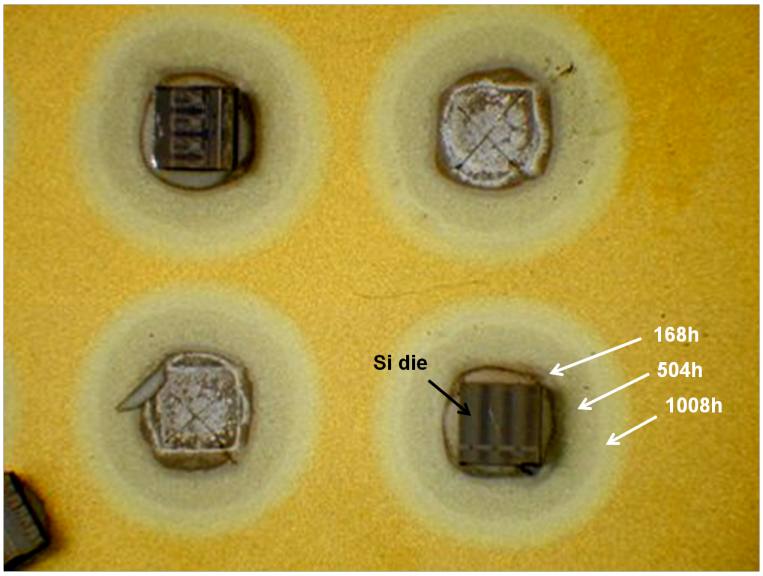


Figure 4.20: Silver migration around JM7000 Si dies on HTCC substrates after ageing for 168, 504 and 1008 hours.

4.6 Conclusions

Ease of manufacture and fewer processing steps were the main reasons why GE AS intended to pursue the ECAs route for die attach materials at high temperature/harsh environment. In this thesis, work was undertaken in order to assess the performance of several commercially available adhesives die attach materials when submitted to long term temperature storage at 250^{o}C up to 2016h. Two unfilled thermoplastic films (Staystik 415 and 482), an Ag-filled epoxy (GEM D4), and an Ag-filled cyanate-ester (Ablebond JM7000) were investigated.

Due to temperature fluctuation caused by thermal cycles, adhesive die attach materials have to sustain cyclic stresses from thermal expansion mismatch between the die and substrate. All adhesives showed limited applicability for use at 200^{o}C or above. Among problems encountered were: voiding which could be caused by retention of solvents or air entrapment; and stresses due to mismatches in CTE. The relatively poor thermal cycling performance of the adhesives has been revealed. Most damaging is the evolution of stress in adhesive layers generated in aggressive thermal cycling that leads to interfa-

cial delamination; voiding and limited Si cracking. Fillet migration/reduction was also seen, but was likely less catastrophic on overall behaviour. In some cases, dies simply fell off the substrate.

Preliminary results and information from the manufacturers and GE AS had suggested that from all the adhesives screened, JM7000 offered the most promise for high temperature use, since it was specifically formulated for this purpose. However, the results here show that even this most promising adhesive gives little encouragement for operation at 200^{o}C and higher, and failure usually occurred by die cracking, delamination, excessive softening or oxidation to a carbonaceous char. The conventional limitation used in industry of 200^{o}C is supported by the results here, even for JM7000.

In order to withstand mechanical shock, thermal shock, and thermal cycling, adhesives should, at least, meet minimum tensile and shear strengths as specified for the intended application. The main drawback to any adhesive based solution is the resistance of the adhesive to oxidative degradation. For any reasonable high temperature reliable operation the packaged system would have to be hermetically sealed, which will introduce a price premium. Specialist adhesives need to be developed for high temperature applications, to reduce the effects of degradation in the presence of air. In particular, the adhesives were exposed to temperature storage in either air or N_2 to ascertain whether there were any different degradation effects. The results showed that for all the adhesives stored in air at 250^{o}C, the shear load to failure decreased to below the 2kg level stipulated by MIL. STD. 883 for the die size, whilst samples stored in N_2 had shear failure loads above 2kg after 2016h at 250^{o}C. This means that providing an inert atmosphere can be maintained within the package to protect the electronics, certain adhesives will be able to meet the requirements for up to 2000h exposure at 250^{o}C.

Further specialist adhesives will need to be developed if adhesives are

to find use for high temperature applications, where the thermal degradation needs to be minimised and thermo-migration effects need to be examined.

CHAPTER 5

Au-Si die attach: results and discussion

The second die attach material system studied was Au-Si eutectic, which is a high temperature solder system that was studied in terms of its performance under harsh conditions, and suitability for use in high temperature/harsh environment applications. This chapter presents and discusses the experimental results to evaluate the Au-Si eutectic die attach system that is the main focus of the thesis. Experimental results are presented and discussed for: 1) Au-Si die bonding and process optimisation in terms of measured bonded area and complementary die shear testing; and 2) Au-Si die bond quality variability.

5.1 Au-Si die bonding

Eutectic Au-Si based alloys in the form of thin preforms are used in limited, niche die attachment applications. Amongst metallic solders it is considered a "hard" solder and at the eutectic composition of Au-2wt%Si it has an invariant melting point of 363^{o}C. As a first step and in order to examine melting and solidification phenomena associated with commercial Au-Si preforms, a Au-Si preform in the form of a foil was heated and cooled at controlled rates in a differential scanning calorimeter (DSC). Individual preforms were heated to 400^{o}C, at 10^{o}C/min in a N_2 atmosphere. DSC heating endotherms confirmed a single melting peak between 363^{o}C and 368^{o}C, which corresponded to the eutectic temperature from the binary phase diagram previously shown

in Figure 2.11.

The bonding mechanism for the Au-Si preform, between a Si die and the metallisation on an Al_2O_3 substrate was investigated. As practised in industry, Au-Si die bonding leads to a wide variability in bond quality, and one of the main barriers to the more widespread use of the Au-Si is this perceived inherent variability. The variability is believed to be due in part to the critical scrubbing action that ruptures preform oxide films during die bonding, which is generally considered difficult to regulate/automate. The inherent variability can obscure systematic attempts to improve lifetimes and reliability. Also, it was known from prior work with GE AS that solder preform alignment and final thickness control can be difficult and the solder surface is apparently easily oxidised which compromises bond integrity. Therefore, the focus of the current work was to explore the factors controlling bonded area between the Si die, the intervening Au-Si die attach material and the Al_2O_3 substrate metallisation, to develop processing strategies to produce better quality bonds reproducibly, and then to explore the inherent variability within many nominally identical bonds formed under optimum conditions.

5.1.1 First experimental design

The first assessment of factors affecting bonded area involved an experimental design approach based on a simple two-level "low" and "high" value for each key process parameter, as specified in Table 3.3. The studied parameters were: temperature of the heating stage, force of the scrubbing head, scrubbing frequency and scrubbing time. The bonded area from all possible combinations (full factorial of 2^4 experiments) was measured, with three repeats of each combination and thus resulting in 48 distinct experiments. The same samples were then assessed for the shear load to failure, in the same way as the adhesive die bonds previously described.

Figure 5.1 shows a top view of a Si die bonded to Au metallised Al_2O_3 substrate using a thin Au-Si preform. The Au-Si alloy reacts with the edge of the Si die, giving rise to a meniscus. This is because Si around the edges of the die participates in the Au-Si soldering reaction by dissolution. The formation of the Au-Si meniscus around the Si die increases the mechanical integrity of the bond [144]. The re-solidified Au-Si solder was evident by the irregularly shaped dark-coloured region surrounding the Si die, and arises from flow of solder when pressure (load) is applied to the die.

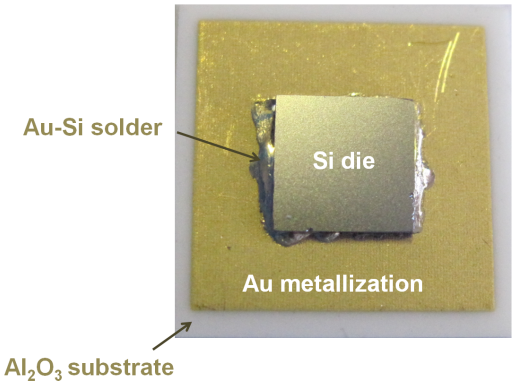


Figure 5.1: Top view of a Si die bonded to Au metallised Al_2O_3 substrate using a Au-Si preform. The darker irregular shape region around the Si die is the re-solidified Au-Si liquid.

SAM was again used to assess the bond quality of the die bonds in the interfacial region. The C-SAM apparatus used frequencies of 230 and 300MHz as described in Chapter 3. Ultrasound was directed from the top side of the Si die (through Si die/Au-Si solder/substrate) and extreme care was taken to achieve as near-identical imaging conditions as possible for every specimen. Similarly to the same procedure with the adhesive bonds, digital image analysis (DIA) measurements were again used to quantify the fraction of unbonded area in a C-SAM image, and both the percentage of unbonded area and the largest single defect (lsd) were determined.

During SAM inspection, all 48 die bonds contained unbonded areas, and these occurred primarily at the Si die/Au-Si solder interface, although there were some unbonded regions also at the Au-Si/metallisation interface.

The total percentage of unbonded area varied from 1 to 98%. The largest single defect spanned practically the whole range from 1 to 98%, thus emphasising the variability in bond quality, even when using semi-automated assembly. Figure 5.2 shows only a few SAM images from the Au-Si die attach region, with grey areas representing bonded regions and white areas representing unbonded regions. Figures 5.2(c), (e), (k) and (m) show some examples of almost completely unbonded Au-Si die bonds where the total percentage of unbonded area was 99%, 78%, 83% and 84% respectively. The accuracy of the unbonded measurements was unlikely to be better than 2%, and areas are given to the nearest 1%. There were few "good" quality Au-Si die bonds. For instance, Figures 5.2(d), (j), (n) and (p) show examples of Au-Si die bonds with unbonded areas $\leq$ 10%, with largest single defects of 1%, 5%, 1%, and 1% respectively. There was no consistency in the large unbonded area location, but there were always small unbonded areas in the central area.

Even for a nominally constant set of conditions, and consistent with the industry view of this approach, the percentage of bonded area varied from specimen to specimen, as shown in Figure 5.3. For example, specimen 6 was manufactured at 400^{o}C, 3.5g/mm^2, 3Hz and 3.5s (Table 3.3), and A, B, and C indicate repeats of the conditions so that 6A (Figures 5.3(a)), 6B (Figures 5.3(b)), and 6C (Figures 5.3(c)) were nominally identical. However, the unbonded area varied significantly between repeats: 19%, 5% and 10% respectively. Table 3.3 shows up to 9 times differences in unbonded area for otherwise constant conditions. The variation in bonded area was generally very much larger than the accuracy of the measurements.

Figure 5.4 shows the raw data distribution of total bonded area for all the 48 Au-Si die bonds. The distribution exhibited a bi-modal shape with peaks at 10-20% and 80-90% area bonded. The mean bonded area was $\approx$ 78%. Note that of the 48 die bonds, 5 had very low bonded areas in the range 0-30%, 1 bond had a bonded area between 40-50%, and 42 bonds had a bonded area

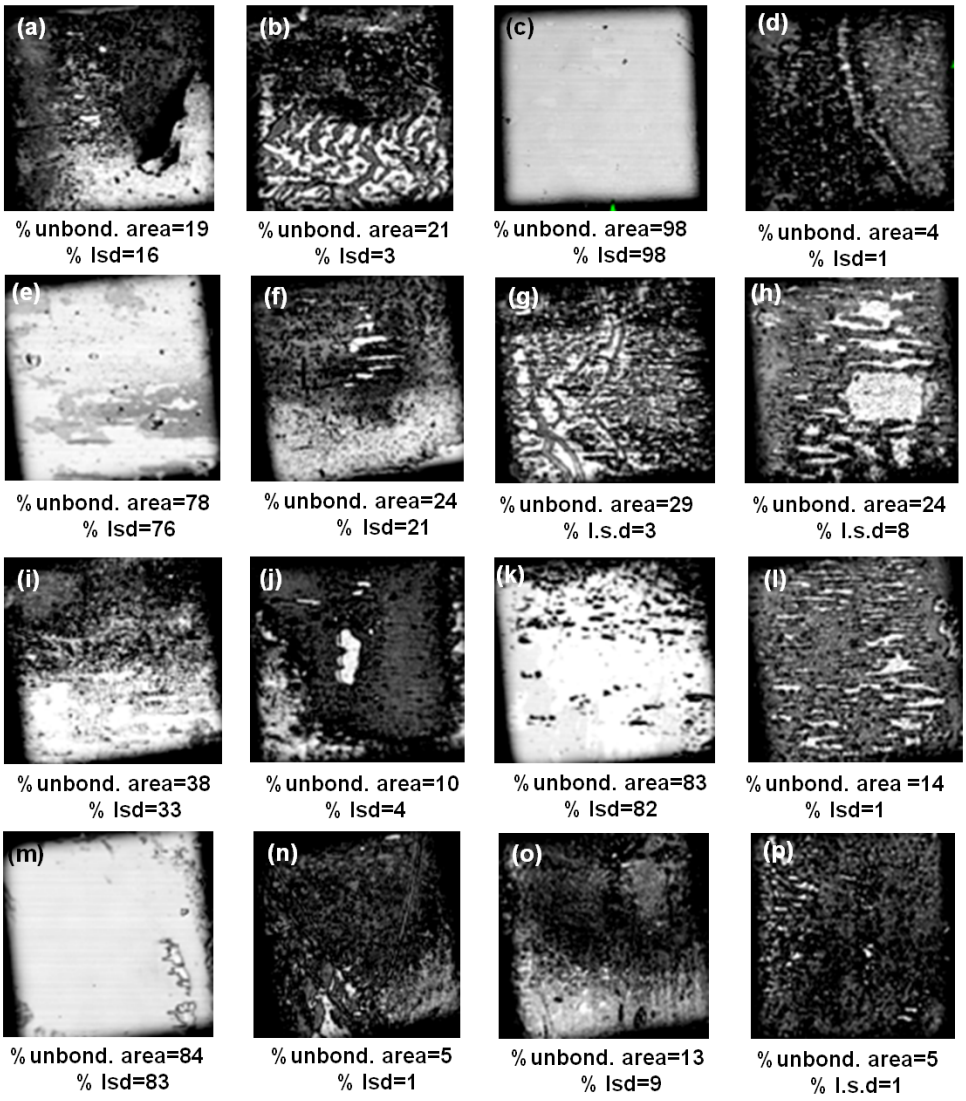


Figure 5.2: Typical SAM images of Si dies attached to Al_2O_3 substrates using Au-Si preforms, manufactured under conditions specified in Table 3.3, and corresponding percentages of unbonded area and largest single defect, (lsd).

higher than 60%. Of these, 20 bonds fell in the range 80-90% and 14 bonds had bonded above 90%.

In order to study the shear load of the 48 Au-Si die bonds, and its possible correlation with the bonded area obtained by SAM imaging and DIA measurements, die shear tests were performed using a Dage 4000 series bond tester with a 100kg load cell (details were given in Chapter 3). Figure 5.5 shows a typical curve for the shear load as a function of displacement for a Au-Si die bond. The small peaks between 100 to 300μm displacement were mainly attributed to minor cracking in the Si die, possibly around the manip-

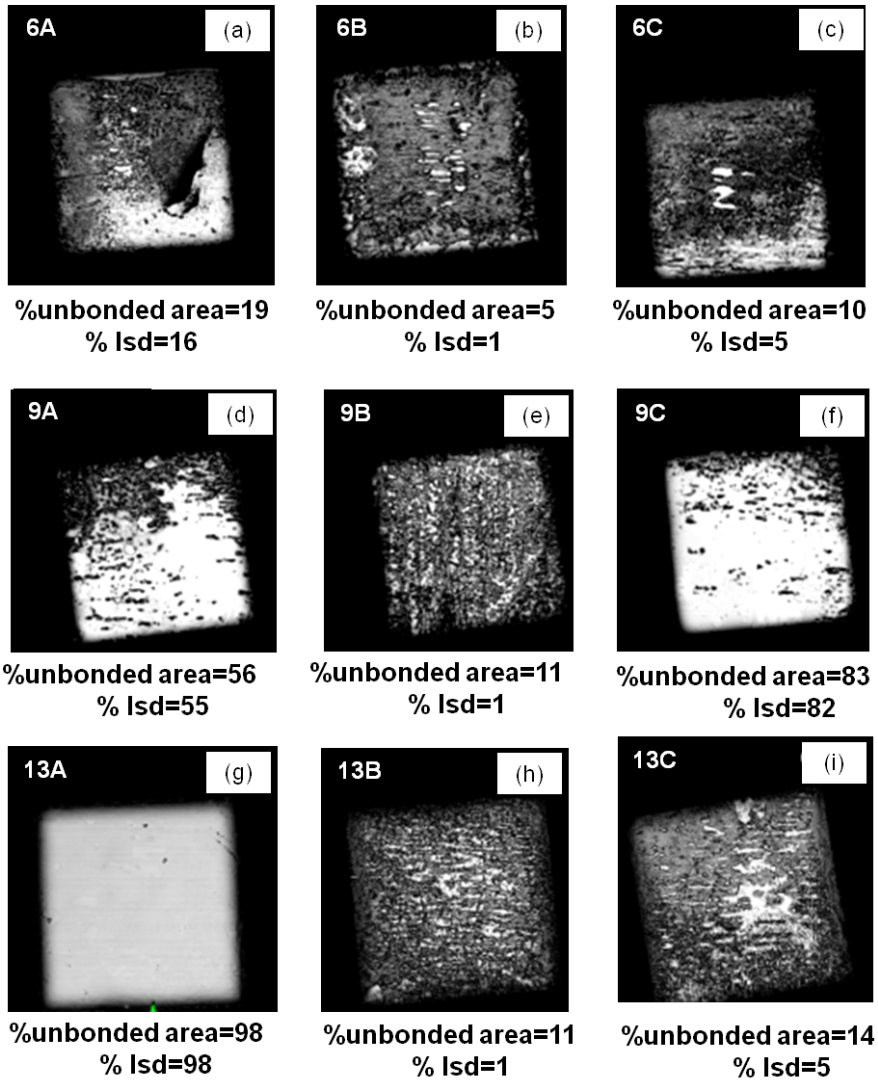


Figure 5.3: Examples of SAM images of Au-Si die bonds manufactured for a constant set of conditions, in accordance with Table 3.3 and, corresponding percentages of unbonded area and largest single defect (lsd). A, B, and C indicate repeats of the conditions so that specimens 6A, 6B, and 6C were nominally identical. The same applied for specimens 9 and 13.

ulator. All the Si dies started to crack during testing. The die bond failed at a load of $\approx$ 55kg and a displacement of $\approx 400 \mu m$. In this case, the Si die was sheared from the substrate with partial Au-Si solder attached.

Figure 5.6 shows the distribution of failure shear loads of the 48 Au-Si die bonds manufactured under the conditions shown in Table 3.3. Shear loads ranged from 5 to 75kg, with a mean shear load of 36kg and standard deviation of 17kg. Unlike bonded area, shear load followed a near normal distribution with one peak at 30-40kg (12 of the 48 die bonds fell in this range).

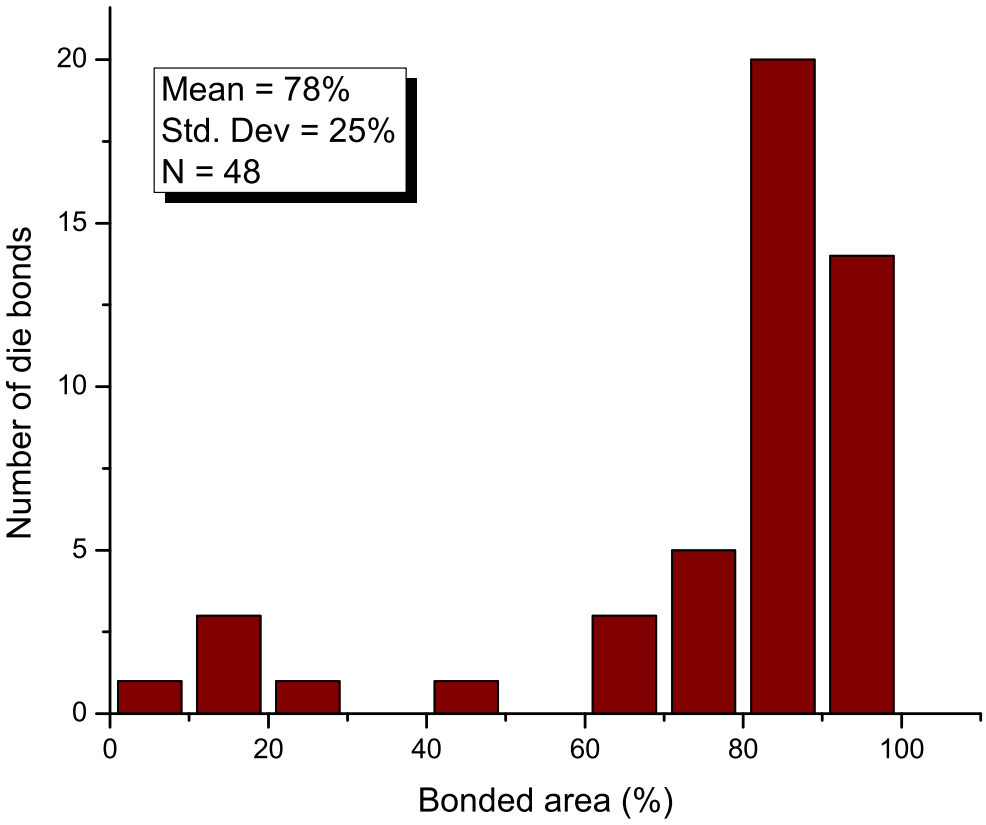


Figure 5.4: Bonded area distribution of 48 Au-Si die bonds manufactured under different 16 conditions (3 repeats) as specified in Table 3.3.

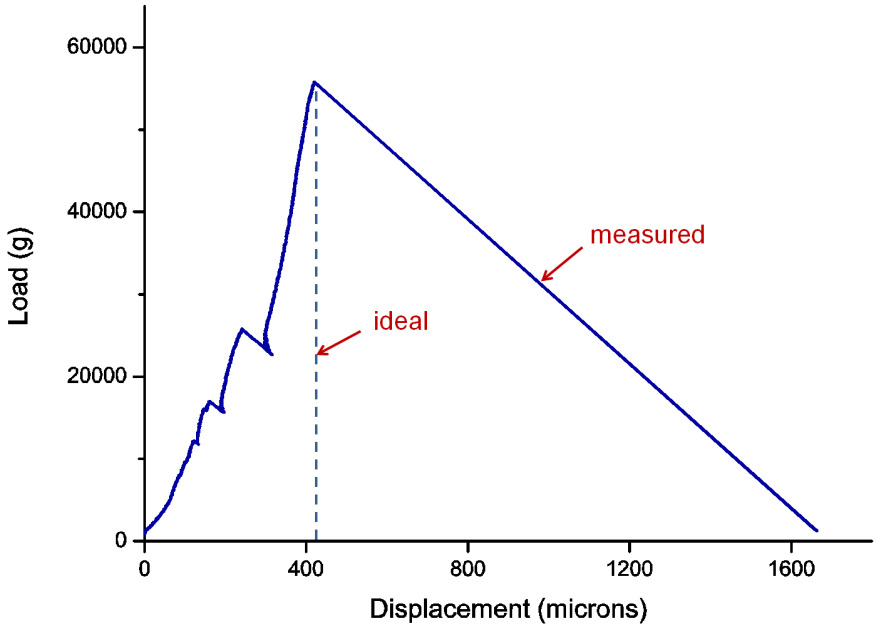


Figure 5.5: Typical load-displacement curve of eutectic Au-Si die bond. Test temperature was 25°C.

The failure mode of the 48 die bonds tested for die shear was also investigated. The failure mode was categorised as: shearing of Si die with residual

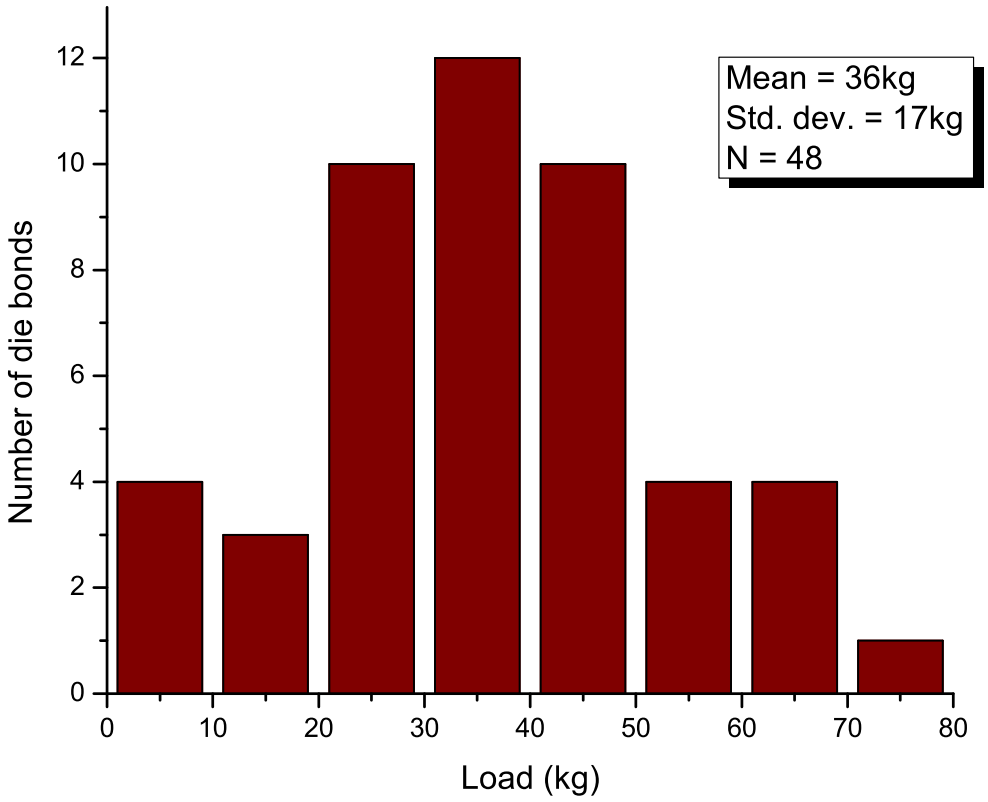


Figure 5.6: Shear load distribution of 48 Au-Si die bonds manufactured under different 16 conditions (3 repeats) as specified in Table 3.3.

Si remaining (failure mode 1); separation of die from die attach medium (failure mode 2); and separation of die and die attach medium from substrate (failure mode 3). Of the 48 die bonds tested, 39 failed under failure mode 1. However, 11 of these 39 specimens presented a combination of failure mode 1 with failure mode 2. Visual inspection of some die bonds showed that only a small part of the Si die (mainly the edges) remained attached to the rest of the package. This could be related to the presence of unbonded areas in the central area of the die bond (as previously shown in the acoustic images) forcing the Si die to lift off in that region. Of the remaining 9 specimens, the failure occurred under failure mode 2; furthermore, 5 of these specimens showed a combined failure at the die attach and substrate levels (failure mode 2 + failure mode 3). This data is consistent with SAM imaging which identified that unbonded areas were primarily located at the Si die/Au-Si solder interface and very occasionally, unbonded areas were found in the Au-Si sol-

der/substrate interface. Figure 5.7 shows an example of an Au-Si die bond after shear testing. In this case, the die bond failed at both Si die/Au-Si solder and Au-Si solder/metallisation interfaces (failure modes 2 and 3). Only a fraction of the Au-Si solder remained attached to the Au metallised substrate.

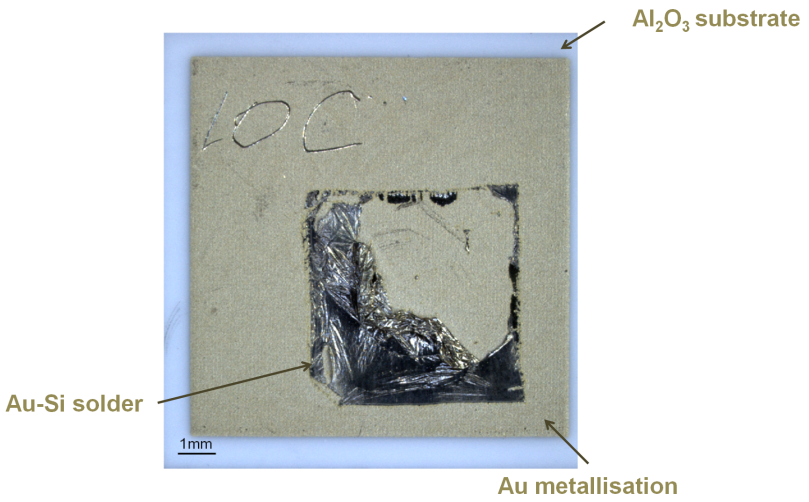


Figure 5.7: Example of a Au-Si die bond after die shear testing. The die bond failed at both Si die/Au-Si solder and Au-Si solder/metallisation interfaces; part of the Au-Si preform remained attached to the rest of the package while the rest broke off with the Si die.

Figure 5.8 shows typical plan view SEM images of fractured surfaces. The shear tool ripped out a significant fraction of Si during testing and the fracture surface was relatively flat as shown in Figure 5.8(a). Brittle fracture without any appreciable deformation was suggested. Figure 5.8(b) shows mixed failure modes. Note that both Au-Si solder and Au metallisation regions were visible.

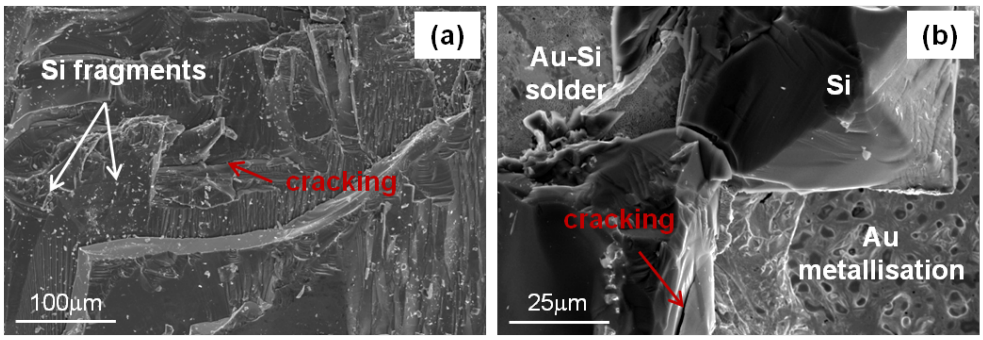


Figure 5.8: Plan view SEM images of fractured surfaces of Au-Si die bonds after die shear testing showing: (a) failure at the Si; (b) mixed failure mode.

Identifying the most influential die bonding parameters

A more detailed analysis of the experimental design approach is presented in this section. Experimental measurements of bonded area were studied by statistical analysis (ANOVA method) that calculates the mean, standard deviation, and signal-to-noise (S/N) ratio for each experiment in Table 3.3.

The S/N ratio represents the general trend of response of the percentage bonded area to each varied parameter. In this case, this ratio was calculated in the larger-the-better case (S/N_L) as bonded area was intended to be maximised, and according to:

$$S/N_L = -10\log(\frac{1}{n}\sum\frac{1}{y^2}), \tag{5.1}$$

where n is the number of observations and y is the measured bonded area. Table 5.1 presents the S/N_L ratio for each experiment which allowed ranking of the sensitivity of the measured bonded area to change in parameter.

In the case of temperature of the heating stage, the relative effects of the low temperature (400^{o}C) and high temperature (450^{o}C) on the bonded area can be obtained by subtracting the average S/N_L ratio for all the experiments using low temperature (experiments 1 to 8) from the average S/N ratio for all the experiments using high temperature (experiments 9 to 16). The same principle is used for the force of the scrubbing head, scrubbing frequency and scrubbing time. The difference between the resulting "high" and "low" S/N_L averages is given in Table 5.2. The strongest parameters influencing the bonded area of the Au-Si solder bonds corresponded to those that had the largest magnitude of difference (Δ). Table 5.2 shows that the parameter that had the greater impact on bonded area (Δ = 1.2) was scrubbing frequency as expected; the scrubbing action is very complex to regulate/automate. Force of the scrubbing head and scrubbing time had the next most significant im-

Table 5.1: Mean bonded area, standard deviation and S/N_L ratio for the Au-Si die bonds.

Experiment no.	**Mean**	**Std. dev.**	**S/N_L**
1	32	32.1	33.2
2	73	44.1	38.6
3	91	3.8	39.2
4	79	11.4	38.0
5	84	19.2	38.7
6	89	6.9	39.0
7	93	4.3	39.4
8	87	10.7	38.9
9	50	36.1	35.8
10	85	5.3	38.6
11	79	9.2	38.0
12	95	1.4	39.5
13	59	49.8	37.7
14	89	6.5	39.0
15	86	3.2	38.7
16	85	8.3	38.6

pact on bonded area (Δ = 1.1 and 0.8 respectively). The temperature of the heating stage had the lowest contribution to bonded area (Δ = 0.1).

Table 5.2: S/N_L ratio analysis of bonded area for the Au-Si die bonds. A - temperature of the heating stage; B - force of the scrubbing head; C - scrubbing frequency; D - scrubbing time.

Level	**A**	**B**	**C**	**D**
low (1)	38.1	37.6	37.6	37.5
high (2)	38.2	38.7	38.8	38.3
Δ (2-1)	0.1	**1.1**	**1.2**	**0.8**

After calculating the S/N_L ratio, the ANOVA method was used to identify the most critical parameters affecting bond quality. The level of significance (confidence percentage) was calculated for each process parameter and for the effect of any interactions between parameters. A hypothesis test using ANOVA method with linear contrast was employed. The ANOVA method

used here is standard and often used for the analysis of this type of data. Full details of the method are given in Appendix 1.

The values of *SST*, *df*, *MSS*, *F-test*, and *Alpha*, and the confidence for each parameter or combination of parameters, were compiled into a standard ANOVA table (Table 5.3). Let A be the temperature of the heating stage; B the force of the scrubbing head parameter; C the scrubbing frequency parameter; and D the scrubbing time. Table 5.3 shows *SST*, *df*, *MSS*, *F-test* for single (A, B, C, D)) and interaction of parameters (AB, AC, AD, BC, BD, CD, ABC, ABD, ACD, BCD, ABCD). The percentage of confidence (column in bold) gives an indication of the level of significance of a given parameter/combination of parameters on the bonded area of the 48 Au-Si die bonds.

Table 5.3 shows that temperature of the heating stage (A) and scrubbing frequency (C) had the lowest and the highest contribution to bond quality respectively. Although substrate temperature was initially thought critical to solder reflow, as long as the temperature was above the eutectic temperature (363^{o}C), the relative importance of temperature was low.

Although the force of the scrubbing head (B) was suggested to be high (66%), this parameter had a comparatively low influence on bond quality. The force applied must be sufficient to break the oxide layer and hold the Si die in place. Moreover, excessive force could damage the component by introducing micro-cracks. During the scrubbing action, the load force was translated into frictional heat by cyclically moving the die left to right (back and forth). Both the time for force application and additional thermal energy due to friction determined the overall extent of the solder reflow. The relative influence of force on bond quality in combination with other parameters was relatively strong. For instance, the confidence percentage for the interaction of force of the scrubbing head with scrubbing time (BD, 71%).

The influence of combination of parameters of 3rd order (K, L, M, N)

and 4th order (O) was low when compared with 1st and 2nd order effects. Factor C (scrubbing frequency) has the highest individual influence on bonded area, and was also influential in many parameter interaction. For example, confidence was comparatively low when scrubbing frequency was ignored (ABD = 10%), reinforcing the importance of scrubbing frequency.

Table 5.3: ANOVA method using the linear contrast technique to identify the parameters with the highest and lowest contribution in bond quality. *SST* - sum of squares total; *df* - degrees of freedom; *MSS* - mean sum of squares; *F* - Fisher test; *Alpha* - test probability; *Conf.* - confidence percentage.

Factor	**SST**	**df**	**MSS**	**F**	**Alpha**	**Conf.(%)**
A	0	1	0.03	0.00	0.99	**1**
B	242.46	1	242.46	2.76	0.34	**66**
C	579.90	1	579.90	6.60	0.24	**76**
D	144.46	1	144.46	1.65	0.42	**58**
E=AB	143.27	1	143.27	1.63	0.42	**58**
F=AC	3.36	1	3.36	0.04	0.88	**12**
G=AD	89.32	1	89.32	1.02	0.50	**50**
H=BC	165.54	1	165.54	1.89	0.40	**60**
I=BD	359.27	1	359.27	4.09	0.29	**71**
J=CD	401.65	1	401.65	4.57	0.28	**72**
K=ABC	52.25	1	52.25	0.60	0.58	**42**
L=ABD	2.43	1	2.43	0.03	0.90	**10**
M=ACD	5.54	1	5.54	0.06	0.84	**16**
N=BCD	26.96	1	26.96	0.31	0.68	**32**
O=ABCD	87.81	1	87.81	1.00	0.50	**50**

The boxplot in Figure 5.9 summarises the statistical measurements of the bonded area (at high and low level of each parameter) in terms of the median, upper and lower quartiles, and minimum and maximum values. In this type of plot, the box itself contains the middle 50% of the data. The upper and the lower parts of the box indicate the 75th and 25th percentile of the data set respectively. The line within the box represents the median value of the data. Note that, if the median line is not equidistant from the box upper and lower bounds, then the data is skewed. The ends of the vertical lines

indicate the amplitude of the data values i.e. difference between minimum and maximum data values. Every point outside the ends of the vertical lines are considered outliers.

Figure 5.9 shows that factor C (scrubbing frequency) at the low level (3Hz) was the parameter that introduced the greatest variability in bonded area, spanning the whole range from $\approx$ 0 to 100%, with a median of 85% and mean of $\approx$ 70%. However, at the higher setting (7Hz), the amplitude was reduced to 72 and 100%. Again, temperature of the heating stage (A) had the lowest influence. Although the amplitude was a little different when using low and A high settings, the mean and median were practically the same. Regarding force of the scrubbing head (B), amplitude also varied only a little when using low and high settings, and corresponding medians and means were 86% and 72% against $\approx$ 90% and 84%. Finally, the last two boxes show the impact of scrubbing time parameter (D) at low and high settings. In this case, the bonded area varied from $\approx$ 45% to 100% with a median of 87% and mean of 72% at the low setting, and $\approx$ 65% to 100% with a median of 90% and mean of 85% at the higher setting.

Because B, C and D (i.e. force of the scrubbing head, scrubbing frequency and scrubbing time) had a higher relative impact, their interaction was considered for further interpretation. Figure 5.10 shows the effect of interactions (BC, BD and CD), at both low and high settings, on the bonded area. The boxplot shows that interaction CD, at high setting (7Hz, 3.5s), was the one that introduced the highest variability in bonded area. Both amplitude and consequently, mean bonded area varied significantly from low to high setting. Therefore, both scrubbing frequency (C) and scrubbing time (D) were varied in the next experimental design of the optimisation bonding process. The remaining parameters, temperature of the heating stage and force of the scrubbing head, were kept constant.

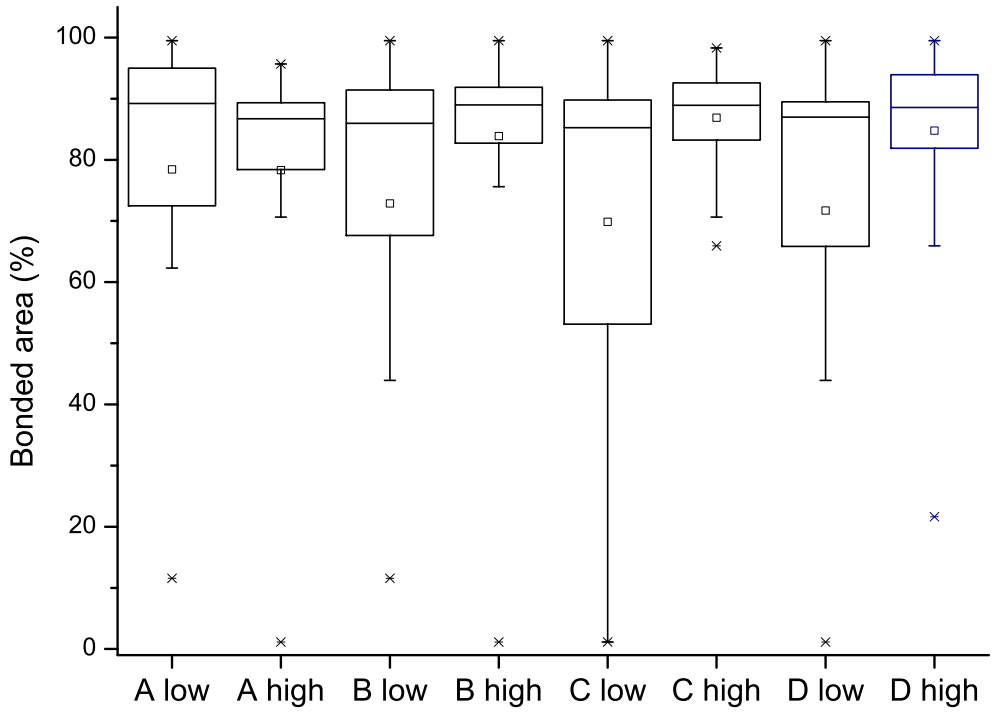


Figure 5.9: Boxplot of the parameters (A, B, C and D) influence on bonded area of the Au-Si solder bonds.

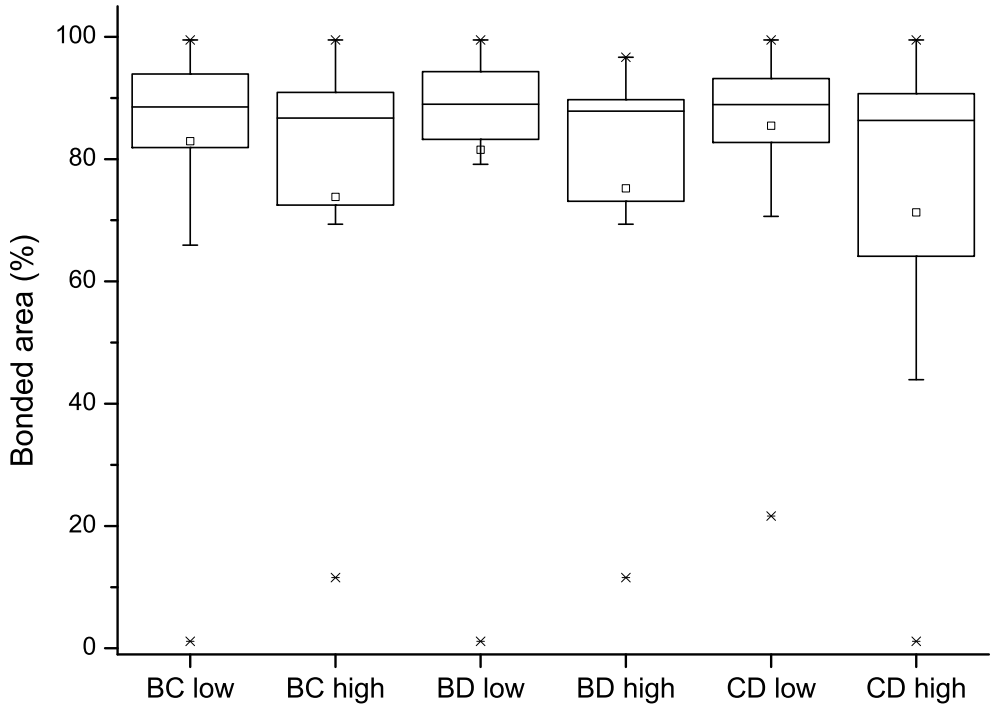


Figure 5.10: Boxplot of interaction of parameters (B, C and D) on bonded area of the Au-Si solder bonds.

5.1.2 Second experimental design

After studying the parameter effects on assessed bonded area, both temperature of the heating stage and force of the scrubbing head were kept constant at their "best" combination of 450^{o}C and 3.5g/mm^2 respectively. The subsequent more focused experimental design varied only the two scrubbing parameters. Three levels were then allocated for each of scrubbing frequency and scrubbing time. All possible combinations, in a full factorial of 3^2 set of experiment, were used to manufacture die attachments (Table 5.4). Three repeats for each combination were again undertaken, resulting in 27 separate experiments and associated measurement of bonded area by SAM.

Table 5.4: First level optimised experimental design for Au-Si eutectic die bonding: nine experiments, three-level. Temperature of the heating stage and force of the scrubbing head were kept constant at 450^{o}C and 3.5g/mm^2, respectively. Parameters under study: scrubbing frequency (S_f) and scrubbing time (S_t).

Experiment no.	S_f **(Hz)**	S_t **(s)**
1	2	1
2	2	2.5
3	2	4
4	5	1
5	5	2.5
6	5	4
7	8	1
8	8	2.5
9	8	4

SAM frequencies of 230 and 300MHz were used and the ultrasound was again directed from the top of the Si die. Near identical imaging conditions were used for each of the 27 die bonds. The percentage of unbonded area and largest single defect within the assemblies were also quantified by DIA measurements.

During SAM inspection, the whole batch of 27 Au-Si die bonds showed some unbonded area at both interfaces: Si die to Au-Si solder and Au-Si sol-

der to Au metallised substrate. The unbonded area varied from 1% to 13% across the set. The largest single defect in a single assembly ranged from 1% to 8% area. Again, only a few of the typical C-SAM images of the first level optimised Au-Si die bonds are shown in Figure 5.11, where again grey represented bonded areas and white represented unbonded areas. The acoustic images in Figures 5.11(a), (b), (d), (e), (f), (i) show very small round dark areas which could be (collapsed) voids that are below the resolution limit. In this case, there was the effect of the dark outline as opposed to the dispersed white spots characteristic of unbonded area. Because of the uncertainty in the nature of these small dark regions, only bright white areas were quantified as unbonded area in DIA analysis. Some of the bonds comprised densely packed voids as shown in Figures 5.11(b), (c), (e), (f), (h), (i), which corresponding unbonded areas of 6%, 6%, 10%, 12%, 13% and 7% respectively. The die bonds often presented a "stripe-like" structure such as Figures 5.11(b), (e), and (h). These stripe structures were possibly due to the higher scrubbing time used for these bonds. This scenario contrasts with the SAM images of Figure 5.11(a), (d) and (g) whose die bonds were manufactured at 2, 5, and 8Hz and 1s only of scrubbing time, which had unbonded areas of 1%, 1% and 5% respectively.

Figure 5.12 shows that for a nominally constant set of conditions, the percentage of unbonded area, within repeats, varied less than in earlier experiments. For example, specimens 23 and 26 were manufactured under different combination of parameters. Specimen 23 was manufactured at 450^{o}C, 3.5g/mm^{2}, 2Hz and specimen 26 at 3.5s and 450^{o}C, 3.5g/mm^{2}, 5Hz and 1s. A, B and C were repeats of the conditions so that 23A (Figure 5.12(a)), 23B (Figure 5.12(b)) and 23C (Figure 5.12(c)) were nominally identical. As examples of reproducibility (or otherwise), there was an unbonded area of 6% for 23A, 23B and 23C; the percentage of unbonded area for 26A, 26B and 26C was 1%, 2% and 1% respectively. Overall, there was a much smaller difference in

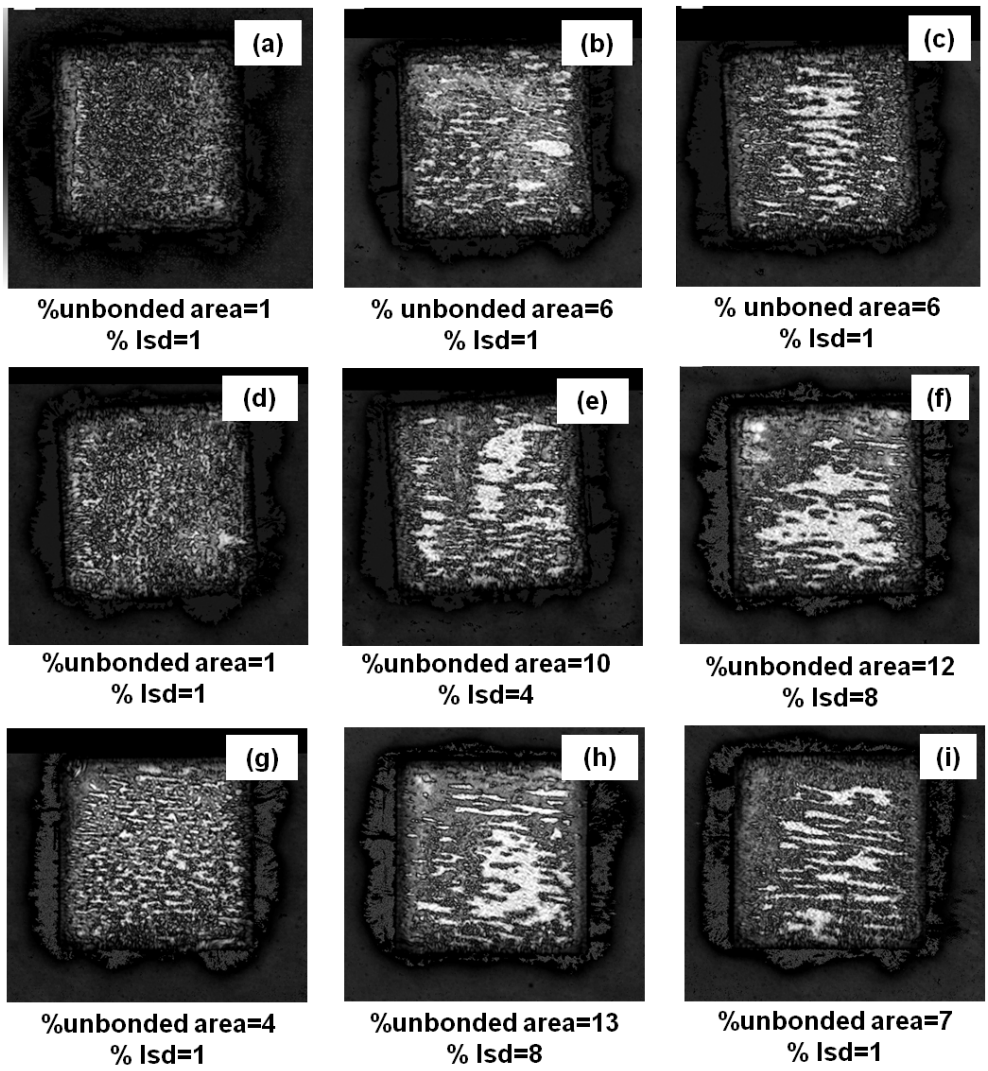


Figure 5.11: Typical SAM images of 27 Si dies attached to Al_2O_3 substrates using Au-Si preforms manufactured under conditions specified in Table 5.4, and corresponding percentages of unbonded area and largest single defect, lsd.

unbonded areas within repeats when compared with the first experiments.

Figure 5.13 shows the raw data distribution of total bonded area for all the 27 Au-Si die bonds manufactured under the conditions specified in Table 5.4. As expected, the overall bonded area increased, and was always more than 80%. The distribution exhibited a peak at 90-100% of area bonded. Only two of the 27 Au-Si die bonds had bonded areas that fell in the range 80-90%, with the rest having bonded areas close to 100%. The first experimental design (48 die bonds) yielded a mean bonded area of 78% against 95% for these second experimental design (27 die bonds). Correspondingly, there

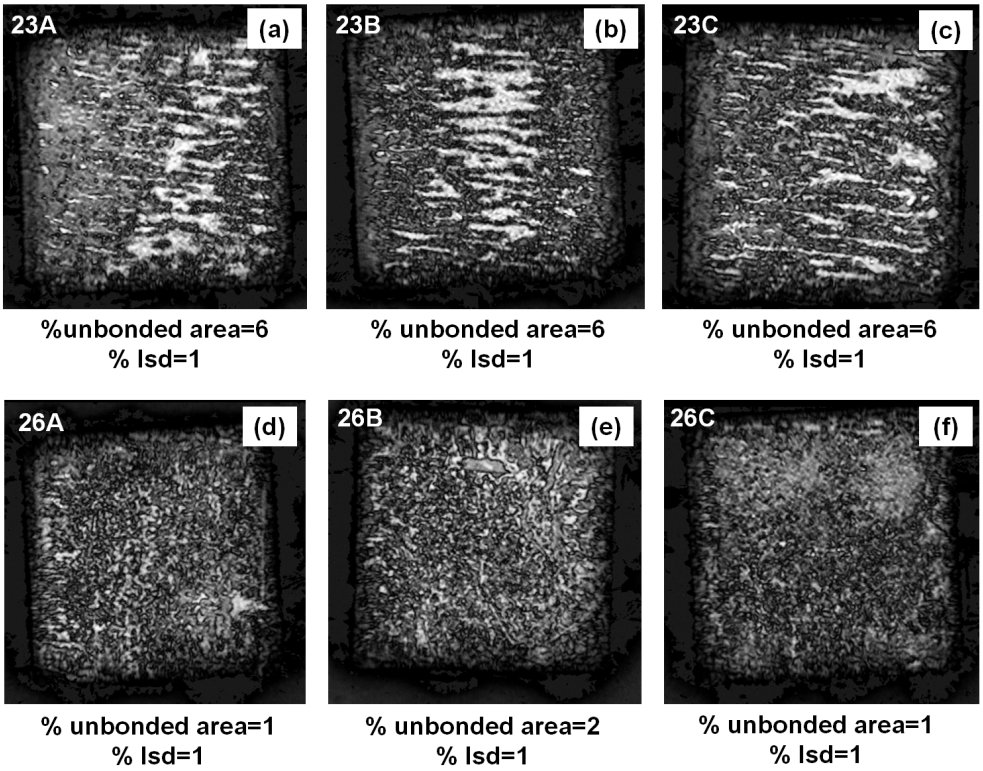


Figure 5.12: Examples of SAM images of Au-Si die bonds manufactured for a constant set of conditions, in accordance with Table 5.4 and, corresponding percentages of unbonded area and largest single defect, (lsd). A, B, and C indicate repeats of the conditions so that specimens 23A, 23B, and 23C were nominally identical. The same applied for specimens 26.

was a much reduced spread of bonded area with a standard deviation of 3% against the strong bimodal distribution in the first experiment.

The shear load to failure of the 27 Au-Si die bonds was studied together with its possible correlation with the bonded area obtained by SAM imaging. Figure 5.14 shows the distribution of failure shear loads of the bond interfaces. The failure loads ranged from 25 to 75kg, in contrast with the first experimental design (48 die bonds) in which shear load ranged from 5 to 75kg. The mean shear load increased from 36 to 44kg, with a standard deviation of 13kg. Of the 27 die bonds manufactured, 4 had die shear loads varying between 20-30kg; 8 with shear loads from 50-60 and 60-70kg; and 1 die bond with an exceptional load (70-80kg). In this case, all the 27 die bonds failed according failure mode 1, i.e. shearing of the Si die with residual Si still attached to the package. All shear strengths (kg of shear force divided by

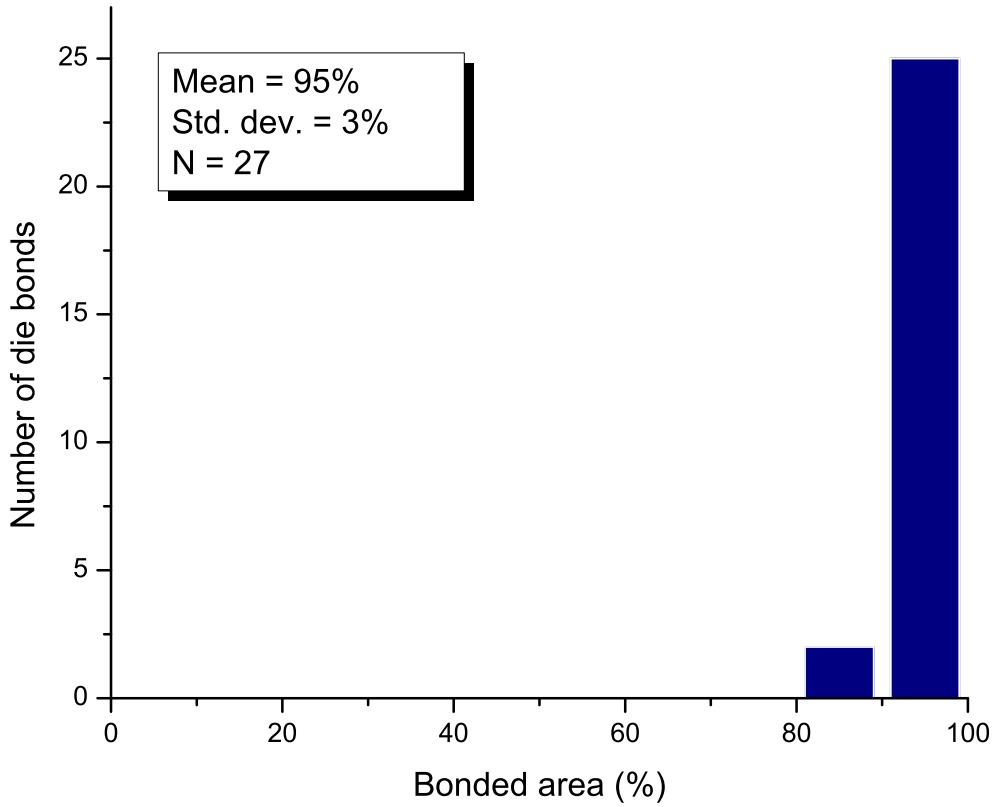


Figure 5.13: Bonded area distribution of the 27 Au-Si die bonds manufactured under 9 different conditions (3 repeats) as specified in Table 5.4.

the die area) were significantly higher than the minimum die shear strength specified in MIL. STD. 883, Method 2019.7 [94].

5.1.3 Experimental design 1 vs experimental design 2

In the first experimental design approach (batch 1), the four die bonder parameters (temperature of the heating stage, force of the scrubbing head, scrubbing frequency and scrubbing time) were varied. The subsequent more focused experimental design (batch 2), varied only the scrubbing parameters (time and frequency).

To show the overall improvement provided by the manufacturing optimisation, Figure 5.15 shows a comparison of how the bonded area increased between batch 1 (48 die bonds) and batch 2 (27 die bonds).

Figure 5.16 shows a boxplot of the comparison of bonded areas gener-

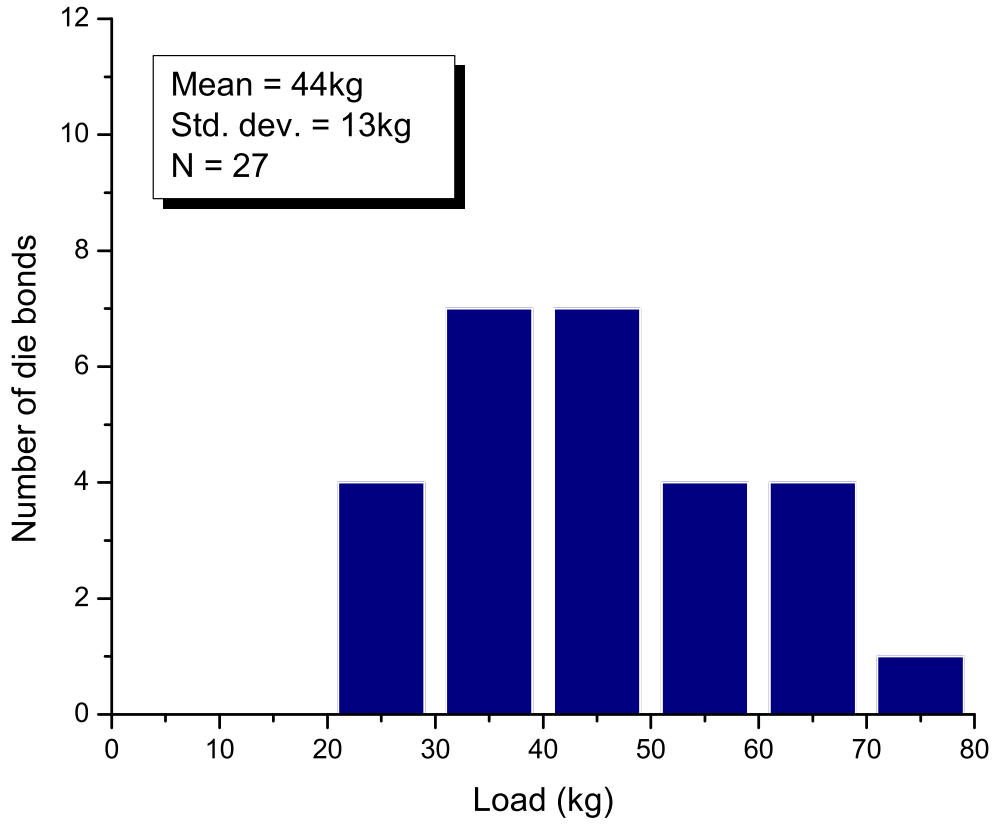


Figure 5.14: Shear load distribution of 27 Au-Si die bonds manufactured under 9 different conditions (3 repeats) as specified in Table 5.4.

ated by each batch of solder die bonds. 1st and 3rd quartiles, known as the inter-quartile range (IQR), decreased from batch 1 to batch 2. The IQR for batch 1 and 2 was 15 and 4 respectively. In addition, the extremes in the median bonded area were closer for batch 2. Skewness for batch 1 of -2.01 reduced to -0.58 for batch 2 (a negative skewness means that the lower tail is longer). Once again, points at greater distance from median than 1.5 times the IQR are plotted individually as asterisks, and are considered outliers.

Similar comparative data for failure load in shear is shown in Figure 5.17. As previously shown, batch 1 had failure loads that spanned the 0-80kg range with a peak at 30-40kg; the die bonds manufactured in batch 2 failed at shear loads of 20-80kg, with a peak at 30-50kg.

A boxplot for failure loads, for both batches 1 and 2 is shown in Figure 5.18. The IQR for each batch were similar at 21 and 23 and extreme values

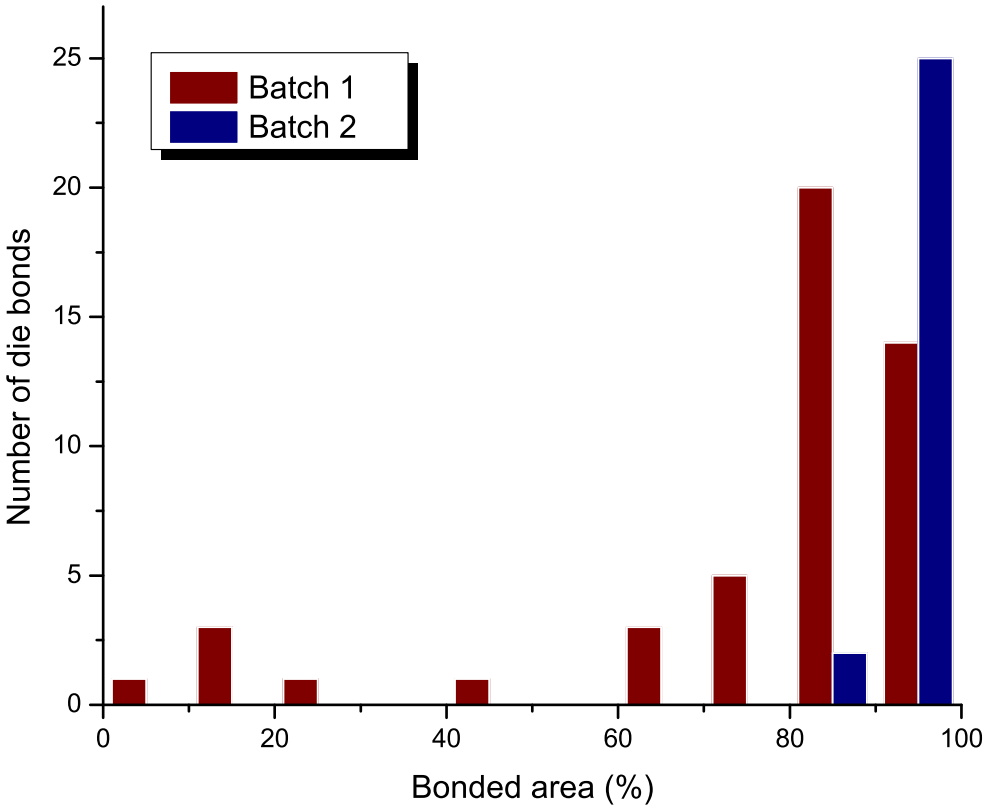


Figure 5.15: Bonded area distributions comparing the Au-Si die bonds from batch 1 (48 specimens in the first experimental design) with batch 2 (27 specimens in the second experimental design).

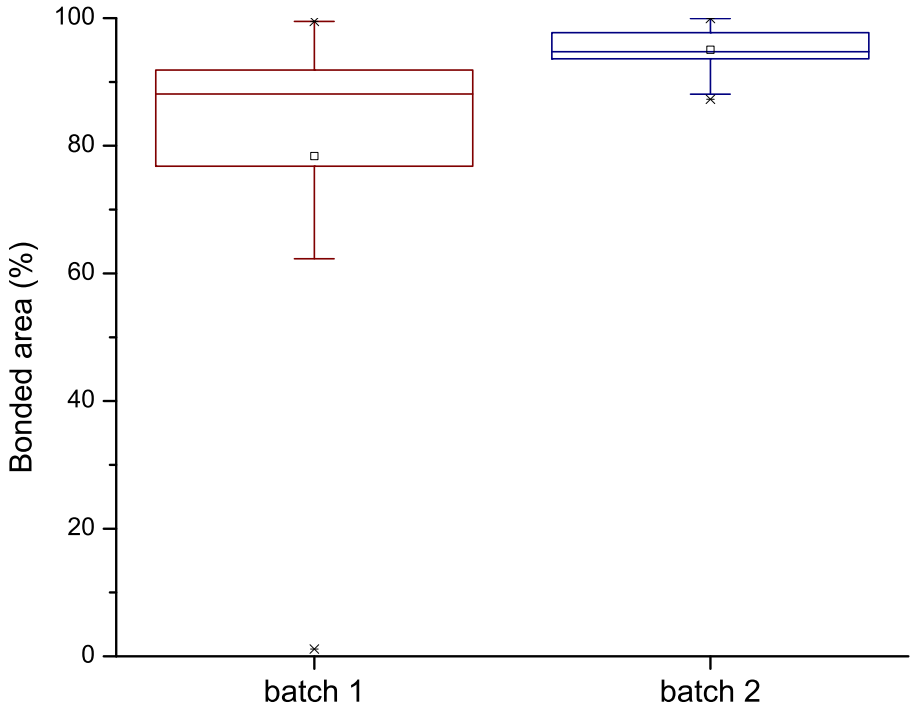


Figure 5.16: Boxplot of batch 1 (48 specimens in the first experimental design) and batch 2 (27 specimens in the second experimental design) for bonded area.

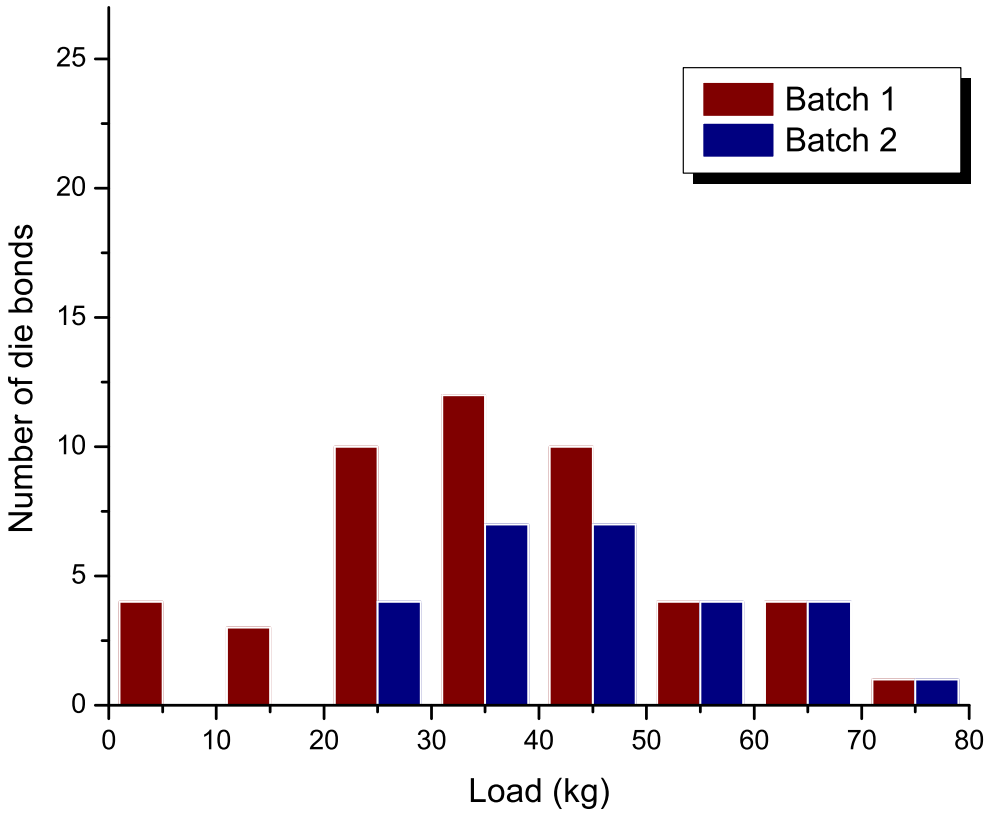


Figure 5.17: Shear load distributions comparing the Au-Si die bonds from batch 1 (48 specimens in the first experimental design) with batch 2 (27 specimens in the second experimental design).

to the median bonded areas were only a slightly closer in batch 2. Skewness for batch 1 of 0.03 increased in batch 2 to 0.37, indicating a bias to failure loads above the mean. However, note that 50% (inside the box) of the die bonds in batch 1 had loads varying from 25 to 47kg and in batch 2 had loads varying from 33 to 56kg which is an indication that higher loads were needed for failure.

Figure 5.19 shows a plot of the shear load to failure as a function of the bonded area. Although batch 2 showed a much narrower distribution of bonded areas, this was not convincingly correlated to failure load, although there were no failures lower than 20kg. For batch 1, failure load was weakly linked to bonded area, with both very high and low failure loads possible for almost any bonded area. Therefore, while this second stage optimisation has been shown to effectively reduce bonded area variability, this was only weakly

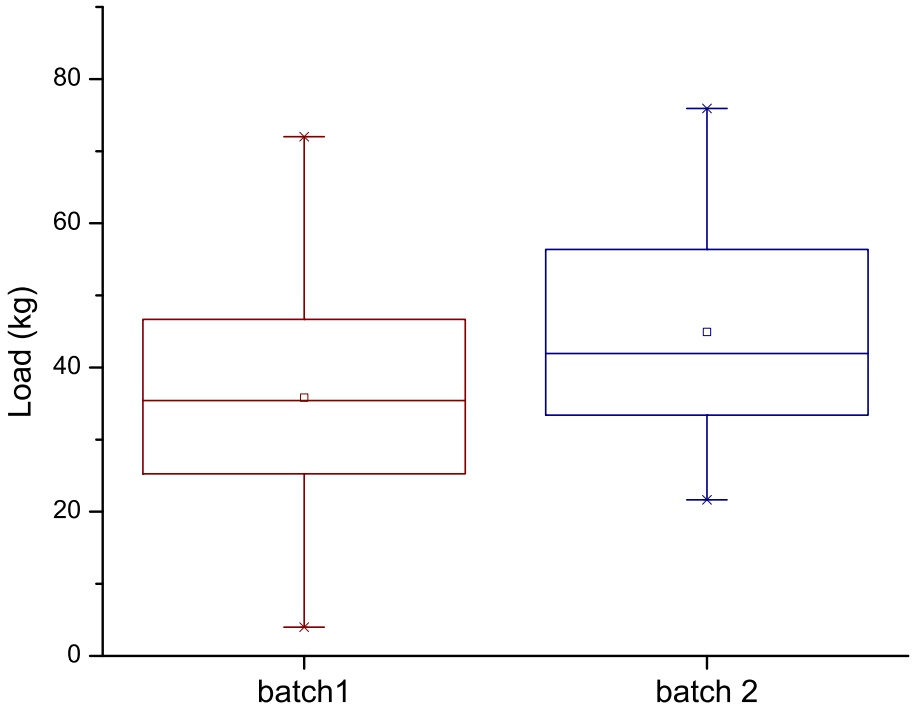


Figure 5.18: Boxplot of batch 1 (48 specimens in the first experimental design) and batch 2 (27 specimens in the second experimental design) for failure load.

manifest in failure behaviour.

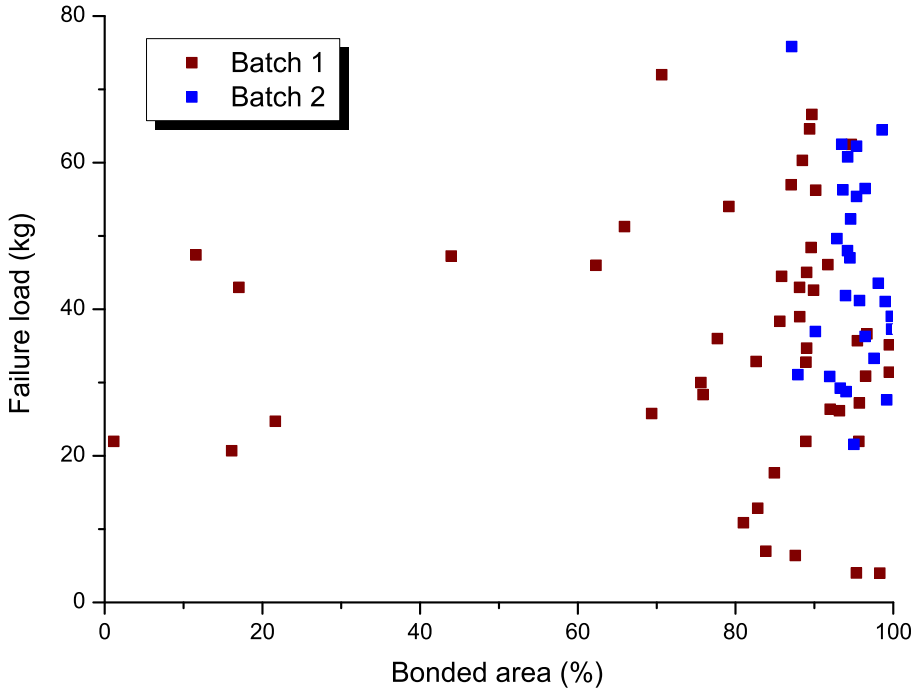


Figure 5.19: Failure load versus bonded area for batch 1 (48 specimens in the first experimental design) and batch 2 (27 specimens in the second experimental design).

Figure 5.20 summarises the effects of the most critical eutectic die bonding parameters of scrubbing frequency and time on bonded area. If the

scrubbing time is too long, or too higher frequency, then the bonded area reduced. This behaviour was qualitatively consistent with the following proposed scenarios that build on current understanding of the Au-Si die attach system:

i) Surface oxide and contamination at the various interfaces must be disrupted for a high area bond to result. Because of the thermodynamic stability of SiO_2, the Si die as-received can be expected to have an oxide layer. Similarly, the Si in the Au-Si preform may provide a thinner SiO_2 surface layer. Scrubbing of the die, during the die bonding process, helps rupture and redistribute the oxide layers, as well as helping in removing any other contaminants, so that "clean" Au-Si, Au and Si surfaces can be exposed for bonding [87].

ii) It was important not to undermine the planarity of the Si or substrate by over scrubbing. Die/preform/substrate alignment should entail more than positional and angular offset in plan view, and should concern ensuring horizontal alignment and equal spacing - a slightly tilted die will preferentially load or unload different areas of the interfaces. If the interfaces become highly non-parallel, then stress and strain can be expected to be concentrated in regions of interface proximity.

iii) Additional oxidation by too hot or too long thermal exposure must be avoided. Prolonged exposure at high temperature prior to bond completion can be expected to promote oxide, perhaps "faster" that it can be cleaned by scrubbing, and will also increase subsequent room temperature residual stresses in the bond when it cools.

iv) Excessive frictional heat can undermine bonding. The Si contained in the Au-Si eutectic die bond again runs the risk of being oxidised [139]. According to Mayer's model [145], the oxidising mechanism of Au-Si is that Si readily diffuses through the Au to react with ambient oxygen at

the interface. The Au-SiO_2 interface itself is largely unaffected by the inward diffusing oxygen because of the low solubility of gaseous oxygen in Au [145], and the SiO_2 simply continues to grow.

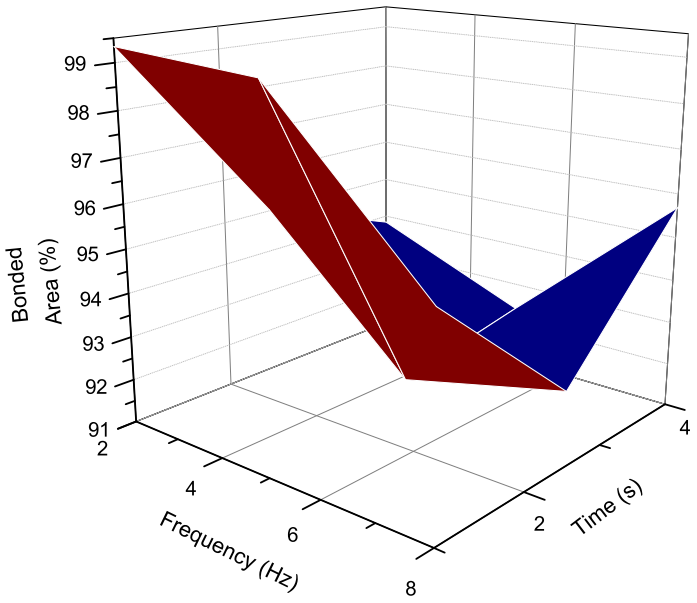


Figure 5.20: Effect of scrubbing frequency and scrubbing time on the assessed bonded area of Au-Si die bonds from batch 2 (27 specimens). The estimated error in the bonded area measurements is 2%.

Figure 5.21 shows the synergistic effects of scrubbing frequency and time on shear load to failure.

To summarise, the optimum die bonding conditions for Au-Si eutectic with bond quality maximised were:

(i) temperature of the heating stage - 450^{o}C;

(ii) force of the scrubbing head - 3.5g/mm^{2};

(iii) scrubbing frequency - 2Hz; and

(iv) scrubbing time - 1s.

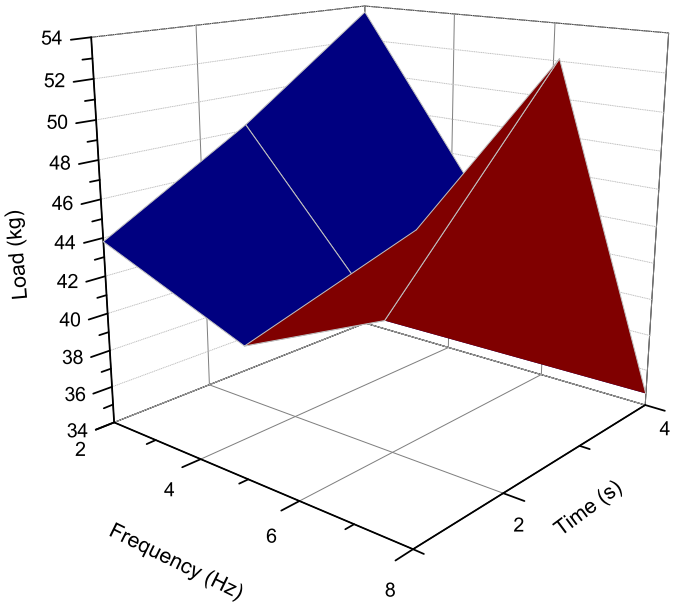


Figure 5.21: Effect of scrubbing frequency and time on failure shear for bonds from batch 2. The estimated error in the shear test measurements is 0.5kg.

5.2 Bond quality variability

After die bonding optimisation, the solder bonds using commercial Au-2wt%Si preforms to bond Si dies to Al_2O_3 substrates retained a reduced but significant variability in terms of bonded area: (1) unbonded areas were still present at both interfaces (Si die/Au-Si preform and Au-Si preform/substrate) during the bonding process; and (2) bonding was non-uniform and very occasionally non-existent. The inherent variability of the Au-Si die bond quality has been shown, in particular, to be sensitive to the scrubbing action itself, and was assumed the primary, ongoing source of variability in bond quality. In order to understand this issue further, it should be considered if the scrubbing is needed to break the oxides on (i) the Au-Si preform; (ii) the Si die; (iii) the Au metallised substrate or (iv) at all interfaces? Also, the lack of adherence of Au-Si is suggested due primarily to surface segregation and compound formation of surface contaminants, notably O, C and Si [146], and these should be considered for further study.

To achieve an acceptable Si die bond, the preform should wet perfectly

two surfaces: the upper, back of the die and the lower, metallisation on the substrate. In reality, the bond was often non-continuous and voids remained. This incomplete or non-wetting essentially caused most of the adverse effects related to die bonding. Poor bonding at these interfaces itself manifests in package related failures of poor mechanical adhesion and high electrical resistance [88].

In this section, a more detailed examination of the metallurgical and environmental interactions at the interfaces was conducted. Si dies, Au-Si preforms and Au metallised Al_2O_3 substrates were all analysed. Cross-sections of interfaces were examined metallographically, and XPS, EPMA and WDX were used to characterise the various surfaces and interfaces.

5.2.1 Au-2wt%Si preforms

The Au-2wt%Si preforms used for die bonding have at least two drawbacks. First, regardless of the inertness of Au, scrubbing is still needed to ensure that Si dies adhere or bond to the Au metallised substrates. Second, voids of significant size are created in the preform surface when the preform melts on the application of temperature and frictional heat [146].

The adhesion of a die to a substrate by eutectic bonding is dependent on the ability of the Si on the back of the Si die to react with, and be wetted by the eutectic liquid. In the simplest case, the wettability of the surface can be assumed to be defined by the contact angle [86] (Figure 5.22). The contact angle θ is determined by the free surface and interfacial free energies of the system (surface tension). The surface tension of Au is higher than that of Si. At 1450^{o}C, the surface tension of Au-Si alloys decreases monotonously from $\approx$ 1.1N/m for Au to 0.7N/m for Si [147].

The case of a liquid drop in equilibrium with a surface is shown in Figure 5.22 and θ is the characteristic angle that is defined by the balance of

the surface energies of that system.

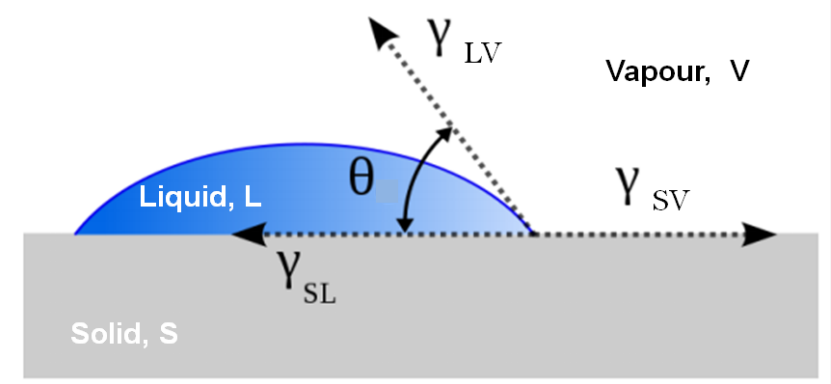


Figure 5.22: Schematic of a liquid drop in equilibrium with a surface. γ_{SV} is the surface energy of the solid-liquid interface, γ_{SL} is the surface energy of the solid-liquid interface, and γ_{LV} is the surface energy of the liquid-vapour interface.

Young's equation relates surface energies to the contact angle by [86]:

$$\gamma_{SV} - \gamma_{SL} = \gamma_{LV} \cos\theta, \tag{5.2}$$

where γ_{SV} is the surface energy of the solid-liquid interface, γ_{SL} is the surface energy of the solid-liquid interface, and γ_{LV} is the surface energy of the liquid-vapour interface. A lower contact angle means better wetting of the solid and thus, a greater tendency to adhesion. When θ equals zero, the liquid spontaneously and freely spreads across the solid surface at a rate depending on the liquid viscosity and the surface roughness [86]. This situation occurs when:

$$\gamma_{SV} > \gamma_{SL} + \gamma_{LV}. \tag{5.3}$$

Spreading of a liquid on a surface when $\theta > 0$ is possible only with the application of force to the liquid. Any oxide or contamination on the back of the Si die can lower the surface energy by as much as two orders of magnitude [86]. From Equation 5.2, θ will then become very large. Thus, a contaminated surface, depending on the element/species, can (and usually does)

become increasingly difficult to wet [86]. Elements which tend to promote wetting are "reactive" and tend to react vigorously with liquid solder.

In order to "simulate" eutectic die bonding (in-house) manufacturing, the same materials in the die bonding optimisation were used. Samples were prepared making use of a bare-faced Si die (4.62mm $\times$ 4.64mm) bonded to a Au metallised Al_2O_3 substrate (10mm $\times$ 10mm) using a Au-Si preform (nominally 2% by weight Si, 5mm square, 25μm thick). The die bonding was performed using the methodology shown in Figure 5.23. The bonding procedure consisted of:

(i) The Au-Si preform was placed on top of the substrate, in a furnace (air atmosphere), set at the optimum temperature of 450^{o}C;

(ii) The Si die was placed in contact with the Au-Si preform on the substrate, and manually scrubbed with tweezers (to promote wetting, experiments showed no adhesion was possible without scrubbing) by exerting motion, back and forth, and pressure on top of the Si die;

(iii) the package formed was removed and cooled to room temperature.

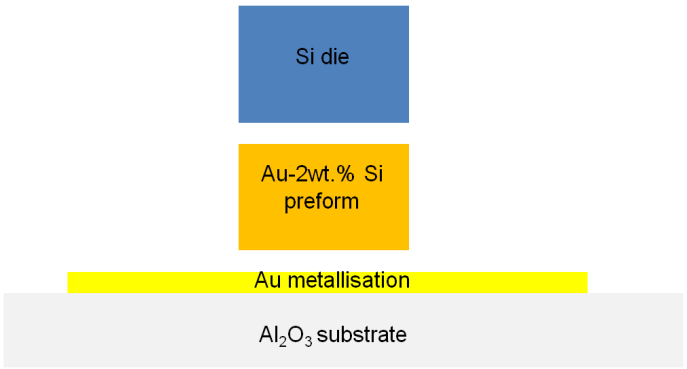


Figure 5.23: Arrangement for bonding a Si die to a Au metallised Al_2O_3 substrate using Au-2wt.%Si.

The principles governing the bond formation are simple: the bonding temperature need only exceed the Au-Si eutectic temperature (363^{o}C) for a brief period, liquid will start to form at the interface. The penetration will be

given by the rate of dissolution of the Si in the melt at the peak temperature (450^{o}C) [148]. In practice, the bonding method can be more complicated due to some secondary features. If wetting was relatively easy (i.e. there was no intervening oxide layer), Si from the die would simply interdiffuse with the fraction of Au-Si eutectic in the preform to form more eutectic liquid according to the lever rule. However, in this thesis, without scrubbing there was no type of bond and no evidence of mixing after 2 mins of contact under load. This difficulty in producing any bond even on "clean" Au-Si preforms suggested that the Au-Si preform easily formed a thin oxide layer. The bonding method must either reduce, dissolve, or disrupt the oxide in order that the alloy bonding can occur.

In order to gain better understanding of the nature of the oxidised surface and how it affects bonding, XPS was performed to examine clean surfaces of Au-Si preforms. Similar investigations of the oxidation of the Au-Si preforms (i.e. after the experiments described above) were carried out for the purposes of comparison.

The XPS spectrum obtained from the surface of the Au-Si preform before heating, i.e. in the as-received condition, is shown in Figure 5.24. Of particular importance is the large peak shown in the inset as Au 4f (Au 4f7/2 peak at 84eV, and a Au 4f5/2 peak at 88eV). This peak exhibited two distinct shoulders on the high binding energy side. The spectral line corresponding to the Si 2p peak, at approximately 105eV, indicated Si in oxide form [149]. Note that C, O, Cu and other impurity peaks were also detected at the surface of cleaned Au-Si preforms. For instance, the relatively strong C peak in the XPS spectrum could be due to handling. An image of the preform placed on the Au metallised substrate is shown on the bottom right side in Figure 5.24, with a shiny surface in the as-received condition.

Similar XPS analysis was conducted on a Au-Si preform immediately

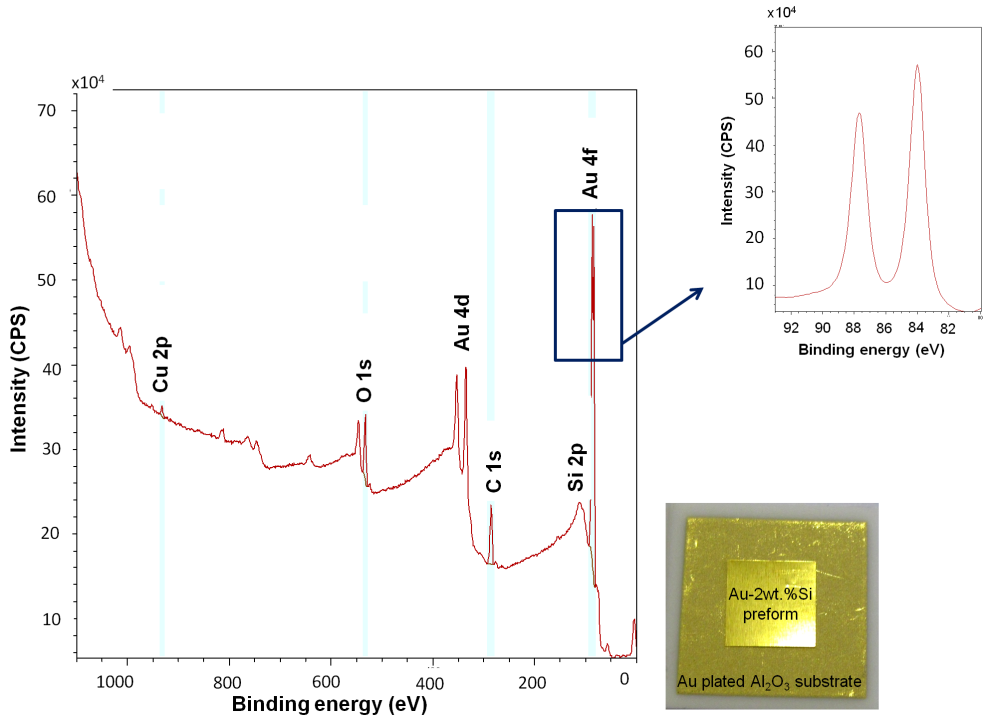


Figure 5.24: XPS spectrum of the Au-2wt%Si preform in the as-received condition. Top image shows the Au XPS peak in detail; bottom image shows the aspect of the examined preform.

after the bonding experiment described above, as shown in Figure 5.25. The binding energy of the Au 4f peaks did not shift but became of much lower relative intensity. The Si 2p peak shifted to a lower binding energy ($\approx$ 100eV) and broadened. This Si peak structure, when combined with the comparatively intense O peak at approximately 540eV, is characteristic of SiO_2 [149]. Furthermore, an intense C 1s peak at $\approx$ 290eV was characteristic of a carbide [146]. C surface segregation is apparently independent of material preparation process. Gray [146] already showed using Auger Electron Spectroscopy (AES) that for a Au-2wt%Si melted preform, both commercial and specially prepared "carbon free" material, C as well as O and Si segregated to the surface after melting. Other surface segregated impurities, particularly P, S, Ca and N were also present in the XPS spectra, which is in accordance with literature [146]. An image of the Au-Si preform is shown on the top right side of Figure 5.25, which was now dull and wrinkled due to oxidation.

An approximate quantitative analysis for the as-received and after

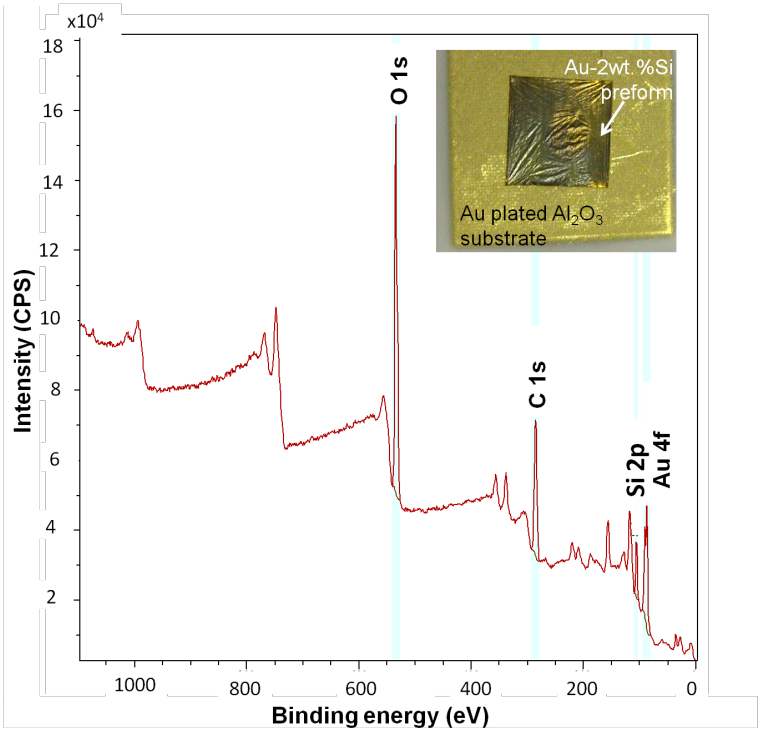


Figure 5.25: XPS spectrum of the Au-2wt%Si preform taken immediately after the sample was heated up to 450^{o}C. Image of the Au-Si preform, placed on top of the Au metallised substrate, after the bonding experiment exhibiting signs of oxidation and no evidence of bonding.

heating up to 450^{o}C preforms is presented in Table 5.5. The atomic concentrations are obtained by measuring the XPS peak area [150] and using peak area sensitivity factors [149,151]. The sensitivity of the technique is $\approx$ 0.1at% depending on the element. In addition to Au, a large concentration (57.2at%) of C and a surface oxide (SiO_2) were present on the as-received surface, along with a small amount of Cu. Although it was also possible to find traces of Ca in the preforms, its presence was not widespread [88], and Ca like many elements has been suggested to segregate to the surface during heating [88]. As the preform was heated to higher temperature, the Au concentration at the surface was reduced whereas the Si concentration increased. Also, the "organic" contamination evidenced by the C content was reduced (45.9at%).

The Si in the Au-Si solder must be supplied by the dissolution of the Si during the Au-Si solder reaction and the maximum amount of dissolved Si is limited by the equilibrium concentration of Si in Au at 450^{o}C, which

Table 5.5: Estimated atomic concentrations of various surface species obtained from the Au-2wt.%Si preforms, as determined by XPS in the as-received condition and after heating up to 450^{o}C.

Species	**As-supplied (at.%)**	**After heating (at.%)**
C 1s	57.2	45.9
O 1s	19.5	41.3
Cu 2p 3/2	0.5	-
Au 4f	22.8	2.2
Si 2p	2.1	10.6

in turn controls the volume fraction of eutectic formed on cooling to room temperature.

Si wafers typically have an oxide thickness of approximately 1.5nm. A 10s dip in 10:1 HF removes oxide, and the regrown oxide thickness one minute after removal from the HF is approximately 0.6nm [152].

Unless the contaminants which normally exist at the bonding interfaces are scavenged, or can be contrived to take part in the bonding process itself, one would expect non-uniform adhesion when Si dies are bonded to their substrates using a melted preform material procedure [146].

Furthermore, the actual bonding conditions must ensure a uniform or even simultaneous dissolution of the oxide and penetration of the Si over the entire area of the Si die. Relatively weak areas of the oxide are penetrated first, and can become alloyed much more deeply than adjacent areas [148]. One way of minimizing the native oxide and the accumulation of carbonaceous contamination is by depositing a layer of "pure" Au on the back of the Si die thus providing a greater margin for attachment to backside surface. Nevertheless, for example, depositing 200nm of Au thick film onto clean Si wafers, subsequent heating produces a 100nm thick SiO_2 on the surface of Au within 10nm. Therefore, rapid and extensive diffusion of Si through Au film to the surface will occur with subsequent oxidation (this diffusion is significantly faster for the Si (100) face than (111) face [152]). Another option

to ensure that the back of the Si die does not suffer from "wet-out" problems during die bonding is to include a barrier metallisation between the Au and the Si which inhibits diffusion prior to die bonding but which breaks down readily in the bonding process [86].

To sum up, at the die bonding temperature, in an ambient atmosphere (which is not reducing), an oxide layer is expected to form at all surfaces of the preform thus apparently inhibiting liquid flow and wetting, and confirms prior thinking that it is oxide break-up that lies at the heart of bond quality in this system.

5.2.2 Au metallised substrate

Poor bonding may occur not only at the Si die/Au-Si preform interface, but also at the Au-Si preform/metallisation interface. Since solder wetting is a surface interaction process, characterisation of the surface finish is important in solderability studies. Therefore, the chemistry and morphology of the Au metallisation on the Al_2O_3 substrate were studied.

A. Composition

In electronic circuits, a primary goal is always to minimise voltage losses in the current carrying connections, and that the electrical properties of connectors do not change with time. In these respects, Au is often chosen in high value electronics for use in harsh environments. Au thick film metallisation is a common method for producing conducting connections on alumina carriers or substrates.

Thick film metallisation usually is composed of: 1) metal micro-powders; 2) inorganic binder (such metal oxides); and 3) fugitive organic vehicle (carrier). During the initial drying process (at approximately 150^{o}C) after the printing of the paste to form a thick film on the substrate, most of the organic

vehicle evaporates and the paste is a mixture of metal powders and inorganic binder. At 850^{o}C (recommended temperature for best adhesion on Al_2O_3 substrates [153]), a solid metal thick film forms through molecular/atomic diffusion at the micro-powder boundaries while the inorganic binder molecules migrate to the Au/Al_2O_3 interface (under the influence of gravity and capillary action) forming reactive binding chains at the interface [153]. The adherence of such thick films is a function of the degree of interfacial bond formation and microstructure development during firing [154]. In addition to providing high electrical conductivity, the fired conductive layer has to adhere firmly to the substrate on which it is printed and that layer in turn then needs to be capable of accepting the solder.

The metallised Au thick film on the substrates used in this thesis were characterised by SEM and Figure 5.26(a) shows a plan view of the fired Au thick film. The metallisation consisted of an open Au network typified by neck formation between Au particles (initial stages of sintering), with pores in the Au "matrix". A higher magnification SEM image in Figure 5.26(b) highlights the porous structure of the film. There were significant isolated pores but they were no longer interconnected. Pores varied from 1.2 to 8μm in size. Figure 5.26(c) shows a cross-section SEM image of the Au metallised substrate. The Au-rich thick film was not continuous, containing large holes (approximately 4μm) through the metallisation layer. The Au film was approximately 10μm thick. If the Au is too thin, the resulting bond will not be very strong and if the quality of the Au metallisation is poor, the whole surface may be depleted in Au. This is a particular risk where the Au is incorporated together with tiny glass particles in a "thick film" conductor. The glass layer in the thick film wets both the metallic content of the paste and the Al_2O_3 substrate. The main function of the glass in a thick film is: (i) to enhance the adhesion between the thick film and the substrate, and (ii) to maintain cohesion among the metallic particles [155]. The preferred microstructure after firing encom-

passes a low porosity metal layer at the top, a thin glass layer between the substrate and the metal layer, and a rough glass-metal interface, essential for high adhesive strength [156]. Although glass is commonly used as a binder in conductive thick films, it is not conducting and the resulting thick film usually is comparatively high in porosity [155]; they are however comparatively cheap and robust.

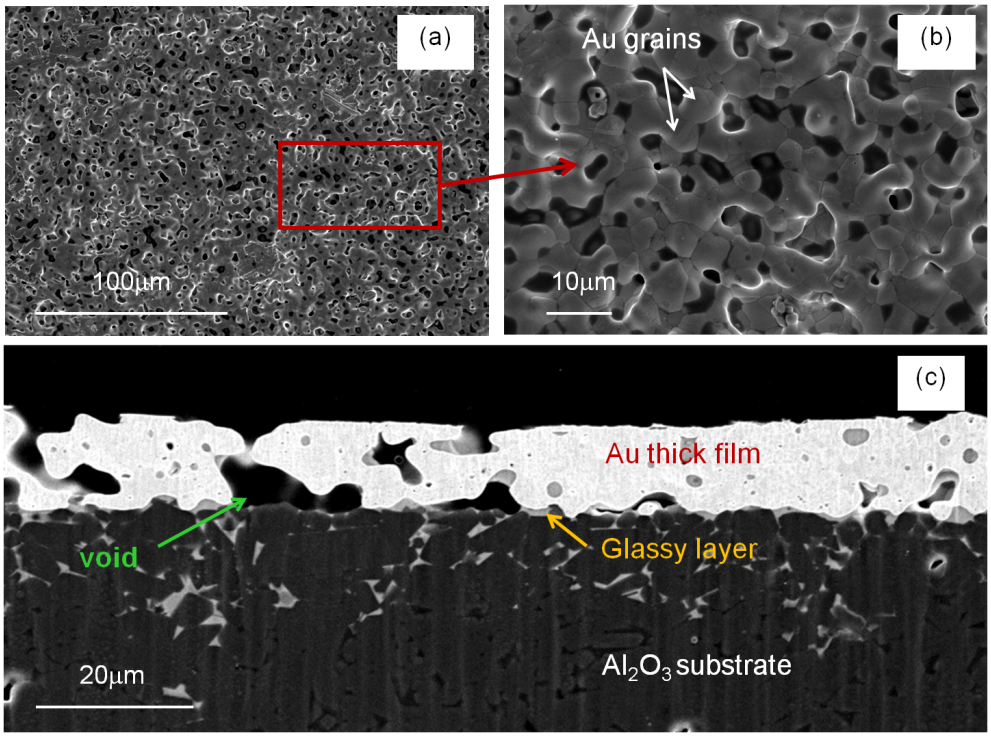


Figure 5.26: SEM images of the Au thick film on the Al_2O_3 substrate used for the Au-Si eutectic die bonding: (a) plan view of the Au thick film fired at 850^{o}C for 60min; (b) higher magnification image of the Au thick film; and (c) cross-section of the Al_2O_3 substrate as-received.

The glass phases present on the metallisation surface are important because they will be involved in developing the interface between the thick film Au and the ceramic substrate. Good adhesion can be obtained by having the fill material soluble in the substrate material, thus forming an interfacial diffusion zone. In order to study the chemistry of the surface of the Au thick film metallisation, surface analysis using XPS (Figure 5.27) was conducted. The resulting spectrum in Figure 5.27(a) indicated a strong Au 4f peak, and evidence of "organic" contamination and C. Carbides can form effective bar-

rier layers to diffusion and reaction [157]. The film contained traces of Bi, Ag, Cd and Cu. The same analysis was carried out after Ar ion bombardment of the surface under vacuum and the corresponding spectrum is shown in Figure 5.27(b). The only major difference was the lower organic contamination, depicted by a weaker C peak, and the Bi, Ag, Cd and Cu remained, known as intermediates or modifiers commonly added to thick films to provide adhesion to the substrate [158]. By measuring the binding energies for the elements comparing them with NIST X-ray photoelectron spectroscopy database [149], it was suggested that Bi may be in the form of an oxide (Bi_2O_3). Au is known to adhere quite well to high lead glasses because of the solubility and reaction with the large lead cations [157]. Nevertheless, Au has generally poor adhesion to other glasses because of the lack of both solubility and chemical reaction between Au and the O anions which form the surface layer of many oxide materials. However Bi oxide is commonly added in small quantities in order to increase the solubility of Au in glass [157]. Other transition metal oxides (for instance, oxides or oxides precursors of Cu) may also be employed as part of the inorganic binder to improve conductor soldered adhesion.

Table 5.6 presents the quantitative analysis for both cases. In addition to Au, there was a large concentration ($\approx$ 42at%) of surface C and a surface oxide (Bi_2O_3) on the as-received substrate. After Ar ion sputter cleaning, the C signal diminished significantly indicating that it was easily removed. An interesting result was the appearance of $\approx$ 2 at% of Cu on the surface of the Au thick film. Cu has been previously found on the surface of Au thick film [159]. The surface Cu was believed to come from Cu oxide which is added to the Au paste by the manufacturer to promote adhesion between the Au and the Al_2O_3 substrate via a spinel reaction [159, 160]. Cu migrates to the Au-air interface during the process [159]. A similar scenario occurs for Cd, and in this case, the spinnel formed is $CdAlO_4$. There was a significant concentration of 5 at% of Ag at the surface which decreased after Ar ion bombardment. This decrease

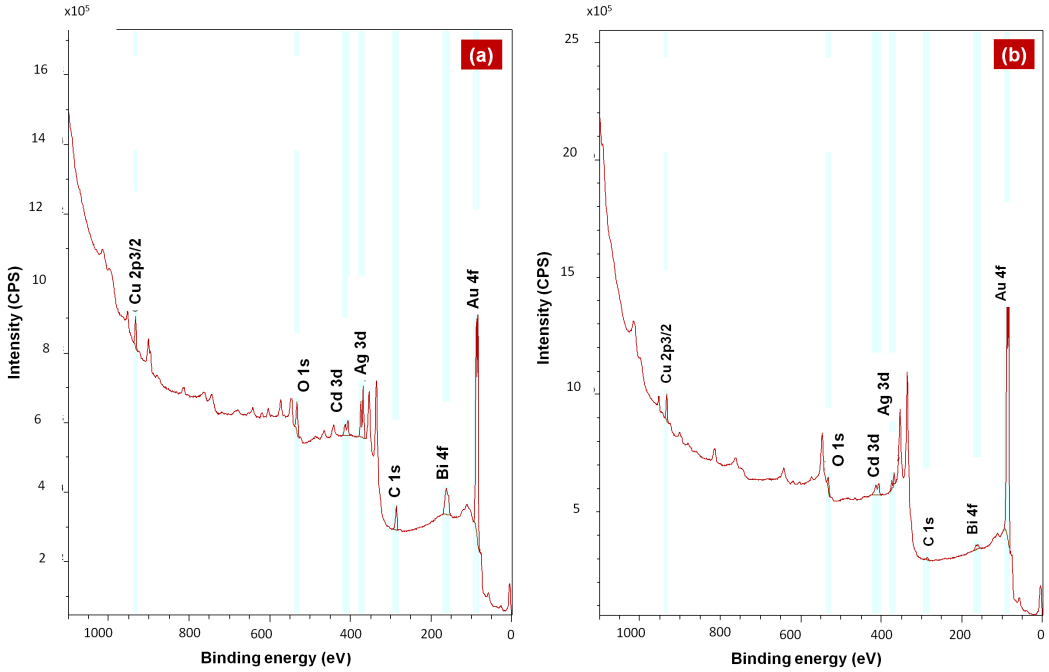


Figure 5.27: XPS spectra of the Au thick film on the substrate in the as-received condition: (a) at the surface, and (b) after Ar ion bombardment in vacuum to clean the surface.

in Ag concentration might be due to surface diffusion over the Au. Diffusion in multilayer metallisation can be very dependent on Au film morphology. If the film was dense the primary diffusion mechanism would probably be by grain boundary diffusion. The thick film Au metallised on substrate was considerably porous as shown in Figure 5.26. Therefore, surface diffusion around pores will probably be predominant since it is much more rapid than either grain boundary or bulk diffusion [157].

For interface reaction studies, a section of the Au metallised substrate was cut out using a low-speed diamond saw. The sample was prepared for cross-sectional examination by mechanically polishing with 30, 6 and 1μm and ion etched afterwards for 40min, at 40kV. The interfacial reaction zone was studied by SEM, wavelength dispersive X-ray analysis (WDX), and electron probe micro-analysis (EPMA). Chemical analysis was performed at different locations across the Au thick film/glass layer/Al_2O_3 substrate interface.

Figure 5.28 shows the WDX analysis performed in the Au metallised

Table 5.6: Estimated atomic concentrations of various surface species obtained from the as-received Au thick film metallised on Al_2O_3 substrates, as determined by XPS in the as-received condition and after Ar ion bombardment to clean the surface.

Species	**As-received surface (at%)**	**After Ar ion bombardment (at%)**
C	42.4	10.1
O	20.3	15.2
Cu	2.4	4.6
Au	26.4	66.4
Bi	3.1	1.1
Cd	0.1	0.2
Ag	5.3	2.4

substrate. Figure 5.28(a) shows a typical cross-section SEM image of the substrate together with the regions where WDX was performed. Area 1 points to the Au metallisation itself, that comprised different "phases" depicted by the various inclusions. According to the corresponding spectrum shown in Figure 5.28(b), in addition to Au, only one of the species from the glass layer (Ag) was identified. Moving further down towards the Al_2O_3 substrate, in area 2, Bi, Cd and Cu were evident, as shown in the WDX spectrum in Figure 5.28(c). Figure 5.28(d) shows the WDX spectrum corresponding to region 3. In addition to Al and O, Mg and Si were present: Si and Mg are common impurity/minority elements in industrial alumina.

WDX analysis of the Au metallised substrate was complemented with (EPMA) showed in Figure 5.29. A cross-section SEM image of the substrate is shown in Figure 5.29(a), and Figures 5.29(b), (c), (d), (e), (f), and (g) show the elemental concentration maps obtained by EPMA for Al, O, Si, Bi, Cd and Au respectively. Note the migration of some of the species included in the glass layer, namely Bi (Figure 5.29(e)) and Cd (Figure 5.29(f)), towards the Au thick film.

In order to gain a better understanding of the different phases in the

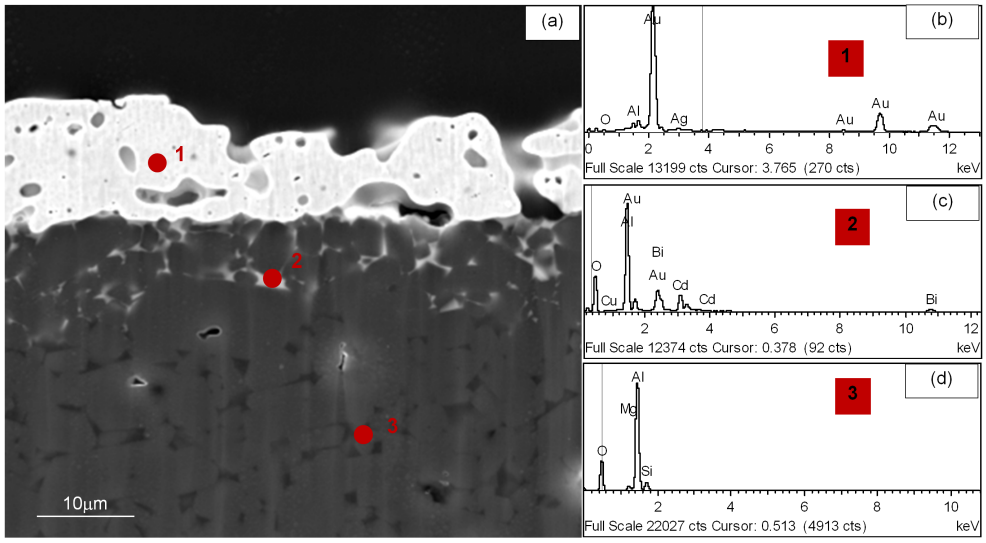


Figure 5.28: WDX analysis of the Au metallised Al_2O_3 substrate: (a) typical cross-section SEM image of the substrate with three different regions where 1, 2 and 3 WDX was performed; (b), (c) and (d) corresponding WDX spectra taken from regions.

Au thick film and the glassy layer between the Au film and the Al_2O_3 substrate, WDX was performed in particular regions of interest (Figure 5.30). The Au thick film/glass layer interfacial area is shown in the backscattered electron image as shown in Figure 5.30(a). The WDX spectrum in Figure 5.30(b) corresponds to region 1, which shows that the inclusions, initially though to be different phases, were melted tiny bits of the glass layer, mainly based on Bi and Cd. Region 2 corresponds to the glass layer immediately below the Au thick film and the WDX spectrum performed showed all expected glass related elements (Bi, Cd, Cu), except for Ag, which was replaced by a small fraction of Zn. Similarly to Cu, also oxides or oxides precursors of Zn may be employed as part of the inorganic bonder to improve conductor soldered adhesion.

EPMA analysis was also undertaken in the same region where WDX was performed, and is shown in Figure 5.31. Figures 5.31(b), (c), (d), (e), (f), (g), and (h) show the elemental concentration maps obtained by EPMA for O, Al, Si, Au, Cd, Bi and Zn respectively. Au persisted in the glass layer to approximately $3\mu m$ below approximate position of the Au/glass phase interface, as shown in Figure 5.31(e). The Al and Au show clearly a difference between

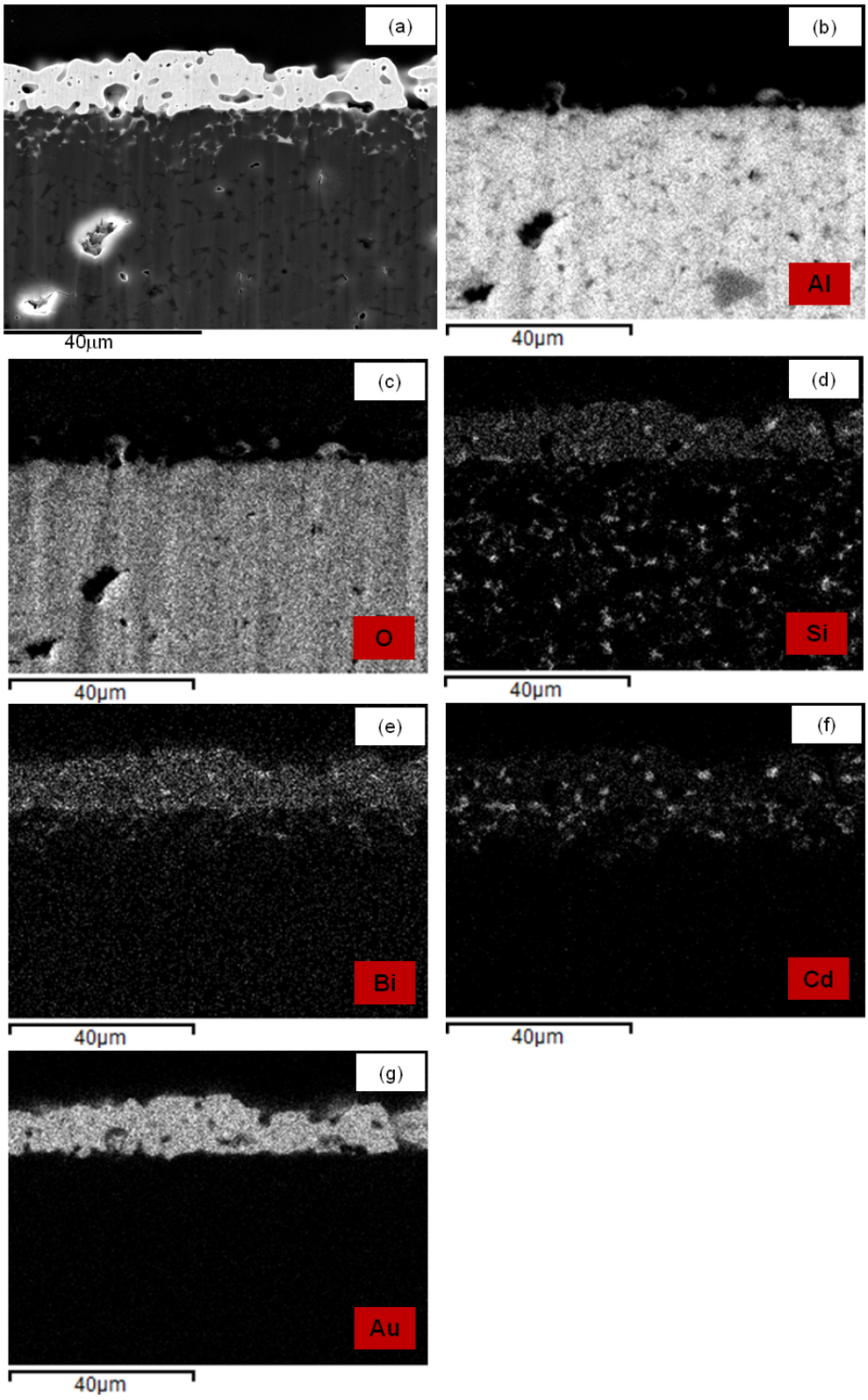


Figure 5.29: EPMA maps of the Au metallised ceramic substrate: (a) secondary electron image of the Au metallization/Al_2O_3 substrate interface; (b) Al map; (c) O map; (d) Si map; (e) Bi map; (f) Cd map; (g) Au map.

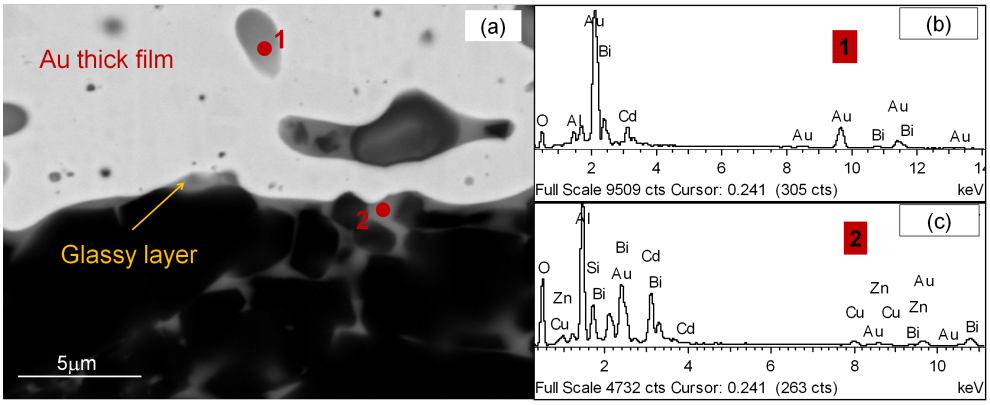


Figure 5.30: WDX analysis of the Au metallised Al_2O_3 substrate: (a) typical cross-section SEM backscattered electron image of the substrate with two different regions in which WDX was performed; (b) and (c) corresponding WDX spectra taken from regions 1 and 2.

the metallisation thick film and the substrate. The Au contains Si, Bi and Zn, with Cd and Si possibly concentrated in "inclusions" although the accumulation of polishing debris from the substrate into pores of the Au to give the impression of inclusions cannot be ruled out, and in the case of the larger pores here, appeared quite likely.

Figure 5.32 shows an elemental line scan across the Au thick film/glass layer/Al_2O_3 substrate interface. The local concentrations for each element in the weight percentage along the line are also shown, extending from the Al_2O_3 at the start to the top surface of the Au metallisation in Figure 5.32. The key finding from this data is that Cd, Bi and Si were relatively concentrated in the glass phase. Higher atomic-number elements diffused into the grain boundaries of the Al_2O_3. Possibly Zn is the element that makes the binder migrate to the interface of the metal and ceramic, most probably in the form of amorphous oxides. Also, Zn could be responsible for holding the major elements (Bi, Cd) in the glass phase and prevent substantial migration into the Al_2O_3 grains.

In order to determine if the cause of poor adhesion and non-wetting of the Au-Si preform onto this thick film Au metallised substrate was related to the presence of elements inherent to this type of Au thick film, a series

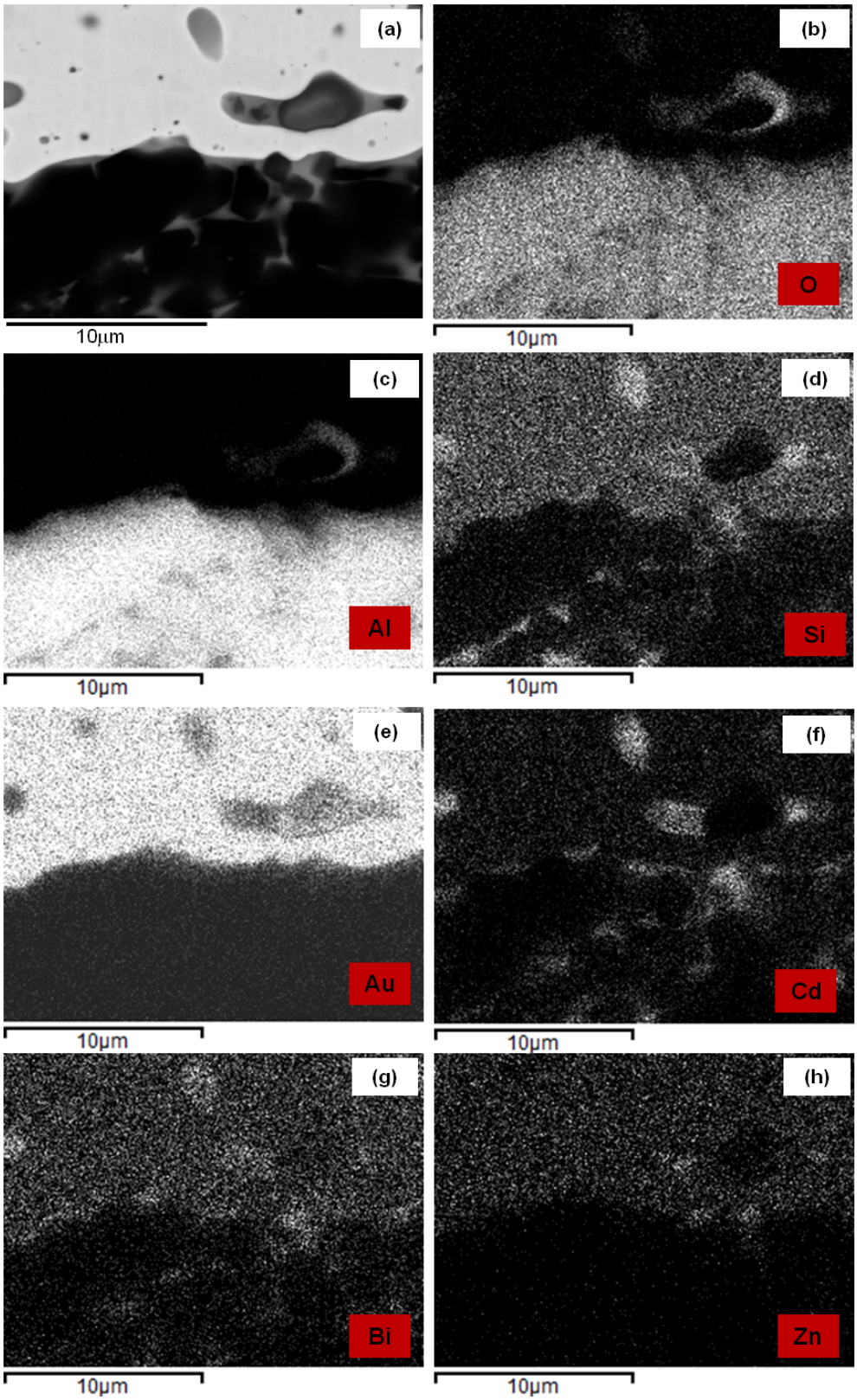


Figure 5.31: EPMA maps of the Au thick film metallised ceramic substrate: (a) backscattered image of the Au metallisation/glass layer interface; (b) O map; (c) Al map; (d) Si map; (e) Au map; (f) Cd map; (g) Bi map; (h) Zn map.

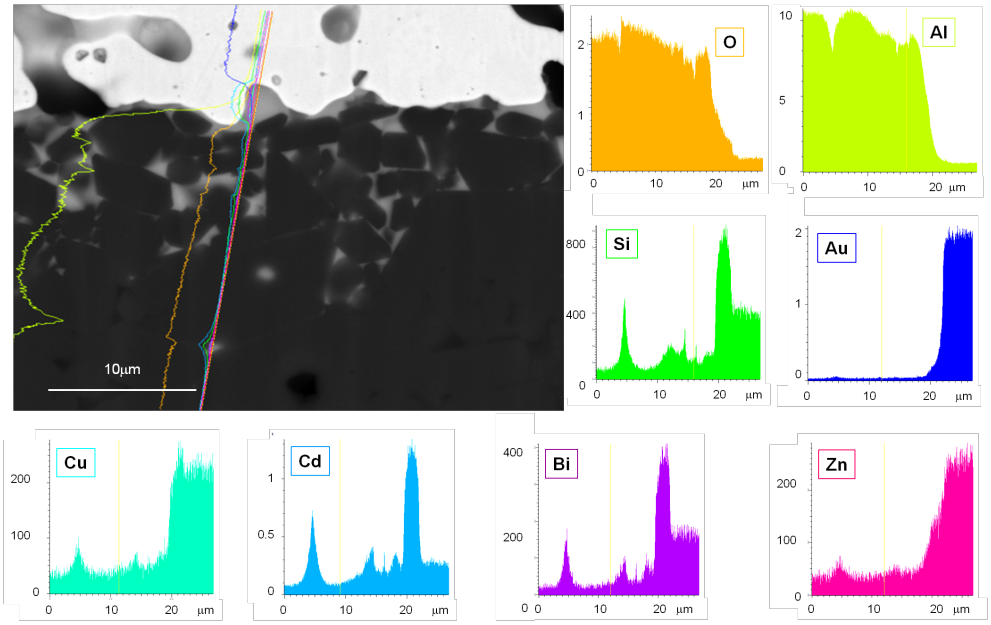


Figure 5.32: Cross-section SEM backscattered image of the Au mettalised Al_2O_3 substrate and corresponding element depth profiling.

of experiments were performed. The initial objective was to identify if any minority elements were strongly responsible for promoting or inhibiting wetting. However, in the time available, it was not possible to deposit Cd, Zn or Bi on top of the Au metallised substrates, and only three modified metallisations were studied:

i) sputtered Ti to a thickness of 50nm;

ii) evaporated "pure" Au to a thickness of 100nm; and

iii) evaporated pure Au film to a thickness of 100nm with a Ag flash on top.

Prior to attempting to bond a Si die onto each of these metallisations using Au-Si preform, each surface was examined by XPS. The substrates finishes were studied after Ar ion bombardment which removes contaminants and the adventitious C, N and O that absorb on every surface exposed to the atmosphere (Figure 5.33). The XPS spectrum of the Ti layer sputtered on the Au metallised substrate is shown in Figure 5.33(a), with strong peaks due to Ti and O. Measuring the binding energy for Ti spectral line (≈458eV) and

comparing it with [149], it was possible to confirm that the surface Ti was combined with O, in the form of TiO_2. Expected traces of C and N were also present. There was no discernible Bi, Ag, Cd, Cu, Si or Zn that are characteristic of Au thick film metallisations. Figure 5.33(b) shows the XPS spectrum of the Au metallised substrate onto which pure Au was deposited, with the expected strong Au peak at ≈ 84-88eV, and "normal" intensities of C and O contamination. Comparing this XPS spectrum with the one obtained for the Au metallised substrate in the as-received condition (Figure 5.27(b)), it was clear that apart from C and O surface contaminations, elements associated with the glass layer and/or the substrate were not detected. The XPS spectrum for evaporated Au plus Ag flash was identical to evaporated Au only, as the Ag flash was readily removed.

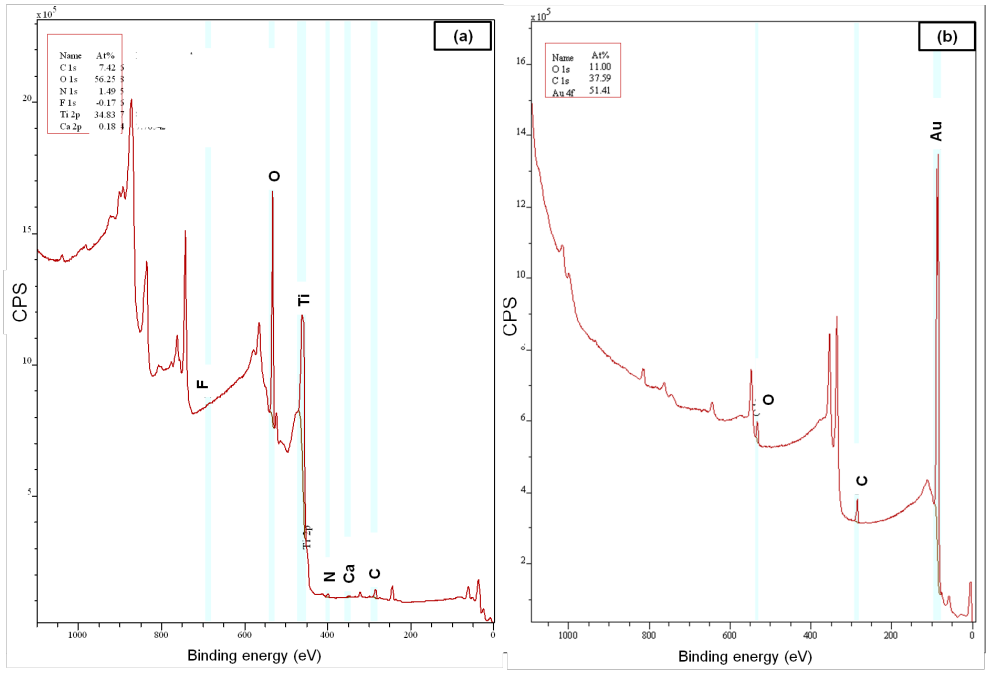


Figure 5.33: XPS spectra of the thick film Au metallised Al_2O_3 substrate with (a) 50nm Ti sputtered, and (b) 100nm Au evaporated each after Ar ion bombardment.

Die bonding was then carried out with the three prepared substrates placed in a small Macor boat built for the experiment. The Au-Si preforms and the Si dies (same dimensions of the components used for the Au-Si die bonding optimisation) were then placed on top of each of the substrates form-

ing a sandwich. No scrubbing was employed as the bonding process took place in a tubular furnace. Instead, static pressure was used. For that, a small macor plate on top of each of the three specimens, which was forced down to 3.5g/mm^2 ($\approx$70g according to die size). The force used matched the optimum force of the scrubbing head previously determined. The boat containing the three specimens, held by the pressure plate, was loaded into the furnace. The furnace was purged with N_2 to prevent oxidation. The bonding was performed by raising the temperature up to 450^{o}C, at a heating rate of 10^{o}C/min. A dwell time of 60 minutes was allowed followed by cooling down (10^{o}C/min) to room temperature before the boat was removed from the furnace.

There was no evidence of bonding between the Si dies and any of the metallised substrates. Figure 5.34 shows the aspect of the components immediately after removal from the furnace. The Au metallised substrate containing the sputtered Ti appeared with the characteristic blue-ish colour which had partially vanished from the substrate surface as shown in Figure 5.34(a). Although some type of reaction occurred, no bonding or mixing was accomplished. The substrate, preform and die were completely separated from each other. A similar scenario occurred when using pure Au on top of the Au metallised substrate as shown in Figure 5.34(b). The back of the Si dies (side used for bonding) and Au-Si preforms are also shown for both cases in Figure 5.34(a) and (b). Even though the Si dies were cleaned in HF prior to the experiment, the dies exhibited signs of oxidation. The Au-Si preforms also showed characteristic features of oxidation by becoming darker, with dull tint and wrinkled. It can be concluded that the static pressure used was not able to break any surface oxide film, and therefore wetting over the Si die was not achieved. An identical result was obtained for the substrate which had evaporated Au and Ag flash surface finish.

These results suggest that eliminating all surface contamination from the components surface, and protecting them from oxidation through the

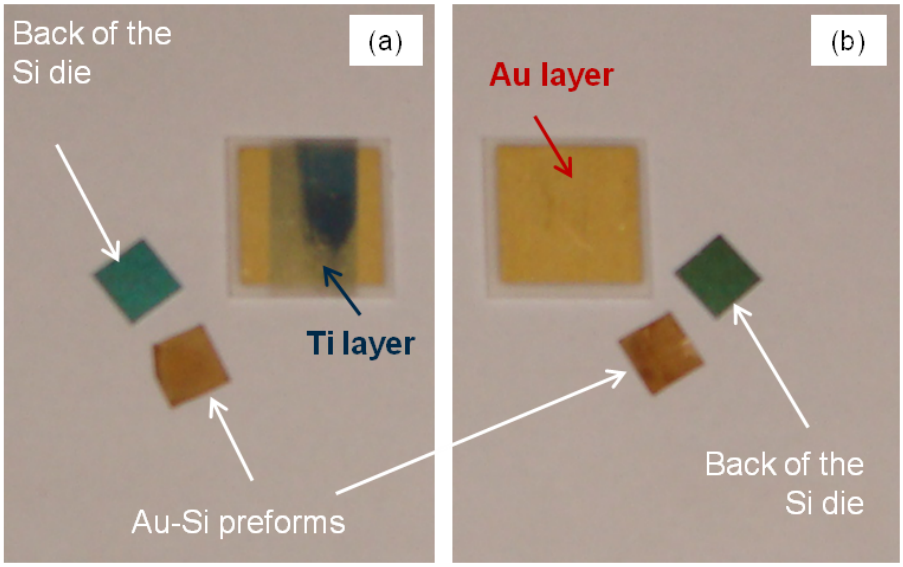


Figure 5.34: Aspect of the Au-Si die bonds after die bonding process in a tubular furnace (under N_2) using (a) sputtered Ti 50nm thick and (b) pure thin film Au on top of the Au metallised substrate. No evidence of bonding.

heating cycle during the bonding process will still likely be insufficient to produce a good quality bond, and that whatever minor chemical effects may operate at the various interfaces due to complex chemistry of thick film formulation, these factors are subservient to the dominating effect of surface oxide, most likely SiO_2.

The function of any Au metallisation layer is to provide adequate thickness and be sufficiently pore-free to ensure adequate mechanical bonding and heat transfer. It has been suggested that Au metallisation as thin as $0.5\mu m$, deposited by sputtering, can be relied on to maintain excellent solderability even when the coated surface is relatively rough [161]. On the other hand, the solderability of a Au layer of the same thickness but applied by electroplating to a relatively (and typical) rough surface (R_a>$3\mu m$) may not offer adequate protection to the underlying base metal from oxidation [162]. Where thicker Au coatings are needed, fluxless soldering tends to be used to avoid catastrophic embrittling phases in thick sections. Finally, the need of a noble metal surface on the parent materials can be eliminated if the solder itself if applied as the barrier coating to previously cleaned component surfaces [161]

but this requires fully integrated manufacturing, rather than the batch processing widely practised in the aerospace and other harsh environment industries.

Despite oxidation, other surface species and scrubbing have so far been considered, surface roughness should also be considered, since another possible critical function of the scrubbing step, alongside the rupturing of surface oxide, could be the wear of surface asperities so that a larger area of contact with the two faces is promoted.

Surface topography

There is no broad consensus on how, in general, surface roughness influences spreading and bond formation during soldering. In the broadest sense "low" surface roughness is preferred since intuitively two "smooth" surfaces will bond better than rough surfaces.

AFM imaging was used to characterise the topography of the thick film Au metallised Al_2O_3 substrate and Figure 5.35 shows a typical AFM image. The surface of Au was irregular with peaks and valleys.

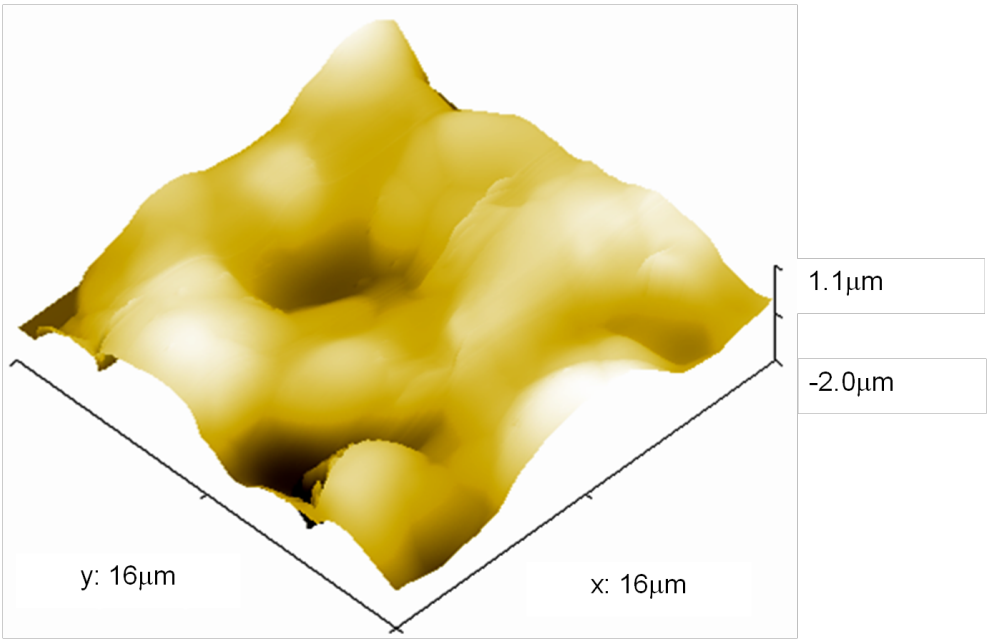


Figure 5.35: AFM image of the thick film Au metallised layer on the Al_2O_3 substrate.

There was some suggestions that at a finer scale, there may have been some faceting of individual Au grains. Au is known to exhibit {1 0 0} and {1 1 1} facets when heated in air at temperatures near 1000^{o}C. This faceting has been attributed to the presence of impurities diffusing to Au surfaces from the bulk and from the atmosphere [160]. These impurities induce a surface energy anisotropy which promotes facet evolution at elevated temperature. Bi and Cu, intentionally added to the thick film Au metallisation here, can diffuse to Au surfaces as well as towards the substrate as shown earlier in this section.

Surface profilometry was used to determine the typical roughness of the Au metallised substrate. The substrate had a maximum peaks and valleys distance of 3.5μm and R_a roughness of 1μm.

In order to understand how surface roughness might affect wettability, a simple experiment was carried out. The idea was to use a substrate that was essentially as free of surface contaminants as possible, and therefore sapphire (Al_2O_3) was chosen. A layer of "pure" Au was then evaporated onto a polished side of the sapphire to a thickness of approximately 200nm. The Dektak 6M profilometer was again used to measure the step heights and roughness of the Au deposited on the sapphire substrate and had a maximum peak to valley height of 0.03μm and a R_a roughness of 0.01μm.

The next step was to attempt to bond Si dies to the sapphire substrates with evaporated Au, using standard Au-Si preforms. Because of the difficulties experienced in achieving bonding with previous experiments without scrubbing, die bonding here was performed again using the Cammax EDB65 semi-automatic die bonder with optimum parameters: heating stage temperature - 450^{o}C; scrubbing head force - 3.5g/mm^2; scrubbing frequency - 2Hz; and scrubbing time - 1s.

Images of Au-Si die bonds using coated sapphire and the "standard"

substrate used elsewhere in this thesis are shown in Figures 5.36(a) and (b) respectively. The flow of the Au-Si preform on the smooth, pure Au was dramatically enhanced - so much that practically all the Au-Si was squeezed out of the bond area, and wetted across the whole substrate, right to the edge. Presumably, the surface of the Au was consumed/dissolved as Au-Si flow progressed. Once wetting had been started, no further pressure was needed to maintain the wetting/dissolution reaction, which progressed even outside the bond area [158]. In contrast, the bond on the standard Au metallised Al_2O_3 substrate in Figure 5.36(b) showed only a limited flow of molten solder beyond the bond line. Furthermore, the preform formed pores around the die area and there was no wetting beyond the bond line and fillet periphery. These pores or "bubbles" were noted once the scrubbing started.

The difference in wettability between the two substrates can be understood in terms of their surface energies. The higher the surface energy of the surface the lower the driving force required to achieve preform wetting and/or reaction with the substrate, and surface roughness of the thick film Au metallisation being ≈ 100 times higher than pure thin film Au metallisation a dramatic effect on wettability. Although the bondability of electrodeposited Au films and their wetting characteristics have been suggested to be improved with increasing surface roughness, the results here strongly suggested opposite behaviour. Indeed, in many cases substrate roughness leads to non-uniform Au films during the metallisation process, which then impairs wetting by the preform [88]. Note that here the rough substrate had a non-uniform and discontinuous Au metallisation while the smooth substrate comprised a completely continuous Au layer.

If on the basis of previous results it is assumed that rupturing of surface oxide is a pre-requisite for any high quality bond in this system, it now further suggested that once this is achieved, surface roughness plays a critical role. It is expected that even the "pure" Au must contained some surface

O and C containing groups, but these obviously did not impede subsequent wettability. Indeed, when the surface was comparatively smooth and free of other elements, wetting was too fast, and progressed rapidly to consume the whole Au coating, including well beyond the bond line. Further, the presence of "impurities" in the thick film Au can now be understood as playing a useful role in inhibiting excessive wettability, and the elements associated with glass layer (Bi, Cd, Cu and Ag) or the glassy inclusions themselves are used to help retain the Au-Si within the bond line.

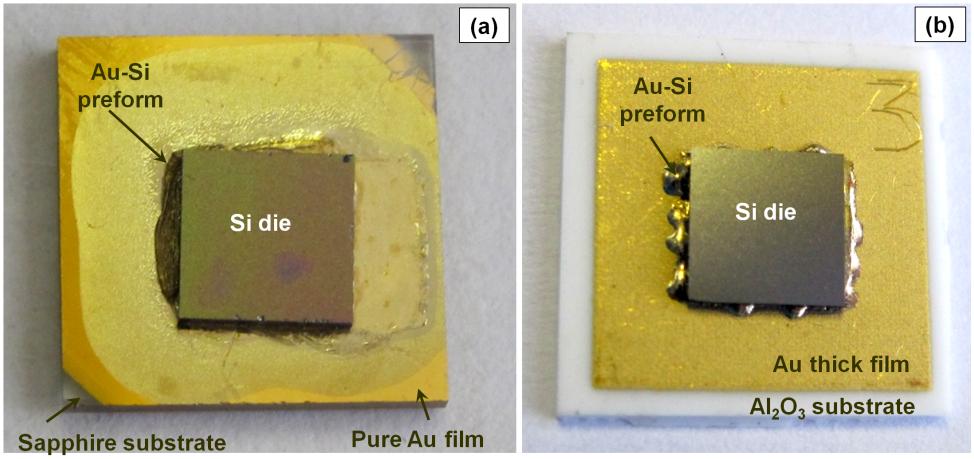


Figure 5.36: Au-Si die bonds manufactured using Camax EDB65 semi-automatic die bonder under optimum conditions (heating stage temperature - 450^{o}C; scrubbing head force - 3.5g/mm^2; scrubbing frequency - 2Hz; and scrubbing time - 1s), comparing (a) pure thin Au film on sapphire substrate and (b) thick film Au on Al_2O_3 substrate.

The bond quality was also investigated by SAM. Figure 5.37 shows a typical SAM image for the sapphire substrate with an unbonded area (depicted by white regions) of $\approx$ 24% with a largest single area defect of $\approx$ 4%. Unfortunately, the bond integrity was so poor that the die separated from the substrate during further SAM inspection with the Au-Si preform attached to the Si die. Only a small area of the preform remained attached to the substrate. Evidently the lack of Au-Si remaining in the bond because it wetted out across the whole of substrate, and consequently the vanishingly small separation between substrate and die, generated large, concentrated strains that exceeded the load carrying capability of the interface.

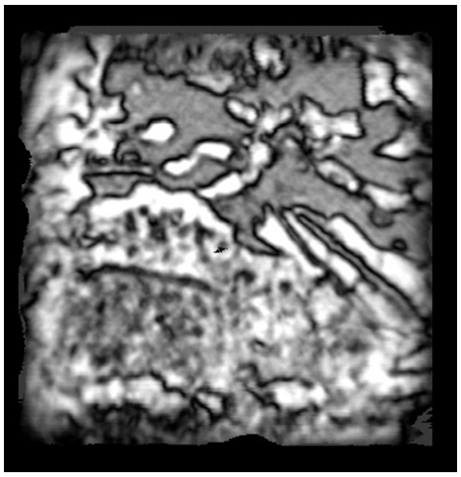


Figure 5.37: SAM image of a model Au-Si solder bond.

5.3 Conclusions

The main objective concerned exploring the key factors that control bonded area between the Si die and the Au metallised Al_2O_3 substrate. The scrubbing action, needed to break away the oxides during bonding, is believed to be responsible for such variability.

Manufacturing parameters that were studied here: temperature of the heating stage, force of the scrubbing head, scrubbing frequency and scrubbing time. Two levels were allocated for each key process parameter, and SAM was used to assess the resulting bond quality in the interfacial region. The total percentage of unbonded area varied from 1 to 98%, emphasizing the variability in bond quality. The corresponding shear loads to failure ranged from 5 to 75kg. The predominant failure mode occurred at the Si die (failure mode 1) although there were still a considerable number of specimens in which mixed failure occurred. The experimental design was followed by statistical analysis, and scrubbing frequency and time were concluded to be the key parameters affecting bond quality.

The second experimental design varied only the scrubbing parameters.

The unbonded areas were then in the range 1 to 13%. The corresponding shear load to failure was then 25-75kg, and the die bonds failed according to failure mode 1. The mean bonded area and mean shear load to failure, for the first experimental design, was 78% and 36kg, against 95% and 44kg for the second. Too long scrubbing time or too higher scrubbing frequency reduced the bonded area. The optimum die bonding conditions were: temperature of the heating stage - 450^{o}C; force of the scrubbing head - 3.5g/mm^{2}; scrubbing frequency - 2Hz; and scrubbing time - 1s.

After die bonding optimisation, the solder bonds using commercial Au-2wt%Si preforms to bond Si dies to Al_2O_3 substrates retained a reduced but significant variability in terms of bonded area, and scrubbing action was assumed as the primary cause. Without scrubbing, no type of bond and no evidence of mixing was accomplished. This difficulty in producing any bond even on "clean" Au-Si preforms suggested that the Au-Si preform easily formed a thin oxide layer. The high melting point Au-Si solders are subject to significant and rapid oxidation owing to the chemical reactivity of Si. Furthermore, unless the contaminants which normally exist at the bonding interfaces are scavenged, or can be contrived to take part in the bonding process itself, one would expect non-uniform adhesion when Si dies are bonded to their substrates using a melted preform material procedure.

Poor bonding may also occur at the Au-Si preform/metallisation interface, and the effect of composition and morphology of the Au metallisation on the substrate has been investigated. It was suggested that once rupturing the surface oxide is achieved, surface roughness may play a critical role in how the wetting/dissolution progresses. The presence of "impurities" in the thick film Au may inhibit excessive wettability, and the elements associated with the glass layer help retain the Au-Si preform and its reaction with the Si die and the Au metallisation within the bond line.

CHAPTER 6
Thermal exposure

This chapter describes the fabrication of 150 die bonds under the optimum conditions identified in the Chapter 5, and their subsequent investigation in terms of reproducibility and response to thermal ageing, thermal shock and thermal cycling. The Au-Si die bonds were characterised microstructurally and bonded area evolution was investigated as a function of thermal exposure. Nano-mechanical characterisation of elastic properties of the Au-Si solder region was carried out. The electrical performance of the resulting devices is also presented.

6.1 As-manufactured

The bonded area of 150 as-manufactured Au-Si die bonds was investigated using SAM. Acoustic images were generated using a transducer operating at 300MHz, and ultrasound was directed from the top side of the Si die, i.e. through the Si die/Au-Si solder/Au metallised substrate. Extreme care was again taken in order to achieve near identical conditions for every analysed specimen. DIA was used to quantify the fraction of bonded area.

All 150 Au-Si die bonds contained some unbonded area, primarily at the Si die/Au-Si solder interface, although some unbonded areas were also located at the Au-Si solder/Au metallisation interface. The total percentage unbonded area varied in the range 1 to 75%. The largest single defect for a single bond ranged from 1 to 72%.

The percentage of unbonded area was converted into percentage of bonded area, and Figure 6.1 shows the distribution of total bonded area. Despite the very occasional low bonded area described above, the distribution had a peak at 90-100%. The mean bonded area was 92% and the standard deviation was 11%; of the 150 die bonds, only 10 had a bonded area lower than 80%. Of these 10 die bonds, only 4 had bonded areas below 50%.

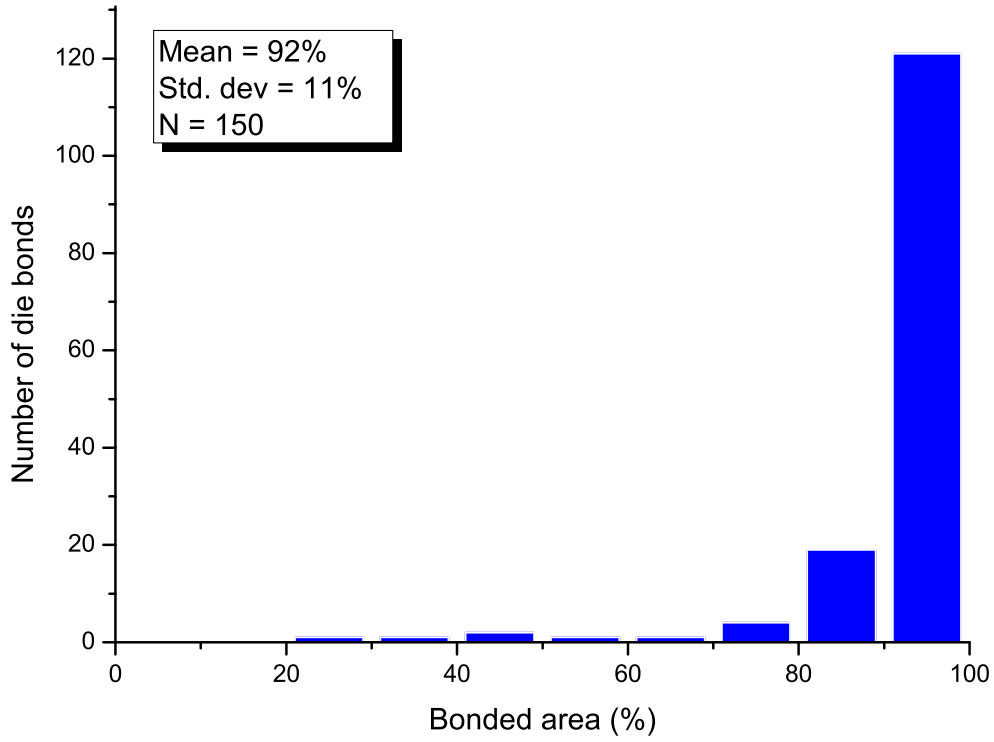


Figure 6.1: Bonded area distribution of nominally identical Au-Si die bonds manufactured under optimum bonding conditions: heating stage temperature - 450°C; scrubbing head force - 3.5g/mm^2; scrubbing frequency - 2Hz; and scrubbing time - 1s.

Cross-sections of some of the as-manufactured Au-Si die bonds were then prepared for metallography and studied by means of SEM, EDX, and EPMA.

Figure 6.2 presents cross-section SEM images of a typical Au-Si die bond in the as-manufactured condition. A general arrangement of the die bond microstructure is shown in Figure 6.2(a). EDX was used to identify the different components of the package and distinguished the Si die, the Au-Si solder and the Au metallisation on top of the Al_2O_3 substrate. The eutectic

matrix is the result of Au and Si diffusion. The diffusion process starts as a result of the atomic contact of Au and Si above the Au-Si eutectic temperature of 363^{o}C. Applying a contact force and increasing the temperature beyond the eutectic temperature results in diffusion of Si into Au, and subsequent liquid formation. This liquid phase will accelerate the mixing and Si continues to dissolve into the liquid, until saturation occurs at a composition corresponding to the Si liquidus line. According to the Au-Si phase diagram, at a bonding temperature of 450^{o}C, the liquidus is at $\approx$ 5wt%Si. The liquid forms on reaction with both the die and substrate metallisation, one is Si rich, the other Au rich, and solidify with residual eutectic formed, forming the eutectic structure between them upon cooling.

Two different interfaces were then formed: the Si/Au-Si and Au-Si/Au. Regarding the Au-Si/Au interface, there was no measurable thickness change of the Au metallisation before and after die bonding. In some locations along the Au-Si/Au interface, such as shown in Figure 6.2(a), it was possible to distinguish where the Au-Si solder layer finishes and the Au metallisation starts. On cooling from 450^{o}C at the Au-Si/Au interface, the primary phase should be Au and it was possible to confirm the presence of few Au dendrites, in globular shape, with subsequent Au-Si eutectic between, along the Au-Si/Au interface. Unfortunately, successful polishing was sometimes difficult to achieve, and polishing debris were retained to a considerable extent, particularly in the Au. It was difficult to discern distinct Au dendrites due to the presence of the polishing features but the harder eutectic regions were comparatively distinct. Figure 6.2(a) shows also that the reaction zone had a constant thickness of $\approx 3\mu m$ along the Si/Au-Si interface. On cooling from 450^{o}C at the Si/Au-Si interface, large primary Si crystals ($\approx 10\mu m$) formed near the die bonding plane (i.e. on the Si die side) as shown in Figure 6.2(a). Nevertheless, Si crystals were mainly concentrated in the fillet region as depicted by the almost square black spots in the backscattered electron image

in Figure 6.2(b). The Si crystals were randomly dispersed in the fillet and their size ranged from 10 to 20μm. The primary Si was interspersed with the Au-Si eutectic, and Figure 6.2(c) shows a higher magnification image of the fillet region exhibiting the typical Au-Si eutectic structure (acicular shape) formed near the Si die side. These eutectic structures were also formed along the Si/Au-Si interface as shown in Figure 6.2(d).

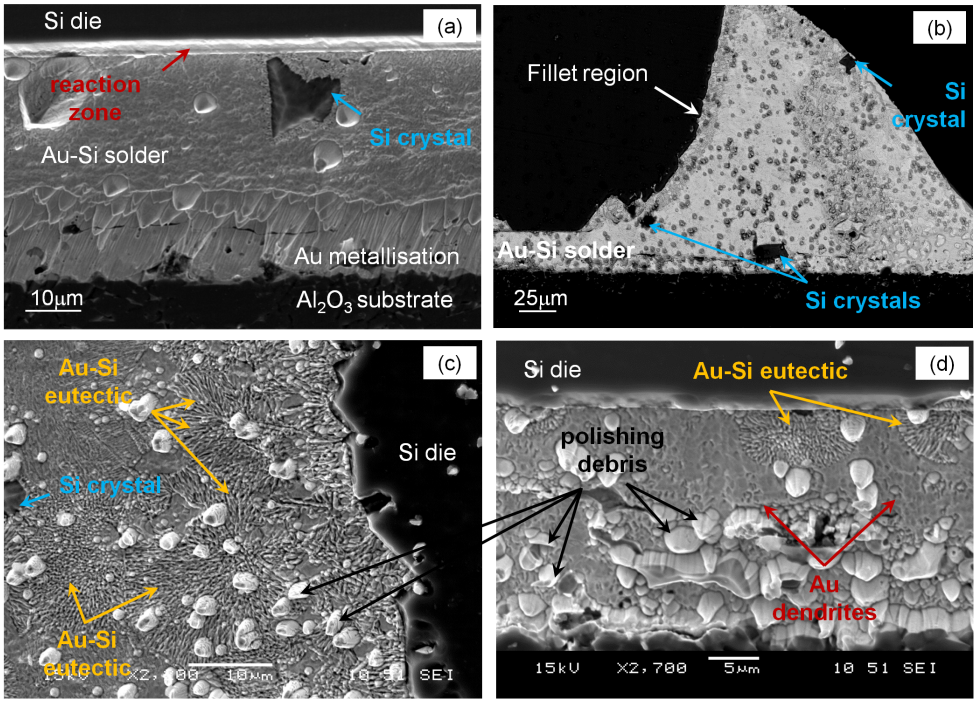


Figure 6.2: Cross-section SEM images of a typical Au-Si die bond in the as-manufactured condition: (a) general arrangement of Si die/Au-Si solder/Au metallised substrate interfacial region; (b) back-scattered electron image of the fillet region exhibiting Si crystals randomly dispersed; (c) high magnification image of the fillet region exhibiting typical Au-Si eutectic structure; and (d) interfacial area exhibiting Au-Si eutectic structure located at the Si/Au-Si interface.

The as-manufactured Au-Si die bonds comprised low levels of unbonded areas as identified previously by SAM. There was some voiding along the Au-Si solder region. Voids ranged from 1 to 5μm in size. Despite the persisting effort in electronic industry to produce good quality die bonds, voids always exist in the bonding layers [86, 88, 95, 96, 146, 163–166], and the presence of voids generally reduces the reliability of the devices. Besides enlarging the probability of die cracking, voids can increase the die operating temperature because of restricted heat transfer function [101]. As shown in detail in the

previous section, the cause for voiding in the die bonds is related to segregation of oxides, C and Si to the molten solder surface. As shown in Figure 6.3(a), the underside of the Si die could be "etched" by the molten preform surface layer and this faceted crater formation at the Si/Au-Si interface has been reported in [167]. Owing to the anisotropic nature of crystalline Si, the Si/Au reaction is highly dependent on the crystallography of the Si wafer. Jang [167] studied the dissolution behaviour of Si (100) and (111) planes by eutectic Au-Si solder, and concluded that on the Si (100) planes (as used in this thesis), the dissolution primarily occurred by the formation of craters resulting in a rough surface. On the other hand, the dissolution of the Si (111) resulted in a relatively smooth surface. The morphology of the Si (100) surface during Au-Si soldering reaction exhibited more time-dependent behaviour, and the etching craters on Si (100) surface grew larger with time whereas Si (111) did not significantly change. This difference was ascribed to the surface energy differences between Si (111) and (100) surfaces that resulted in the 2- and 3- dimensional dissolution behaviours, respectively [167]. The surface energy of Si (100) and (111) planes is 2130mJ/m^2 and 1230mJ/m^2 respectively [168]. The atoms of Si (111) plane are more closely packed and have fewer number of dangling bonds of the surface atoms, and thus is comparatively resistant to dissolution in eutectic liquid, so Si dissolution proceeds preferentially along particular planes, with usually the planes with the highest surface energy, showing the faster dissolution rate [169]. As the dissolution proceeds, the high energy surface may change locally to a number of low energy surfaces in order to reduce the total surface energy [169]. To sum up, as Si reacts with and dissolves in Au, faceted craters form in the Si. The distribution of the crater size ranged from 15 to 30μm. A higher magnification image of this feature is shown in Figure 6.3(b).

Furthermore, the faceted craters play a key role in the formation of voids during the Au-Si die bonding. It has been proposed that the craters on

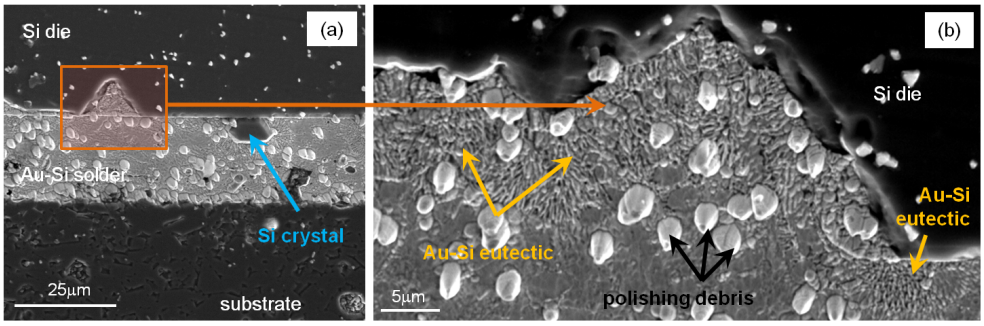


Figure 6.3: Cross-section SEM images of a Au-Si die bond in the as-manufactured condition showing: (a) etched regions formed along the Si/Au-Si interface and; (b) higher magnification image of a "crater" formed in the Si.

the Si (100) act as a Au-Si solder sink and the regions surrounded by etch-pits tend to become voids [167]. The densities of Si and Au-Si liquid alloy are very different at 2.33 g/cm^3 and 18.64 g/cm^3, respectively [170]. As Si dissolves into Au during the Au-Si die bonding process, the incremental volume of the Au-Si alloy is insufficient to compensate for the volume of Si consumed, and so the liquid tends to flow in an attempt to feed the severe shrinkage occurring at the interface. Figure 6.4 illustrates how a void forms by the craters on the back of the Si die, and how the craters exist at the voided/non-voided boundary. When the craters absorb the eutectic Au-Si liquid, the liquid is drawn from the surroundings to a crater as shown in Figure 6.4. If there is a region "surrounded" by craters, the region has a lack of Au-Si liquid and forms a void [167]. Figure 6.5 shows schematically this arrangement for void formation on the back of the Si (100) die.

In order to gain a better understanding of the interdiffusion behaviour of Au and Si in the Au-Si die bonds, EPMA mapping was carried out. Figure 6.6 shows EPMA maps for the as-manufactured die bond in the Si die/Au-Si solder/Al_2O_3 substrate region. Figures 6.6(a), (b), (c), (d), (e) and (f) show the elemental concentration maps for Au, Si, Al, Ag, Bi and Cd respectively. The corresponding backscattered electron image is shown in Figure 6.6(g). The colour bars indicate the relative concentration of each element. As expected, Au was uniformly distributed, as shown in Figure 6.6(a). On the other hand,

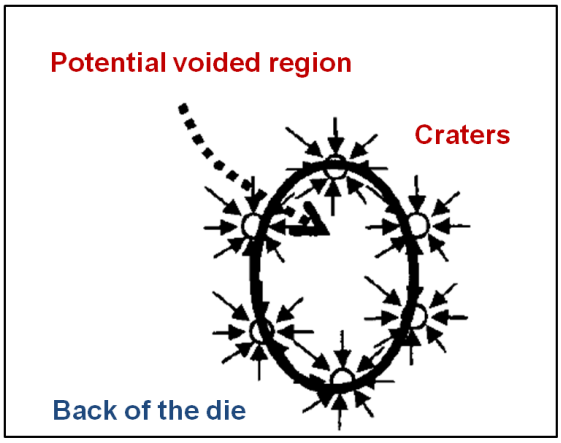


Figure 6.4: Schematic illustration of the potential voided region surrounded by craters. Even though a crater may pull in the Au-Si eutectic liquid uniformly, when some region is surrounded by craters, the region can have a lack of Au-Si and a void is then formed [167].

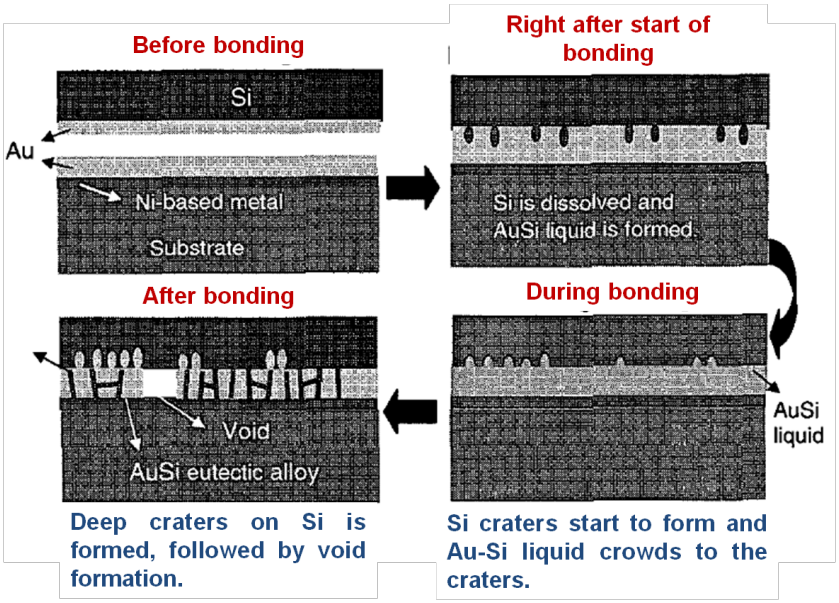


Figure 6.5: Schematic illustration showing the void formation sequence in Si (100) die [167].

Figure 6.6(b) shows that there were regions almost apparently free of Si due to "pull-out" from the polishing process. Si did not diffuse very far into the Au-Si solder region during bonding. The Si map did not show a decaying diffusion profile of Si into the Au but instead, there was a more complicated distribution arising from the solidification of the transient liquid in the Au-2wt%Si in contact with the pure Si. Figure 6.6(d) shows only very small traces of Ag from the thick film Au metallisation layer in the Au-Si solder region. On

the other hand, Bi (Figure 6.6(e)) and Cd (Figure 6.6(f)) diffused further into the Au-2wt%Si preform to a distance of $\approx 10\mu m$ beyond the nominal position of the Au-Si solder/substrate interface.

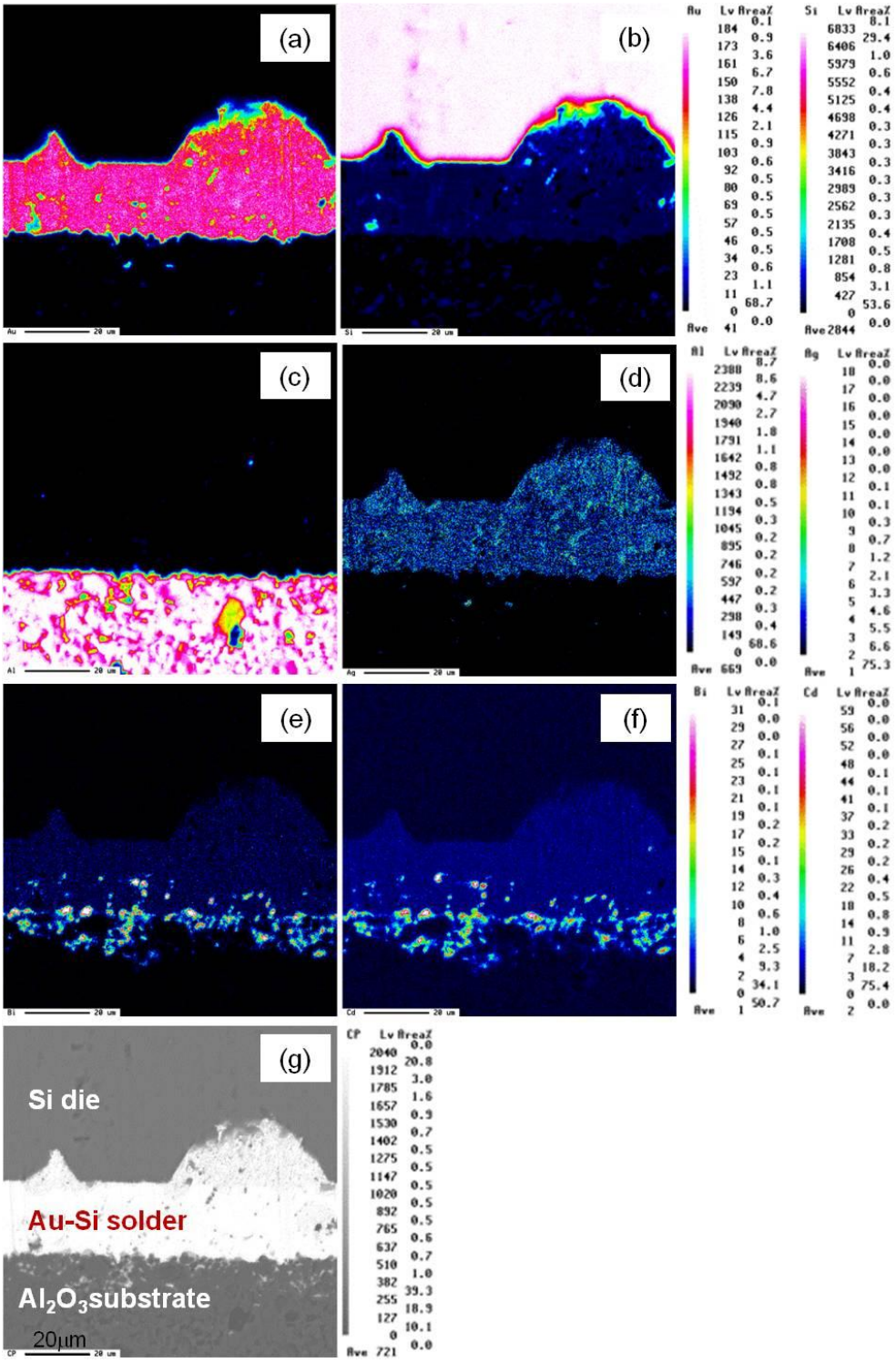
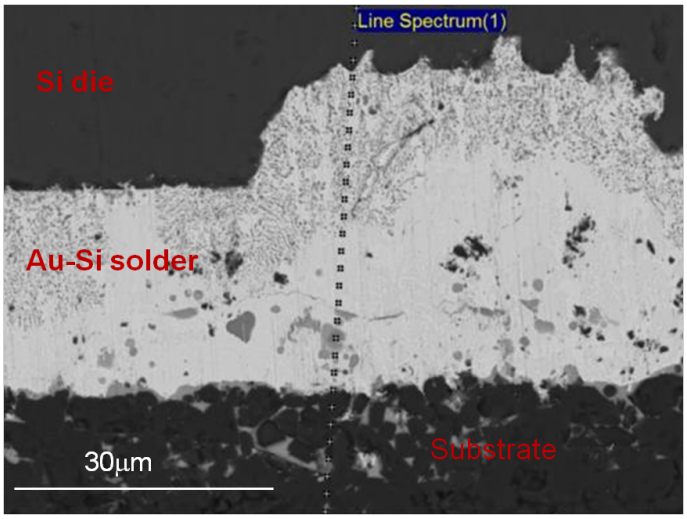
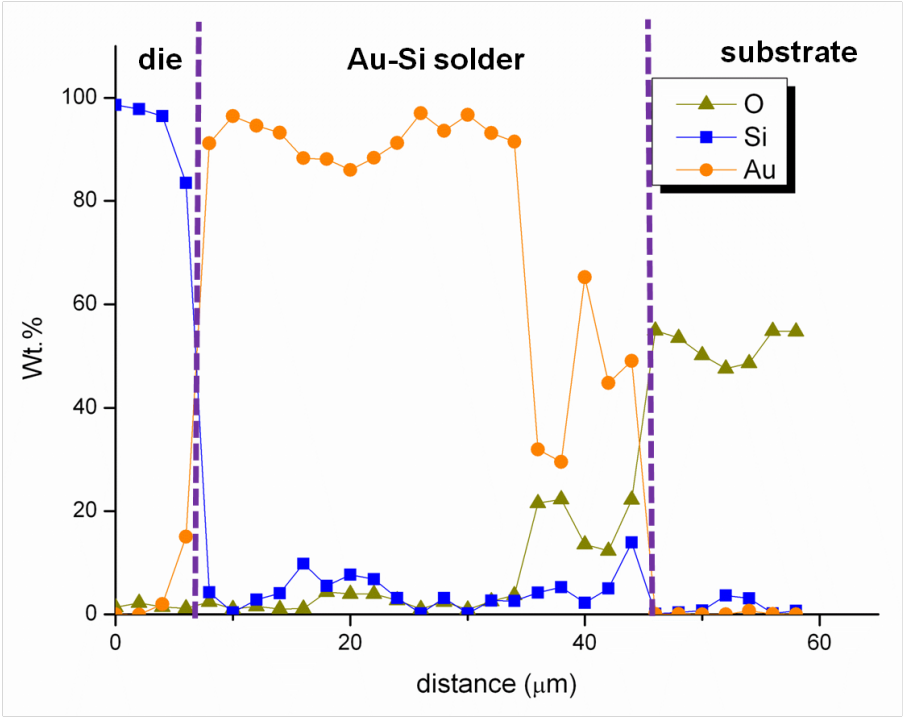


Figure 6.6: EPMA mapping of a typical as-manufactured Au-Si die bond in the region Si die/Au-Si solder/Al_2O_3 substrate interface: (a) Au map; (b) Si map; (c) Al map; (d) Ag map; (e) Bi map, (f) Cd map, and (g) corresponding backscattered electron image.

Figure 6.7 is a EPMA line-scan from the Si die towards the substrate, with a step size of $2\mu m$, and a total length of $60\mu m$ for Au, Si and O concentrations. The backscattered electron image where the line-scan was performed is shown in Figure 6.7(a). Figure 6.7(b) shows that the Si concentration gradually decreased as the interface with the Au-Si was approached, and then drastically reduced to $\approx$ 5wt% at a distance of $8\mu m$. Conversely, there was no detectable Au in the Si until the approximate position of the interface was reached, indicating very limited diffusion penetration. In the Au-Si solder region, at a line scan distance of approximately $10\mu m$, the Si concentration was no longer measurable, suggesting that Si in the eutectic liquid after reaction with the Si die formed epitaxially, onto pre-existing primary Si in the die rather than by nucleation and growth of a significant thickness of eutectic. Earlier SEM images in Figures 6.2 and 6.3 showed that the thickness of any eutectic zone was typically $\approx 25\mu m$. In the central regions of the solder preform, Si concentration increased as this was Si that did not precipitate in the bonding reaction, and there was a corresponding decrease in the Au concentration. At the Au-2wt%Si/thick film gold interface (at $\approx 46\mu m$ distance) the Si concentration decreased. In this region there was also an increase in O concentration, not seen on the upper side of the Au-2wt%Si preform next to the die. It was not clear if this was associated with the pre-existing SiO_2 on the underside of the preform, oxides on the surface of the thick film Au, or oxides formed due to diffusion of O from the porous Al_2O_3 substrate itself. Shukla and Mencinger [87] showed rapid diffusion of Si through a Au layer even at room temperature, with the subsequent oxidation of the Si on the Au surface. Line scans (not shown) showed that both Bi and Cd migrated from the ceramic substrate towards the Au-Si solder region rising to a maximum concentration of Bi $\approx$ 10wt% and Cd $\approx$ 35wt% in the region of Au-Si/Au interface, and as previously shown in Figures 6.6(e) and (f).



(a)



(b)

Figure 6.7: EPMA line-scan from the Si die towards the substrate for a Au-Si die bond in the as-manufactured condition: (a) SEM backscattered electron image where the line-scan was performed, with a step size of $2\mu m$ and a total length of $60\mu m$; (b) diffusion profiles for Au, Si and O across the Si die/Au-Si solder/Al_2O_3 substrate region.

6.2 Ageing

A selected number of optimised Au-Si die bonds were subjected to thermal exposure in order to study the microstructural evolution at the interfaces and

also the effect of thermal exposure on bonded area. Isothermal ageing was carried in-house, at 300^{o}C for different periods of time: 168, 672 and 2016h. A total number of 45 Au-Si die bonds were subjected to ageing (15 die bonds for each ageing time). Accelerated ageing was also carried out using 30 Au-Si die bonds at 350^{o}C for 500 (5 specimens) and 850 hours (25 specimens). The effect of temperature on bond quality was subsequently evaluated.

6.2.1 Isothermal ageing at 300^{o}C

Figures 6.8, 6.9 and 6.10 showcase acoustic images for the die bonded samples before (i.e. in the as-manufactured condition) and after being stored at 300^{o}C, for 168, 672 and 2016h respectively. Again, white and grey areas represent unbonded and bonded regions respectively.

Die bonds aged for 168h contained 1 to 6% unbonded area in which the largest single area defect varied from 1 to 2%. Figure 6.8 shows some examples of the unbonded area variation prior to ((a), (c), (e)) and after isothermal ageing ((b), (d), (f)). Overall, the unbonded area increased on ageing, although only slightly, with a slight change in the amount of white area in the SAM images for the same specimen, before and after thermal exposure. Also, of the 15 die bonds aged for 168h, the unbonded area decreased in three specimens. It is possible that voids may have collapsed or even shrunk due to a sintering type process during ageing, but this was not the dominant behaviour.

On increasing the ageing time to 672h, the percentage unbonded area increased, varying from 1 to 16%. In this case, the largest single defect also increased, now varying from 1 to 4%. The corresponding set of SAM images is shown in Figure 6.9. For instance, one of the die bonds showed an increase in unbonded area from 6 to 16% (Figure 6.9(e) and (f)).

Die bonds aged for 2016h had percentage of unbonded area ranging from 6 to 23%, with the largest single defect spanning the region from 1 to

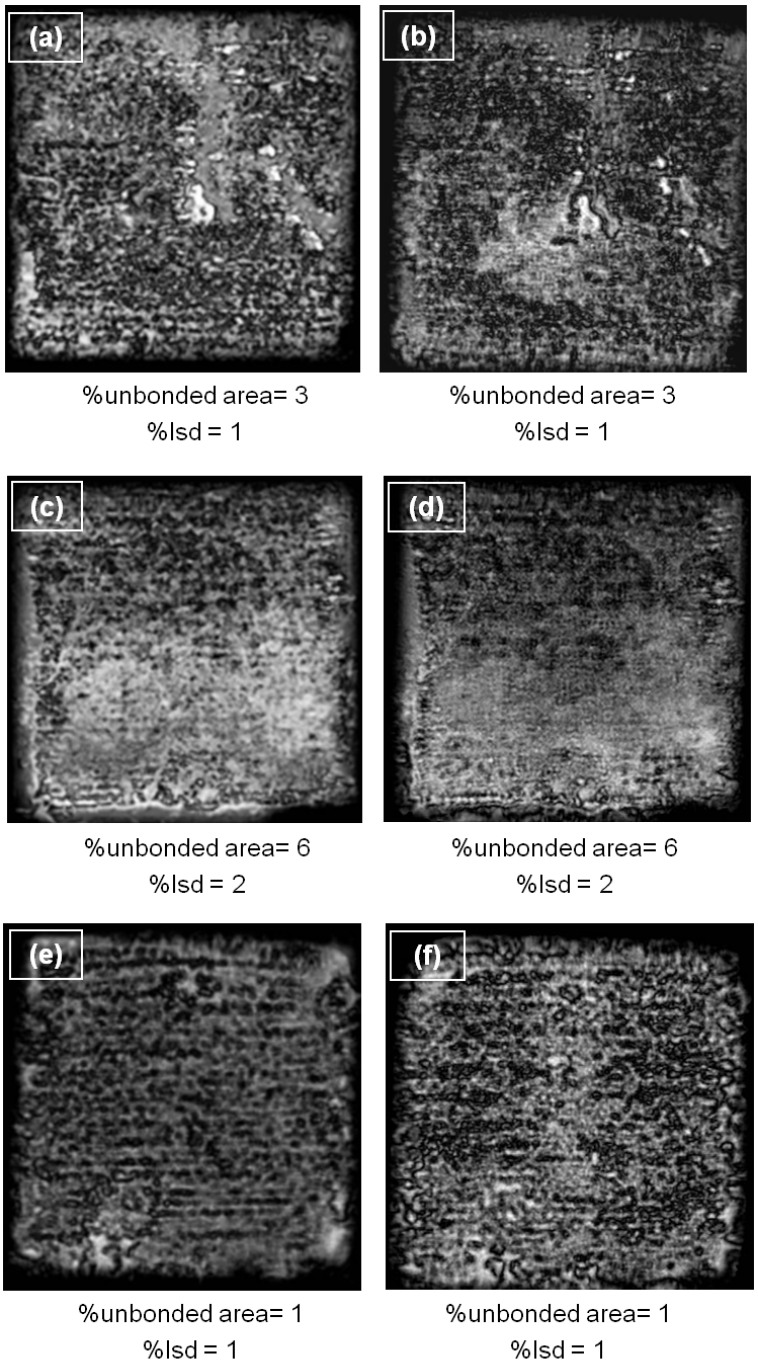


Figure 6.8: SAM images of Au-Si die bonds, from the optimised batch: (a), (c), and (e) in the as-manufactured condition; (b), (d), and (f) after isothermal ageing at 300^{o}C, for 168h. Percentages of unbonded area and largest single defect, (lsd) are given for each C-SAM image.

4% (Figure 6.10). The change in unbonded area increased, with one die bond increasing from an unbonded area of 4% (Figure 6.10(c)) to 23% after ageing (Figure 6.10(d)).

Table 6.1 summarises the variation in bonded area (BA) before and af-

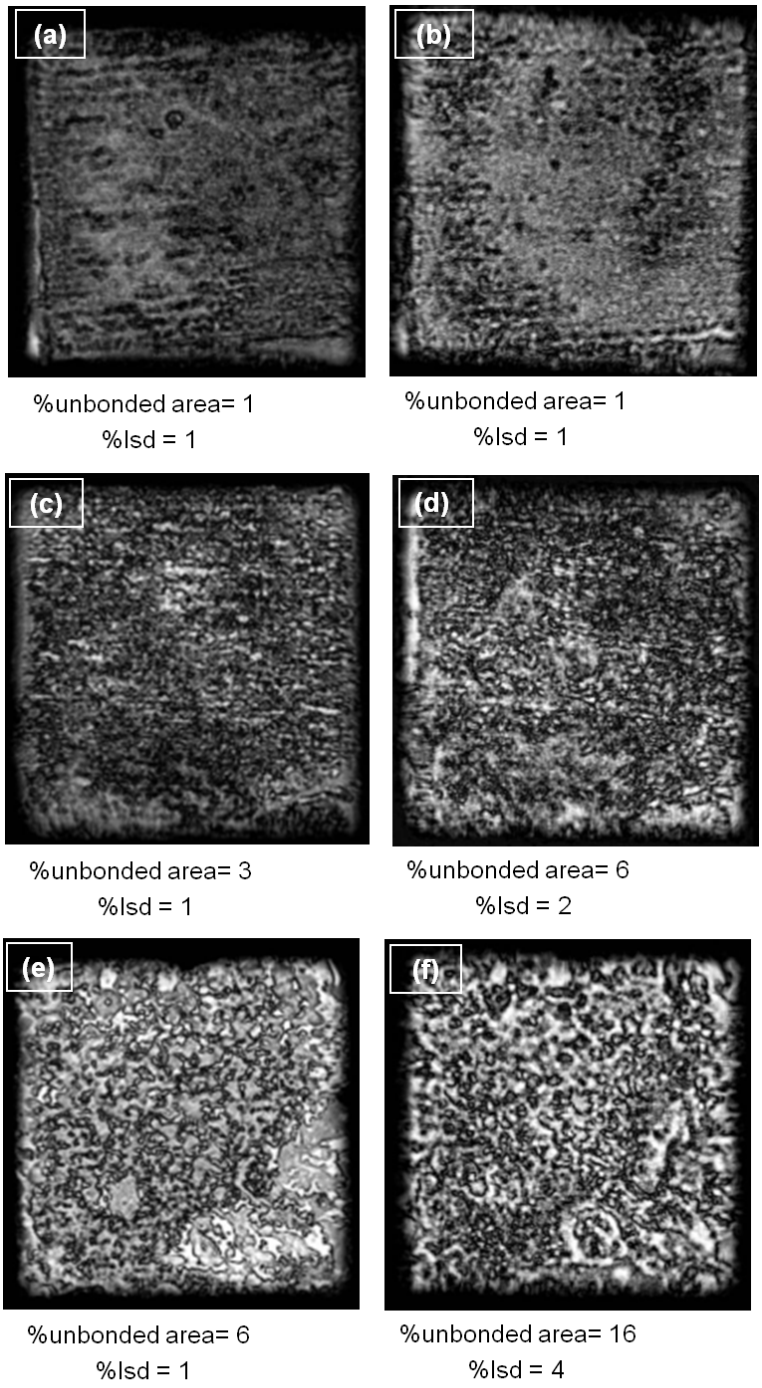


Figure 6.9: SAM images of Au-Si die bonds, from the optimised batch: (a), (c), and (e) in the as-manufactured condition; (b), (d), and (f) after isothermal ageing at 300^{o}C, for 672h. Percentages of unbonded area and largest single defect, (lsd) are given for each C-SAM image.

ter isothermal ageing at 300^{o}C. Note that the BA_i values are different for each ageing time as they were independent samples (i.e. sub-batches of the large batch of 150 Au-Si die bonds). Overall, there was a reduction in the bonded

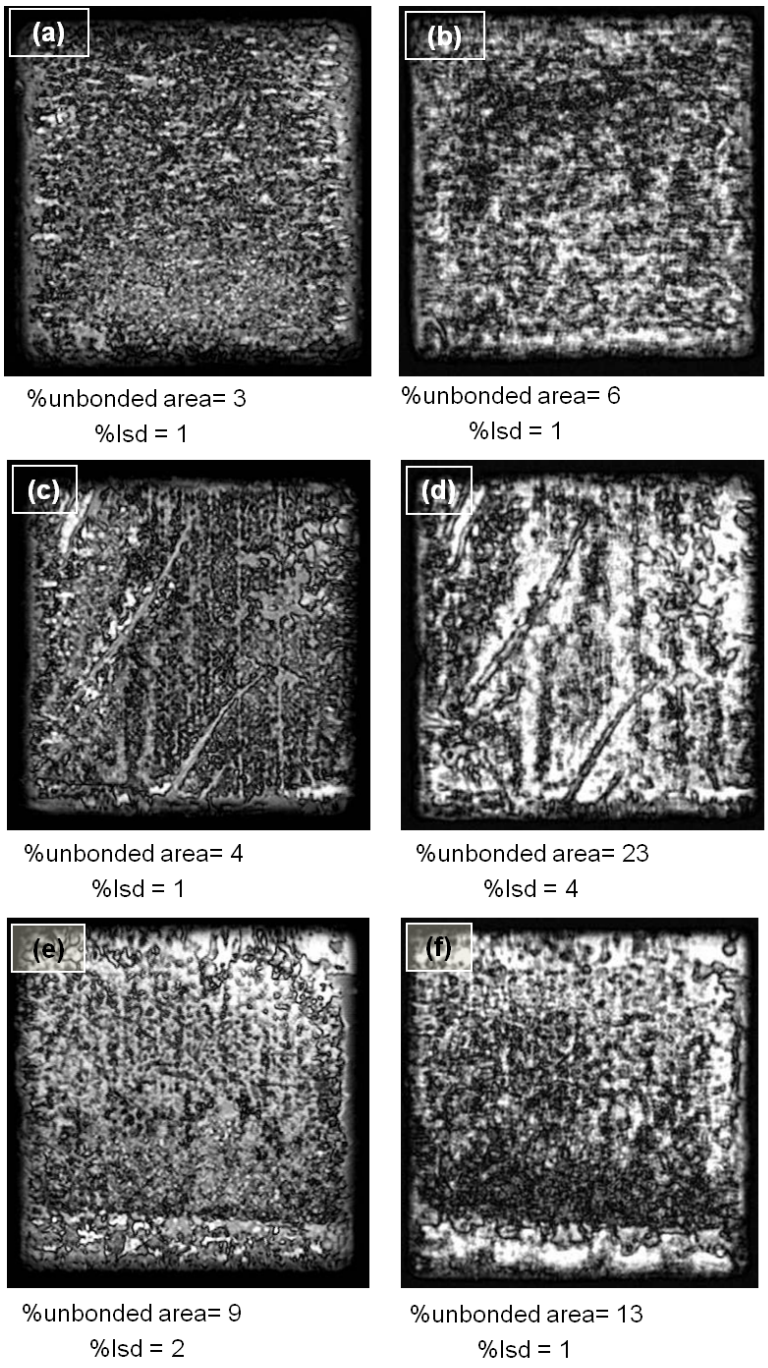


Figure 6.10: SAM images of Au-Si die bonds, from the optimised batch: (a), (c), and (e) in the as-manufactured condition; (b), (d), and (f) after isothermal ageing at 300^{o}C, for 2016h. Percentages of unbonded area and largest single defect, (lsd) are given for each C-SAM image.

area that became more pronounced at longer exposure times. Small voids or regions of no bonding formed initially during the eutectic attachment process due to imperfections or contamination tended to grow with time at high temperature, presumably driven by the release of strain due to any thermal

Table 6.1: Bonded area ranges of Au-Si die bonds before (BA_i) and after isothermal ageing (BA_f) at 300^{o}C, for various periods of time.

Ageing time (h)	$\mathbf{BA_i}$ **(%)**	$\mathbf{BA_f}$ **(%)**
168	94-99	94-99
672	91-100	84-99
2016	90-98	77-94

mismatch on heating.

The boxplot in Figure 6.11 shows a comparison of bonded area distribution for the Au-Si die bonds as a function of high temperature storage time. At a first glance, it is clear that the maximum bonded area was practically the same ($\approx$ 99%) for die bonds aged for 168 and 672h. Nevertheless, the maximum bonded area for the longest storage time (2016h) decreased to $\approx$ 94%. On the other hand, the minimum value registered for the bonded area decreased with time; the minimum bonded areas obtained for 168, 672 and 2016h were $\approx$ 94, 84 and 77%, respectively. Consequently, the amplitude (difference between maximum and minimum bonded areas) increased and was 5% for 168h, 15% for 672h and 17% for 2016h. The mean bonded area (small square within the boxes) for the aged die bonds decreased with increasing exposure time, and was 97(2)% for 168h, 94(5)% for 672h, and 88(4)% for 2016h (stand. deviation in brackets). For the lowest storage time, the variance was 3.2, and increased for longer times and was 7 and 6 times higher for 672 and 2016h. The skewness was negative for all three ageing conditions which meant that the lower area side of the distribution for each box was more pronounced. Despite the degrading effect of thermal exposure on bonded area, somewhat surprisingly, the aged Au-Si die bonds from the optimised batch maintained a significant bonded area.

Shear testing was also then performed on the Au-Si die bonds. Of the 45 Au-Si die bonds aged at 300^{o}C, 42 specimens (14 for each storage time) underwent shear testing using the Dage Series 4000 shear machine with a

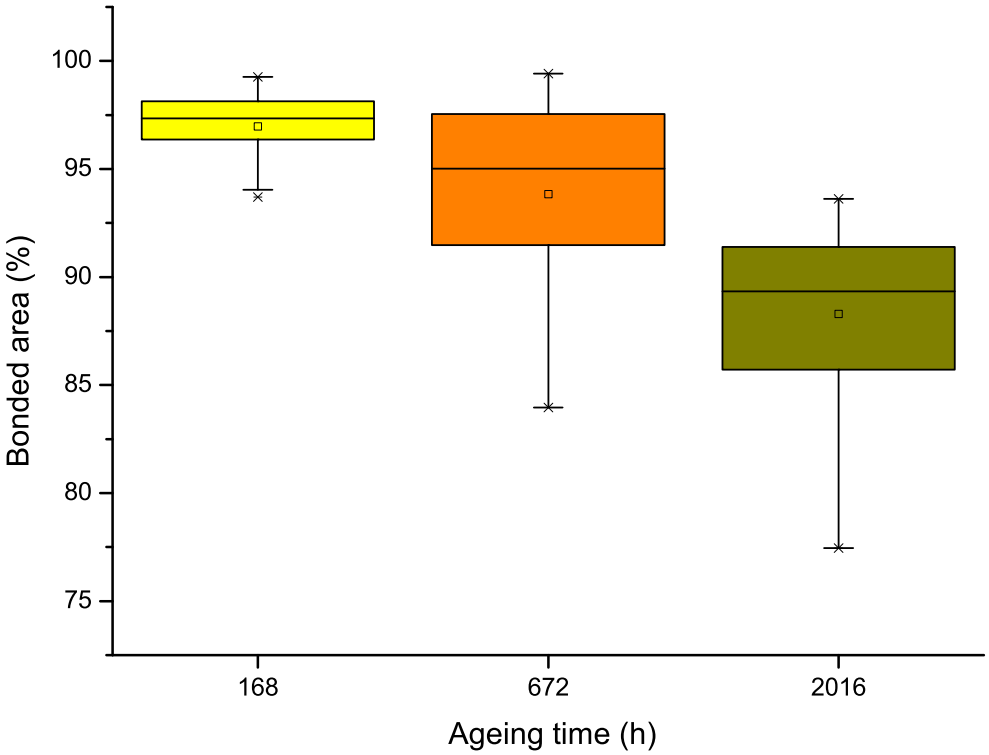


Figure 6.11: Boxplot of bonded area of Au-Si die bonds as a function of isothermal ageing at 300^{o}C for 168, 672 and 2016 hours.

100kg load cartridge.

The boxplot in Figure 6.12 shows a representation of the failure shear loads as a function of storage time. The mean shear load decreased with increasing ageing time: ageing for 168, 672 and 2016h produced mean shear loads to failure of 27(12), 25(9) and 18(9)kg (stand. deviation in brackets). This data is consistent with the distribution of bonded areas shown in Figure 6.11; a decrease in the mean bonded areas promoted a corresponding decrease in mean shear load to failure with increasing storage time. Nevertheless, the aged Au-Si die bonds maintained comparatively high mean shear load to failure in all cases.

The failure mode for the sheared die bonds was investigated. Die bonds aged for 168h suggested two possible failure modes. Failure within the die attach/substrate interface was the most predominant failure mode (failure mode 3); 11 of the 14 die bonds fell in this category. In addition, the separation of die attach from the substrate was accompanied with partial or total

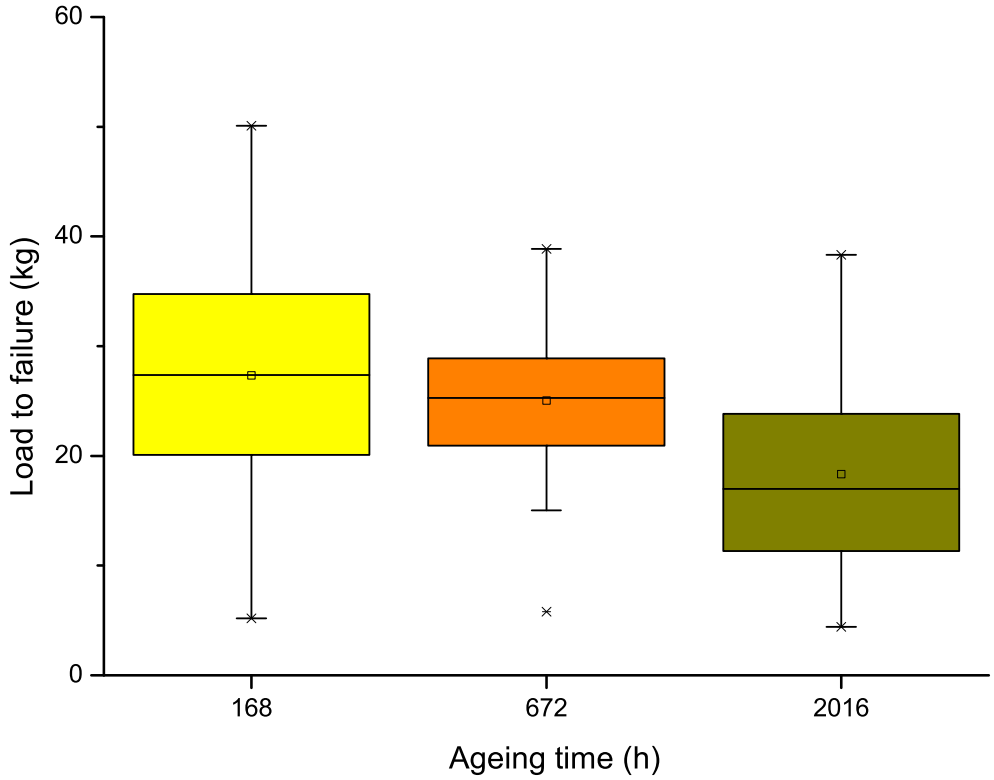


Figure 6.12: Boxplot of load to failure of Au-Si die bonds as a function of isothermal ageing at 300^{o}C for 168, 672 and 2016 hours.

removal of the Au metallisation from the substrate. There was also shearing of the Si die with residual Si remaining (failure mode 1) in 3 die bonds. After 672h, there was a slight decrease in shear load to failure, and the predominant failure mode was again mode 3 between the Au-2wt%Si preform and the substrate. There was a similar scenario for the longest ageing time with all die bonds at 2016h showing failure mode 3 as the most predominant (14 die bonds). Table 6.2 summarises the different failure modes for each sub-batch of Au-Si die bonds aged at 300^{o}C.

The effect of thermal exposure at 300^{o}C on the average shear strength is shown in Figure 6.13. The data is plotted as the shear force (kg) divided by the die area (mm^2). Each value represents an average value of 14 measurements. There was an overall decrease in the average shear strength, which was more significant during the first 168h of ageing. The average initial die shear strength was $\approx$ 2kg/mm^2 with the failure occurring at the Si die (failure

Table 6.2: Failure modes registered for the die sheared Au-Si die bonds aged at 300^{o}C for 168, 672 and 2016 hours. A total of 42 die bonds were subjected to die shear; 14 die bonds for each storage time. Mode 1 - shearing of Si die with residual Si remaining; mode 2 - separation of die from the die attach medium; mode 3 - failure within the die attach/substrate interface.

	Ageing time (h)		
	168	672	2016
Mode 1	3	-	-
Mode 2	-	1	-
Mode 3	11	13	14

mode 1). After 168h ageing at 300^{o}C, the average shear strength decreased to 1.3kg/mm^2 with mixed failure mode, but preferentially at the Au-Si/substrate interface where the thick film Au lifted off. On increasing the ageing time, the average shear strength decreased gradually to 1.2kg/mm^2 for 672h and 0.9kg/mm^2 for 2016h.

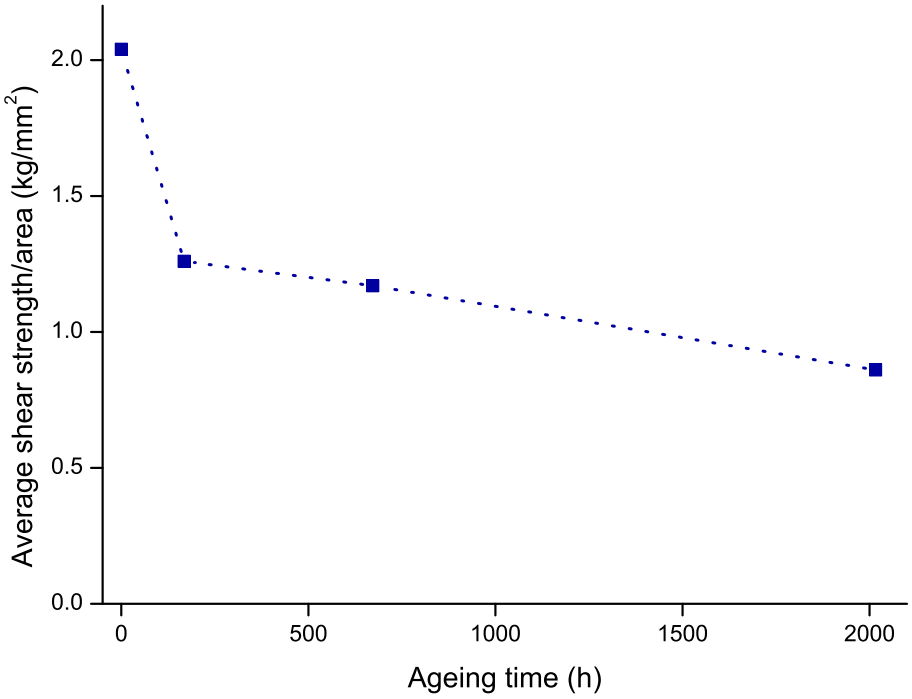


Figure 6.13: Average die shear strength as a function of ageing at 300^{o}C with Si/Au-Si/Au metallised substrate bond.

Interdiffusion in the Au-Si die bonds for the as-manufactured condition was studied earlier in this section. For comparative purposes, the same analysis was carried out after the die bonds underwent thermal exposure.

The aged solder bonds, at 300^{o}C for 2016h, were also cross-sectioned and examined by EPMA. Figure 6.14 shows EPMA maps for the aged die bond in the Si die/Au-Si solder/Al_2O_3 substrate region. Figure 6.14(a) shows the backscattered electron image and Figures 6.14(b), (c), (d), (e), (f), (g) and (h) show the elemental concentration maps for C, O, Al, Si, Au, Bi and Cd respectively. Figure 6.14(a) shows a considerable degree of chemical inhomogeneity in the solder region following thermal exposure. Figure 6.14(e) shows that Si-rich regions were formed within central regions of the solder, suggesting the comparatively rapid diffusion of Si in Au. Comparing the O (Figure 6.14(c)) and Si (Figure 6.14(e)) signals, it was possible to confirm that there was Si precipitating out of the Au close to the die. There was also a thin diffusion layer of Si in the surface of the Al_2O_3 substrate not remarked prior to ageing. This ready and continued Si diffusion may have caused the adhesion decrease of the thick film Au. This would explain why the aged die bonds, when shear tested, changed failure mode from as-manufactured bonds, with the Au peeling of the substrate becoming the dominant mode. The Au map in Figure 6.14(f) shows that Au was not as uniformly distributed as it was in the as-manufactured condition (Figure 6.6(a)); instead there were now Au rich regions dispersed within the Au-Si solder layer. The maps in Figures 6.14(g) and (h) show that Bi and Cd diffused into the Au-Si solder.

Figure 6.15 is a EPMA line-scan from the Si die towards the substrate, with a step size of 1μm and a total length of 83μm for Au, Si, and O concentrations. The backscattered electron image where the line-scan was performed is shown in Figure 6.15(a). Figure 6.15(b) shows that the Si concentration slightly varied as the interface with the Au-Si was approached, dropped to close to zero within the first part of the preform and then drastically increased to $\approx$ 40wt% after at a distance of 30μm into the preform. This region of high Si concentration within the preform was associated with O, and was therefore concluded to be SiO_x formation as Si diffusing from the die met O

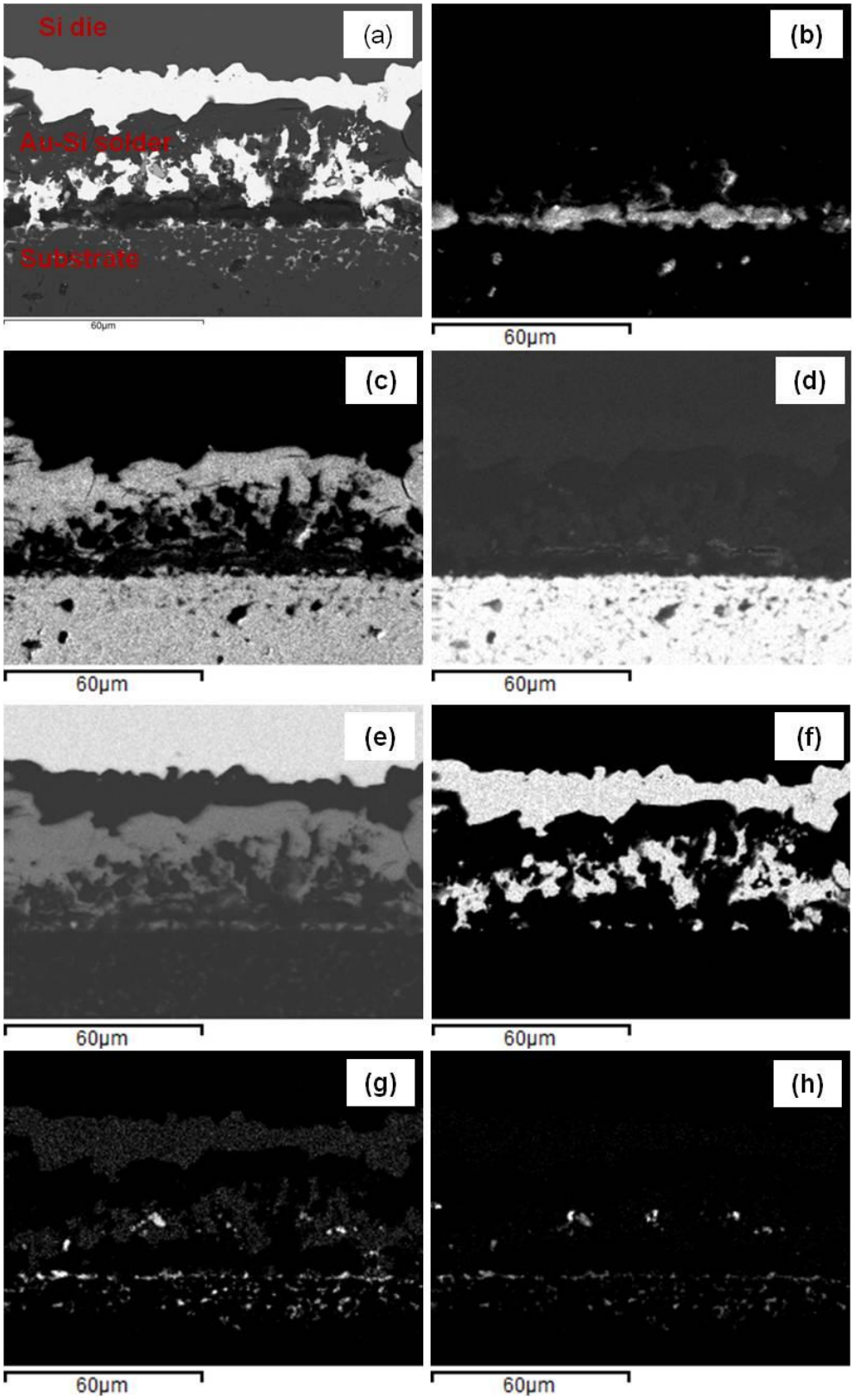
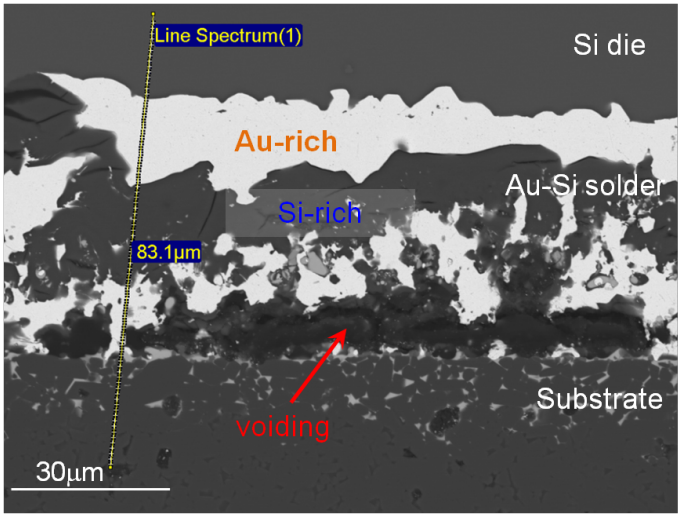


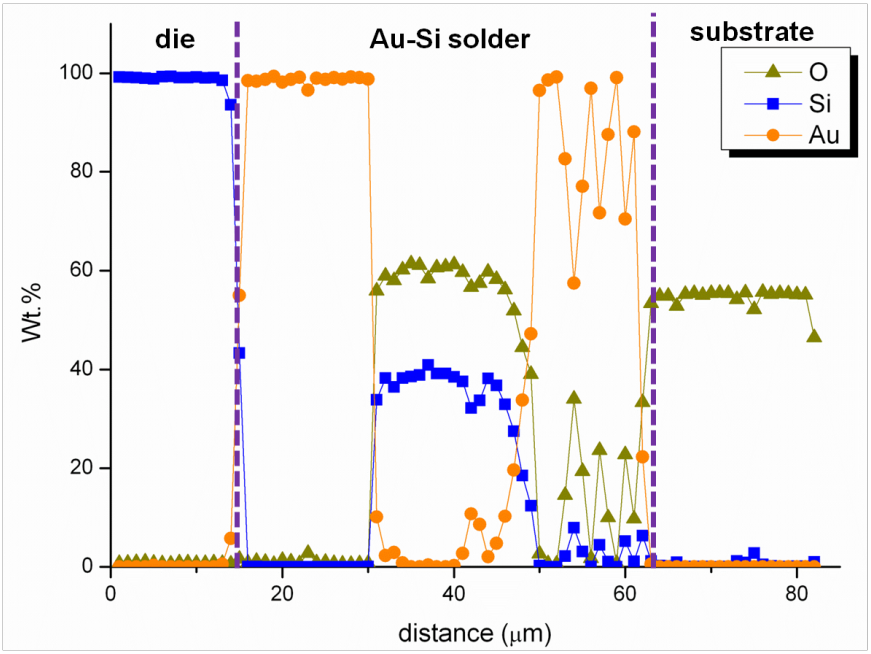
Figure 6.14: EPMA mapping of a typical Au-Si die bond after isothermal ageing at 300°C, for 2016 hours, in the region Si die/Au-Si solder/Al_2O_3 substrate: (a) backscattered electron image; (b) C map; (c) O map; (d) Al map; (e) Si map; (f) Au map; (g) Bi map; and (h) Cd map.

diffusion from the substrate. The SiO_x was not uniform, but occurred in apparently randomly dispersed islands throughout the preform. Similarly to the as-manufactured condition (Figure 6.7(b)), there was no detectable Au in the Si until the approximate of the Si/Au-Si interface was reached, and thus indicating again very limited diffusion penetration. Beyond the SiO_x region, the Si concentration again reduced. The backscattered electron image in Figure 6.15(a) confirms that Au and Si were not evenly distributed but rather formed Au-rich and SiO_x-rich areas. At the Au-2wt%Si/thick film gold interface (at $\approx 62\mu m$ distance) the Si concentration decreased accompanied with an increase in O concentration, not seen on the upper side of the Au-2wt%Si preform next to the die. A similar scenario occurred for the die bonds in the as-manufactured condition (Figure 6.7(b)). In addition, there was high number of voids at the Au-Si/substrate interface which could further explain the failure of the aged die bonds at this interface.

Nanoindentation was used to determine the mechanical properties of the solder on Au-Si die before and after ageing at 300^oC for 2016 hours. The mechanical characterisation of the solder was carried out by performing several indentations in the area of interest using the Micro Materials Nanotest platform, at room temperature, as described in Chapter 3. The residual stress that may evolve in the solder layer is dependent not only on its coefficient of thermal expansion but also on the elastic modulus. The hardness and Young's modulus of the Au-Si solder region, before ageing, were determined by nanoindentation to be 2.3GPa and 150GPa respectively. After ageing, the hardness reduced to 1GPa and the elastic modulus was reduced by half to 72GPa. Although the indentation values are only indicative, the relative change after ageing suggested that one way that residual strain is accommodated during/after ageing is by the degradation of the solder properties which makes the solder much more compliant, protecting the interfaces from accumulating damage. This may explain in part how the die bonds, when sub-



(a)



(b)

Figure 6.15: EPMA line-scan from the Si die towards the substrate for a Au-Si die bond after isothermal ageing at at 300°C for 2016 hours: (a) SEM backscattered electron image where the line-scan was performed, with a step size of $1\mu m$ and a total length of $83\mu m$; (b) diffusion profiles for Au, Si and O across the Si die/Au-Si solder/Al_2O_3 substrate region.

jected to time at high temperature, still presented a reasonable shear load to failure.

6.2.2 Accelerated ageing at 350^{o}C

To investigate how the Au-Si die bond microstructure might evolve during service, accelerated ageing at a higher temperature, 350^{o}C, was performed on optimised Au-Si die bonds. This temperature exceeds any service temperature forecast by GE AS at the project outset. Thirty specimens were aged, with 5 samples removed after 500h of thermal exposure, and the others aged to 850h. Visual inspection showed a slight darkening of the Au-Si solder protruding from around the die for both batches. Very occasionally, the Si dies showed edge cracks in the batch exposed for the longest time.

Digital image analysis measurements of the percentage unbonded area before and after the accelerated ageing were performed. Rather than relying on previous measurements of the as-manufactured bonded area from other batches to give the "baseline" behaviour, this was re-measured for this specific batch. After 500h at 350^{o}C, the range of unbonded area increased to 1-16%. The largest single defect increased up to 4%. On extending exposure time up to 850h, there was an increase in the variability of the assessed unbonded area to 6-74%. A similar trend occurred for the largest single defect, with the range increased to 1-74%. In a few cases, unbonded areas appeared to link together so that the largest single defect occupied the whole region of unbonded area.

The batch of samples that underwent accelerated ageing at 350^{o}C for 500h were generally well-bonded. Figure 6.16 shows two SAM images in which the contrast between as-manufactured and after accelerated ageing was chosen to demonstrate the cases where the change was more marked. The development of the white unbonded areas was clear in both cases, but especially in die bond shown in Figure 6.16(b) which had an unbonded area $\approx$ 10 times larger than as-manufactured in Figure 6.16(a). The die bond in Figure 6.16(d) had a more pronounced contrast and ageing promoted a three

fold increase in final unbonded area. Unbonded areas were generally located preferentially at the periphery of the die.

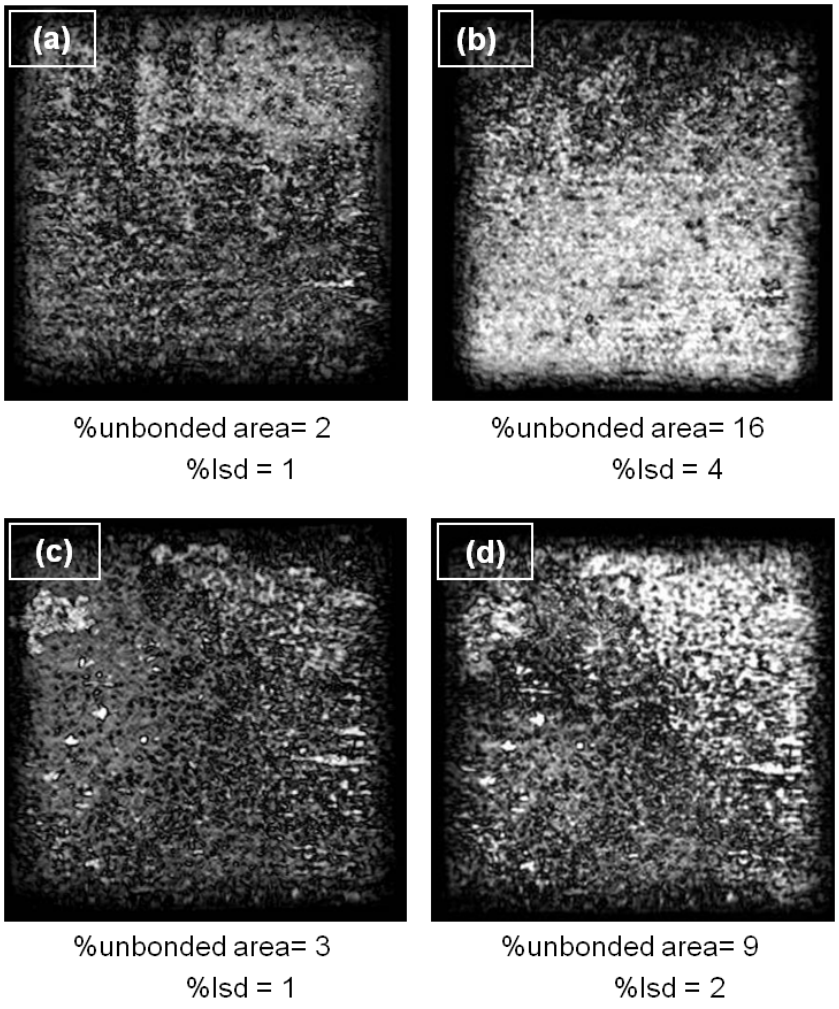


Figure 6.16: SAM images of two typical Au-Si die bonds before ((a) and (c)) and after accelerated ageing at 350^{o}C for 500h ((b) and (d)), and corresponding percentages of unbonded area and largest single defect, (lsd). Note the increase in white regions (unbonded areas) after ageing.

Figure 6.17 shows 9 of 25 imaged specimens after 850h at 350^{o}C. As expected, there was a high fraction of white area. Yellow arrows point to examples of black areas where the signal was lost which was almost always specifically due to edge cracking of the Si die (see microstructures later). Small unbonded areas, randomly dispersed, in the as-manufactured condition gave rise to larger and contiguous unbonded areas after accelerated ageing.

Table 6.3 summarises the bonded area ranges for the Au-Si die bonds

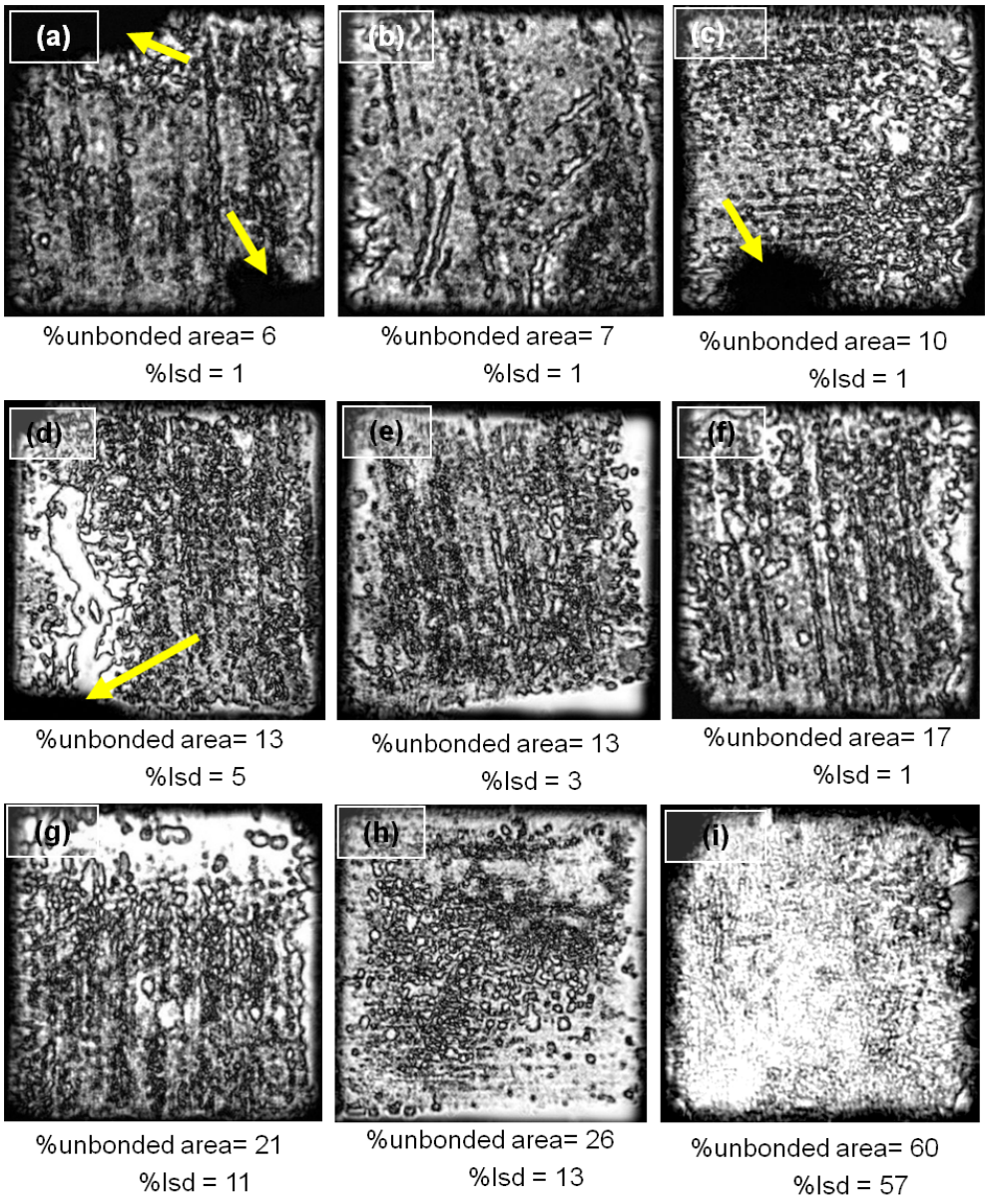


Figure 6.17: SAM images of various Au-Si die bonds after accelerated ageing at 350°C for 850h. The percentage of unbonded area and largest single defect, (lsd) are given for each case.

before and after accelerated ageing at 350°C for 500 and 850h. Somewhat surprisingly, the aged die bonds maintained a significant mean bonded area. Accelerated ageing for 500 and 850h yield a mean bonded area of 94(7) and 65(25)% respectively (std. deviation in brackets).

The effect of accelerated ageing on the Au-Si die bonded area for 500 and 850h is shown in Figures 6.18 and 6.19 respectively. Figure 6.18 confirms a broadening of the initial narrow spread of bonded areas. Although the max-

Table 6.3: Bonded area range for Au-Si die bonds before and after accelerated ageing at 350^{o}C for 500 and 850 hours.

Ageing time (h)	**BA_i (%)**	**BA_f (%)**
500	97-99	84-98
850	83-99	26-94

imum bonded area was approximately the same before and after ageing, the minimum bonded area reduced to 83%.

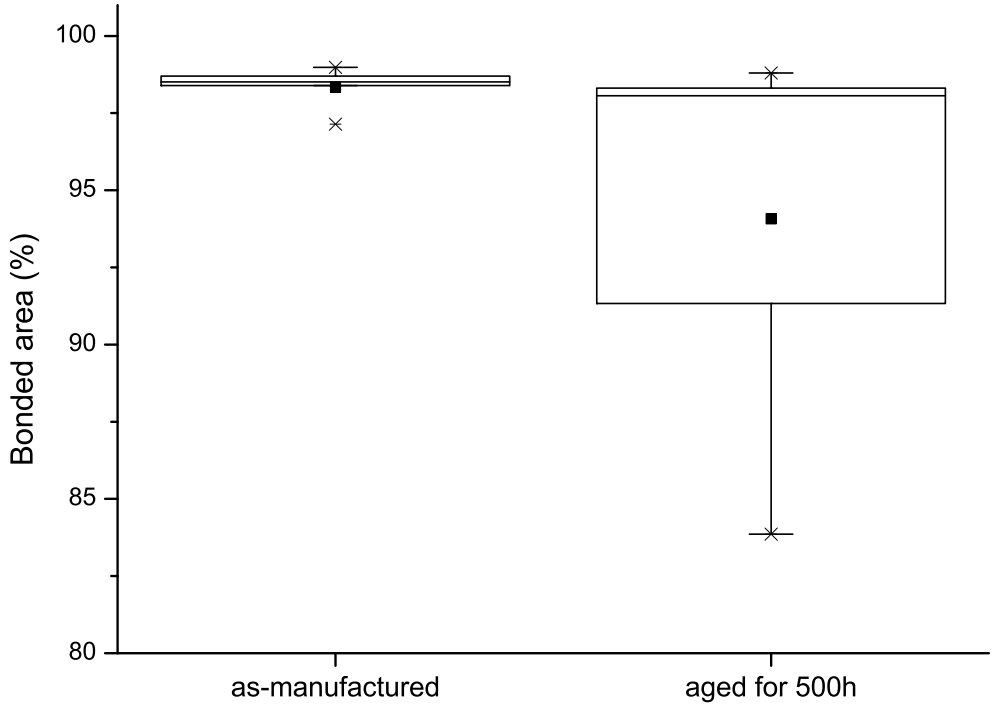


Figure 6.18: Boxplot of bonded area of Au-Si die bonds before and after accelerated ageing at 350^{o}C for 500 hours.

Figure 6.19 shows that despite a much broader range of the initial bonded areas in this particular batch, this range was nonetheless further increased by ageing at 350^{o}C for 850h.

The failure shear load Au-Si die bonds after ageing at 350^{o}C was also investigated. Every die bond exposed for 500h was sheared tested whereas of the 25 die bonds aged for 850h, only 20 were shear tested with the others retained for metallography and/or forwarded to GE AS for further work. The failure mode was investigated for both ageing times. The main failure mode was the same for 500 and 850h, and occurred at the die attach/substrate in-



Figure 6.19: Boxplot of bonded area of Au-Si die bonds before and after accelerated ageing at 350^{o}C for 850 hours.

terface (failure mode 3), 5 specimens aged for 850h showed peeling of the Au metallisation from the substrate.

The boxplot in Figure 6.20 shows that most of the shear load failure of the samples aged for 500h fell in a narrow distribution with a mean of 32kg, a standard deviation of 13.8kg, with a single outlier at $\approx$ 8kg . After 850h, the spread of most failure loads had increased and the mean failure load had reduced to 16kg with a standard deviation of 8.1kg. Note that the mean bonded area obtained was 94% for 500h and 65% for 850h so that broadly a decrease in bonded area led to a lower failure load in shear.

The Au-Si die bonds after 350^{o}C for 850h were cross-sectioned, as shown in Figure 6.21. Figure 6.21(a) shows that one of the Si die edges was fractured. The other edge exhibited a crack in the Si die exactly in the same spot. Au-eutectic bonds are considered "hard" and are considered to readily transmit stress to the die [84], which can result in die cracking. Also, because the stresses increase as the radial distance from center increases, the highest

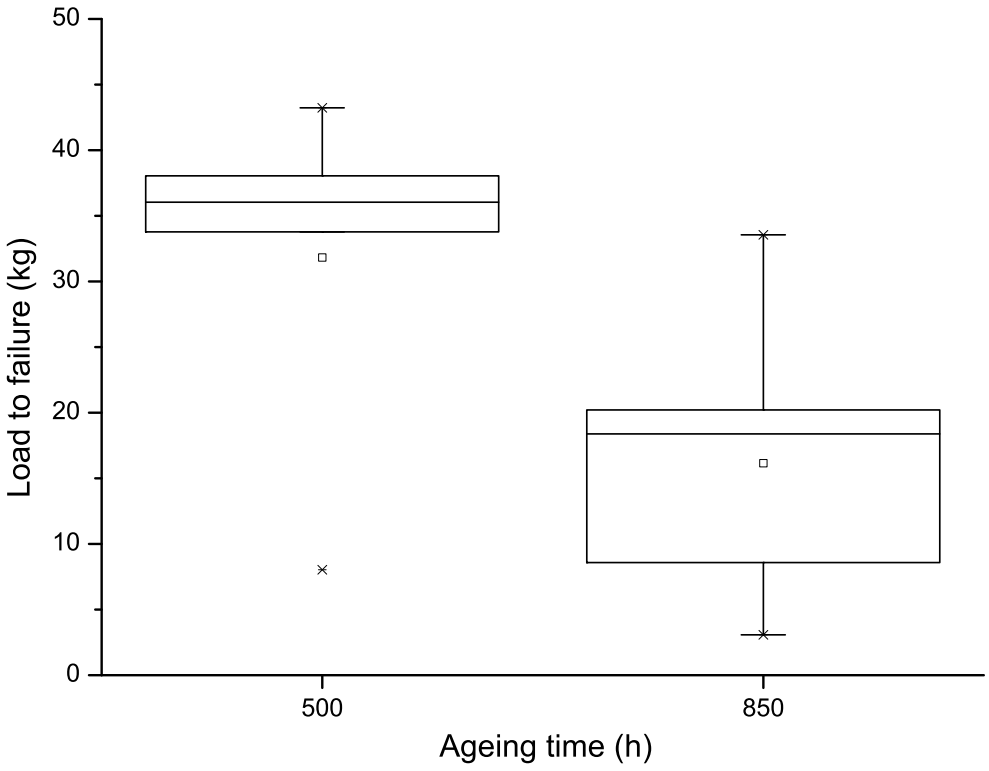


Figure 6.20: Boxplot of shear load to failure of Au-Si die bonds after accelerated ageing at 350^{o}C for 500 and 850h.

stresses are found at the corner of the Si die, and thus cracks are prone to occur. The shape of the typical fillet region formed against the vertical walls of the Si die was completely altered by ageing. Also, the fillet was partially cracked and detached from the Si die. Very occasionally, there were fragments of fractured Si in the fillet area but otherwise the fillet showed a few Si crystals that primarily had coarsened during the ageing process. Despite the low solubility of Si in Au, there was sufficient diffusion for Si from within the preform and from the die itself to diffuse to feed the coarsening of the larger Si crystals. This effect led to the dissolution of any fine scale Au-Si eutectic formed during solidification. In Au-rich regions, the largest Au grains were $\approx$ 15μm compared with an average Au grain size of $\approx$ 2.5μm as-manufactured. In addition, debonding often occurred in the die lower corner, with partial separation of the Si from the Au-Si die attach layer. Unbonding also occurred along the Au-Si/substrate interface as shown in Figure 6.21(b). Figure 6.21(c) shows that the Au-Si solder layer exhibited cracking as a result of stresses

derived from the CTE mismatch between the Si die, the Au-Si die attach material and the ceramic substrate. Crack forming in the die attach material was accompanied by voiding mainly located at the Au-Si/substrate interface. Kessel *et al.* [95] concluded that failure of eutectically bonded devices by vertical die cracking can be attributed to locally high stresses caused by voids. Furthermore, using FE analysis, they showed that stresses developed at centre voids are not likely to initiate cracks. As the area of the die increases, the problem with voiding becomes more important because of larger stresses and greater difficulty in controlling void formation. The largest void found at the Au-Si preform/substrate interface measured $\approx 35\mu m$. Furthermore, these unbonded areas located at the Au-Si/substrate interface were consistent with the failure mode for the aged die bonds when shear tested. Note that the die bonds failed at that same interface together with some Au peeling. Accelerated ageing also promoted some fractured surface of the Au-Si solder (mainly in the fillet region) together with material removal as can be seen in Figure 6.21(d).

6.3 Thermal cycling and thermal shock

To evaluate the thermal cycle performance of the Au-Si die bonds, temperature cycling and thermal shock stressing of dies mounted on the Au metallised Al_2O_3 substrates using Au-Si preforms was performed. The thermal profiles for thermal cycling and thermal shock, were described in Chapter 3, and can be summarised as a -40 to 250^{o}C cycle with > 3 hours high and low temperature dwell. The transfer time between the maximum and minimum temperature was $\approx$ 30min for thermal cycling and $\approx$ 5min for thermal shock. The effect of these thermal cycles on bond integrity was evaluated.

Due to limited access and availability of the thermal cycling rig at GE AS, and the long time required for cycling experiments, samples were tested

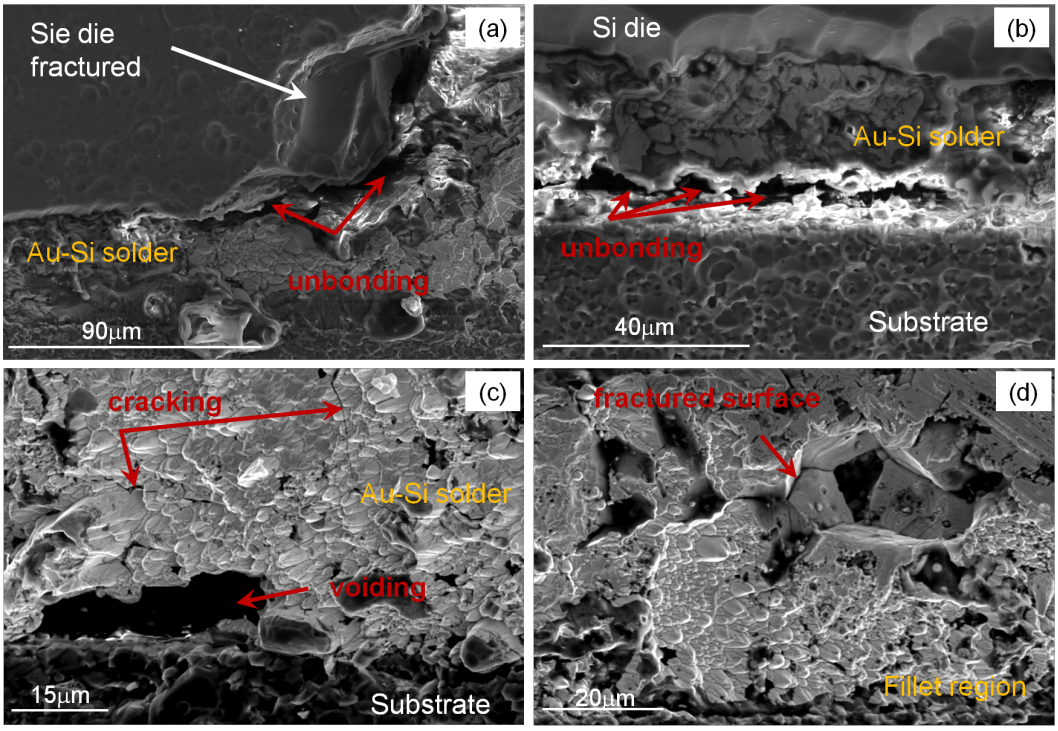


Figure 6.21: Cross-section SEM images of Au-Si die bonds after accelerated ageing at 350^{o}C, for 850h, showing some interfacial defects: (a) fracture of Si die lower corner; (b) debonding at the Au-Si preform/substrate interface; (c) cracking in the die attach material and voiding at the Au-Si preform/substrate interface; and (d) fillet region exhibiting fractured surface in the Au-rich region.

only for 10 and 40 cycles, and this data set was too small to perform a meaningful statistical analysis. Nevertheless, useful information and insights were gained, and cross-sections were studied that showed accumulated damage and deterioration of the die bonded areas. A "failure criterion" for the die bonds was developed based on the variation of bonded area relative to the as-manufactured bonded area.

6.3.1 Assessing bond quality

A total number of 20 Au-Si die bonds were subjected to cyclic thermal exposure: 10 for thermal shock and 10 for thermal cycling. Of the 10, 3 were removed after 10 cycles, with the remaining receiving a total of 40 cycles. The only visual degradation of the solder bonds after thermal cycling and thermal shock was a dark coloration in the Au-Si solder region. Occasionally, Si die

edges appeared cracked.

The Au-Si die bonds subjected to thermal shock for 10 cycles comprised unbonded areas of 6 to 8%, and the corresponding largest single defect ranged up to 6%. Thermal cycling, for the same number of cycles, yielded unbonded areas between 5 to 13%, and the largest single defect spanned a narrower range of 1 to 2%. Figure 6.22 shows typical SAM images for 10 cycles of thermal shock (Figures 6.22(a), (b), and (c)) and thermal cycling (Figures 6.22((d), (e) and (f)). The yellow arrows in the acoustic images in Figures 6.22(a) and (c) point to black regions where the signal was lost due to Si edge cracking. There was no clear trend in this more limited number of samples in the location of white unbonded areas but the general impression was that large and contiguous unbonded areas were preferentially located around the die periphery.

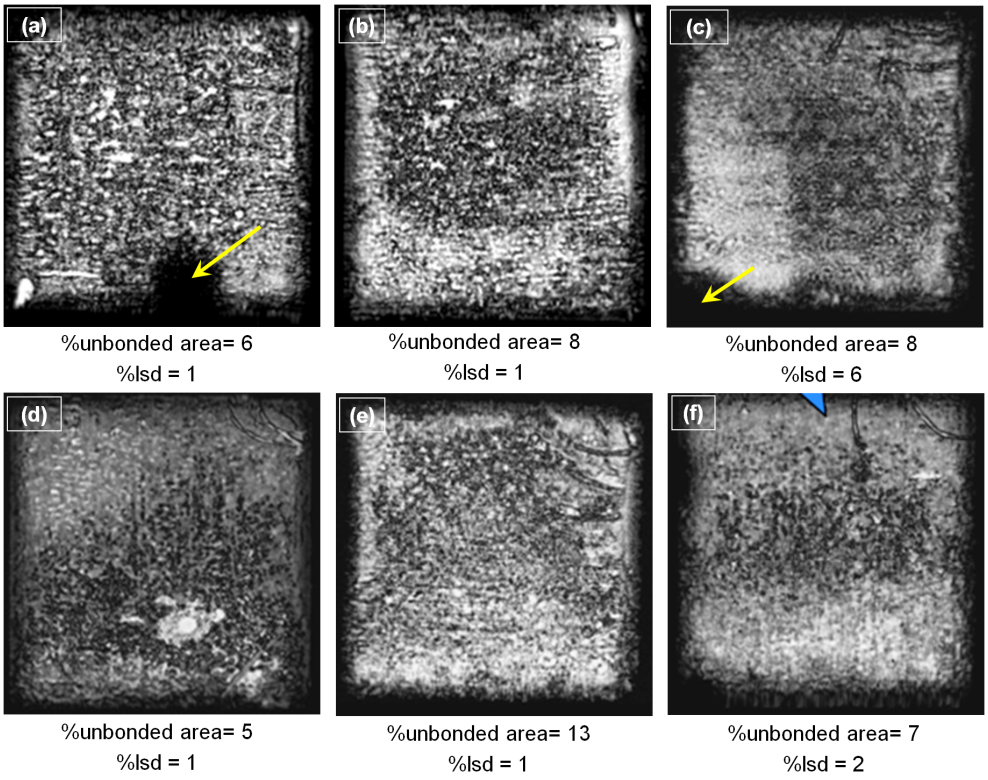


Figure 6.22: SAM images of Au-Si die bonds after thermal shock ((a), (b), and (c)) and thermal cycling ((d), (e), and (f)), from -40 to 250^{o}C, 3 hours dwell, for 10 cycles. Percentages of unbonded area and largest single defect, (lsd) are presented.

Table 6.4 shows the conversion of percentage of unbonded area into

percentage of bonded area, summarising the variation in bonded area before and after thermal exposure. Of 3 specimens tested for thermal shock, only 1 showed a possible, slight change in bonded area from 98 to 92% (almost within estimated experimental error). The range of final bonded areas remained comparatively high and ranged from 92-94%, again within experimental error. Of 3 die bonds subjected to thermal cycling, 2 saw their final bonded area decreased and the overall bonded area varied from 87-95%. Recognizing the small data sets, these observations suggested that thermal cycling over 10 cycles may promote more damage to the bond than thermal shock. Nevertheless, the overall bonded areas remained comparatively high, and the bond was surprisingly robust.

Table 6.4: Variation in bonded area ranges for Au-Si die bonds in the as-manufactured condition (BA_i) and after thermal shock and thermal cycling (BA_f), from -40 to 250^{o}C, for 10 cycles.

	$\mathbf{BA_i}$ (%)	$\mathbf{BA_f}$ (%)
Thermal shock	92-98	92-94
Thermal cycling	91-95	87-95

On increasing the number of thermal cycles to 40, the range of unbonded area increased and was accompanied by increase in the area of the largest single defect. All die bonds that underwent thermal shock and thermal cycling showed evidence of unbonded areas located at both Si die/Au-Si solder and Au-Si solder/substrate interfaces, with increases in unbonded area generally concentrated at the Au-Si solder to ceramic substrate interface region.

Figure 6.23 shows SAM images from die bonds that underwent 40 cycles of thermal shock. The unbonded area varied from 5 to 17% and the largest single defect spanned the range 1 to 12%. For example, Figure 6.23(e) shows a large contiguous unbonded area distributed along the periphery of the die area. The majority of this type of contiguous unbonded area (Fig-

ures 6.23(a), (b), (d) and (g)) was mainly concentrated in the peripheral die area whereas small, random distributed voids were dispersed in the central die area. Two die bonds showed a decrease in percentage of unbonded area (and consequently, in the largest single defect). Voids might have collapsed or diminished to an extent that if below the resolution limit, the DIA measurements would not be able to quantify those. Again, the yellow arrows in the corresponding SAM images point to dark regions as a result of signal loss.

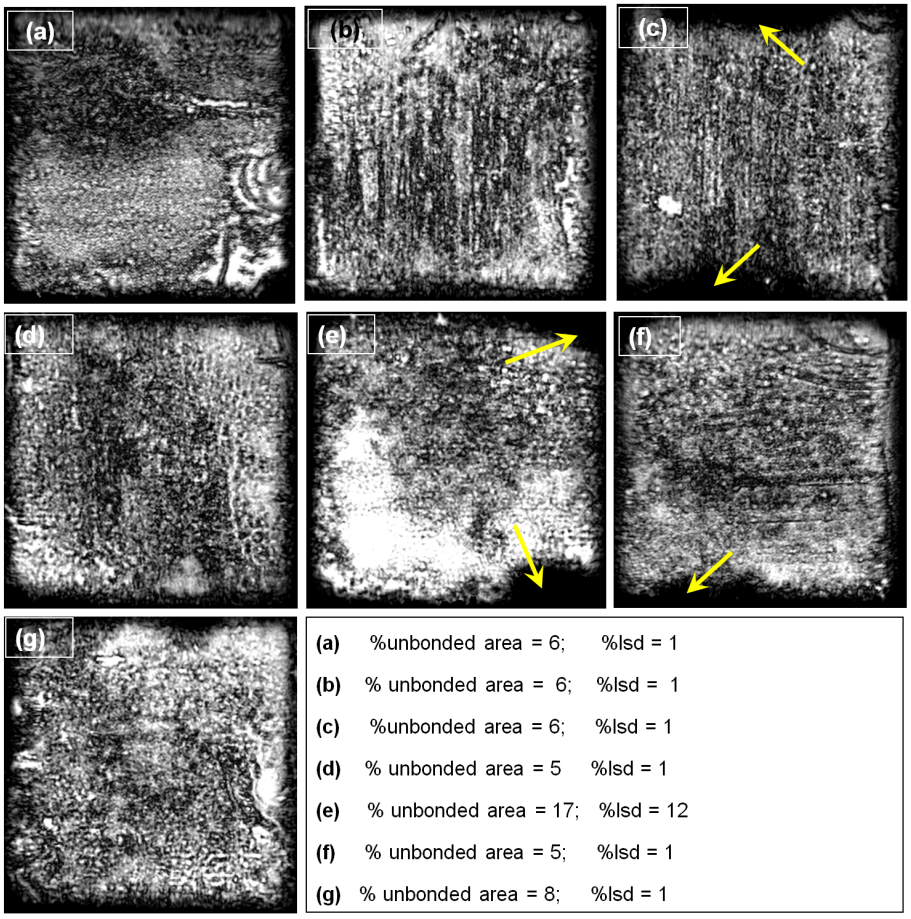


Figure 6.23: SAM images of the Au-Si die bonds after thermal shock, -40 to 250^{o}C, for 40 cycles. Percentages of unbonded area and largest single defect, (lsd) are given for each case.

Similarly to the behaviour for 10 cycles, the unbonded area after thermal cycling for 40 cycles showed little change from the as-manufactured condition, and consequently, no SAM images are shown. The unbonded area ranged from 2 to 25%, and the largest single defect from 1 to 20%. Only one die bond suffered a considerable increase in unbonded area.

The variation in bonded area before and after 40 cycles of thermal exposure is summarised in Table 6.5. Overall, the bonded area of the Au-Si die bonds after thermal shock and thermal cycling for up to 40 cycles showed only a slight degradation. The final bonded area of die bonds after thermal cycling fell in the range of 75 to 98% with a mean bonded area of 93% (standard deviation of 4.3%). Thermal shock led to bonded areas ranging from 83% to 95%; the mean bonded area was again 93% (standard deviation of 4.2%).

Table 6.5: Bonded area ranges for Au-Si die bonds before (BA_i) and after 40 cycles of thermal shock and thermal cycling (BA_f).

	$\mathbf{BA_i}$ (%)	$\mathbf{BA_f}$ (%)
Thermal shock	91-96	83-95
Thermal cycling	90-99	75-98

The data is also summarised in the boxplot in Figure 6.24 that confirms that the various die bonds sub-batches suffered only a slight decrease in the mean bonded area after 40 thermal shock cycles (TS40). The main effect was to decrease the minimum bonded area from 91% to 83%. The majority of the die bonds were in the upper half of the distribution. Similarly for thermal cycling, the minimum bonded area was reduced, decreasing from 90% to 75%, and again, most of the distribution was also concentrated in the upper half of bonded areas. Overall, thermal cycling induced slightly more "damage" in bond integrity at the lower end of the bonded area distribution although the mean bonded areas were essentially the same. Assuming the small data set is representative, then 75% of the die bonds comprised bonded areas > 92% for thermal shock and > 88% for thermal cycling.

The Au-Si die bonds that underwent 40 cycles were also tested for die shear force to failure, 5 for thermal cycling and 5 for thermal shock, with remaining samples retained for microstructural analysis. The distribution of the die bonds shear load after thermal shock (TS40) and thermal cycling (TC40) are shown in the boxplot of Figure 6.25. The failure mode for the

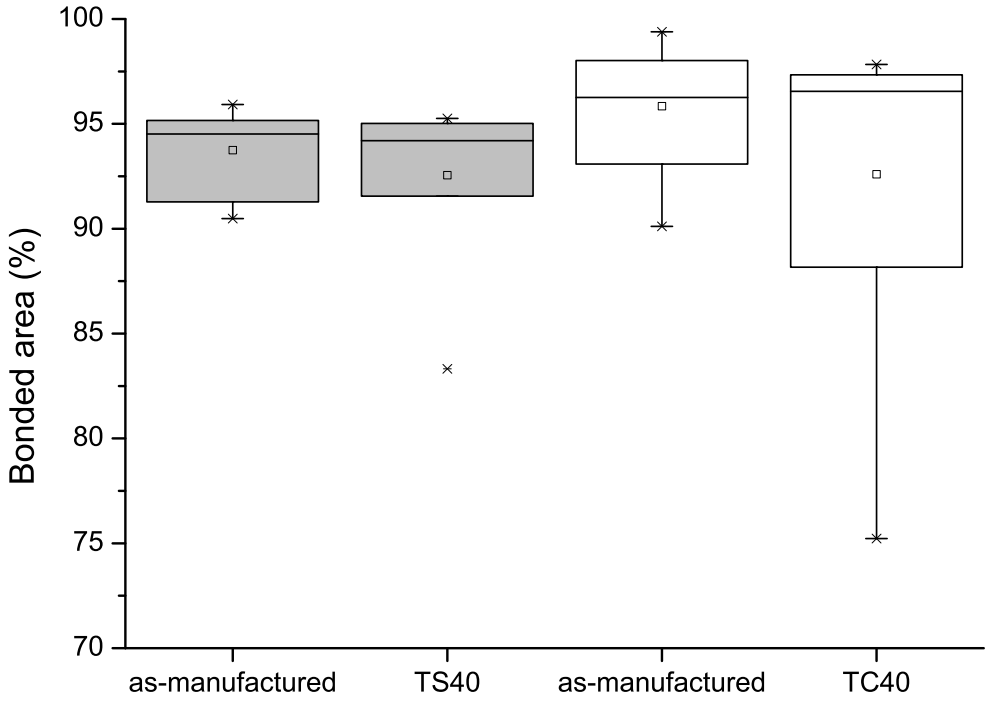


Figure 6.24: Boxplot of bonded area for the Au-Si die bonds in the as-manufactured condition and after thermal shock (TS40), and as-manufactured and after thermal cycling (TC40), from -40 to 250^{o}C, for 40 cycles.

sheared Au-Si die bonds was also evaluated. The failure for the die bonds after thermal shock occurred preferentially with shearing of Si die with residual Si remaining (failure mode 1), with some partial separation of die and die attach medium from the substrate (failure mode 1 combined with failure mode 3). In addition, the Au metallisation on the substrate was seen to spall from the substrate. Failure mode 1 was also the predominant failure mode for the die bonds that underwent thermal cycling.

The boxplot in Figure 6.25 shows a comparison of the distribution of shear load to failure for thermal shock and thermal cycling. The variance of shear load distribution for the solder bonds after thermal shock was half that of thermal cycling, which was consistent with the bonded area distribution shown in Figure 6.24. The minimum and maximum shear loads to failure were 18kg and 80kg in the TS40 batch against 24kg and 108kg for TC40. Thermal shock yielded a mean shear load to failure of 44kg (s.d.=25kg) lower than that of thermal cycling of 62kg (s.d.=35kg). Note that the standard de-

viation of the distributions was comparatively large - and consistent with the increase in range of bonded areas previously shown. The effect of cyclic thermal exposures was to primarily increase the spread of failure loads rather than produce dramatic decreases for all specimens; again, thermal cycling appeared slightly more damaging than thermal shock.

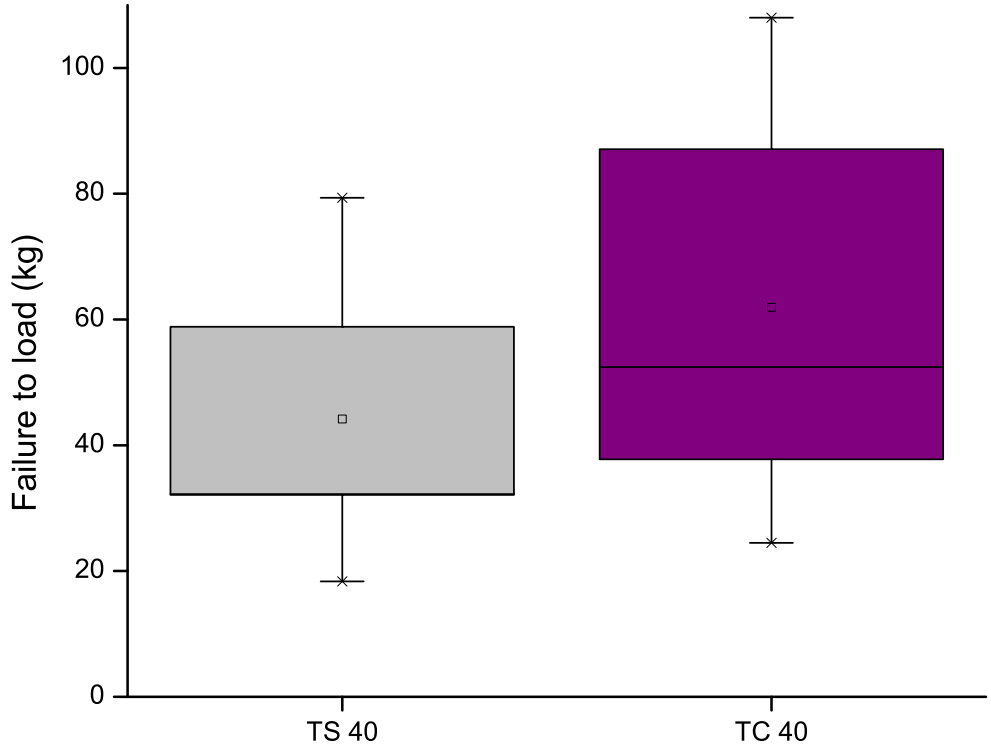


Figure 6.25: Boxplot of shear load to failure of Au-Si die bonds after thermal shock (TS40) and thermal cycling (TC40) from -40 to 250^{o}C, for 40 cycles.

Figure 6.26 shows a plot of die shear loads against the corresponding bonded areas for the Au-Si die bonds after thermal shock and thermal cycling indicating only a weak correlation on a sample-by-sample basis, reinforcing the need to always describe die attach behaviour in the systems in terms of statistical data, drawn from meaningfully large data sets.

6.3.2 Microstructural characterisation

Figure 6.27 shows cross-section SEM images of the solder bonds that underwent 10 cycles of thermal cycling. Thermal cycling induced microcracks in

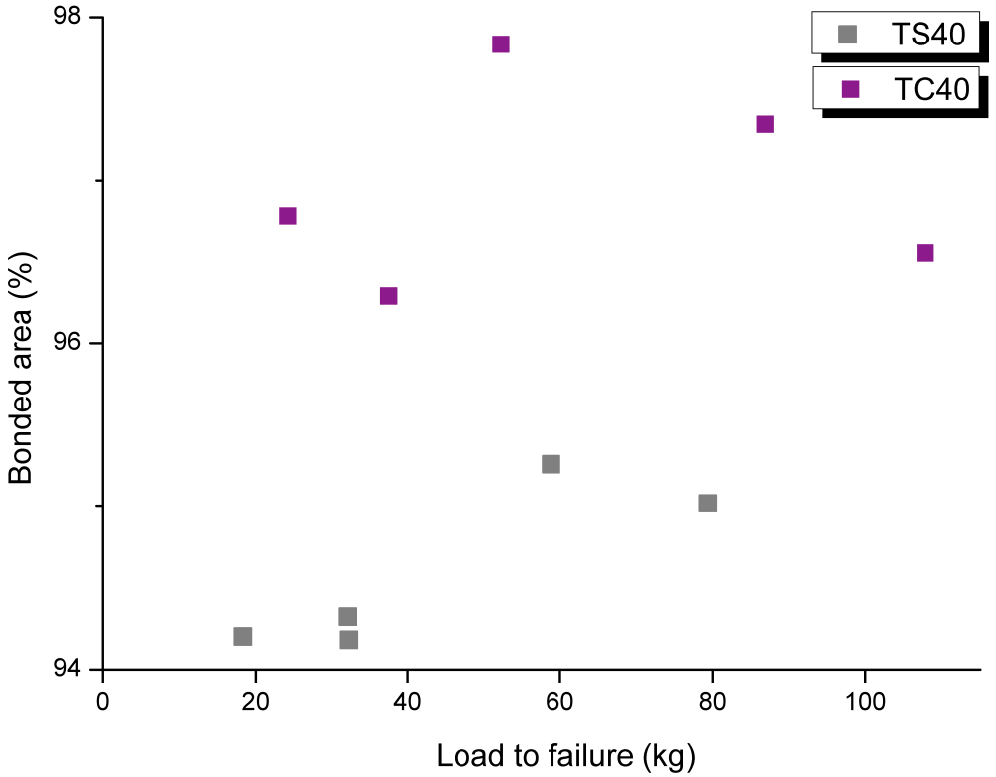


Figure 6.26: Correlation between bonded area and load to failure of the Au-Si die bonds after thermal shock (TS40) and thermal cycling (TC40) from -40 to 250^{o}C, for 40 cycles.

the Au-Si solder layer, as shown in Figure 6.27(a). The microcracks were due to stresses deriving from the differential thermal expansion of the Si die and the Al_2O_3 substrate. The cracks in the Au-Si solder generally followed a pronounced zig-zag path, and generally extended for only a short distance of 5-10μm. Figure 6.27(a) shows also that cracking was frequently initiated or accompanied by voiding within the Au-Si solder layer where voids typically were few μm in size (in cross-section). There was horizontal Si die cracking and unlike the Au-Si layer, cracks were often comparatively straight and extended, resulting often in complete fracture of the Si, especially at the die edges. The bonding layer generally had adequate mechanical strength withstand and/or ability to relax thermally induced strains to endure without leading to highly damaging thermal fatigue [143]. Voids in the solder tended to generate localised stress on the back of the die, which may cause die cracking either during the bonding or during thermal cycling [96]. Figure 6.27(b)

shows interfacial delamination with partial separation of the Si die from the solder. Note the lack of solder in this area. The delamination extended for $\approx 40\mu m$. It was not always possible to reliably discern between a void (usually induced by manufacture) and delamination (usually induced by thermal exposure). As shown in Figure 6.2(c), the Au-Si microstructure consisted of dispersed sub-micron sized Si crystals as either plates or angular particles depending on the extent of microstructural coarsening in a soft matrix of essentially pure Au. Figure 6.27(c) was typical of many images that suggested Si preferentially diffused to the fillet region of the bond, where it coarsened with time. This Si may originate from within the Au-2wt%Si preform by dissolution at the Si/Au-Si interface or occasionally be derived from Si fragments from the cracked Si die periphery. The average size of the Si crystals was $\approx 10\mu m$.

On increasing the number of cycles to 40, the Au-Si die bonds presented similar features: cracking in the Au-Si solder in zig-zag and crack blunting, Si die cracking (especially at edges), voids encouraging cracking in the die, and coarsening. One of the fillets was partially detached from the Si die in the upper corner (Figure 6.27(d)) whereas the other fillet region showed fracture of the Si die in the lower corner (Figure 6.27(e)).

The microstructure of the Au-Si die bonds after 10 cycles of thermal shock, from -40 to 250^{o}C, is presented in Figure 6.28. The cross-section SEM image in Figure 6.28(a) shows that cracking within the Au-Si solder layer was more pronounced and, similarly to thermal cycling microstructure, the crack propagated in a zig-zag path. Figure 6.28(b) shows that cracking also occurred at the die/Au-Si solder interface. Voiding in the Au-Si solder, horizontal cracking in the Si die and interfacial delamination at the Si/Au-Si solder region were also visible on die bonds after 10 and 40 cycles of thermal shock.

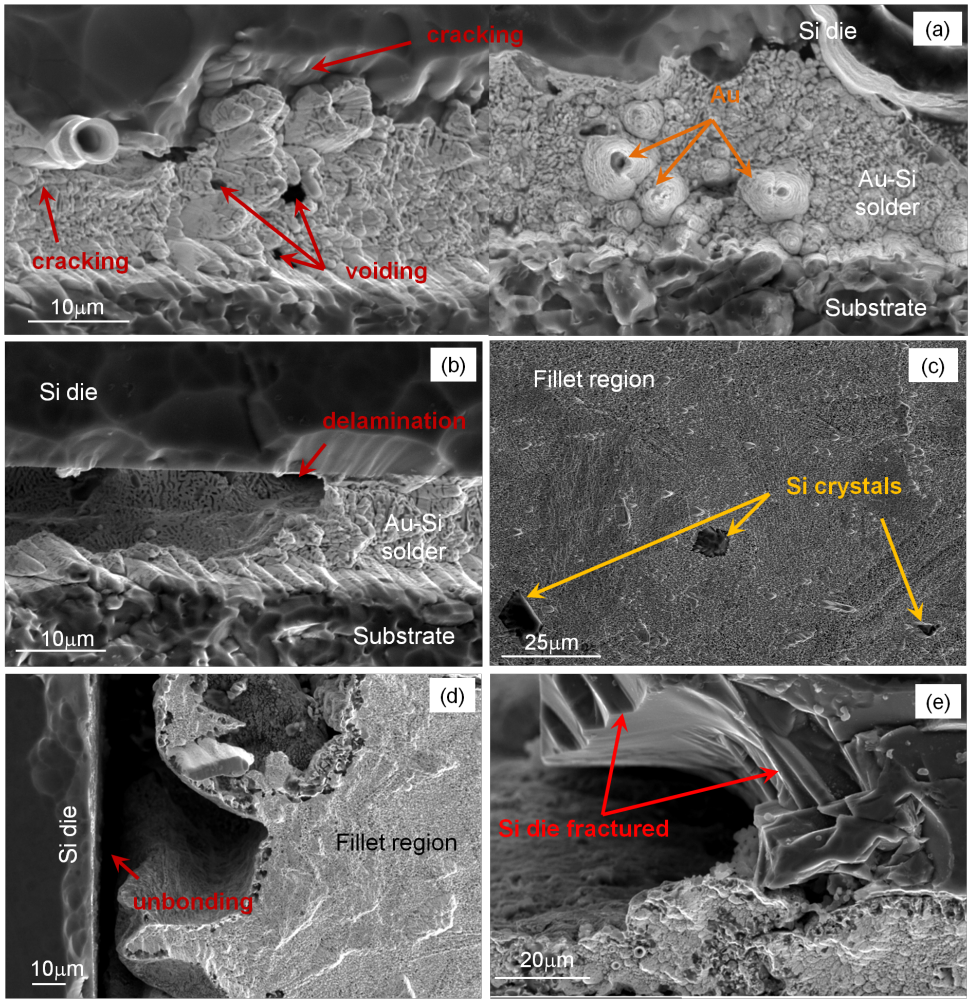


Figure 6.27: Cross-section SEM images of the Au-Si die bonds after thermal cycling, from -40 to 250^{o}C, for 10 cycles ((a), (b) and (c)) and 40 cycles ((d) and (e)), showing: (a) horizontal Si die cracking, voiding and microcracks within the solder region; (b) delamination at the Si die/solder interface; (c) and Si crystals located in the fillet region; (d) fillet unbonded from the Si die; (e) Si die fractured.

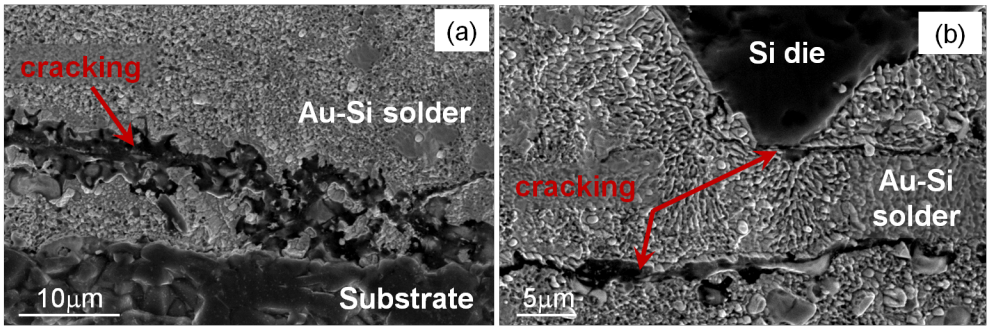


Figure 6.28: Cross-sections SEM images of the Au-Si die bonds after thermal shock, from -40 to 250^{o}C, for 10 cycles showing: (a) pronounced crack at the Au-Si solder region in a zig-zag path; (b) Au-Si solder cracking with a zig-zag propagation path.

6.4 High temperature performance of SOI devices

Although Si based electronics have been shown to function at temperatures of up to 200^{o}C, the key problem is the performance degradation due to an increase in leakage currents at elevated temperatures. This problem can be virtually eliminated through the use of silicon on insulator (SOI) technology where a monocrystalline film of Si is deposited on top of an insulating layer.

This section presents results of high temperature endurance studies on SOI devices combined with high temperature packaging technologies relevant to signal conditioning, and processing functions for sensors in downwell and aero-engine applications. The endurance studies were performed for up to 11088h at 250^{o}C, with device electrical performance measurements being tested at room temperature, 125^{o}C and 250^{o}C. Different die attach and wire bond options have been included in the study and the performance of multiplexers, transistors, bandgap voltage, oscillators and voltage regulators functional blocks have been characterised.

Die attach materials, wire-bond interconnect, passive attach materials and, ceramic and insulated metal substrates were identified as being of particular concern for the development of reliable high temperature packaging solutions packaging solutions [5], and the results of the work carried out were presented in the previous sections.

Most of the work undertaken in the thesis was conducted on Al_2O_3 substrates and HTCC packages which can withstand the 250^{o}C temperature exposure requirements. A SOI based integrated circuit based on the X-FAB $1\mu m$ SOI process was designed at GE AS and manufactured with analogue signal conditioning, ADC/DAC (analogue to digital conversion/digital to analogue conversion) and simple logic control as described in Table 3.4 and Figure

3.9 [171]. The SOI device had dimensions of 4.5mm x 4.0mm.

6.4.1 SOI devices in HTCC packages

Based on the packaging technologies developed above, samples using SOI device were assembled into HTCC packages. The assembled packages were submitted to temperature storage at 250^{o}C for up to 11088h. Measurements were conducted at 25^{o}C, 125^{o}C and 250^{o}C before and after high temperature storage for 3360, 4704, 7056 and 11088h, and Table 6.6 summarises the electrical test results of the various functions on SOI devices assembled in HTCC packages. Functions multiplexer and N-transistor used Au-Si as die attach material whilst bandgap voltage, oscillator and voltage regulator used JM7000 adhesive. The results are described in a publication [172] by GE AS, based on the work developed in this thesis, and showed that, in general, stable performance was achieved for all the functions evaluated, indicating that the device architecture and packaging technology can withstand the continuous 250^{o}C environment for at least up to 7056h exposure as reported in [173]. However, extending the exposure time up to 11088h led to some devices showing a deterioration in their functionality as shown in Table 6.6 [172].

The samples assembled using a conductive high temperature adhesive were analysed in an optical microscope. Figure 6.29 shows an optical micrograph of the surface of the adhesive bonded SOI device after a total of 11088h exposure at 250^{o}C. Whiskers had grown in these samples around the bond pad areas. The whiskers appeared to grow randomly from the bond pads over the surface of the device.

Further examination in the SEM revealed that whiskers were present on both unbonded pads and wire bonded pads as shown in Figures 6.30(a) and (b), respectively. The nature of the whiskers was not determined but were likely Ag based, arising from the Ag used to fill the JM7000 adhesive,

Table 6.6: Electrical test results on SOI device assembled in HTCC packages [172].

Device function	**T °C**	**Storage time at 250°C, h**				
		0	**3360**	**4704**	**7056**	**11088**
Multiplexer	25	3405Ω	3740Ω	3517Ω	3434Ω	3902Ω
	125	3667Ω	3779Ω	3782Ω	3768Ω	3912Ω
	250	3795Ω	3838Ω	3778Ω	3778Ω	3838Ω
N-transistor	25	112μA	110μA	110μA	109μA	118μA
	125	190μA	188μA	190μA	161μA	1050μA
	250	295μA	295μA	268μA	294μA	5438μA
Bandgap voltage	25	2.61V	2.61V	2.61V	2.62V	2.61V
	125	2.66V	2.66V	2.66V	2.64V	2.65V
	250	2.70V	2.69V	2.69V	2.69V	2.69V
Oscillator	25	4.97V	4.96V	3.34V	3.19V	0.43V
	125	5.26V	4.95V	4.89V	4.89V	0.37V
	250	4.32V	4.95V	4.87V	4.87V	0.57V
Voltage regulator	25	4.38V	4.38V	4.36V	4.36V	4.36V
	125	4.56V	4.56V	4.55V	4.50V	4.53V
	250	4.82V	4.80V	4.80V	4.79V	4.76V

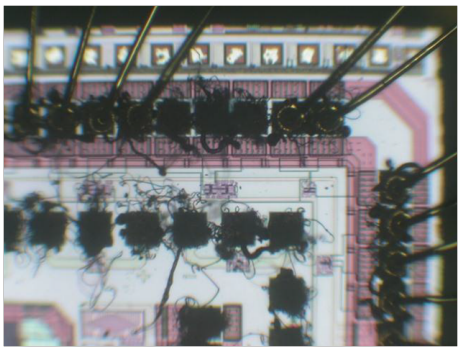


Figure 6.29: Optical micrograph of surface of the adhesive bonded SOI devices after 11088h exposure to 250^{o}C showing whiskers centred around the bond pads, taken from [172].

although whiskers were often coated with C-rich material from the adhesive.

The same analysis was conducted for the samples bonded using Au-2wt%Si eutectic as die attach material. SEM images of a typical unbonded bond pad and a wirebonded bond pad of Au-Si eutectic bonded SOI device after 11088h exposure to 250^{o}C are shown in Figure 6.31. In this case, the devices did not show any sign of whiskers either on the unbonded bond pads

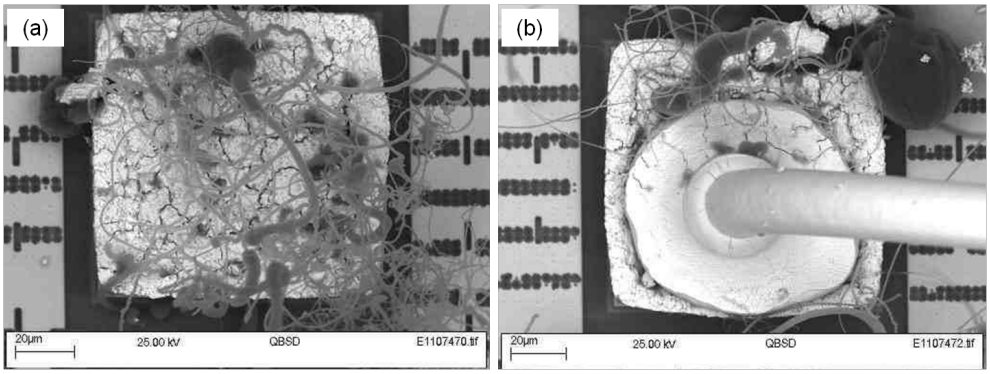


Figure 6.30: SEM images of (a) unbonded bond pad and (b) wirebonded bond pad of adhesive bonded SOI device, after 11088h exposure to 250^{o}C [172].

or the wirebonded bond pads [172].

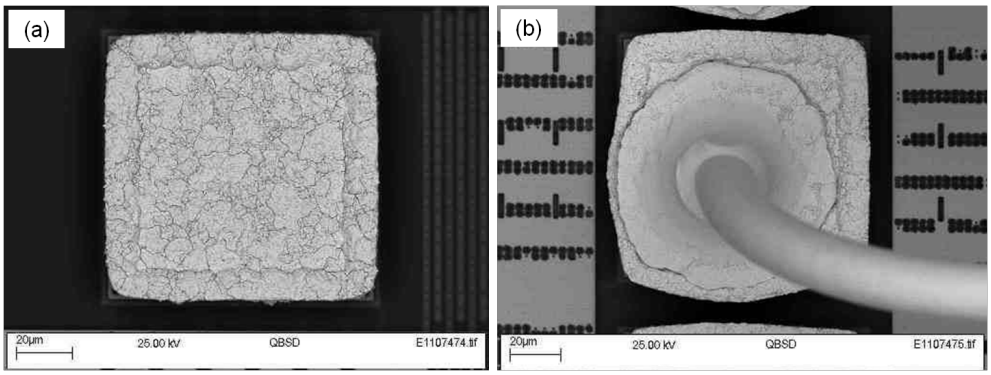


Figure 6.31: SEM image of (a) unbonded bond pad and (b) wirebonded bond pad of Au-Si eutectic bonded SOI device, after 11088h exposure to 250^{o}C [172].

Residual gas analysis (RGA) was undertaken on the HTCC package cavities containing the devices assembled with the high temperature adhesive and Au-Si eutectic. The analysis showed that there were considerable quantities of high mass organics and CO_2 within the package cavity for the conductive adhesive bonded sample which were not found in the sample bonded using Au-Si eutectic. It is suggested that the adhesive die attach material degraded after the continuous exposure to 250^{o}C for 11088h. The whiskers around the bond pads may have developed from the Ag organic deposits produced by degradation of the adhesive die attach material. The reason for the congregation of the whiskers around the bond pads remained unclear.

It was not clear if the degradation in electrical performance was related to degradation effects taking place in the bond pad metallisation or due to

the formation of whiskers - that might be expected to lead to electrical short circuits. Some type of balling effect occurred in the Al metallisation under the Au plating, but was not seen when Au-Si eutectic was used as the die attach material.

There was no clear conclusion from these limited samples on whether the die attach material affected the long term electrical performance directly and more extensive work is required. Nonetheless, qualitative information from microscopy suggested that Au-2wt%Si appeared essentially "inert" throughout thermal exposure whereas the Ag/adhesive based die attach clearly underwent degradation, but with a surprisingly small effect on electrical properties over the range studied.

6.5 Conclusions

Optimised die bonding parameters were used to manufacture many nominally identical bonds that were subsequently investigated in terms of their bond quality reproducibility and response to thermal exposure. All specimens contained some unbonded area primarily at the Si die/Au-Si solder, and the mean bonded area was 92%.

Die bonds aged at 300^{o}C showed an overall reduction in bonded area, which increased at longer exposure times. Small voids tended to grow with time at high temperature, presumably driven by the release of strain due to any thermal mismatch on heating. The mean shear load to failure decreased with increasing ageing time which was consistent with the decrease in mean bonded area. Nevertheless, the aged Au-Si die bonds were able to carry significant shear loads (>18kg). Failure within or at the die attach/substrate interface was the most predominant failure mode.

Somewhat surprisingly, die bonds aged at very high temperature of

350^{o}C for 500 and 850 maintained a significant mean bonded area. Microstructural analysis showed cracking within the Au-Si solder region derived from the CTE mismatch between components. Crack formation was accompanied by voiding mainly at the Au-Si/substrate interface which is in agreement with a failure mode predominantly at this interface.

Despite the use of smaller data sets due to access and time availability issues, thermal cycling was suggested to promote slightly more damage to bond quality than thermal shock, suggesting that isothermal high temperature thermal exposure was more damaging than transient effects. Nevertheless, the bonded areas remained comparatively high. In this case, shearing of the Si die with residual Si remaining was the predominant failure mode for die bonds under thermal cycling and thermal shock. The effect of cyclic thermal exposures was to primarily increase the spread of failure loads rather than produce dramatic decreases for all specimens. Thermal shock and thermal cycling yielded mean shear loads to failure of 44 and 62kg, respectively. Cracking within the Au-Si solder layer was more pronounced for bonds after thermal shock and, similarly to thermal cycling microstructure, the crack propagated in a zig-zag path. Cracking also occurred at the die/Au-Si solder interface. Voiding in the Au-Si solder, horizontal die cracking and interfacial delamination at the Si/Au-Si solder region were the main interfacial defects.

High temperature endurance studies on SOI devices combined with high temperature packaging technologies relevant to signal conditioning and processing functions of sensors in down well and aero-engine applications were performed. The results showed an overall stable performance for all the functions evaluated which indicated that the device architecture and packaging technology can withstand continuous 250^{o}C environment for at least 7056h. Microscopy was used to view the packages when the electrical performance of the various functional blocks started to show signs of deterioration, usually at the 11088h exposure point, when some end of life effects on SOI

devices were observed. Whisker growth around bond pads of degraded adhesive die attach material occurred, indicating that organic materials should continue to be carefully assessed before being included in HTE modules.

In the case of Au-2wt%Si, this chapter has shown strong encouragement for its use at 250^{o}C. Although the microstructure undergoes significant change during thermal exposure, and this led to a decrease in bonded area and shear load to failure, residual performance was still well above that required (so far) by industry standards. The results here suggest that critical to realising this potential performance in practice, is by careful optimisation of the initial manufacturing itself, in particular to reduce the spread (variability) of the as-manufactured bonded area, and to maximise the mean bonded area.

CHAPTER 7
Conclusions and future work

The main objectives of this work were to investigate how die attach materials behave under thermal regimes relevant to the harsh down-well environment. This comparative study of die attach strategies for use in harsh environment focused on two die attach systems: adhesives and a Au-2wt%Si eutectic. The main findings of this thesis were:

i) The major obstacle that hampers the application of adhesives for HTE is the rapid deterioration in properties with increasing temperature. Based on thermal exposure tests and cross-section observations, voiding, die cracking, fillet migration/reduction were the main features shown by adhesive die bond on thermal exposure. Ag migration is another concern in package reliability when using Ag-filled adhesives, and was shown by some adhesives studied here.

ii) All adhesives, stored in air at 250^{o}C, showed a reduction in shear load to failure below the 2kg level stipulated by MIL. STD. 883, but which did not occur for samples stored in N_2. Where a protective atmosphere could be guaranteed, adhesives may show some encouragement for elevated temperature use.

iii) Process optimisation and the manufacture of die bonds based on a Au-2wt%Si thin preform was performed under industrial conditions at a subcontractor. The key factors that controlled bonded area between the Si die and substrate were scrubbing parameters (frequency and time). As practised in industry, Au-Si eutectic die bonding leads to a wide variability in

bond quality. The comparatively high melting point of the Au-Si eutectic leads to significant and rapid oxidation of various interfaces in the Si/Au-2wt%Si/Au system used on Al_2O_3 substrates, owing to the relatively high affinity of Si for O. Ensuring oxide break-up lies at the heart of promoting bond quality in this system. In addition, chemical effects and morphology (roughness) of the Au metallisation also played a role in bond quality. Initial ideas that contamination of thick film Au metallisation during manufacture and from the substrate itself inhibited bonding were shown to be less important than ensuring lack of oxidation on surfaces, or its successful break-up. However "contaminants" in the Au were suggested to be important in stopping *excessive* wetting of Au-2wt%Si onto Au, which otherwise and after oxide rupture, was shown to be extremely easy and rapid, removing die bond from out of the bond-line almost completely.

iv) The optimised die bonding parameters were used to manufacture 150 nominally identical bonds and to investigate their subsequent behaviour in terms of reproducibility and response to thermal exposure. High temperature storage yielded an overall reduction in bonded area. Nevertheless, die bonds maintained a significant mean bonded area even after accelerated ageing at 350^{o}C, for up a total of 850h. Because of limited access and availability of the thermal cycling rig at GE AS, and the long time required for cycling experiments, samples were tested only for a total of 40 cycles. Nevertheless, cross-sections showed accumulated damage and deterioration of the die bonded areas. Time at high temperature was more critical for the integrity of the die bonds rather than thermal cycling and thermal shock. Aged die bonds showed more dramatic changes confirmed by microstructural assessment. Nonetheless, shear load to failure degradation was comparatively restricted.

v) The routes for achieving long term stable performance at 250^{o}C for HTE operating at temperatures up to 250^{o}C showed that the use of organic

based adhesives needs to be carefully assessed, as end of life effects after 11088h exposure were observed. Although the whiskering effect may be specific to the high temperature adhesive studied in this programme, any high temperature adhesive used in the electronics industry will need to be investigated particularly for degradation in an inert atmosphere over a long duration (higher than 10000h). This level of assessment was beyond the scope of this thesis. On the other hand, inorganic die attach (Au-2wt%Si), was more stable over long temperature exposure.

Suggestions for future work include:

i) Accelerated ageing for 800h, at 350^{o}C, has been completed on equipment at GE AS, and the experiments will run to completion at 50,000h. These packages should then be inspected at both cross-sectional microscopy and through die scanning acoustic microscopy performed to assess the way in which "damage" is developed and bond integrity undermined.

ii) The data arising from these types of experiments should be used to calibrate numerical simulations of Au-Si die attach transient stresses and strains in service, and to develop appropriate ideas of a failure criterion for these materials. This may be based on accumulated damage ideas i.e. the small amount of plastic strain accumulated in each cycle; or on kinetic models of microstructural change i.e. the coarsening behaviour of voids, or the growth of SiO_2 inside the bond-line, etc. A true "physics of failure" model would require trying these effects together since accumulated strain and microstructural change are likely inter-related, and this in turn would require the measurement of thermophysical parameters (modulus, etc), perhaps by nanoindentation, and kinetic constants (coarsening exponents, diffusion rates, etc).

iii) The formulation of adhesives for high temperature die attach applications. Despite the generally non-encouraging behaviour of adhesives in this thesis, their low cost and simple processing retains attractions for the HTE sector. It is not inconceivable that with additional development, improved and acceptable behaviour might be achievable - with a niche but lucrative potential market.

Bibliography

[1] R. Schaller, "Moore's law: past, present and future," *Spectrum, IEEE*, vol. 34, no. 6, pp. 52–59, jun 1997.

[2] G. Moore, "VLSI: some fundamental challenges," *IEEE Spectrum*, vol. 16, no. 4, pp. 30–37, 1979.

[3] P. McCluskey, R. Grzybowski, and T. Podlesak, *High Temperature Electronics*. CRC Press, 1997.

[4] A. Elshabini and F. Barlow, *Semiconductor Packages. Encyclopedia of Materials: Science and Technology*. Elsevier Science Ltd., 2008.

[5] S. Riches, C.Johnston, J. Gulliver, *et al.*, "Assessment of the reliability of high temperature electronics packaging technology," in *Proceedings of HiTEC Conference*. Albuquerque, NM, USA: IMAPS, May 2008.

[6] R. Ulrich and W. Brown, *Advanced electronic packaging*. IEEE Press Series on Microelectronic Systems, 2006.

[7] B. Parmentier, O. Vermesan, and L. Beneteau, "Design of high temperature electronics for well logging applications," in *The Global High Temperature Electronics Network (HiTEN)*. Oxford Applied Technology Ltd, July 2003.

[8] *MIL-HDBK-217, Military handbook - Reliability prediction of electronic equipment*, Department of Defense Std., 1991. [Online]. Available: http://www.mil-hdbk-217.com

[9] C. Johnston, A. Crossley, and R. Sharp, "The possibilities for high temperature electronics in combustion monitoring," in *Proc. Advanced Sen-*

sors and Instrumentation Systems for Combustion Processes (Ref. No. 2000/080) IEE Seminar, 2000.

[10] R. Kirschman, *High-Temperature Electronics*. IEEE Press, 1999. [Online]. Available: http://books.google.co.uk/books?id=bKWLQgAACAAJ

[11] J. Rogers, B. Ohme, and R.Normann, "New paradigm in electronics needed to take the heat of deep gas drilling," The American Gas & Oil Reporter, Tech. Rep., November 2005.

[12] Sondex/GEAS [Online]. Available: http://www.ge-energy.com/products_and_services/products/wireline_systems/index.jsp

[13] R. Normann, "First high-temperature electronics product survey," Sandia National Laboratories, Albuquerque, New Mexico , US, Tech. Rep., 2005.

[14] "EU ROHS annex review for Pb die attach exemption." [Online]. Available: www.eicta.org/web/news/telecharger.php?iddoc=815

[15] D. Shangguan, Ed., *Lead-free solder: interconnect reliability*, 1st ed. Materials Park, OH 44073-0002: ASM International, 2005.

[16] P. L. Fevre, "Environmental issues in power electronics (lead-free)," *IEEE Applied Power Electronics Conference and Exposition*, vol. 1, pp. 121–125, 2002.

[17] O. Ogunseitan, "Public health and environmental benefits of adopting lead-free solders," *Jornal of the Minerals, Metals and Materials Society*, vol. 59, pp. 12–17, 2007.

[18] J. Lau, "Reliability of lead free solder joints," *Journal of Electronic Packaging*, vol. 128, pp. 298–301, 2006.

[19] A. Shapiro, J. Bonner, D. Ogunseitant, *et al.*, "Implications of Pb-free microelectronics assemby in aerospace applications," *IEEE Transaction on Components and Packaging Technologies*, vol. 29, pp. 60–70, 2006.

[20] K. Kessel, "NASA lead-free soldering for space applications: lead-free solder body of knowledge." NASA, Kennedy Space Center, Florida, Tech. Rep., May 2005.

[21] J. Cannis, "Green IC packaging," *Adv. Packag*, vol. 8, pp. 33–38, 2001.

[22] J. Nottay, M. Dusek, and C. Hunt, "Creep properties of Sn-Ag-Cu solder in surface mount assemblies," National Physical Laboratory, Tech. Rep. MATC(A)51, 2001.

[23] Q. Xiao, L. Nguyen, and W. D. Armstrong, "Ageing and creep behavior of Sn3.9Ag0.6Cu solder alloy," in *Proc. 54th Electronic Components and Technology Conf*, vol. 2, 2004, pp. 1325–1332.

[24] A. Schubert, H. Walter, R. Dudek, *et al.*, "Thermo-mechanical properties and creep deformation of lead-containing and lead-free solders," in *Proc. Int Advanced Packaging Materials: Processes, Properties and Interfaces Symp*, 2001, pp. 129–134.

[25] J. H. L. Pang, B. S. Xiong, and T. H. Low, "Creep and fatigue characterization of lead free 95.5Sn-3.8Ag-0.7Cu solder," in *Proc. 54th Electronic Components and Technology Conf*, vol. 2, 2004, pp. 1333–1337.

[26] U. Kattner, "Calculation of phase equilibria in candidate solder alloys," *Z. Metallkd*, vol. 92, pp. 1–11, 2001.

[27] N.-C. Lee, "Getting ready for lead-free solders," *Soldering & Surface Mount Technology*, vol. 9, no. 2, pp. 65–69, 1997.

[28] K. Broth, "Lead free solder paste: Effects on the pastes, circuit boards and reflow process," *SMT - Lead free solder paste*, 2000.

[29] J. Bath, "Research update: Lead free solders alternatives," *Circuits Assembly*, pp. 36–40, 2000.

[30] K. Putlitz, "Eliminating lead in electronic assemblies," in *IEEE Electronic and the Environment Conference*, Denver, 2001.

[31] C. Handdwerker, "Processing and properties for lead free solders," in *IEEE Electronic and the Environment Conference*, Denver, 2001.

[32] J. Liu, "Recent advances in conductive adhesives for direct chip attach applications," in *Proc. Symp. The First IEEE Int Polymeric Electronics Packaging*, 1997, pp. 107–122.

[33] D. Lu and C. Wong, "Novel conductive adhesives for surface mount applications," in *Proceedings. International Symposium on Advanced Packaging Materials: Processes, Properties and Interfaces, 1999.*, mar 1999, pp. 288 –294.

[34] Y. Li and C. Wong, "Recent advances of conductive adhesives as a lead-free alternative in electronic packaging: Materials, processing, reliability and applications," *Materials Science and Engineering: R: Reports*, vol. 51, no. 1-3, pp. 1 – 35, 2006.

[35] R. Kisiel and Z. Szczepanski, "Die-attachment solutions for SiC power devices," *Microelectronics Reliability*, vol. 49, pp. 627–629, 2009.

[36] E. Savrun, "Packaging considerations for very high temperature microsystems," in *Proceedings of IEEE Sensors*, vol. 2, 2002, pp. 1139 – 1143.

[37] M. Topfer, *Thick-film microelectronics; fabrication, design, and applications*. New York :: Van Nostrand Reinhold Co., 1971.

[38] R. Johnson, C. Wang, Y.Liu,*et al.*, "Power device packaging technologies for extreme enviroments," *IEEE Transactions on Electronics Packaging Manufacturing*, vol. 30, no. 3, pp. 182–191, July 2007.

[39] M. M. J. Nicolics, "Electrically conductive adhesives." [Online]. Available: http://publik.tuwien.ac.at/files/pub-et_12396.pdf

[40] A. Lyons, "Electrically conductive adhesives: effect of particle composition and size distribution," *Polymer Engineering and Science*, vol. 31, no. 6, pp. 445–450, 1991.

[41] A. M. Lyons, "Electronic packaging: conductive adhesives." *Encyclopedia of Materials: Science and Technology*, pp. 2654 - 2659, 2001.

[42] R. Keusseyan and J. Dilday, "Electric contact phenomena in conductive adhesive interconnections," in *Proceedings of International Symposium on Microelectronics*, Port Erin, Isle of Man, British Isles, 1993, pp. 44–49.

[43] R. A. Pearson, T. B. Lloyd, H. R. Azimi, *et al.*, "Adhesion issues in epoxy-based chip attach adhesives," *IEEE Transactions on Components, Packaging, and Manufacturing Technology, Part A*, vol. 20, no. 1, pp. 31–37, 1997.

[44] M. N. Nguyen and M. B. Grosse, "Low moisture polymer adhesive for hermetic packages," *IEEE Transactions on Components, Hybrids, and Manufacturing Technology*, vol. 15, no. 6, pp. 964–971, 1992.

[45] M. N. Nguyen, I. Y. Chien, M. B. Grosse, *et al.*, "Polycyanate die-attach adhesives for microelectronic applications," in *Proc. th Electronic Components and Technology Conf.*, 1995, pp. 682–687.

[46] K. Suganuma, "Conductive adhesives: Alternative to high temperature solders and the future," in *Proc. 6th Int. Conf. Polymers and Adhesives in Microelectronics and Photonics Polytronic 2007*, 2007, pp. 30–35.

[47] J. Park and J. Osenbach, “Processability and reliability of epoxy adhesive used in microelectronic devices linked to effects of degree of cure and damp heat aging,” *Microelectronics and Reliability*, vol. 46, no. 2-4, pp. 503 – 511, 2006.

[48] I. Mir and D. Kumar, “Recent advances in isotropic conductive adhesives for electronics packaging applications,” *International Journal of Adhesion and Adhesives*, vol. 28, no. 7, pp. 362 – 371, 2008.

[49] K. Vu, “Silver migration - the mechanism and effects on thick film conductors,” *Materials Science Enginnering*, vol. 234, 2003.

[50] C. Kooring and D. Riphagen, “Application of conductive adhesives in microcircuits for "long-life",” *Equipment, Electrocomponent Science and Technology*, vol. 7, pp. 69–75, 1980.

[51] P. McCluskey, “High temperature packaging technology, passives, and reliability - workshop on extreme environments technologies for space exploration,” NASA JPL, NASA JPL, Pasadena, CA., Tech. Rep., May 2003.

[52] J. Licari and D. Swanson, *Adhesives Technology for Electronic Applications - Materials, Processing, Reliability*, 2nd ed. William Andrew Publishing, Jun 2011.

[53] J. Comyn, *Polymer Permeability*. Chapman & Hall, 1985.

[54] S. S. Lawrence, J. L. Willett, and C. J. Carriere, “Effect of moisture on the tensile properties of poly(hydroxy ester ether),” *Polymer*, vol. 42, no. 13, pp. 5643 – 5650, 2001.

[55] L. M. Butkus, P. D. Mathern, and W. S. Johnson, “Tensile properties and plane-stress fracture toughness of thin film aerospace adhesives,” *J. of Adhesion*, vol. 66, pp. 251–273, 1998.

[56] M. K. Antoon and J. L. Koenig, "Irreversible effects of moisture on the epoxy matrix in glass-reinforced composites," *Journal of Polymer Science: Polymer Physics Edition*, vol. 19, no. 2, pp. 197–212, 1981.

[57] A. Apicella, L. Nicolais, G. Astarita, *et al.*, "Effect of thermal history on water sorption, elastic properties and the glass transition of epoxy resins," *Polymer*, vol. 20, no. 9, pp. 1143 – 1148, 1979.

[58] Y. Diamant, G. Marom, and L. J. Broutman, "The effect of network structure on moisture absorption of epoxy resins," *Journal of Applied Polymer Science*, vol. 26, no. 9, pp. 3015–3025, 1981.

[59] R. A. Gledhilla and A. J. Kinlocha, "Environmental failure of structural adhesive joints," *The Journal of Adhesion Volume*, vol. 6, no. 4, pp. 315 – 330, 1974.

[60] D. Klosterman, L. Li, and J. Morris, "Materials characterization, conduction development, and curing effects on reliability of isotropically conductive adhesives," *IEEE Transactions on Components Packaging and Manufacturing Technology*, vol. 21, pp. 23–31, 1998.

[61] A. Lovinger, "Development of electrical conduction in silver-filled epoxy adhesives," *The Journal of Adhesion*, vol. 10, no. 1, pp. 1–15, 1979.

[62] D. Lu, Q. Tong, and C. Wong, "Conductivity mechanisms of isotropic conductive adhesives (ICAs)," *IEEE Transactions on Electronics Packaging Manufacturing*, vol. 22, no. 3, pp. 223–227, 1999.

[63] C. Khoo., J. Liu, M. Agren, *et al.*, "Influence of curing on the electrical and mechanical reliability of conductive adhesive joints," in *Proceedings of International Electronics Packaging Socieity Conference*, Austin, TX, Sep/Oct 1996.

[64] J. Liu, K. Gustafsson, Z. Lai, *et al.*, "Surface characteristics, reliability, and failure mechanisms of tin/lead, copper, and gold metallizations," *IEEE Transactions on Components, Packaging, and Manufacturing Technology, Part A*, vol. 20, no. 1, pp. 21–30, 1997.

[65] R. S. Rorgren and J. Liu, "Reliability assessment of isotropically conductive adhesive joints in surface mount applications," *IEEE Transactions on Components, Packaging, and Manufacturing Technology, Part B: Advanced Packaging*, vol. 18, no. 2, pp. 305–312, 1995.

[66] J. C. Jagt, "Reliability of electrically conductive adhesive joints for surface mount applications: a summary of the state of the art," *IEEE Transactions on Components, Packaging, and Manufacturing Technology, Part A*, vol. 21, no. 2, pp. 215–225, 1998.

[67] R. Dudek, H. Berek, T. Fritsch, *et al.*, "Reliability investigations on conductive adhesive joints with emphasis on the mechanics of the conduction mechanism," *IEEE Transactions on Components and Packaging Technologies*, vol. 23, no. 3, pp. 462–469, 2000.

[68] V. Chidambaram, J. Hattel, and J. Hald, "High-temperature lead-free solder alternatives," *Microelectronic Engineering*, vol. 88, no. 6, pp. 981–989, June 2011.

[69] J. D. Venables, "Adhesion and durability of metal-polymer bonds," *Journal of Materials Science*, vol. 19, no. 8, pp. 2431–2453, 1984.

[70] B.-S. Yim, Y. Kwon, S. Oh, *et al.*, "Characteristics of solderable electrically conductive adhesives (ECA) for electronic packaging," *Microelectronics Reliability*, vol. 52, no. 6, pp. 1165 – 1173, 2012.

[71] Y. Li and C. P. Wong, "Silver migration control in electrically conductive adhesives," in *Proc. HDP'06 High Density Microsystem Design and Packaging and Component Failure Analysis Conf*, 2006, pp. 206–212.

[72] G. Giacomo, *Electrochemistry of Semiconductors and Electronics: Processes and Devices*, J. McHard and F. Ludwig, Eds. Park Ridge, New Jersey, USA: Noyes Publications, 1992.

[73] J. Lin and J. Chan, "On the resistance of silver migration in Ag-Pd conductive thick films under humid environment and applied d.c. field," *Materials Chemistry and Physics*, vol. 43, no. 3, pp. 256 – 265, 1996.

[74] J. Gagne, "Silver migration model for Ag-Au-Pd conductors," *Components, Hybrids, and Manufacturing Technology, IEEE Transactions on*, vol. 5, no. 4, pp. 402 – 407, dec 1982.

[75] J. V. G.D. Davis, *Durability of Structural Adhesive*, A. Kinloch, Ed. Essex, UK: Applied Science Publishers Ltd, 1983.

[76] S. Xu and D. A. Dillard, "Determining the impact resistance of electrically conductive adhesives using a falling wedge test," *IEEE Transactions on Components and Packaging Technologies*, vol. 26, no. 3, pp. 554–562, 2003.

[77] D. Lu and C. P. Wong, "Conductive adhesives for solder replacement in electronics packaging," in *Proc. Int Advanced Packaging Materials: Processes, Properties and Interfaces Symp*, 2000, pp. 24–31.

[78] J. E. Morris, "Isotropic conductive adhesives: Future trends, possibilities and risks," in *Proc. 5th Int. Conf. Polymers and Adhesives in Microelectronics and Photonics, Polytronic Polytronic 2005*, 2005, pp. 233–234.

[79] D. Lu and C. P. Wong, "High performance conductive adhesives," *IEEE Transactions on Electronics Packaging Manufacturing*, vol. 22, no. 4, pp. 324–330, 1999.

[80] J. Hwang, "Filler size and content effects on the composite properties of anisotropic conductive films (ACFs) and reliability of flip chip assembly using ACFs," *Microelectronics Reliability*, vol. 48, no. 4, pp. 645 – 651, 2008.

[81] J. Casady and R. Johnson, "Status of silicon carbide (SiC) as a wide-bandgap semiconductor for high-temperature applications: A review," *Solid-State Electronics*, vol. 39, pp. 1409–1422, 1996.

[82] H. Kato, "Eutectic reactions and textures of Au-Si alloy films on single-crystal silicon," *Japanese Journal of Applied Physics*, vol. 28, no. Part 1, No. 6, pp. 953–956, 1989.

[83] W. Gerlach and B. Goel, "Gold silicon phase diagram," *Solid-State Electronics*, vol. 10, no. 6, pp. 589 – 592, 1967.

[84] J. Harris and E. Rubel, "The role of interfacial compound formation on package reliability," *Advancing Microelectronics*, vol. 35, no. 4, pp. 20–27, July/August 2008.

[85] SGTE - alloy phase diagrams. [Online]. Available: http://www.crct.polymtl.ca/fact/documentation/SGTE/SGTE_Figs.htm

[86] N. Mencinger, M. Carthy, and R. McDonald, "Use of wetting angle measurements in reliability evaluations of Au-Si eutectic die attach," *IEEE/IRPS*, pp. 173–179, 1985.

[87] R. K. Shukla and N. P. Mencinger, "A critical review of VLSI die attachment in high reliability application," *Solid State Technol.*, vol. 28, pp. 67 – 74, 1985.

[88] C. E. Hoge and S. Thomas, "Some considerations of the gold-silicon die bond based on surface chemical analysis," in *Reliability Physics Symposium, 1980. 18th Annual*, april 1980, pp. 301 –311.

[89] R. W. Johnson, P. Zheng, A. Wiggins, *et al.*, "High temperature electronics packaging," in *Proceedings of the HITEN International Conference on High Temperature Electronics*, Oxford, UK, Sep 2007, pp. 17–19.

[90] S. Hsu and C. Liu, "Fabrication of thin-GaN LED structures by Au-Si wafer bonding," *Electrochemical and Solid-State Letters*, vol. 9, pp. G171–G173, 2006.

[91] A. Saunders, "Trends in packaging and interconnection of integrated circuits," *Microelectronics Journal*, vol. 12, no. 1, pp. 23 – 29, 1981.

[92] E. L. Zigler, and D. E. Hillyer, "AES/ESCA/SEM/EDX studies of die bond materials and interfaces,", in *Proc. 22nd Annual Reliability Physics Symposium,*, April 1984,pp. 169–174, 1984.

[93] R. Wolffenbuttel, "Low-temperature intermediate Au-Si wafer bonding; eutectic or silicide bond," *Sensors and Actuators A: Physical*, vol. 62, no. 1-3, pp. 680 – 686, Jul 1997.

[94] *Test method standard for microcircuits, MIL-STD-883 (2010)*, USA Department of Defense Std. [Online]. Available: http://elsmar.com/pdf_files/Military%20Standards/Mil-Std-883.pdf

[95] C. V. Kessel and J. Murphy, "The quality of die attachment and its relationship to stresses and vertical die cracking," in *Proc. 33rd Electronics Components Conf.,*, May 1983, pp. 237–244.

[96] S. Chiang and R. Shukla, "Failure mechanism of die cracking due to imperfect die attachment," in *Proc. 34th IEEE Electron. Components Conference*, 1984, pp. 195–202.

[97] M. Hutter, M. Suchodoletz, H. Oppermann, *et al.*, "Electroplated AuSn solder for flip chip assembly and hermetic sealing - the 7th VLSI packaging workshop of Japan ·," Kyoto, Japan, Tech. Rep., 2004.

[98] F. P. McCluskey, Z. Wang, M. Dash, *et al.*, "Reliability of high temperature lead-free solder alternative," in *Proc. 1st Electronics Systemintegration Technology Conf*, vol. 1, 2006, pp. 444–447.

[99] A.He, B. Djurfors, S. Akhlaghi, *et al.*, "Pulse plating of gold-tin alloys for microelectronic and optoelectronic applications," *Plating and surface finishing*, vol. 89, no. 11, pp. 48–53, 2002.

[100] G. Zeng., S. McDonald, and K. Nogita, "Development of high-temperature solders: Review," *Microelectronics Reliability 52 (2012)*, vol. 52, pp. 1306–1322, 2012.

[101] G. Matijasevic and C. Lee, "Void-free Au-Sn eutectic bonding of GaAs dice and its characterization using scanning acoustic microscopy," *Journal of Electronic Materials*, vol. 18, no. 2, pp. 327–337, 1989.

[102] P. Hagler, P. Henson, and R. W. Johnson, "Packaging technology for electronics applications in harsh, high temperature environments," *IEEE Transactions on Industrial Electronics*, vol. 58, pp. 2673–2682, 2011.

[103] D. Jacobson and G. Humpston, "Gold coatings for fluxless soldering," in *Gold Bull*, 1989, vol. 22, p. 9.

[104] S. K. Kang, P. Lauro, D.-Y. Shih, *et al.*, "Microstructure and mechanical properties of lead-free solders and solder joints used in microelectronic applications," *IBM Journal of Research and Development*, vol. 49, no. 4, pp. 607–620, 2005.

[105] [Online]. Available: www.cmcinterconnect.com/interfaces.pdf

[106] R. Fields, "Physical and mechanical properties of intermetallic compounds commonly found in solder joints," National Institute of Standards and Technology, USA, Tech. Rep., 2001.

[107] [Online]. Available: http://www.cmcinterconnect.com/recent_pub.htm

[108] M. Palmer and R. Johnson, "Thick film modules for 300°C applications," in *Proceedings of the International High Temperature Electronics Conference (HiTEC)*, Santa Fe, NM, US, May 2006, pp. 118–124.

[109] J. Madeni, "Intermetallics formation and growth at the interface of tin based solder alloys (Sn-3.5Ag, Sn-0.7Cu, Sn-3.2Ag-0.8Cu and Sn-9Zn) and copper substrates," in *International Brazing and Soldering*, San Diego, 2003.

[110] G. Y. Li and B. L. Chen, "Formation and growth kinetics of interfacial intermetallics in Pb-free solder joint," *IEEE Transactions on Components and Packaging Technologies*, vol. 26, no. 3, pp. 651–658, 2003.

[111] E. Suhir, "Accelerated life testing in microelectronics and photonics, its role, attributes, challenges, pitfalls, and its interaction with qualification tests," in *Proc. 2nd Int. IEEE Conf. Polymers and Adhesives in Microelectronics and Photonics POLYTRONIC 2002*, 2002, pp. 44–48.

[112] S. Ridout and C. Bailey, "Review of methods to predict solder joint reliability under thermo-mechanical cycling," *Fatigue Fracture of Engineering Materials and Structures*, vol. 30, no. 5, pp. 400–412, 2007.

[113] Y. Qian, X. Ma, and F. Yoshida, "The stress field characteristics in the surface mount solder joints under temperature cycling: temperature effect and its evaluation," *Supplement to the Welding Journal*, vol. 81, no. 6, pp. 85S–89S, 2002.

[114] G. M. Zhang, D. M. Harvey, and D. R. Braden, "Microelectronic package characterisation using sparse signal representation," *NDT & E International*, vol. 40, pp. 609–617, 2007.

[115] P. Yalamanchili, A. Christou, S. Martell, *et al.*, "C-SAM sounds the warning for IC packaging defects," *IEEE Circuits and Devices Magazine*, vol. 10, no. 4, pp. 36–41, 1994.

[116] "Sonix," Sonix, Tech. Rep. [Online]. Available: http://www.sonix.com/learning/files/Plastic_Encapsulated_Integrated_Circuits.pdf

[117] J. Barton, T. Randles, S. Hearne, *et al.*, "Scanning acoustic microscopy and SIMS investigation of CdTe detectors," *Nuclear Instruments and Methods in Physics Research Section A: Accelerators, Spectrometers, Detectors and Associated Equipment*, vol. 458, no. 1-2, pp. 431 – 436, 2001.

[118] R. Ross, Ed., *Microelectronic failure analysis*, 6th ed. ASM International, 2011.

[119] L. J. Balk, "Scanning acoustic microscopy," *Surface and Interface Analysis*, vol. 9, no. 1, pp. 47–54, 1986. [Online]. Available: http://dx.doi.org/10.1002/sia.740090109

[120] M. Hoppe and J. Bereiter-Hahn, "Applications of scanning acoustic microscopy- survey and new aspects," *IEEE Transactions on Sonics and Ultrasonics*, vol. 32, no. 2, pp. 289–301, 1985.

[121] R. Maev, *Acoustic Microscopy*. Wiley-VCH Verlag GmbH & Co, 2008.

[122] L. Herard, "Packaging reliability," *Microelectronic Engineering*, vol. 49, pp. 17–26, 1999.

[123] B. Partee, "The use of scanning acoustic microscopy in electronics manufacturing applications," National Electronics Manufacturing Center of Excellence, Tech. Rep., 2004. [Online]. Available: http://www.empf.org/empfasis/dec04/micro1204.htm

[124] I. Alig, S. Tadjbach, P. Krüger, *et al.*, "Characterization of coating systems by scanning acoustic microscopy: Debonding, blistering and surface topology," *Progress in Organic Coatings*, vol. 64, no. 2-3, pp. 112 – 119, 2009, coatings Science International 2008.

[125] T. Moore, R. McKenna, and S. Kelsall, "Correlation of surface mount plastic package reliability testing to nondestructive inspection by scanning acoustic microscopy," in *29th Annual Proceedings of Reliability Physics Symposium*, Dallas, TX, USA, Apr 1991, pp. 160–166.

[126] T. Chung, J. Jhang, J. S. Chen, *et al.*, "A study of large area die bonding materials and their corresponding mechanical and thermal properties," *Microelectronics Reliability*, vol. 52, pp. 872–877, 2012.

[127] F. Latip, A. Hassan, and R. Yahya, "Delamination and void analysis on die attach epoxy of a QFN package," *Solid State Science and Technology*, vol. 16, no. 2, pp. 207–213, 2008.

[128] X. Deng, N. Chawla, K. K. Chawla, *et al.*, "Deformation behavior of (Cu, Ag)-Sn intermetallics by nanoindentation," *Acta Materialia*, vol. 52, no. 14, pp. 4291 – 4303, 2004.

[129] R. R. Chromik, D.-N. Wang, A. Shugar, *et al.*, "Mechanical properties of intermetallic compounds in the Au-Sn system," *Journal of Materials Research*, vol. 20, pp. 2161–2172, 2005.

[130] A. C. Fischer-Cripps, *Nanoindentation-Mechanical Engineering Series*. Springer Science - Second Edition, 2004.

[131] F.-X. Che, J. H. L. Pang, and L. H. Xu, "IMC consideration in FEA simulation for Pb-free solder joint reliability," in *Proc. Tenth Intersociety Conf. Thermal and Thermomechanical Phenomena in Electronics Systems ITHERM '06*, 2006, pp. 1018–1023.

[132] W. Oliver and G. Pharr, "An improved technique for determining hardness and elastic modulus using load and displacement sensing indentation experiments," *J. Mater. Res*, vol. 7, pp. 1564–1583, 1992.

[133] A. Fischer-Cripps, "Critical review of analysis and interpretation of nanoindentation test data," *Surface and Coatings Technology*, vol. 200, no. 14-15, pp. 4153 – 4165, 2006.

[134] X. Li and B. Bhushan, "A review of nanoindentation continuous stiffness measurement technique and its applications," *Materials Characterization*, vol. 48, no. 1, pp. 11 – 36, 2002.

[135] M. Doerner and W. Nix, "A method for interpreting the data from depth-sensing indentation instruments," *Journal of Materials Research*, vol. 1, pp. 601–616, 1986.

[136] *Die shear strength, MIL-STD-883F, Method 2019.7*, USA Department of Defense Std., Mar. 2003. [Online]. Available: http://elsmar.com/pdf_files/Military%20Standards/Mil-Std-883.pdf

[137] Staystik 415 non-filed dielectric interposer film. Cookson Group. [Online]. Available: http://www.matweb.com/search/datasheettext.aspx?matguid=7d3d2114423b49c4ada1a916137aa228

[138] Staystik 482 non-filed dielectric interposer film. Cookson Group. [Online]. Available: http://www.matweb.com/search/datasheettext.aspx?matguid=e753a874951a451abfd428d51551fe90

[139] G. Selvaduray, "Die bond materials and bonding mechanisms in microelectronic packaging," *Thin Solid Films*, vol. 153, pp. 431–445, 1987.

[140] J. Bauer and M. Bauer, "Cyanate ester based resin systems for snap-cure applications," *Microsystem technologies - micro- and nanosystems - information storage and proc*, vol. 8, no. 1, pp. 58–62, Mar 2002.

[141] Alebond JM7000 technical data sheet. Ablestik. [Online]. Available: http://tds.loctite.com/tds5/docs/ABLEBOND%20JM7000-EN.PDF

[142] S. Gee, C. V. Kessel, J. Murphy, *et al.*, "Acoustic emissions monitoring of die shear testing," *Int. J. Hybrid Microelectronics*, vol. 6, no. 1, pp. 410–418, 1983.

[143] D. Olsen and H. Berg, "Properties of die bond alloys relating to thermal fatigue," *IEEE Transactions on Components, Hybrids, and Manufacturing Technology*, vol. 2, no. 2, pp. 257 – 263, 1979.

[144] M. P. S. Ganesan, Ed., *Lead-free Electronics*. John Wiley & Sons Inc, March 2006.

[145] J. Mayer, "Gold contacts to semiconductor devices," *Solid State Technol.*, pp. 149–157, July 1984.

[146] H. F. Gray, "Surface segregation of non-bonding impurities in gold-silicon preforms," *15th Annual Reliability Physics Symposium*, pp. 272 – 275, 1977.

[147] Y. V. Naidich, V. M. Perevertailo, and L. P. Obushchak, "Density and surface tension of alloys of the systems Au-Si and Au-Ge," *Powder Metallurgy and Metal Ceramics*, vol. 14, pp. 403–404, 1975.

[148] J. E. Johnson, "Die bond failure modes," in *Reliability Physics Symposium, 1974. 12th Annual*, april 1974, pp. 150 –154.

[149] NIST X-ray photoelectron spectroscopy database. [Online]. Available: http://srdata.nist.gov/xps/

[150] D. Shirley, *Phys. Rev. B*, vol. 5, p. 4709, 1972.

[151] M. S. D. Briggs, Ed., *Practical surface analysis*, 2nd ed. Wiley, 1990, vol. 1.

[152] *Properties of Silicon*. INSPEC, The Institution of Electrical Engineers, London and New York, 1988, no. 4.

[153] L. Chen, G. Hunter, and P. Neudeck, "Silicon carbide die attach scheme for 500^{o}C operation," in *MRS Proceedings*, 2000.

[154] P. Becher and W. Newell, "Adherence-fracture energy of a glass-bonded thick-film conductor: effect of firing conditions," *Journal of Materials Science*, vol. 12, pp. 90–96, 1977.

[155] Z. Liu and D. D. L. Chung, "Development of glass-free metal electrically conductive thick films," *Journal of Electronic Packaging*, vol. 123, no. 1, pp. 64–69, 2001.

[156] Y. Enokido and T. Yamaguchi, "Adhesion strength of silver thick-film conductors by solder-free test," *Journal of Materials Science*, vol. 32, pp. 4967–4971, 1997.

[157] D. Mattox, "Thin film metallization of oxides in microelectronics," *Thin Solid Films*, vol. 18, no. 2, pp. 173 – 186, 1973.

[158] S. Achmatowicz and E. Zwierkowska, "Lead free thick film circuits," *Materialy Elektroniczne*, vol. 34, pp. 5– 47, 2006.

[159] N. Panousis, "Copper and silver contamination of thick film gold surfaces," *Thin Solid Films*, vol. 64, no. 1, pp. 41 – 45, 1979.

[160] T. Nordstrom and F. Yost, "Sintering behaviour of a reactively bonded thick film gold ink," *Journal of Electronic Materials*, vol. 7, no. 1, pp. 109–118, 1978.

[161] D. M. Jacobson and G. Humpston, "Fluxless soldering," *International Materials Reviews*, vol. 51, no. 5, pp. 313–328, 2006.

[162] D. J. G. Humpston, Ed., *Principles of soldering*. ASM International, 2004.

[163] W. Bascom and J. Bitner, "Void reduction in large-area bonding of IC components," *Solid-State Technol.*, vol. 18, pp. 37–44, 1975.

[164] S. Kong, D. Feucht, and R. Hecke, "Structure studies in the region of the sofi-soldered joint in silicon power transistor using scanning electron microscopy," *Microstrucl. Sci.*, vol. 3, pp. 511–524, 1975.

[165] D. Kitchen, "Physics of die attach interfaces," in *Reliability Physics Symposium*, no. 18, 1980, pp. 312 – 317.

[166] S. Tan, K. Chang, S. Hu, *et al.*, "Failure analysis of die-attachment on static random access memory (SRAM) semiconductor devices," *J. Electron. Mat.*, vol. 16, pp. 7– 11, 1987.

[167] J. Jang, S. Hayes, J. Lin, *et al.*, "Interfacial reaction of eutectic AuSi solder with Si (100) and Si (111) surfaces," in *Proceedings. 53rd Electronic Components and Technology Conference*, 2003, pp. 1243–1247.

[168] R. Jaccodine, "Surface energy of germanium and silicon," *Journal of Elecrochemical Society*, vol. 10, no. 6, pp. 524–527, June 1963.

[169] E. Jing, B. Xiong, and Y. Wang, "The bond strength of Au/Si eutectic bonding studied by IR microscope," *IEEE Transactions on Electronics Packaging Manufacturing*, vol. 33, no. 1, pp. 31 – 37, 2010.

[170] W. Callister, *Materials science and engineering: an introduction*, 6th ed. Wiley, 2003.

[171] S. Riches, J. Gulliver, M. Langley, *et al.*, "Application of high temperature electronics packaging technology to signal conditioning and processing circuits," in *Proceedings of High Temperature Electronics Conference (HiTEC)*, Albuquerque, NM, US, May 2010.

[172] S. Riches, C. Johnston, A. Crossley, *et al.*, "End of life failure modes for packaged SOI devices for signal conditioning and processing applica-

tions," in *High Temperature Electronics Conference (HiTEC) Proceedings*, Albuquerque, New Mexico, US., May 2012.

[173] S. Riches, C. Johnston, M. Sousa, *et al.*, "High temperature endurance of packaged SOI devices for sigmal conditioning and processing applications," in *Proceedings of High Temperature Electronics Network (HiTEN)*, Oxford, UK, July 2011.

APPENDIX A
ANOVA

Linear contrast is a technique for partitioning ANOVA sum of squares (SS) into individual degrees of freedom (df) and is used to compare mixed effects. In this case, the significance of comparisons using linear contrasts was tested.

Let $x_1, x_2, \ldots, x_p$ denote p numerical quantities from the data obtained (statistics or the raw observations). A linear combination of $x_1, x_2, \ldots, x_p$ is defined to be a quantity L as:

$$L = c_1x_1 + c_2x_2 + \ldots + c_px_p, \tag{A.1}$$

where the coefficients $c_1, c_2, \ldots, c_p$ are predetermined numerical values. If the coefficients $c_1, c_2, \ldots, c_p$ satisfy the condition:

$$c_1 + c_2 + \ldots + c_p = 0, \tag{A.2}$$

then the linear combination L is called a linear contrast.

A hypothesis test was then undertaken in which two hypotheses were considered: H_0= all means are equal, and H_A= all means are not equal. ANOVA partitions total variation into its appropriate components. The total sum of squares (SST) term can be defined as,

$$SST = \sum_{i,j}(y_{ij} - Y)^2, \tag{A.3}$$

where y_{ij} is the result obtained in trial i and combination j, and Y is the mean

of all y_{ij}.

However, SST can be calculated by:

$$SST = SSW + SSB = \sum_{ij}(y_{ij} - Y_i)^2 + \sum_{i} n_i(Y_i - Y)^2, \tag{A.4}$$

where SSW is the sum of squares within groups and SSB the sum of squares between groups. In this case, Y_i is the mean of all i trials for the j combination of factors.

However, once the ANOVA method has been used with linear contrast, SST is defined as:

$$SST_L = \frac{nL^2}{c_1^2 + c_2^2 + \ldots + c_p^2}, \tag{A.5}$$

where n is the number of trials. While performing ANOVA, degrees of freedom should also be considered together with each sum of squares. The degrees of freedom for testing the linear contrast is:

$$df_L = 1. \tag{A.6}$$

In ANOVA analysis with a certain test error, the determination of error variance is very important. The obtained data was then used to estimate F value of Fisher test (F-test). The F ratio for testing the linear contrast is given by:

$$F = \frac{SST_L/1}{MSE}, \tag{A.7}$$

where MSE is the mean square error. Under ANOVA conditions, the MSE is equal to the mean square within groups (MSW) which is given by:

$$MSW = \frac{SSW}{df_W}, \tag{A.8}$$

where df_W is the degree of freedom within groups.

Variation observed (total) in an experiment attributed to each significant factor or interaction is reflected in the percent contribution which shows relative power of a factor or interaction for reducing variation. Factors and interactions with substantial percent contribution play an important role. The percent contribution is dependent on the F-test probability (α) given by:

$$\alpha \sim F_{1,df_W}, \tag{A.9}$$

which is then converted in percentage of confidence:

$$Conf = 100(1 - \alpha). \tag{A.10}$$